ROTATION, VORTEX DYNAMICS AND DISORDER IN NON-EQUILIBRIUM BOSE GASES

RYAN DORAN

Thesis submitted for the degree of
Doctor of Philosophy

School of Mathematics, Statistics and Physics,
Newcastle University,
Newcastle upon Tyne,
NE1 7RU,
United Kingdom

January 2022

Acknowledgements

I am enormously grateful to my main supervisor, Thomas Billam, who has been a fantastic (and very patient) mentor throughout the last 4 years, and has helped me grow as a researcher. I would also like to thank my second supervisor, Nick Parker, who first introduced me to the field of superfluids in a Summer Project many moons ago. I would like to express my gratitude to Andrew Baggaley and Davide Proment for taking the time to examine this thesis.

Some of the greatest distractions during my PhD have come from the lovely people I have shared an office with: Nicola Hewett, Kieran Peel, Cameron Williams, Nick Keepfer, Holly Middleton-Spencer and James Murray. Other members of the department who have made Newcastle a great place to work include Tom Lowe, Alex Hindle, Hannah Kreczak, Sri Prasad, Laura Wadkin and Joe Matthews. It would be remiss if I didn't acknowledge friendships from the wider quantum group: Thomas Flynn, Gary Liu, Richard Tattersall, Keaghan Krog, Luca Galantucci, Em Rickinson, Clarissa Barratt, George Stagg, Andrew Groszek, and Tom Bland. I would also like to thank various members of staff who have offered support over the past years, including Magda Carr, Kate Henderson, Toby Wood, Tami Rogers, Anvar Shukurov, Anne Archibald, Graeme Sarson, Colin Gillespie, Danielle Leonard and Paul Bushby.

Outside of the department, there's a huge number of people who have made the past years infinitely more enjoyable. In no particular order I'd like to thank Jack, Chris W, Joe, Martin, James L, Rob, James G, Eve, Jonathon, Sam, Luke, Rory, Molly, Becky, Bryan, Chris G, Trent, Will and Ben, Devon, Mike, Andrew, Poppy, Scooter, Dr Phil and The Cat.

Of course, none of this would have been possible without the constant love and support of my Mum and Dad. I must also mention my wonderful Nan who showed encouragement with the best lemon meringue pie on earth, and Nathan and Georgia, for never letting me forget that I'm a nerd.

Finally, I thank Hamish whom I hope will never let me forget that bottle of Negroni.

Abstract

Quantum fluids consisting of weakly-interacting atomic Bose Einstein Condensates (BECs) are superfluids, meaning they are able to flow without viscous effects. Superfluids have incredible properties, two of which are particularly interesting. Firstly, unlike the solid body rotation of a normal fluid, when a BEC is forced to rotate an array of quantized vortices is formed. These vortices are topologically protected defects which have a circulation with a fixed magnitude. Secondly, for a sufficiently slow velocity, the flow around an obstacle is a steady laminar flow and no vortices are nucleated; above some critical velocity, quantized vortices are nucleated signalling the appearance of dissipation in the system. In this thesis, we perform numerical and theoretical investigations in two dimensions into BECs which are forced to rotate, and into BECs which flow through a disordered potential.

We present a method for evolving the projected Gross-Pitaevskii equation in an infinite rotating BEC, using quasi-periodic boundary conditions to investigate the behavior of the bulk superfluid in this system in the absence of boundaries and edge effects. We show that by choosing suitable simulation parameters, such as the size of the spatial grid and the number of energy levels considered, the numerical error of this method can be made negligible. Adding dissipation, we use our method to find the lattice ground state for a given number of vortices. We can then perturb the ground-state, to investigate the melting of the lattice at finite temperature. This method opens the door to be able to investigate the dynamics of the superfluid phase transition in a rotating Bose gas without edge effects.

Although superfluid flow past a single obstacle is a well studied problem, far fewer studies have considered the case of a flow through a point-like disorder potential. We identify the relationship between the relative position of two point-like barriers and the critical velocity of such an obstacle. We then show that there is a good mapping between the critical velocity of a system with two barriers, and the critical velocity of a system with a large number of barriers. Driving a superflow through a disordered potential above the critical velocity, we use the projected Gross-Pitaevskii equation to study how the flow is arrested through the nucleation of vortices and the break down of superfluidity, a problem which has interesting connections to quantum turbulence and coarsening. We characterise the vortex decay as the effective width of the barriers is increased, and observe that vortex pinning becomes an important effect.

Finally, we use a modified Point Vortex Model to model a number of quantized vortices which are subject to a continuously varying background potential. We investigate how the interplay of disorder strength and scale affect scaling laws in vortex dynamics.

Contents

List of Figures

Part I

Introduction and Theory

Chapter 1

Introduction

The existence of Bose-Einstein Condensates (BECs) was originally predicted by Satyendra Nath Bose [1], and was later developed theoretically by Albert Einstein [2, 3]. Quantum mechanics stipulates that there are two classes of particles, bosons and fermions. Fermionic particles (such as electrons) have half-integer spin and obey the Pauli exclusion principle, which is to say that fermionic particles are forbidden from entering the same quantum state. Bosonic particles (such as protons) have integer spin and, unlike fermions, may populate the same quantum state. In the gases which occupy the majority of the universe, the constituent particles undergo billiard ball like collisions which dominate the governing dynamics. At very low but finite temperatures, it was predicted that a large number of bosons would occupy the ground state macroscopically. Here the bosons cease to behave like individual particles, bouncing off each other, and instead the wavepackets of each of the particles overlap. As the bosons have entered the same quantum state, there is a coherence across the system as the millions of bosons present behave like one, single, macroscopic quantum object.

Many years passed after Bose and Einstein's prediction without an experimental realisation of a BEC. One of the major stumbling blocks for laboratories was the need to cool the atoms to within a few millionths of a degree of absolute zero. However, due to advances in cooling techniques, a BEC was first experimentally realised in 1995 when the JILA[1] group obtained a condensate of two-thousand ^{87}Rb atoms at a temperature of 170nK [4]. Shortly after this breakthrough, Bose-Einstein Condensation was achieved in ^{7}Li by Bradley *et al.* [5], and then in ^{23}Na by Davis *et al.* [6]. Collectively, these achievements led to huge interests in BEC experiments, and this exciting field of research continues to grow to this day.

In 2001, Cornell, Wieman and Ketterle received a Nobel prize for their studies on BECs [7]; in the following two decades, several prizes have followed for work on the fields of condensed matter and superfluidity. To this day, Bose-Einstein Condensates remain a very active area of research because they are highly experimentally controllable,

[1] Joint Institute for Laboratory Astrophysics, National Institute of Standards and Technology (NIST), and University of Colorado.

they are a versatile test bed for quantum mechanics, and they have widespread potential applications. Around the globe, there are currently hundreds of novel experiments taking place. These experiments range from the manipulation of light using cold atoms [8], to the study of BECs in microgravity [9], to the realisation of turbulence in quantum gases [10]; collectively they are unearthing a plethora of results in this rich and diverse field.

In the remainder of this chapter we provide a more formal definition of Bose-Einstein Condensation, and discuss some of the techniques which are key to its experimental realisation. We then introduce superfluidity, along with two of the excitations which may be present in a superfluid: vortices and solitons. A quick comparison between turbulence in classical fluids and quantum turbulence follows. We end this chapter by motivating the work in this thesis, and providing an overview of the structure of this thesis.

1.1 Bose-Einstein Condensation

Suppose we have a gas of N bosonic particles that occupy a volume V, and are in thermal equilibrium with temperature T, moving with some average velocity $\mathbf{v}$. On average, these particles are separated by some distance d, which may be approximated as $d = (N/V)^{-1/3}$, i.e., one over the cube root of the number density of the gas. The characteristic wavepacket size of each of these particles is given by the thermal de Broglie wavelength

$$\lambda_{\mathrm{DB}} = \sqrt{\frac{2\pi\hbar^2}{mk_BT}}, \tag{1.1}$$

where $\hbar = 1.05 \times 10^{-34}$Js is the reduced Planck constant, and $k_B = 1.38 \times 10^{-23}\mathrm{JK}^{-1}$ is the Boltzmann constant [11]. For our purposes, this wavelength becomes "interesting" at the point where λ_{DB} is comparable to the mean inter-particle spacing d; at this point the gas condenses and its behaviour may be described by a single macroscopic wavefunction. A schematic of this can be found in Fig. 1.1. In the remainder of this part we derive the temperature at which this condensation takes place for a non-interacting gas of bosons, and comment on its applicability to a trapped gas of interacting bosons.

Considering a gas of non-interacting bosons, which are confined in a hard-walled box[2]. Assuming that the bosons are in thermal equilibrium, the occupation number of a single particle state may, on average, be described by the Bose distribution,

$$f_{\mathrm{Bose}}\left(\varepsilon_s\right) = \frac{1}{\exp\left(\frac{\varepsilon_s - \mu}{k_BT}\right) - 1}, \tag{1.2}$$

where μ is the chemical potential of the gas, and ε_s is the energy of the s-th single particle state [3].

[2]This derivation closely follows that of Pethick and Smith [13]. We discuss the differences between the Bose-Einstein condensation temperature derived here, and the Bose-Einstein Condensation temperature for an interacting gas of bosons which are subjected to a trapping potential, at the end of this section.

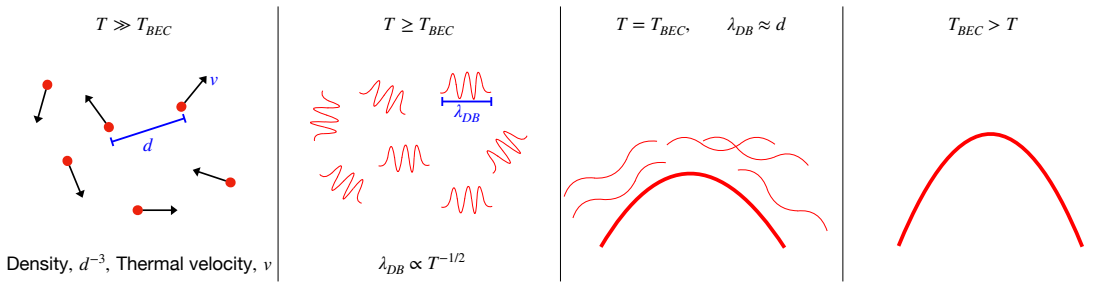

Figure 1.1: A schematic of a gas as it is cooled below the BEC transition temperature. From left to right: At high temperatures, relative to the BEC transition temperature the Bose gas behaves as a classical thermal gas. As $T/T_{\rm BEC}$ is lowered, the de Broglie wavelength of the particles increases. When $T = T_{\rm BEC}$ the de Broglie wavelength is comparable to the mean inter-particle distance. As the temperature is lowered below $T_{\rm BEC}$, the bosons which macroscopically occupy the ground state form a condensate. Figure adapted from Ref. [12].

On average, in a 3D gas, a particle in a particular internal state[3] occupies one quantum state per volume, $(2\pi\hbar)^3$, of phase space. The kinetic energy of a particle with momentum $\mathbf{p} = m\mathbf{v}$ is given by $E_{\mathbf{p}} = |\mathbf{p}|^2/(2m)$, and the region of momentum space where momentum is less than $|\mathbf{p}|$ is simply a sphere with radius $|\mathbf{p}|$. We can use these results to write the total number of states with a lower energy than some value ε as

$$G(\varepsilon) = \frac{1}{(2\pi\hbar)^3} V \frac{4\pi|\mathbf{p}|^3}{3} = \frac{V\sqrt{2}}{3\pi^2}\frac{(m\varepsilon)^{3/2}}{\hbar^3}. \tag{1.3}$$

Therefore, the *density* of states, $g(\varepsilon)$, is the number of states in the infinitesimally thin shell between ε and $\varepsilon + d\varepsilon$. This density is

$$g(\varepsilon) = \lim_{d\varepsilon\to 0}\left[\frac{G(\varepsilon + d\varepsilon) - G(\varepsilon)}{d\varepsilon}\right] = \frac{Vm^{3/2}}{\sqrt{2}\pi^2\hbar^3}\varepsilon^{1/2}. \tag{1.4}$$

Consider the number of particles in an excited state, $N_{\rm ex}$. If $N_{\rm ex} < N$ then not all of the particles are in excited states, and so the remaining particles must be in the single-particle ground state. This means that a Bose-Einstein Condensate is present in the system. The number of atoms in this condensate state is $N_{\rm cond} = N - N_{\rm ex}$. The highest temperature at which the ground state is macroscopically occupied is referred to as the BEC transition temperature, $T_{\rm BEC}$, and is determined by the condition that all of the particles in the system can be placed in excited states.

The Bose distribution, Eqn. (1.2), can be used to calculate the number of excited states. Assuming that N is sufficiently large so that we can write

$$N_{\rm ex} = \int_0^\infty g(\varepsilon)\, f_{\rm Bose}(\varepsilon)\, d\varepsilon = \frac{Vm^{3/2}}{\sqrt{2}\pi^2\hbar^3}\int_0^\infty \frac{\varepsilon^{1/2}}{\exp\left(\frac{\varepsilon-\mu}{k_BT}\right) - 1}, \tag{1.5}$$

[3]Note that, throughout this thesis, we assume that all particles are in the same internal state.

which ignores the zero-point energy of the gas and assumes that the discrete energy levels ε_s can be replaced with the continuous variable ε. The value of this integral is maximised when $\mu = 0$. When $T = T_{\mathrm{BEC}}$, all particles are contained in excited states so Eqn. (1.5) becomes

$$N_{\mathrm{ex}} = \frac{Vm^{3/2}}{\sqrt{2}\pi^2\hbar^3} \left(k_B T_{\mathrm{BEC}}\right)^{3/2} \Gamma\left(\frac{3}{2}\right) \zeta\left(\frac{3}{2}\right), \tag{1.6}$$

where we have introduced the Gamma function

$$\Gamma(n) = \int_0^\infty x^{n-1} e^{-x}\, dx, \tag{1.7}$$

and the Riemann zeta function

$$\zeta(n) = \sum_{x=1}^{\infty} \frac{1}{x^n}. \tag{1.8}$$

For $n = 3/2$, Eqns. (1.7) and (1.8) converge to $\Gamma(3/2) = \sqrt{\pi}/2$ and $\zeta(3/2) \approx 2.612$ respectively. The result of this is that the BEC transition temperature for a uniform, non-interacting, 3D Bose gas is given by

$$T_{\mathrm{BEC}} = \frac{2\pi\hbar^2}{m\left[\zeta(3/2)\right]^{2/3}} \left(\frac{N}{V}\right)^{2/3}. \tag{1.9}$$

It should also be noted that condensation of bosons is not limited to the super cold. Rearranging Eqn. (1.9) we find that

$$\zeta\left(\frac{3}{2}\right) = \lambda_{DB}^3 \frac{N}{V} \tag{1.10}$$

at the BEC transition temperature. The fact that $2.612 \approx \lambda_{DB}^3 N/V$ means that, for the correct balance of density and temperature, a condensate can be realised in any system of bosonic particles. For example, neutron stars are expected to play host to BECs, despite having temperatures of approximately 10^9K [14].

It should be noted that the results quoted in this section are applicable to a three dimensional gas of non-interacting bosons which is not subjected to a trapping potential. Modifications to the value of T_{BEC} are required for Bose gases in systems with reduced dimensionality, as well as for systems which are subject to a trapping potential. In general, Eqn. (1.5) can be written as

$$N_{\mathrm{ex}} = A_\delta \Gamma(\delta)\, \zeta(\delta) \left(k_B T_{\mathrm{BEC}}\right)^\delta, \tag{1.11}$$

where A_δ is a constant, and the value of δ depends on both the dimensionality of the system, and the trapping potential which the bosons are subject to. In a uniform 2D gas, $\delta = 1$ and $\zeta(\delta)$ is the harmonic series which diverges, requiring $T_{\mathrm{BEC}} = 0$. Fortunately, however, Bose-Einstein Condensation is possible in 2D by use of a trapping potential. In the case of a 2D gas in a harmonic trap, $\delta = 2$ and the constants in Eqn. (1.11) are finite.

Finally we note that, while it was originally theorized that BEC would be limited to a gas of non-interacting bosons [1], it was later predicted that the interaction between the bosons would actually assist in the formation of a condensate [15].

1.2 Experimental Realisations

As we have mentioned, a BEC was first experimentally realised in 1995 [4–6], seven decades after they were originally predicted. The observation of a BEC was made possible by developments in laser cooling[4] [16–18] and evaporative cooling [19]. In the following paragraphs, we describe the process by which a gas of bosons may be cooled below T_{BEC}.

The experiment of Anderson *et al.*, [4], begins by collecting about 10^7 atoms of dilute, room temperature, ^{87}Rb gas in a hybrid magnetic and optical trap. The gas is then cooled by lasers. Three pairs of counter-propagating lasers are directed into the trap; the atoms scatter photons from the beams they are travelling towards, creating a "frictional force" which slows the atoms [20]. At this point, approximately half of the atoms are left in the trap, with a temperature of the order of 100μK. The lasers are then switched off, leaving the atoms to be trapped by a magnetic field.

After laser cooling, the next stage is evaporative cooling. The idea behind evaporative cooling is simple: by permitting the highest-energy atoms to leave the trap, the average energy of the remaining atoms is reduced [19]. The number of atoms which escape is controlled by carefully ramping down the magnetic trapping potential [4]. This resulted in an almost pure BEC of 2000 ^{87}Rb atoms at a temperature of 170nK.

For a dilute, ultra-cold, gas of bosons, the interactions between particles are dominated by the s-wave scattering length a_s. If a_s is positive, the inter-particle interactions are repulsive, and a_s can be though of as the length at which atoms rebound in a billiard ball like collision. If a_s is negative, the particles are attracted to each other and the condensate requires an external trapping potential to prevent the collapse of all particles onto a point: a *Bose-nova* [21]. Most importantly, however, in order to ensure that the gas remains sufficiently dilute the s-wave scattering length must be smaller than the mean inter-particle distance. For several species of atomic BECs, it is possible to tune the scattering length by using Feshbach resonances [22]. The ability to tune the interaction strength of an atomic species gives experimentalists unprecedented control over BEC experiments.

While the first BEC experiments were performed by trapping the bosons in harmonic traps [4–6], in order to investigate systems with more complex geometries, there is a need to develop a wider variety of trapping potentials.

The first steps at creating an arbitrary potential were taken by Henderson *et al.* [23]. They were able to form a variety of new traps such as a torus, a diamond, and a ring of spots by using a scanning tweezer beam. This beam played the role of a repulsive optical potential whose effective strength can be controlled by a combination of the velocity and

[4] S. Chu, C. Cohen-Tannoudji and W. D. Phillips would go on to win the Nobel Prize for Physics in 1997 "for developments of methods to cool and trap atoms with laser light".

intensity of the beam. As well as extending the geometries of the traps available, this technique was pioneering in that the trap could be dynamically altered, allowing the strength of the trap to be varied in time as well as space. Later, the group of Gaunt *et al.* [24] used a similar method involving a spatial light modulator to study atomic BECs in a quasi-uniform three dimensional potential.

Further advances have since been made by Gauthier *et al.* [25]. They were able to show that using a digital micromirror device along with a repulsive blue-detuned laser allows for arbitrary control over the trapping potential. It is now possible to directly image high-resolution potentials with minimal heat transfer to the trapped atoms. This enables experimentalists to have an unprecedented level of control over the system geometry.

At the time of writing, BECs have now been realised in a variety of atomic species including spin-polarized atomic Hydrogen [26], metastable Helium [27], alkali metals such as Potassium [28] and Cesium [29], alkaline earth metals such as Calcium [30] and Strontium [31], Chromium [32], and the Lanthanide elements Ytterbium [33], Dysprosium [34], Erbium [35], and Thalium [36]. Aside from their inherent scientific interest, ultra-cold atomic gases have a range of applications. The highly tunable interactions make them ideal for use as a quantum simulator [37, 38] or a quantum computer [39, 40]. Moreover, the atoms are sensitive to the presence of external forces, such as those due to gravitational and magnetic fields, and as such are perfect candidates for use in precise sensing [40–44].

1.3 Superfluidity

The initial connection between Bose-Einstein Condensation and superfluidity is due to London [45] and Tisza [46], who were attempting to find an explanation for superfluidity in liquid ^{4}He [47–49]. The term superfluidity was coined in analogy to "superconductivity", as the fluid appears to flow without viscous effects. The superfluid property of atomic BECs leads to several remarkable properties.

As described above, a BEC flows without viscous effects. This is true so long as the velocity of the flow is lower than some critical velocity of the system, which was predicted by Landau [50]. Above this critical velocity, excitations are created in the fluid, which leads to dissipative effects [51]. We discuss the behaviour of a superfluid in depth in Part III.

In a finite temperature superfluid, a normal fluid component (which is subject to viscous effects) exists alongside a superfluid component. The fraction of the fluid which is in the normal or superfluid components depends on the temperature of the system. This model has led to the prediction and observation of *thermal counterflow*, where the system attempts to diffuse the temperature throughout the system (see, for example, Ref. [52]).

A superfluid does not rotate as a solid body, in the way that a normal fluid does. If a superfluid is forced to rotate with sufficient angular velocity, a series of vortex lines which

carry angular momenta are nucleated, mimicking solid body rotation. The number of vortices in the system depends on the speed of the rotation: the sum of the circulation of all of the vortex lines must be the same as the circulation of a normal fluid rotating at the same speed. The ground state of the rotating superfluid is an ordered lattice of vortices. We will discuss rotating superfluids in detail in Part II. It is important to remark that while a dilute, weakly interacting BEC is a superfluid, the converse is not true. While we have alluded to the fact that temperature has an effect on the condensate and the superfluid fractions, it is not true that these fractions are equivalent. In Part V we give detailed descriptions of how one may calculate the condensate or superfluid fractions; fundamentally, these calculations depend on different observables.

1.3.1 Vortices

A key feature of this thesis is the role and dynamics of quantised vortices. Vortices have been predicted and observed in both two and three-dimensional superfluids [53–57]. These vortices are similar to their classical counterparts (such as you might find by the plug hole in your bath), in that they have a core around which the flow circulates. Unlike vortices in classical fluids, however, the velocity field around a vortex is irrotational [12]. Moreover, in classical systems the size of the vortex core and the strength of the associated velocity field is arbitrary; in a BEC, however, the size of the core is fixed (approximately 10^{-7}m in an atomic Bose Einstein Condensate) and the circulation around the vortex is quantised. The core of a vortex in a BEC is a density depleted "hole", the structure of which will be discussed in Chapter 3. There are several means by which a vortex might be created in a BEC, including phase imprinting [53], forcing the condensate to rotate at sufficiently high angular velocities [58, 59], or by dragging an obstacle through the fluid faster than some critical velocity [60].

While we defer the details of quantized vortices to Chapter 3, we note that they are *topologically protected* objects. A vortex can only be removed from the system by colliding with a boundary, or by annihilating with a vortex which has equal and opposite circulation (an anti-vortex). The rate at which vortices decay is of great importance to turbulent systems, and we will discuss this in Parts III and IV.

1.3.2 Solitons

A second excitation which has been predicted and observed in BECs is a soliton. A soliton is a non-linear wave which has a permanent (localised) form, able to withstand collisions with other solitions [61].

Strictly speaking, a soliton is an exact solution to the one-dimensional Gross-Pitaevskii Equation. In a 3D BEC, however, it is still possible to observe waves which maintain their shape [62–65], which we will refer to as solitary matter waves. Solitons (and solitary matter waves) come in two flavours, bright and dark; these names derive from their connections

to optics.

Bright solitons are conceptually easy to imagine: they consist of a density peak which travels along the background density of the fluid. In atomic BECs, bright solitons can be realised by tuning the inter-particle interactions to be attractive (that is to say, the s-wave scattering length $a_s < 0$) [62–64, 66]. This self-attraction balances dispersive effects via the non-linearity in the Gross-Pitaevskii Equation. Bright solitons in atomic BECs have numerous potential applications, such as in the precision sensing achieved in interferometry [42].

Dark solitons on the other hand are characterised by a density dip about which the phase jumps. These excitations travel with speed $\mathbf{u}$, where $0 < |\mathbf{u}| \leq c$, and c is the speed of sound of the system [12]. If $|\mathbf{u}| = 0$, the soliton is a *black* soliton, where the density is zero at the centre of the soliton and the phase jumps by π. These solitons are found in atomic BECs which have repulsive effective interactions ($a_s > 0$). Dark solitons are of particular interest because of the link between dark solitons and vortices [67]. It has also been found that a dark soliton structure is present in the annihilation process of a vortex anti-vortex pair [68]. This will be discussed further in Chapter 3.

1.4 Classical and Quantum Turbulence

1.4.1 Turbulence in Classical Fluids

Turbulence, a highly random flow with rapid irregular fluctuations in both space and time [69], has been a widely studied phenomenon in classical fluids for centuries. In a normal fluid, which is subject to viscous effects, the degree of turbulence in the flow can be encoded by the dimensionless Reynolds number [70]

$$\mathrm{Re} = \frac{UL}{\nu}, \tag{1.12}$$

where U is the typical velocity of the flow, L is the lengthscale of the system, and ν is the kinematic viscosity of the fluid. Dynamical similarity allows us to map flows with different values of U, L and ν, to the same flow pattern, so long as the combination in Eqn. (1.12) is the same. A *classical* turbulent state involves the nucleation of vortices, which can be as large as the system, L. The energy from these large vortices causes the formation of smaller "eddies", which in turn create smaller eddies, and so on until the eddies are of a lengthscale at which viscous effects dominate. This length scale is known as the Kolmogorov length, and is approximately $\mathrm{Re}^{-3/4}L$. The energy distribution per scale is the celebrated Kolmogorov $-5/3$ law [71], and is found by dimensional analysis to be

$$E(k) \propto k^{-5/3}, \tag{1.13}$$

where k is the wavenumber. This energy distribution is responsible for the decay of turbulence in a classical fluid: the energy which is injected at large scales is transported to smaller length scales, and is then dissipated by viscosity. Turbulence in classical fluids is typically associated with high Reynolds numbers, which lead to energy transfers across length scales which vary by many orders of magnitude.

1.4.2 Turbulence in Atomic BECs

In atomic BECs, unlike in a classical fluid, there is no viscosity. Moreover, in an atomic BEC, the size of a vortex is fixed by the healing length of the condensate, ξ, which we will discuss further in Chapter 2. Turbulence in atomic BECs consists of a tangle of superfluid vortex lines [72, 73]. These vortex lines can be deformed from a straight line [74], and interact with each other by reconnecting [75], processes which cause the emission of sound into the system [76, 77]. In superfluid systems, the dissipation of sound is analogous to dissipation due to viscosity in normal fluids [73].

There are two types of quantum turbulence. The first type of quantum turbulence is *quasiclassical* turbulence (which is also known as Kolmogorov turbulence). Quasiclassical turbulence is present in superfluid systems when a classical energy cascade from large to small length scales can be found in a specific range [78, 79]. In this case, the vortex tangle contains metastable bundles of parallel vortex lines, and energy is transferred from the scale of vortex bundles down to individual vortices [80]. The second type of quantum turbulence is *ultraquantum* turbulence (which is also known as Vinen turbulence). Ultraquantum turbulence is characterised by a random tangles of vortices, in the absence of large scale structures. This form of turbulence has been theoretically predicted [81] and experimentally observed [82].

It would appear that quantum turbulence is simpler than its classical counterpart, since vortices are clearly defined structures; unfortunately, there are experimental limitations to the observation of turbulence in atomic BECs [73]. Firstly, BECs are often formed within harmonic trapping potentials, which means that quantities such as density and speed of sound are spatially dependent. This meant that initial realisations of quantum turbulence were subject to these inhomogeneities [72, 83]. With the recent development of box-like trapping potentials, however, it has been possible to observe an energy cascade in a homogeneous BEC [10, 84]. Secondly, turbulent BEC experiments are limited by the lengthscales available. In the recent experiment of Navon *et al.* [84], the condensate was confined in an optical trap of length 2.7×10^{-5}m, while the healing length of the condensate was approximately 1.2×10^{-6}m. Since the size of the system and the width of the vortex core are roughly comparable, it is difficult to extract a reliable scaling law [73].

1.4.3 2D Quantum Turbulence

Given that this thesis is a study of two dimensional Bose gases, we end this section with a discussion of two dimensional quantum turbulence (2DQT). As discussed above, turbulence in 3D is characterised by the transfer of energy from large scales to small scales. On the other hand, in 2D flows that are subject to small scale forcing, the transport of energy towards shorter scales is suppressed, and kinetic energy is transferred to larger scales [85, 86]. This mechanism is often referred to the *inverse* energy cascade, and has been shown to be a feature of 2DQT in BECs both theoretically [87–89] and experimentally [83, 90]. In addition to the energy cascade exhibited by 2DQT, Reeves *et al.* [91] observed signatures of an enstrophy cascade in simulations with a large number of vortices.

A result of the inverse energy cascade is the prediction that like-sign vortices will cluster, leading to the formation of large scale Onsager Vortex structures. These large scale vortex structures grow from small scales, and were predicted to occur at negative temperature states [92]. We note that a system with a limited phase space, where increasing energy will eventually decrease the entropy of the system, is defined as a state with negative absolute temperature [93]. Since Onsager's original prediction, such vortex clusters have been studied theoretically [88, 93–96] and experimentally observed [90, 97]. These structures are particularly interesting as they link the spectral condensation of kinetic energy at the system scale with the negative-temperature vortex clusters of vortices predicted by Onsager [88].

BECs are the perfect system in which to study 2DQT, given that they are formed in trapping potentials which can be controlled to give 2D vortex dynamics [98]. Research in this area is pertinent in many systems, as realising 2DQT in atomic BECs offers a highly controllable fluid system which one may use as a test-bed for long standing questions in classical turbulence. This link is supported by the recent predictions that the dimensionless Reynolds number might extend to describe superfluid flows [99], and the observation of the celebrated von Kármán vortex street in a quasi-2D superfluid [100]. Moreover, they may be used to explore different quantum systems which do not have classical counterparts.

1.5 Thesis Motivation

This thesis contains theoretical and numerical studies into the dynamics of a two dimensional Bose gas. There are two main systems of interest. We begin by considering how one might model the bulk of a rotating BEC at finite temperature, in the absence of edge effects. In order to do this, we use the *projected* Gross Pitaevskii Equation (PGPE), a classical field equation which is widely used in describing weakly interacting Bose gases at finite temperature. We present a psuedo-spectral method for evolving the PGPE in an infinite rotating system, and we show that the numerical error of our method is negligible for suitable simulation parameters. We find that, allowing our system to relax, the ground

state is the expected hexagonal lattice of quantized vortices.

As an application of our method, we consider the dynamics of the rotating system after the ground state has been perturbed. As the amount of noise which is added to the system is increased, we observe that the lattice ground state melts, to be replaced with a chaotic system filled with short-lived vortex-antivortex pairs. We mathematically develop the standard first order correlation function so that it may be used in our system; in doing so, we find evidence that the system has undergone a phase transition not previously seen in an unbounded rotating system.

The second system which we consider is that of a BEC in the presence of a disordered trapping potential. There are two, quite distinct, methodologies by which we study this problem, dubbed the 'Dirty Boson' problem. In the first instance we use the PGPE to simulate a BEC with a potential which is zero everywhere, other than at a series of point-like repulsive barriers. These barriers are sufficiently well separated that, in the space between them, the condensate recovers its background density. To the best of our knowledge, this is the first time such a system has been considered.

We begin the study of the point-like disordered potential by calculating the critical velocity for vortex nucleation past a pair of barriers, before comparing this result to a system with many barriers. We then observe the effect of a disordered potential on a superfluid BEC which is initially faster than the critical velocity. The speed of the superfluid is slowed as vortices are nucleated, and we find that the rate at which these vortices annihilate is significantly different to the rate one would expect in a homogeneous system. Furthermore, we find that vortex pinning becomes an important phenomenon as the size of the barriers is increased.

Progressing our survey of BECs in the presence of disorder, we examine a system where the background trapping potential is disordered and varies continuously over some scale. In order to consider the dynamics of this system, we use a point vortex model which takes into account the effect of fluctuations in the background of the fluid in which the vortices exist. Considering the rate at which the vortices annihilate (which is related to the growth of the correlation length of the system), we find that, as the amplitude and scale of the disordered potential increases, there is a significant deviation from the results found for a homogeneous system.

1.6 Thesis Overview

This thesis is arranged in 5 parts, the contents of which are as follows:

I - Introduction and Theory

- In this Chapter we have introduced Bose Einstein Condensation, superfluidity, and quantum turbulence in weakly interacting dilute condensates. We have also highlighted some key experiments which have been performed to date.

- In Chapter 2 we introduce the theoretical groundwork which we will build upon in the main part of the thesis. We introduce the Gross–Pitaevskii equation (GPE), used to model Bose gases at zero temperature, and go on to introduce the *projected* Gross–Pitaevskii equation (PGPE) which accounts for Bose gases at finite temperature and plays a central role in this thesis.

- In Chapter 3 we introduce quantum vortices which are an elementary excitation in superfluids. We describe the mechanisms by which these vortices may be generated, and discuss the key differences between quantum vortices in two and three dimensional systems.

II - Rotating Bose Einstein Condensates

- In Chapter 4 we discuss the effect of rotation on a 2D system, and consider previous approaches to simulate systems of BECs which undergo rotation.

- In Chapter 5 we construct a method for implementing the PGPE in an infinite rotating system. We show how the convergence of this model depends on simulation parameters such as the size of the spatial grid, and the number of Landau levels. We confirm that our method produces a vortex lattice as the ground state of this system.

- In Chapter 6 we look at the effect of perturbing the lattice ground state of a rotating system, and compare this to thermal effects in the search for a phase transition in 2D rotating superfluids. We measure some of the statistics which are characteristic of a BKT transition.

III - The Dirty Boson Problem

- In Chapter 7 we introduce the Dirty Boson Problem, which concerns the presence of disorder in a Bosonic system. We go on to identify the relationship between the relative position of two point-like barriers and the critical velocity of such an arrangement. We then show that there is a good mapping between the critical velocity of a system with two obstacles, and a system with a large number of obstacles.

- In Chapter 8 we establish an initial superflow through a point-like disordered potential, moving faster than the critical velocity, and then study how the superflow is arrested through the nucleation of vortices and the breakdown of superfluidity. We then calculate the vortex decay rate as the effective width of the barriers is increased, and show that vortex pinning becomes a more important effect for these larger barriers.

IV - Point Vortex Models

- In Chapter 9 we introduce the point vortex model, and discuss current theoretical progress in using this model to simulate the dynamics in a BEC. We then introduce a dissipative point vortex model which takes into account variations in the background density of the BEC.

- In Chapter 10 we investigate the behaviour of many vortices which are subjected to a continuously varying, disordered, background potential. These simulations are carried out using the updated point vortex model described in Chapter 9.

V - Conclusions, Future Work and Appendices

- In Chapter 11 we draw conclusions for the work presented, and suggest future avenues of research.

- In Appendix A we present a derivation of the GPE, show how it may be modified for a 2D system, and derive the hydrodynamic equations of motion. We also detail the methods used to extract the condensate fraction and the superfluid fraction of a system.

- In Appendix B we give detailed derivations of the analytic results presented in Part II.

- In Appendix C we provide information on the ring plaquette method, the means by which we detect pinned vortices in Part III.

- In Appendix D we provide a detailed derivation of the 2D point vortex model which takes into account background fluctuations in density. We also present some simple analytic solutions to this model.

1.7 List of Publications

Work in this thesis has been partially covered in the following publications:

[101] *Numerical method for the projected Gross–Pitaevskii equation in an infinite rotating 2D Bose gas*, R. Doran and T. P. Billam, *Phys. Rev. E* **102**, 033309 (2020).

[102] *Critical Velocity and Arrest of a Superfluid in a Point-Like Disordered Potential*, R. Doran, A. J. Groszek and T. P. Billam, submitted to *Phys. Rev. A*. Pre-print available at: arXiv:2201.11887

- *Point Vortex Dynamics in a Disordered Potential*
  R. Doran and T. P. Billam, in preparation.

Other work

[103] *Engineering bright matter-wave solitons of dipolar condensates*
M. J. Edmonds, T. Bland, R. Doran and N. G. Parker *New J. Phys.* **19**, 023019 (2017).

Chapter 2

Theoretical Modelling of Bose-Einstein Condensates

In this chapter we introduce the key theoretical models by which we might describe an atomic Bose-Einstein Condensate. The majority of these models are based on the Gross-Pitaevskii Equation (GPE). We will discuss the assumptions made when using this equation, as well as some of its key properties.

2.1 The Mean Field Description

Typically, in order to describe the behaviour of N quantum particles which interact with one and other, one must construct an N-body wavefunction $\Psi\left(\mathbf{r}_1, \mathbf{r}_2, \ldots, \mathbf{r}_N, t\right)$, which obeys the many-body Schrödinger equation. Here the coordinate $\mathbf{r}_j$ describes the position of the j-th atom. This approach, however, is prohibitively computationally expensive when one considers the number of atoms which are present in a BEC experiment, which is of the order of 10^6 [104].

Making the assumption that the number of atoms N in the condensate mode is large, it is possible to neglect the difference between N and $N-1$ [105]. In this case, the creation and annihilation operators are approximately commutative and the many-body quantum operator may be replaced by a macroscopic wavefunction which behaves classically [106]. The evolution of this wavefunction is described by the celebrated Gross-Pitaevskii Equation (GPE) [107–109]. In the remainder of this section, we give a brief derivation of this equation; a full derivation, following Ref. [110], can be found in Appendix A.1.

The second quantised Hamiltonian for an interacting Bose gas is

$$\begin{aligned}\hat{\mathcal{H}}(t) &= \int d^3\mathbf{r}\ \hat{\Psi}^\dagger\left(\mathbf{r},t\right)\hat{\mathcal{H}}_{\text{s.p.}}\left(\mathbf{r},t\right)\hat{\Psi}\left(\mathbf{r},t\right) \\ &+ \frac{1}{2}\int d^3\mathbf{r}\ \int d^3\mathbf{r}'\hat{\Psi}^\dagger\left(\mathbf{r},t\right)\hat{\Psi}^\dagger\left(\mathbf{r}',t\right)V_{\text{int}}\left(\mathbf{r},\mathbf{r}'\right)\hat{\Psi}\left(\mathbf{r}',t\right)\hat{\Psi}\left(\mathbf{r},t\right), \end{aligned} \tag{2.1}$$

where the quantum field operator $\hat{\Psi}(\mathbf{r},t)$ may be written in terms of single-particle wave-

functions as

$$\hat{\Psi}(\mathbf{r},t) = \sum_j \psi_j \hat{a}_j, \tag{2.2}$$

where $\hat{a}_j$ annihilates a boson located in the ψ_j state [111]. The first integral in Eqn. (2.1) corresponds to a non-interacting ideal gas, whose single-particle Hamiltonian is

$$\hat{\mathcal{H}}_{\text{s.p.}}(\mathbf{r},t) = -\frac{\hbar^2}{2m}\nabla^2 + V_{\text{ext}}(\mathbf{r},t), \tag{2.3}$$

for some external (trapping) potential, V_{ext}, which in general depends on both position and time. Here $\hbar$ is the reduced Planck's constant, $\hbar = h/(2\pi)$, and m is the mass of the atomic species. We assume that the gas is sufficiently dilute that 3-body collisions are rare, so V_{int} need only describe interactions between two bosons. Assuming that the temperature of the gas is sufficiently low, the interactions between particles are low energy collisions which take place on length scales of the s-wave scattering length of the particles, a_s. Mathematically, this means that we can model the effective interactions using a delta function pseudo potential [13]

$$V_{\text{int}}(\mathbf{r},\mathbf{r}') = g\delta(\mathbf{r}-\mathbf{r}'), \tag{2.4}$$

where the interaction strength is given by

$$g = \frac{4\pi\hbar^2 N a_s}{m}. \tag{2.5}$$

Experimentally, the sign and magnitude of g can be tuned by using Feshbach resonances [22]. For $g > 0$, the interactions are repulsive and the collisions between atoms are similar to the elastic collisions of two hard spheres. If $g < 0$ the system has attractive interactions which, in a homogeneous system, will lead to a collapse of the condensate [112, 113]. Throughout this thesis we will only consider repulsive interactions, given by $g > 0$.

The Bose field operator $\hat{\Psi}(\mathbf{r},t)$ evolves according to the Heisenberg equation of motion

$$i\hbar\frac{\partial}{\partial t}\hat{\Psi}(\mathbf{r},t) = \left[\hat{\Psi}(\mathbf{r},t), \hat{\mathcal{H}}\right], \tag{2.6}$$

and the derivation continues by expanding the commutator on the right hand side of Eqn. (2.6) to get

$$i\hbar\frac{\partial}{\partial t}\hat{\Psi}(\mathbf{r},t) = \hat{\mathcal{H}}(\mathbf{r},t)\hat{\Psi}(\mathbf{r},t) + \int d^3\mathbf{r}''\ \hat{\Psi}^\dagger(\mathbf{r}'',t)\, V_{\text{int}}(\mathbf{r},\mathbf{r}'')\hat{\Psi}(\mathbf{r}'',t)\hat{\Psi}(\mathbf{r},t). \tag{2.7}$$

Assuming that the gas is at zero temperature, so that we may ignore thermal excitations, and that there are a large number of atoms present in the condensate, $N \gg 1$, the many-body wavefunction can be approximated by a single macroscopic wavefunction. This means that we may decompose the operator $\hat{\Psi}(\mathbf{r},t)$ as the sum of a mean field term,

$\left\langle \hat{\Psi}(\mathbf{r},t) \right\rangle = \Psi(\mathbf{r},t)$, and a fluctuation term, $\delta\hat{\Psi}(\mathbf{r},t)$, where $\left\langle \delta\hat{\Psi}(\mathbf{r},t) \right\rangle = 0$. Substituting this decomposition into Eqn. (2.7) and integrating over the delta function in Eqn. (2.4) before taking expectation values leads to the Gross-Pitaevskii Equation.

2.2 The Gross Pitaevskii Equation

The result of the mean-field description is the Gross-Pitaevskii Equation (GPE)

$$i\hbar\frac{\partial\Psi}{\partial t} = -\frac{\hbar^2}{2m}\nabla^2\Psi + V_{\text{ext}}\Psi + g|\Psi|^2\Psi - \mu\Psi. \tag{2.8}$$

The first term on the right hand side is the kinetic term, and the second term is the potential term (due to the external potential in which the condensate is trapped). For a homogeneous system the trapping potential is $V_{\text{ext}} = 0$, but generally V_{ext} may be a function of both position and time. The third term, $g|\Psi|^2\Psi$, represents the atomic interactions. In the case where there are no interactions, $g = 0$, Eqn. (2.8) reduces to the Schrödinger equation. The final term contains the chemical potential, μ, which will be introduced in Sec. 2.2.2. Formally, Eqn. (2.8) conserves the particle number even without the final term, however in the grand-canonical ensemble we require this extra term. We add it here to ensure that the ground state has no time dependence.

Surprisingly, despite the fact that the GPE is only strictly valid at zero temperature, the equation still provides a quantitative model for systems of ultra-cold gases at finite temperature, so long as the temperature is small compared to the critical temperature for Bose-Einstein condensation [110]. The role of the GPE when the temperature of the system is finite is discussed in Sec. 2.5.

2.2.1 Conserved Quantities

The GPE is an equation of motion which describes a classical microcanonical field in which the number of atoms and energy are conserved quantities. The macroscopic wavefunction is normalised to the total number of atoms, N, so that

$$N = \int d^3\mathbf{r}|\Psi|^2. \tag{2.9}$$

This is to say that the norm of the wavefunction is conserved since the number of atoms is conserved. The energy functional of the system may be written as [110]

$$\mathcal{E}[\Psi] = \frac{\hbar^2}{2m}|\nabla\Psi|^2 + V_{\text{ext}}|\Psi|^2 + \frac{1}{2}g|\Psi|^4 - \mu|\Psi|^2, \tag{2.10}$$

and the total energy is

$$E[\Psi] = \int d^3\mathbf{r}\mathcal{E}[\Psi] = E_{\text{kin}} + E_{\text{pot}} + E_{\text{int}} - E_{\text{chem}}. \tag{2.11}$$

Here we have identified the terms as the kinetic energy E_{kin}, the potential energy E_{pot}, the interaction energy E_{int}, and the energy due to the chemical potential term E_{chem}. Providing that the external trapping potential V_{ext} is independent of time, the total energy is conserved during the evolution of the condensate. The Gross-Pitaevskii Equation may also be derived by minimising Eqn. (2.10) at fixed μ, where μ is a Lagrange multiplier ensuring that particle number is conserved [13].

2.2.2 The Time Independent GPE and the Chemical Potential

Suppose that both the wavefunction and the trapping potential are steady, so that $\Psi(\mathbf{r},t) = \Psi_0(\mathbf{r})$ and $V_{\text{ext}}(\mathbf{r},t) = V_{\text{ext}}(\mathbf{r})$. Then Eqn. (2.8) may be re-written as

$$\mu\Psi_0 = -\frac{\hbar^2}{2m}\nabla^2\Psi_0 + V_{\text{ext}}(\mathbf{r})\Psi_0 + g|\Psi|^2\Psi_0, \tag{2.12}$$

meaning that μ is the eigenvalue of the time-independent GPE. We note that the norm of the stationary and time-independent solutions are independent of the global phase, $|\Psi(\mathbf{r},t)|^2 = |\Psi_0(\mathbf{r})|^2$. Integrating Eqn. (2.12) allows one to write the chemical potential as

$$\mu = \frac{1}{N}\left(E_{\text{kin}} + E_{\text{pot}} + 2E_{\text{int}}\right), \tag{2.13}$$

indicating that μ is a useful energy scale. More generally, for large N, as is required by the mean-field theory, the difference in ground-state energies $E_N - E_{N-1}$ is small, allowing us to write $\mu = \partial E/\partial N$ [13], and so μ can be thought of as the energy required to add a particle to a system with a large number of atoms, N.

2.2.3 Quasi-Two-Dimensional GPE

Throughout this thesis, we will use the GPE to simulate a 2D dimensional system, while Eqn. (2.8) describes a 3D system. In this subsection we give a brief derivation as to how one finds an effective 2D GPE.

Experimentally, a quasi-2D system was first achieved by Görlitz *et al.* [114], and has remained an area of experimental interest (see, for example, Refs. [83, 100, 115–124]). Typically, it is possible to realise a 2D condensate by working in a system which has a strong harmonic trapping in the z direction,

$$V_{\text{3D}}(\mathbf{r},t) = V_{\text{ext}}(x,y,t) + \frac{1}{2}m\omega_{\parallel}^2 z^2. \tag{2.14}$$

Such a potential results in a highly oblate ("pancake" shaped) condensate when the trapping frequencies are set so that $\hbar\omega_{\parallel} \gg \mu$. With this tight confinement in the z direction, the excitation of modes in the z direction is prevented. This leads to a 3D wavefunction

$$\Psi_{\text{3D}}(x,y,z,t) = \frac{1}{\sqrt{\pi}\sqrt{l_z}}\Psi_{2D}(x,y,t)\exp\left(-\frac{z^2}{2l_z^2}\right), \tag{2.15}$$

where the z dependence is a Gaussian ground state, and l_z is the oscillator length in the z direction, $l_z = \sqrt{\hbar/\left(m\omega_\parallel\right)}$. The numerical pre-factors of this wavefunction are chosen so that $\int d^2\mathbf{r}\,|\Psi_{2D}|^2 = N$. We note, however, that the confinement does not need to be especially strong in order to observe effectively 2D vortex dynamics; Rooney *et al.* [98] found that the critical oblateness to "freeze out" the third dimension is $\omega_\parallel/\omega_\perp \approx 8$.

It is possible to derive a quasi-2D GPE by substituting Eqn. (2.15) into the energy functional of Eqn. (2.8) and integrating out the z dependence. This yields

$$i\hbar\frac{\partial\Psi_{2D}}{\partial t} = -\frac{\hbar^2}{2m}\nabla^2\Psi_{2D} + V_{\text{ext}}(x,y,t)\Psi_{2D} + g_{2D}\,|\Psi_{2D}|^2\,\Psi_{2D} - \mu_{2D}\Psi_{2D}, \tag{2.16}$$

which has exactly the same functional form as Eqn. (2.8), however the quasi-2D inter-particle attraction parameter is given by

$$g_{2D} = \frac{g_{3D}}{\sqrt{2\pi}l_z} = \frac{\sqrt{8\pi}\hbar^2 a_s}{m l_z}, \tag{2.17}$$

and the 2D chemical potential is

$$\mu_{2D} = \mu_{3D} - \frac{1}{2}\hbar\omega_\parallel. \tag{2.18}$$

In the remainder of this thesis, where the number of dimensions is clear, we will drop the $2D$ subscripts. A detailed derivation of the updated parameters g_{2D} and μ_{2D} can be found in Appendix A.2. It is possible to construct a similar argument for a 1D condensate, with updated parameters g_{1D} and μ_{1D}, however this calculation is omitted from this thesis.

2.2.4 The Thomas-Fermi Profile

Here we introduce an approximation which allows us to find the ground state of a condensate with an analytic treatment. For the purposes of clarity, we only show the solution to a 1D harmonic trap in Fig. 2.1. In general, however, the Thomas-Fermi approximation can be applied to a wide variety of trapping potentials.

Consider a 1D condensate which is trapped by a potential $V_{\text{ext}}(x)$. Suppose that we can ignore the kinetic term, then the time-independent GPE simplifies to

$$\mu\Psi = V_{\text{ext}}\Psi + g|\Psi|^2\Psi. \tag{2.19}$$

This approximation is known as the Thomas-Fermi approximation, and is well suited to steady states of condensates which are subject to strong repulsive interactions (the latter condition is required so that the condensate is flattened in the centre of the trap). The

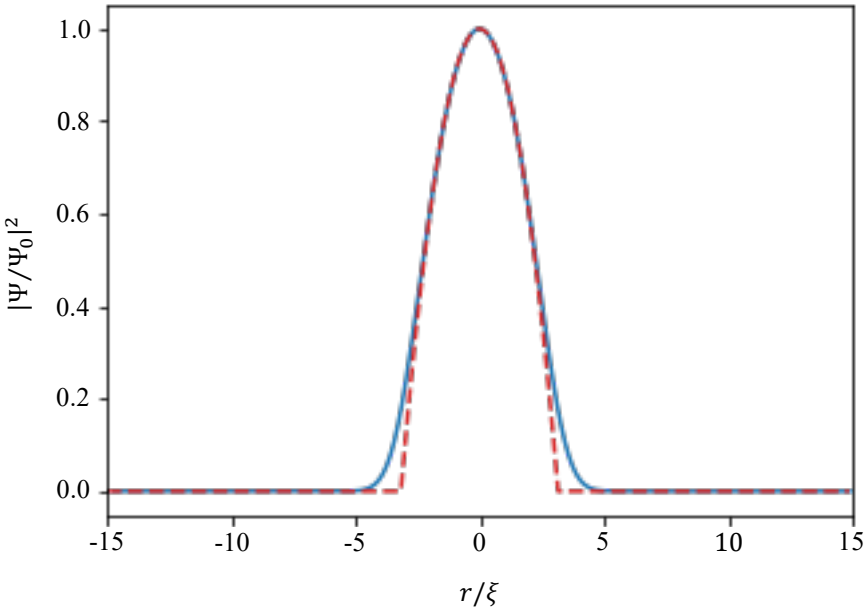

Figure 2.1: The density profile of a condensate in a harmonic trap. The density profile given by the Thomas-Fermi solution, red dashed line, and the density profile given by numerically integrating the GPE, blue solid line.

wavefunction of this condensate is then given by

$$\Psi_{TF} = \sqrt{\frac{\mu - V_{\text{ext}}(x)}{g}}\, \Theta\left(\mu - V_{\text{ext}}(x)\right), \tag{2.20}$$

where $\Theta(\cdot)$ is the Heaviside step-function, used to ensure that the density is non-negative. Using the Heaviside step-function leads to an inequality which tells us where the wavefunction is non-zero, $\mu \geq V_{\text{ext}}(x)$, which in general we can solve for x. This leads to the Thomas-Fermi radius, R_{TF}, which satisfies $\mu = V_{\text{ext}}(R_{TF})$.

In the case where a one-dimensional condensate is in a harmonic trap, $V_{\text{ext}}(x) = m\omega_x^2 x^2/2$, the Thomas-Fermi radius is given by $R_{TF} = \sqrt{2\mu/m\omega_x^2}$. A plot of the Thomas-Fermi density for a harmonically trapped condensate is shown in Fig. 2.1. Note that the density has the form of an inverted parabola and is an excellent fit in the centre of the trap. There is a small disagreement between the Thomas-Fermi and numerical solutions at the edge of the trap, since gradients of the condensate are not negligible here.

2.3 Hydrodynamic Interpretation

The GPE is closely linked to hydrodynamic equations of motion, as we will uncover in this section. As a complex field, it is often enlightening to re-write the wavefunction Ψ in the form

$$\Psi(\mathbf{r}, t) = \sqrt{\rho(\mathbf{r}, t)} e^{i\theta(\mathbf{r},t)}, \tag{2.21}$$

which we shall refer to as a Madelung transform [125]. This form allows us to identify the density of the wavefunction, $\rho(\mathbf{r},t) = |\Psi(\mathbf{r},t)|^2$. We are also able to identify the fluid velocity field, $\mathbf{v}$ which is proportional to the gradient of the phase,

$$\mathbf{v}(\mathbf{r},t) = \frac{\hbar}{m}\nabla\theta(\mathbf{r},t), \tag{2.22}$$

meaning that the physical interpretation of the phase of the condensate is as the velocity potential.

Substituting the Madelung transform, Eqn. (2.21), into the GPE, Eqn. (2.8), and considering real and imaginary parts yields two equations. Considering the imaginary parts, one arrives at the continuity equation

$$\frac{\partial\rho}{\partial t} + \nabla\cdot(\rho\mathbf{v}) = 0. \tag{2.23}$$

This equation describes the conservation of the mass of the fluid. We note, if we multiply the GPE Eqn. (2.8) by $\Psi^*(\mathbf{r},t)$ and subtract the complex conjugate of the resulting equation, then we can derive a similar continuity equation[1]

$$\frac{\partial}{\partial t}|\Psi|^2 + \nabla\cdot\left[\frac{\hbar}{2mi}\left(\Psi^*\nabla\Psi - \Psi\nabla\Psi^*\right)\right] = 0. \tag{2.24}$$

Comparing the forms of Eqn. (2.23) and Eqn. (2.24), we can identify the condensate velocity

$$\mathbf{v}(\mathbf{r}) = \frac{\hbar}{2mi}\left[\frac{\Psi^*(\mathbf{r})\nabla\Psi(\mathbf{r}) - \Psi(\mathbf{r})\nabla\Psi^*(\mathbf{r})}{|\Psi(\mathbf{r})|^2}\right], \tag{2.25}$$

and from there, the current density of the wavefunction

$$\mathbf{J}(\mathbf{r}) = \frac{\hbar}{2mi}\left[\Psi^*(\mathbf{r})\nabla\Psi(\mathbf{r}) - \Psi(\mathbf{r})\nabla\Psi^*(\mathbf{r})\right], \tag{2.26}$$

which is equivalent to the result $\mathbf{J} = \rho\mathbf{v}$.

If, on the other hand, we substitute Eqn. (2.21) into Eqn. (2.8) and consider the real parts, we arrive at

$$\frac{\partial\mathbf{v}}{\partial t} + (\mathbf{v}\cdot\nabla)\mathbf{v} = -\frac{1}{\rho}\nabla P - \nabla\Pi - \frac{1}{m}\nabla V_{\text{ext}}, \tag{2.27}$$

which is similar in form to the Euler equation for an inviscid fluid. We introduce $P = -g\rho^2/(2m)$ which is a pressure term, and a quantum pressure term

$$\Pi = \frac{\hbar^2}{2m^2}\frac{1}{\sqrt{\rho}}\nabla^2\sqrt{\rho}. \tag{2.28}$$

We note that the pressure P depends only on the density, so surfaces of constant density

[1] This assumes that the external trapping potential V_{ext} is real, which is physically the case.

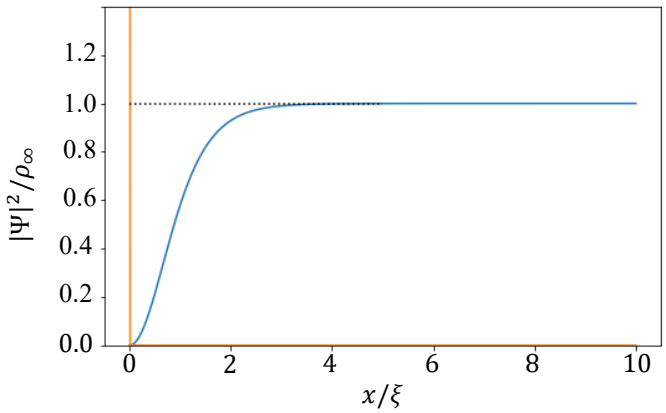

Figure 2.2: The density of the condensate wavefunction, $|\Psi|^2$, (blue) in the presence of a semi-infinite hard wall potential, $V(x) = \infty$ when $x < 0$ and $V(x) = 0$ when $x \geq 0$, (orange). The stationary state is given analytically as $\Psi(x) = \rho_\infty \tanh(x/\xi)$, where ξ is the healing length. The black dotted line is added as a guide to the eye to show the scale on which the condensate recovers the background density, ρ_∞.

also have constant pressure. The quantum pressure term is a quantum effect ($\Pi = 0$ if $\hbar = 0$), which also depends only on the density. The quantum pressure term provides a resistance to deformations of the shape of the condensate (i.e. against bending). In a uniform condensate, the quantum pressure is zero as the density is constant.

The coupled equations Eqn. (2.23) and Eqn. (2.27) are collectively known as the superfluid hydrodynamic equations, and their derivation from the GPE can be found in Appendix A.3.

2.3.1 The Healing Length

We have seen in the previous sub-section that the main difference between the superfluid hydrodynamic equations Eqn. (2.27) and the inviscid Euler equation is the addition of a quantum pressure term Π. If we suppose that the length-scales over which the condensate responds to a large perturbation is ξ, then $[\rho^{-1}\nabla P] \sim g\rho_\infty/(\xi m)$ and $[\nabla\Pi] \sim \hbar^2/(m^2\xi^3)$, where ρ_∞ is the background density of the condensate (far away from the obstacles). The length-scale on which the two terms are comparable is when ξ is given by

$$\xi = \frac{\hbar}{\sqrt{gm\rho_\infty}}. \tag{2.29}$$

Close to an obstacle (for lengths much smaller than ξ) the quantum pressure term dominates $\Pi \gg P$, while far away from an obstacle (lengths much greater than ξ) the normal pressure term dominates, $P \gg \Pi$. The length-scale ξ is called the healing length, since it is literally the length from an object at which the density is "healed" to the background value. A sketch of this is provided in Fig. 2.2.

2.4 Transforming the Reference Frame

2.4.1 Rotation

The dynamics of a rotating Bose gas can be studied by transforming the GPE into the rotating frame. The difficulty with rotating traps is that in the laboratory frame the potential is generally time-dependent [13]. Instead, it is numerically convenient to transform the GPE into the reference frame which is rotating with the trapping potential. This is possible by remembering that the angular momentum operator for a particle is $\mathbf{r} \times \mathbf{p}$, where $\mathbf{p} = -i\hbar\nabla$ is the usual quantum momentum operator [126]. For a gas which is rotating with angular momentum $\mathbf{\Omega}$, the GPE is

$$i\hbar\frac{\partial\Psi}{\partial t} = \left[-\frac{\hbar^2}{2m}\nabla^2 + V_{\text{ext}} + g|\Psi|^2 - \mu - \mathbf{\Omega}\cdot(\mathbf{r}\times\mathbf{p})\right]\Psi. \tag{2.30}$$

This equation and its applications are discussed in detail in Part II.

2.4.2 Linear Translation

We can consider a system in which an obstacle (imposed via the external trapping potential) is dragged through the fluid at some velocity $\mathbf{v}_{\text{obst}}$. In such a system, the coordinate of the obstacle reference frame is $\mathbf{r} = \mathbf{r}_L + \mathbf{v}_{\text{obst}}t$, and the lab-frame wavefunction is $\Psi(\mathbf{r}, t) = \Psi_L(\mathbf{r}, t)$. The GPE governing the lab-frame wavefunction is given by

$$i\hbar\frac{\partial\Psi}{\partial t} = \left[-\frac{\hbar^2}{2m}\nabla^2 + V_{\text{ext}}(\mathbf{r}) + g|\Psi|^2 - \mathbf{v}_{\text{obst}}\cdot\mathbf{p} - \mu\right]\Psi, \tag{2.31}$$

where the Gallilean shift to the obstacle frame (from the lab-frame) is given by the $\mathbf{v}_{\text{obst}}\cdot\mathbf{p}$ term, with $\mathbf{p} = -i\hbar\nabla$ the usual quantum momentum operator [127]. This equation and its application are discussed in further detail in Part III.

2.5 c-Field Treatments

Thus far, we have introduced the GPE which applies to a dilute and weakly-interacting BEC at zero temperature. The GPE describes the evolution of the wavefunction Ψ, which (in the zero temperature limit) is also the condensate mode. In BEC experiments, however, the condensate fraction is less than one, and so the consideration of thermal excitations is important in determining the dynamics of the system. In this case, the wavefunction Ψ is not the condensate mode, rather it is the superposition of the condensate and non-condensate modes. As a non-linear partial differential equation, the GPE enables mixing between modes, and a natural question arises as to how to deal with this mixing.

Consider a system where the Bose operator may be written as a superposition of single particle basis functions $\psi_{\mathbf{k}}$,

$$\hat{\Psi}(\mathbf{r}) = \sum_{\mathbf{k}} \hat{a}_{\mathbf{k}} \psi_{\mathbf{k}}(\mathbf{r}). \tag{2.32}$$

These modes are labelled by the wave-numbers $\mathbf{k}$, which can be related to momentum by $\mathbf{p} = \hbar\mathbf{k}$, and the operator $\hat{a}_{\mathbf{k}}$ annihilates an atom in mode $\mathbf{k}$. We may then separate $\hat{\Psi}(\mathbf{r})$ into the c-field, $\mathcal{C}$, and incoherent, $\mathbb{I}$, regions. The *projected* Gross-Pitaevskii Equation (PGPE) sits within a broader range of techniques known as the c-field methodology [128–133].

The c-field region

The first such region is the c-field region, so called because the modes in this region may be treated *classically*. In the same way that the GPE treats the highly occupied condensate mode as a classical field in a BEC at zero temperature, we assume that the lower-energy modes comprising the c-field region are highly occupied, (i.e. the number of atoms in a given mode is much greater than unity), meaning that quantum fluctuations are small. A cut-off energy, E_{cut} is chosen to ensure that the modes in the c-field region are classical. Of course, the choice of E_{cut} must not affect the underlying physics of the system.

The incoherent region

The second region is referred to as the *incoherent* region, with energy $E_{cut} < E < E_{max}$ for some maximum energy E_{max}, the choice of which is discussed by Blakie *et al.*, [133]. Essentially, E_{max} cuts off high momentum modes to ensure that the effective field theory considers length scales which are greater than the effective range of the inter-atomic potential, the length scales of interest in ultra-cold atom experiments. The high energy modes contained within the incoherent region are not well occupied, and so quantum effects are significant. The quantum mechanical treatment required by the incoherent region will be discussed in Sec. 2.5.4 and 2.5.5. A schematic of the c-field and incoherent regions can be found in Fig. 2.3.

2.5.1 The PGPE

The separation between the c-field and incoherent regions is implemented by imposing the projection operator $\mathcal{P}$ in the basis of non-interacting single particle modes, $\psi_{\mathbf{k}}$. That is to say,

$$\mathcal{P}\left[\hat{\Psi}(\mathbf{r})\right] = \sum_{\mathbf{k}\in\mathcal{C}} \hat{a}_{\mathbf{k}} \psi_{\mathbf{k}}(\mathbf{r}). \tag{2.33}$$

This projection, introduced by Davis *et al.* in the context of a homogeneous 3D system [129], is performed by setting all modes outside of some 2D circle (3D sphere), whose

radius is set by the cut off energy, to zero. This can be directly implemented in the GPE giving it the advantage of making it relatively computationally simple. The PGPE is given by [129]

$$i\hbar\frac{\partial\Psi}{\partial t} = \mathcal{P}\left\{\left[-\frac{\hbar^2}{2m}\nabla^2 + V_{\text{ext}}(\mathbf{r}) + g|\Psi|^2 - \mu\right]\Psi\right\}, \tag{2.34}$$

which ultimately is a classical field equation for simulating a weakly interacting Bose gas at finite temperatures. The equation is a microcanonical equation of motion for the system in the sense that the atom number and total energy are conserved quantities; this requires all couplings to the incoherent region $\mathbb{I}$ to be neglected.

The importance of implementing the projection in the correct non-interacting single-particle basis has been demonstrated [134]. Ideally, the numerical projection operation used to evolve the equation should be numerically exact in terms of the relevant single-particle basis, necessitating a (pseudo-)spectral approach to numerical implementations.

The GPE is, generally speaking, intractable analytically and so must be solved numerically. This can lead to issues involving mode aliasing and the choice of how to discretise a spatial gird. For this reason, it is advantageous to solve the PGPE since an explicit projector defines the calculation without concerns over the numerical representation[2]. The use of a projector also prevents aliasing problems, since higher-modes are truncated. For some systems, it is also possible to find exact quadrature rules for the eigenfunctions of the single particle Hamiltonian, which makes it numerically efficient to solve the PGPE using spectral methods. The PGPE was originally introduced in the context of a homogeneous 3D Bose gas [128] and has been extended to describe trapped gases [132], as well as a Bose gas within a harmonic trapping potential subject to long-range dipolar interactions [135].

2.5.2 The validity of the PGPE

By construction, the modes which are described by the PGPE are highly occupied and so quantum fluctuations may be neglected, and we don't need to add quantum noise in numerical treatments. This reduces the number of conditions which must be fulfilled in order for the PGPE to be valid, by comparison with the methods which we shall discuss later in this section.

The first essential validity condition of the PGPE is that the modes which are included in the c-field provide a good basis. That is to say that the cut off energy, E_{cut}, is sufficiently large that the eigenfunctions of the single particle Hamiltonian provide a good basis for the interacting modes.

The second essential validity condition of the PGPE is that the modes which are included in the c-field are highly occupied. This condition is essential to the construction of the PGPE, nevertheless it can not be understated that the cut off energy, E_{cut} must

[2]In other words, irrespective of the number of grid points used, provided enough points are used to stop aliasing, the projection operator controls the number of modes which are evolved ensuring that the conserved energy of the system is correctly distributed.

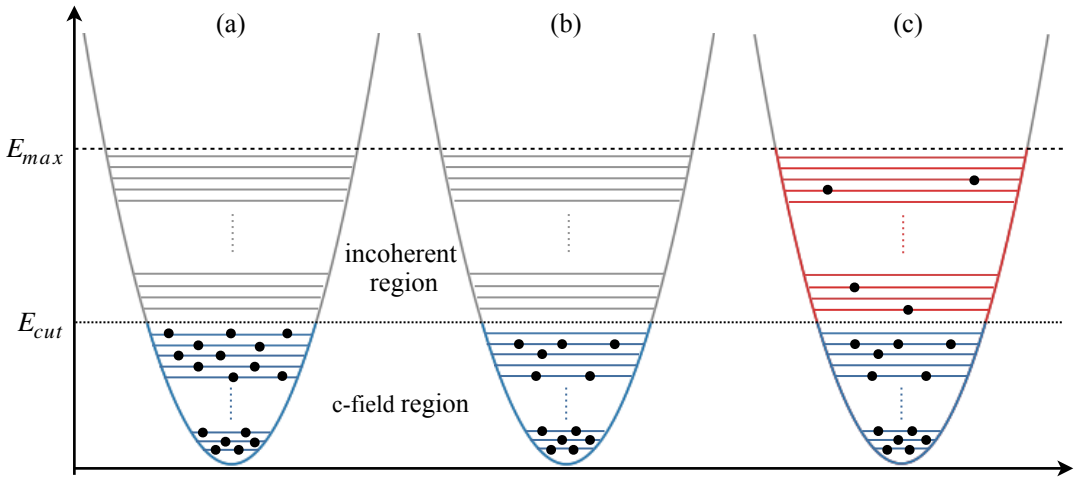

Figure 2.3: Schematic of the c-field and incoherent regions for a harmonically trapped condensate. Panel (a), a sketch of the PGPE regime - all of the modes below the energy cut-off E_{cut} are highly occupied, allowing for a mean-field treatment. Panel (b), a sketch of the TWPGPE regime - modes below the energy cut-off E_{cut} may be highly or sparsely occupied. Panel (c), a sketch of the SPGPE regime - the c-field region is coupled to the incoherent region. Figure re-drawn based on Ref. [133].

be chosen so that the occupation of all of the modes below E_{cut} is greater than unity. Although the precise choice of E_{cut} is subtle, as it should not affect the underlying physics of the simulation, only a few studies have considered the impact of this choice on simulation results [136, 137].

The validity of the PGPE has also been confirmed by comparison with Quantum Monte Carlo simulations [138], although these Monte Carlo simulations are necessarily limited to equilibrium statics of a system, rather than dynamics.

2.5.3 The Dissipative PGPE

Neither the GPE in Eqn. (2.8) nor the PGPE in Eqn. (2.34) contains a term which accounts for damping, by contrast both equations conserve particle number and energy. In real experiments, however, there exists a damping of collective excitations [139, 140] which is due to finite temperature effects [59, 141–143]. Throughout this thesis we will use the dissipative PGPE (dPGPE) which is used to model a system which relaxes to equilibrium. This equation was introduced by Choi *et al.* [144], and has also been adapted by (for example) Refs. [145–149]. The argument for the dPGPE which we present here closely follows that of Ref. [144].

We wish to extend the GPE to describe a damping process which will eventually lead to an equilibrium state. As discussed earlier, a condensate in equilibrium at zero temperature is described by the time independent GPE, Eqn. (2.12). We now consider the equation of motion,

$$i\hbar\frac{\partial\Psi}{\partial t} = \hat{\mathcal{L}}\Psi. \tag{2.35}$$

Since we wish to describe a relaxation process, the norm and energy of Ψ should not be conserved. Physically, this corresponds to the interaction of the condensate with a thermal cloud, by which the condensate may lose (or gain) energy [147, 150]. Mathematically, this means that the operator $\hat{\mathcal{L}}$ can not be Hermitian. Suppose we write the operator $\hat{\mathcal{L}}$ as the sum of a Hermitian and anti-Hermitian operators,

$$\hat{\mathcal{L}} = \hat{\mathcal{H}} + \hat{\mathcal{D}}, \tag{2.36}$$

where the Hermitian operator $\hat{\mathcal{H}}$, which describes the condensate at equilibrium, is given by Eqn. (2.12). The anti-Hermitian operator $\hat{\mathcal{D}}$ describes the process by which equilibrium is approached, and should vanish at equilibrium. This suggests that the anti-Hermitian operator $\hat{\mathcal{D}}$ should be written as

$$\hat{\mathcal{D}}\Psi = i\Lambda \left[-\frac{\hbar^2}{2m}\nabla^2 + V_{\text{ext}}(\mathbf{r}) + g|\Psi|^2 - \mu \right] \Psi, \tag{2.37}$$

where Λ is a dimensionless parameter which is inversely proportional to the system's relaxation time. For damping, $\Lambda < 0$ and for the remainder of this thesis we shall write $\Lambda = -\gamma$, where γ is the damping parameter. We can consider γ to be an estimate of the rate at which an excited component turns into the condensate [144]. The argument above leads to the damped PGPE, which is written as

$$i\hbar\frac{\partial\Psi}{\partial t} = (1 - i\gamma)\,\mathcal{P}\left\{ \left[-\frac{h^2}{2m}\nabla^2 + V_{\text{ext}}\left(\mathbf{r}\right) + g|\Psi|^2 - \mu \right] \Psi \right\}. \tag{2.38}$$

For good choices of Ψ and γ (i.e. a wavefunction Ψ which is close to the equilibrium condition, and a physical value of γ, ideally $0 \leq \gamma \leq 1$), Eqn. (2.38) will evolve to the ground state of the system.

Other authors [147, 149] write the dPGPE in alternative form

$$(1 + i\gamma)\,\hbar\frac{\partial\Psi}{\partial t} = \mathcal{P}\left\{ \left[-\frac{h^2}{2m}\nabla^2 + V_{\text{ext}}\left(\mathbf{r}\right) + g|\Psi|^2 - \mu \right] \Psi \right\}. \tag{2.39}$$

Multiplying this equation by $(1 - i\gamma)$ and dividing by $(1 + \gamma^2)$ yields

$$i\hbar\frac{\partial\Psi}{\partial t} = \frac{(1 - i\gamma)}{(1 + \gamma^2)}\mathcal{P}\left\{ \left[-\frac{h^2}{2m}\nabla^2 + V_{\text{ext}}\left(\mathbf{r}\right) + g|\Psi|^2 - \mu \right] \Psi \right\}, \tag{2.40}$$

where the right hand side of this form differs from that of Eqn. (2.38) by a factor of $(1 + \gamma^2)$. Typical values of the damping parameter range from $\gamma = 0.01$ [149] to $\gamma = 0.03$ [144, 147], so this difference is small. Later in this thesis, however, we shall use the "over-damped" dPGPE, which is Eqn. (2.38) with $\gamma = 1$, to find the ground state of a system; here we would expect the dynamics of the system to be different, although the ground state would be the same.

2.5.4 The Truncated Wigner PGPE

While introducing the PGPE in the previous section, we explained the importance of the modes in the c-field region having an occupation which is greater than unity. This is a requirement of the PGPE, to ensure that such modes may be treated classically. A sensible correction to this methodology would be to determine how such a system may evolve if we relax the condition that all of the modes in $\mathcal{C}$ are highly occupied, and consider the resulting quantum fluctuations. Broadly speaking, this motivates the Truncated Wigner Projected Gross-Pitaevskii Equation (TWPGPE) which we will discuss in this section. Throughout this sub-section we assume that the incoherent region $\mathbb{I}$ is unoccupied, and that there are modes within the c-field region $\mathcal{C}$ which are unoccupied, necessitating a quantum treatment. This is a c-field method which extends the PGPE to a "quantum" version of the PGPE.

The GPE facilitates mixing between modes, however, special consideration must be made for modes within the c-field region which have a low occupation. In a real system, this isn't a problem since quantum fluctuations allow modes which initially have zero population to grow without requiring seeding [151]. In the classical field simulations which we have discussed, a solution to this problem was proposed by Berloff and Svistunov [152] who evolved a homogeneous system whose initial condition was to fill every mode with uniform plane waves with random phases. This is a good first approximation, since the GPE will evolve to the correct equilibrium state.

It is also possible to study the dynamics of a system by using 'Stochastic Phase Space Methods'. These methods involve sampling initial conditions from probability distributions, and evolving these initial conditions by considering them as stochastic trajectories which each obey classical mean field dynamics [151]. The choice of probability distribution is made so as to ensure that the initial condition is as close as possible to the initial thermal distribution or quantum statistical correlation. The best description of classical mean-field dynamics is the Wigner distribution, since it can be shown that a Wigner function exists for any density operator [153, 154]. The 'Truncated' Wigner approximation corresponds to the fact that third-order derivative terms which come from the full evolution equation of the Wigner function are ignored, an assumption which is rigorously argued in Ref. [155]. The result is therefore in the form of a Liouville equation, meaning that it describes an ensemble of trajectories obeying a classical equation of motion [156].

The TWPGPE methodology prescribes that initial conditions which include a random element which represents half a quantum occupation per mode are evolved with the PGPE, Eqn. (2.34). The initial conditions are given by

$$\Psi(\mathbf{r},0) = n_0\psi_0 + \frac{1}{\sqrt{2}}\sum_{\text{n.c.}}\psi_k\left(n_k + \alpha_k + i\beta_k\right) \tag{2.41}$$

where n_0 is the condensate number, and ψ_0 is the condensate mode. The sum on the right

hand side is taken over the non-condensate modes[3], with n_k the equilibrium occupation of the k-th mode. The real numbers $\alpha_k \sim N(0,1)$ and $\beta_k \sim N(0,1)$ are independent random variables which are normally distributed. The inclusion of the noise terms in Eqn. (2.41) mimic the quantum mechanical vacuum fluctuations present in c-field modes with low occupation.

An important distinction between the TWPGPE describer here, and the formulation of Steel *et al.* [153] is the implementation of the projection operator, $\mathcal{P}$. Implementing the projector imposes a level of control over the vacuum noise; without the projector the TWPGPE is only accurate for simulations which are limited to relatively short times or low temperatures [110, 133], since adding noise in all modes adds to the energy of the system, which may cause non-physical "heating" and damping effects [136]. It is also worth noting that the TWPGPE will not result in an accurate description of a system if the number of basis modes which are considered is too large, since vacuum noise is added to every mode in the system [156]. The TWPGPE is most effective in the regime where quantum processes dominate thermal effects [110].

2.5.5 The SPGPE

We have now introduced two GPE-like methods which are valid for Bose gases which are at finite temperature. The PGPE is a simple extension of the GPE, and is valid when every mode in the c-field region has an occupation number which is greater than one. The Truncated Wigner PGPE relaxes this condition, and describes a c-field where some modes may have low or no occupation. However, on evolution, the TWPGPE necessarily treats the entire system as a classical microcanonical system, which neglects the presence of a thermal cloud.

In this section, we introduce the Stochastic Projected Gross-Pitaevskii Equation (the SPGPE) [131, 134, 157, 158] which is an equation of motion for the c-field region $\mathcal{C}$ coupled to the incoherent region $\mathbb{I}$ which comprises of high-energy atoms assumed to be in thermal equilibrium. Unlike the PGPE and TWPGPE which are microcanonical approaches, the SPGPE is a grand canonical approach as the particle number and energy of the c-field is not conserved; the c-field is coupled to a thermal reservoir, which in this case is the thermally occupied modes in the $\mathbb{I}$-region, which is parameterised by its temperature T and chemical potential μ. The SPGPE can be thought of as a higher temperature theory of the PGPE.

The simple growth SPGPE can be written

$$i\hbar d\Psi(\mathbf{r},t) = \mathcal{P}\left[\mathcal{L}\Psi(\mathbf{r},t)\,dt + i\frac{\gamma\hbar}{k_B T}\left(\mu - \mathcal{L}\right)\Psi(\mathbf{r},t)\,dt + i\hbar dW_\gamma(\mathbf{r},t)\right] \tag{2.42}$$

[3]The identification of the condensate and non-condensate modes within the c-field methodology are described in Chapter 8.

where

$$\mathcal{L}\Psi(\mathbf{r},t) = \left[-\frac{\hbar^2}{2m}\nabla^2 + V_{\text{ext}}(\mathbf{r},t) + g|\Psi(\mathbf{r},t)|^2\right]\Psi(\mathbf{r},t), \tag{2.43}$$

and the complex noise associated with the growth of the condensate is $dW_\gamma(\mathbf{r},t)$, whose mean and variance is given by the equal time correlation

$$\left\langle dW_\gamma^*(\mathbf{r},t) dW_\gamma\left(\mathbf{r}',t\right)\right\rangle = 2\gamma\delta\left(\mathbf{r},\mathbf{r}'\right)dt. \tag{2.44}$$

The SPGPE is a stochastic differential equation, since the coupling between the c-field region $\mathcal{C}$ and the thermally occupied $\mathbb{I}$-region introduces damping (as high energy atoms may transfer from $\mathcal{C}$ to $\mathbb{I}$, reducing the energy of the condensate) and the process by which the condensate grows, through the collision of atoms, is stochastic. It has been extensively used in studies describing condensate formation in one [157] and two [159] spatial dimensions, as well as vortex nucleation in a rotating gas [134], and the equilibration of binary Bose gases [160]. The SPGPE is appealing for these and other finite temperature studies since one may prescribe the temperature of the system at the outset, rather than having to extract it *a priori*. It is also commonplace to use initial conditions such as those described in the previous system on the TWPGPE, Eqn. (2.41), as an initial condition for the SPGPE. Generally, one must average over an ensemble of initial conditions evolved by the SPGPE to determine the properties of a given system.

The version of the SPGPE that we have presented here is known as the 'simple growth' SPGPE as it neglects scattering terms. These terms are numerically challenging to include, and are expected to be far less significant than the terms which are included in Eqn. (2.42) which describes the interaction between the thermal cloud on the condensate [133]. Perhaps a more concerning limitation is the assumption that the thermal cloud to which the c-field modes are coupled by the SPGPE is *stationary*. For non-equilibrium systems, we would expect that this cloud should be treated dynamically. In fact, there is a large body of work which accounts for these dynamics by coupling a dissipative GPE description of the condensate mode (allowing particles to enter and leave the condensate) to a kinetic Quantum Boltzmann equation which describes the thermal cloud. This treatment, the ZNG scheme [161], fully describes the back action of the dynamical thermal cloud on the condensate mode. It should be emphasised that the ZNG scheme is not a c-field based method, as it does not separate modes into the regions $\mathcal{C}$ and $\mathbb{I}$.

Throughout this thesis, we will only use the PGPE method described above. For an excellent review of the methods discussed in this section, as well as other methods available for modelling Bose gases at finite temperature, we direct the reader to Refs. [133, 151].

Chapter 3

Superfluid Vortices

This last chapter in the introductory part of this thesis will introduce the theory and experimental observation of vortices in a BEC. Unlike vortices in classical fluids, which may have arbitrary size and circulation, these quantized vortices are a striking property of superfluids as they constrained to be of fixed size and integer charge.

3.1 Quantized Circulation

Consider a fluid which is rotating with constant angular velocity $\mathbf{\Omega}$. A classical fluid which rotates with this angular velocity will rotate, in stationary conditions, as a solid body, with velocity field

$$\mathbf{v} = \mathbf{\Omega} \times \mathbf{r}. \tag{3.1}$$

The vorticity of a fluid flow is defined as the curl of the velocity field [69], $\boldsymbol{\omega} = \nabla \times \mathbf{v}$, and so in a fluid rotating as a solid body the vorticity is

$$\boldsymbol{\omega} = \nabla \times \mathbf{v} = 2\mathbf{\Omega}, \tag{3.2}$$

meaning that it is uniform and equal to twice the angular velocity. In Sec. 2.3, we introduced the Madelung transform $\Psi = \sqrt{\rho}\exp(i\theta)$ for the wavefunction Ψ, and identified that the velocity of a superfluid is given by Eqn. (2.22),

$$\mathbf{v} = \frac{\hbar}{m}\nabla\theta.$$

The vorticity of the superfluid therefore is

$$\boldsymbol{\omega} = \frac{\hbar}{m}\nabla \times \nabla\theta = 0, \tag{3.3}$$

implying that the superfluid velocity is irrotational. The second equality in Eqn. (3.3) assumes that θ is a smooth, differentiable function; it is possible, however, for θ to have singularities around which the value of θ varies by 2π. If we take some 2D region of the

fluid $\mathcal{R}$ which contains such a singularity, we can integrate over this surface using Stokes' theorem to get

$$\int_{\mathcal{R}} \boldsymbol{\omega} \cdot d\mathbf{r}^2 = \int_{\mathcal{R}} \nabla \times \mathbf{v} \cdot d\mathbf{r}^2 = \oint_{\partial\mathcal{R}} \mathbf{v} \cdot d\mathbf{r}, \tag{3.4}$$

where $\partial\mathcal{R}$ is a closed curve bounding $\mathcal{R}$. The superfulid velocity $\mathbf{v}$ is a conservative field since it can be written as the gradient of a scalar function, Eqn. (2.22), and so this integral does not depend on the path about the singularity. However, since the curve is closed, the wavefunction Ψ must be equal at the initial and final points of $\partial\mathcal{R}$, which means that the circulation of the fluid is

$$\oint_{\partial\mathcal{R}} \mathbf{v} \cdot d\mathbf{r} = \frac{2\pi\hbar}{m} n, \tag{3.5}$$

where $n \in \mathbb{Z}$. If n is not zero (and hence the vorticity does not vanish), a singularity must exist in this region of fluid implying that the curl of the velocity field may be written as

$$\nabla \times \mathbf{v} = \frac{2\pi\hbar}{m} \delta\left(\mathbf{r} - \mathbf{r}_{\mathrm{v}}\right) \hat{\boldsymbol{n}}, \tag{3.6}$$

where $\hat{\boldsymbol{n}}$ is normal to the surface $\mathcal{R}$, and $\mathbf{r}_{\mathrm{v}}$ is the location of the singularity [162]. At the centre of the singularity, the phase is multi-valued and so to ensure that Ψ is single-valued the density must vanish. In a 3D condensate, these singularities are quantized vortex lines, while in 2D these are quantized vortex points [126]. A sketch of the density and phase of a vortex core can be found in Fig. 3.1. The integer n is a quantity known as the charge of the vortex, and by convention a vortex with negative charge may be called an "antivortex". Quantized vortices are topologically protected – they can only be annihilated by colliding with a vortex with an opposite charge, or by colliding with the edge of the condensate.

Since these quantized vortices were observed experimentally in a BEC [53], they have been a widely studied quantum phenomenon [72, 142, 163–169]. Systems with a large number of vortices have been revealed to display a rich selection of dynamics such as the dipole interactions of vortices with opposite charges [170, 171], the mechanisms of vortex lattice formations [134, 147, 172–175], and vortex turbulence [72, 83, 176–181]. Quantum vortices provide an excellent testing ground for more general vortex systems, such as the shedding of vortices from moving obstacles [51, 182–185] which can lead to von Kármán vortex streets [100, 186], vortex dynamics in a constricted flow such as a Josephson junction [187] or an acoustic oscillator circuit [188], vortex scattering [189–191] and pinning [192], leapfrogging [193], vortex knots [194, 195] and clustering [25, 88, 93, 196].

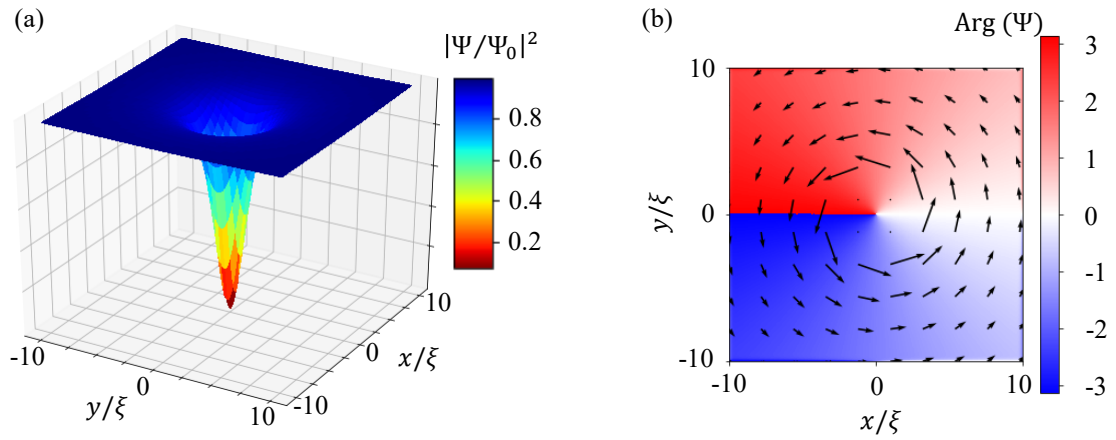

Figure 3.1: Panel (a), the density profile of a vortex core positioned at the origin, determined by numerically integrating the GPE. Panel (b), the phase of a vortex core; arrows indicate the velocity field about the core of the vortex.

3.2 Rotating BECs

Transforming to a frame of reference which is rotating with angular velocity $\mathbf{\Omega}$, as in Eqn. (2.30), the energy functional given by Eqn. (2.10) becomes

$$\mathcal{E}_\Omega[\Psi] = \mathcal{E}[\Psi] - \mathbf{\Omega}\cdot(\mathbf{r}\times\mathbf{p})\,\Psi, \tag{3.7}$$

which has a total energy

$$E[\Psi] = \int d^3\mathbf{r}\,\left[\frac{\hbar^2}{2m}|\nabla\Psi|^2 + V_{\rm ext}(\mathbf{r})|\Psi|^2 + \frac{1}{2}g|\Psi|^4 - \mu|\Psi|^2\right] - \mathbf{\Omega}\cdot\int d^3\mathbf{r}\,\left[\Psi^*(\mathbf{r}\times\mathbf{p})\,\Psi\right]. \tag{3.8}$$

Finding the ground state of the system now explicitly involves the angular velocity; since the last term in Eqn. (3.8) lowers the total energy, the ground state must be one which includes positive angular momentum [197].

As discussed in Sec. 3.1, unlike a normal fluid which rotates as a solid body, a superfluid is irrotational except around a vortex line, where the circulation is quantized in units of $2\pi\hbar/m$. Since each vortex line has identical quantization, Feynman [198] argued that a dense array of vortex lines can mimic solid body rotation, when the vorticity is coarse-grained over a large number of quantized vortices. If we consider the circulation of a fluid computed around a closed contour $\partial\mathcal{R}$ containing $N_{\rm v}$ vortices, the quantization condition of Eqn. (3.5) ensures that the circulation is $2\pi\hbar N_{\rm v}/m$. One can also use the result for solid body rotation to compute the circulation

$$\int_{\mathcal{R}} \nabla\times\mathbf{v}\cdot d^2\mathbf{r} = \int_{\mathcal{R}} 2\mathbf{\Omega}\cdot d^2\mathbf{r} = 2\Omega|\mathcal{R}|, \tag{3.9}$$

where $|\mathcal{R}|$ is the area of the region $\mathcal{R}$. Comparing the two gives the average vortex density

in a rotating superfluid,

$$\overline{N_{\mathrm{v}}} = \frac{N_{\mathrm{v}}}{|\mathcal{R}|} = \frac{\Omega m}{\pi\hbar}, \tag{3.10}$$

which is Feynman's relation [198]. The area per vortex is obtained by inverting Eqn. (3.10) to get

$$\frac{1}{\overline{N_{\mathrm{v}}}} = \frac{\pi\hbar}{\Omega m}, \tag{3.11}$$

meaning the inter-vortex spacing decreases as the rotation speed increases. The results above suggest that a quantum fluid rotating with angular velocity $\mathbf{\Omega}$ mimics solid body rotation by distributing quantized vortex lines as uniformly as possible; this was experimentally confirmed by Abo-Shaeer *et al.* [199] who observed a "crystallized" vortex lattice. These Abrikosov lattices were originally predicted to exist in type-II superconductors, where the nodes of the lattice are lines of magnetic flux [200]. It was later shown that the lowest energy configuration of this lattice in an infinite system is a triangular lattice [201].

For the remainder of this thesis, since we are working in a 2D system, we will assume that the axis of rotation is $\hat{\boldsymbol{z}}$, so that the angular velocity $\mathbf{\Omega} = \Omega\hat{\boldsymbol{z}}$.

3.3 Experimentally Generating Vortices

In a typical experiment involving rotating superfluid helium, both superfluid and normal liquid helium are contained within a cylindrical bucket which is then rotated around the axis of the cylinder. Initially the normal fluid rotates with the bucket as a rigid body; as the angular velocity of the bucket is increased, a vortex line is nucleated at the edge of the container and then moves towards the centre of the bucket (which is also the axis of rotation). Spinning the bucket faster and faster nucleates more vortex lines which then form a lattice [201, 202]. Unfortunately, this procedure does not work for an atomic BEC, as a BEC is typically created in a harmonic optical and or magnetic trap; unlike a bucket containing liquid helium, this trap does not have any surface roughness to assist with vortex nucleation [203].

In this section, we describe some of the means by which vortices have been realised experimentally in a BEC. We note that, while we presented an extensive list of methods for experimentally realising quantum vortices, it should be emphasised that this list is not exhaustive. Processes such as thermal quenches [204] similar to the Kibble-Zurek mechanism [205–207], overlapping condensates from different lattice sites [115], and many others may be employed to generate vortices in BECs, ensuring that it remains an active and exciting area of research.

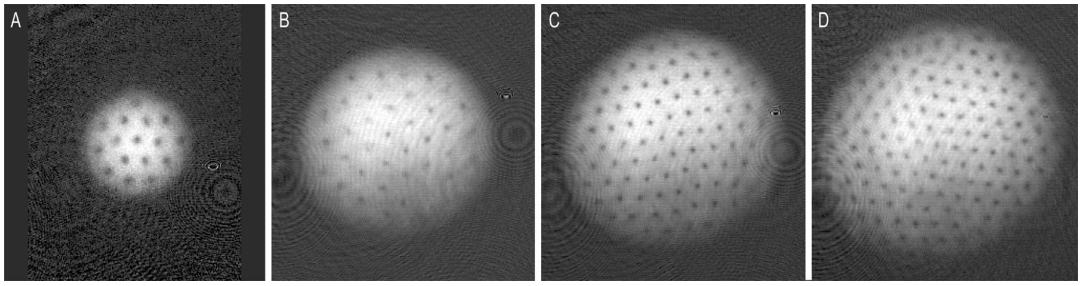

Figure 3.2: An experimental image of a BEC forced to rotate by two blue-detuned laser beams rotating symmetrically around the condensate. The result is a triangular vortex lattice containing approximately (a) 16 vortices, (b) 32 vortices, (c) 80 vortices, and (d) 130 vortices. Image taken from [199], reprinted with permission from AAAS.

3.3.1 Artificial Phase Imprinting

Vortices were first realised in an atomic BECs by using a phase imprinting method on a two component BEC [53]. The method by which vortices are created using a phase imprinting method is described theoretically by Dobrek *et al.*, [208]. Essentially, a laser beam is passed through an absorption plate which has a spatially dependent absorption coefficient, on to the condensate. The spatial dependence varies linearly around axis of the plate, varying the transfer of orbital angular momentum from the laser to the condensate [209], and causing a relative phase to be imprinted on the atoms in the condensate. The vortex state which is created by this process is an axially symmetric ring with a 2π phase winding around a central depleted region (the vortex core). This technique has since been applied to study the procession of a vortex core in a harmonic confining potential [54], as well as in the production of dark solitons which decay into a vortex ring [67].

3.3.2 Stirring

A second method for generating vortices in a BEC is to rotate the condensate, where angular momentum is imparted to the condensate by the nucleation of quantized vortex lines. This approach was pioneered by Madison *et al.* [59] who stirred the condensate with a laser. Initially the condensate is in a cylindrically symmetric magnetic trap, which is elongated in the z direction. A blue-detuned laser, which forms a repulsive potential, is shone onto the condensate and is then uniformly rotated with fixed angular frequency[1]. The system is then allowed to reach thermal equilibrium, before the stirring laser is slowly ramped down. The vortices which are nucleated can then be studied using time-of-flight analysis [59]. This technique was later used to study a rotating condensate which was subjected to a harmonic trap which was also rotating [141].

[1] A similar approach was also taken by Onofrio *et al.* [210] who used a red-detuned laser to form an attractive potential which could be used to excite quadrupole standing waves or rotating modes.

The ability to make a condensate rotate led to a host of experimental results. Chevy *et al.* [211] used laser-stirring to measure the angular frequency of a BEC, showing that there is a critical rotation frequency above which vortices are nucleated, this nucleation process was later studied by Raman *et al.* [143]. In 2001, Abo-Shaeer *et al.* [199] used the laser-stirring technique to observe a vortex lattice. This lattice was (as predicted [200, 201]) a well ordered triangular lattice, with an angular momentum of $\hbar N_{\rm v}/2$ per particle, containing up to $N_{\rm v} = 130$. Performing similar experiments at finite temperature, the dynamics of such a vortex lattice was observed to decay due to the damping of a thermal cloud [150].

3.3.3 Spinning the Trapping Potential

In close analogy to the rotating-bucket experiments carried out in superfluid helium [202], the third method for generating vortices in a BEC is to force the condensate to rotate by spinning the trapping potential. This is possible by using the experimental set-up of Arlt *et al.* [58], who constructed a time-orbiting potential trap which has different trapping frequencies in each of the three axes. Calibrating these trapping frequencies[2] so that $\omega_x < \omega_y < \omega_z$, a cigar shaped condensate which is elliptical in the xy-plane is formed. The magnetic fields can then be rotated around the $\hat{\boldsymbol{z}}$ axis, which causes the condensate to rotate and vortices to be nucleated. This method was first employed by Hodby *et al.* [212], and has the advantage that it does not reduce the number of atoms in the condensate, by contrast with the laser-stirring experiments [59].

A similar experiment has also been performed by rotating a normal fluid in an anisotropic trap, and then cooling the fluid below the critical temperature for Bose-Einstein Condensation [142]. Beginning with an elliptic cloud of atoms which is just above T_{BEC}, the rotating frequency of the trap is gradually increased until the cloud is rotating with the chosen angular velocity, at which point the asymmetry of the trap is ramped off. The cloud is then cooled by preferentially evaporating atoms with large angular momenta, reducing the temperature of the remaining atoms below T_{BEC}, while the cloud rotates at a frequency of 94% of the radial trapping frequency, $\omega_\perp$. Using this evaporative spin-up technique, along with an optical spin-up [163], has allowed other experiments to achieve rotation frequencies of $\Omega \geq 0.99\omega_\perp$ [165, 166].

3.3.4 Vortex Shedding

The final technique for generating vortices in a BEC involves dragging an "obstacle" through the fluid. This was originally predicted by Frisch *et al.* [51] who studied the drag on an obstacle in a superfluid. At sufficiently slow velocities, the flow around an obstacle such as a blue-detuned laser beam [182] is a steady laminar flow, where no vortices are nucleated and no drag is exerted by the fluid on the obstacle. This is the hallmark of a

[2] Here, ω_j is the trapping frequency in the j-th axis.

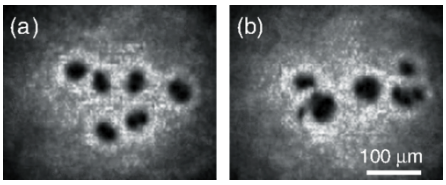

Figure 3.3: Quantum vortex shedding from a moving obstacle in a highly oblate $\left(\omega_\perp/\omega_\parallel = 11.1/400\right)$ BEC. Panel (a) shows a regular shedding pattern of six clusters of two like-sign vortices, a von Kármán vortex street. Panel (b) shows a typical irregular shedding pattern. The charge of each cluster can be inferred from the area of the density-depleted hole. Image taken from Kwon *et al.* [100] with permission from APS.

superfluid flow. Above a critical velocity (the nature of which will be discussed in detail in Part III) vortices are shed periodically. As the velocity of the obstacle relative to the fluid increases, the shedding of vortices becomes more irregular, eventually forming a turbulent wake.

The first experimental realisation of vortices emitted from a obstacle dragged through a BEC was achieved by Inouye *et al.* [60], who dragged a blue-detuned laser beam through a "sample" condensate, before interfering this with a second condensate in order to identify the presence of vortices from the interference fringes (the theory of this measurement can be found in Refs. [213, 214]). As with the rotating BEC experiments, the ability to generate vortices by linearly translating a blue-detuned laser through the condensate led to a raft of experimental results. Moving an obstacle relative to a trapped condensate, Neely *et al.* [215] were able to determine the critical velocity for the nucleation of a vortex dipole. Experiments were then performed to systematically study the critical velocity for vortex nucleation as a function of obstacle height [216], as well as investigating the frequency of vortex shedding as a function of obstacle speed [184]. As predicted [51, 99], once above the critical velocity, further increasing the obstacle velocity leads to the shedding of an irregular pattern of vortices. For certain obstacle widths and velocities, vortex clusters of two like-sign vortices may be emitted by the obstacle, forming a configuration like a von Kármán street; in a landmark experiment by Kwon *et al.* in 2016 [100], this configuration was observed in a superfluid.

As well as the studies of obstacles in a flow, which have a close analogy to the study of turbulence in classical fluids [69], Kwon *et al.* [179] swept a trapped condensate with a repulsive blue-detuned laser in order to observe the decay of the vortex number. This has connections to the correlation length scales of a system L_c, which is the relevant length scale after a quench [217]. We will discuss the vortex decay rate further in Parts III and IV.

3.4 3D Vortex Lines

In 3D superfluids, such as liquid helium [218] and dilute BECs [219], it has been confirmed that quantized vortices are 1D vortex lines (or vortex "tubes", on account of the finite width of the vortex core) about which the phase of the wavefunction winds by an integer multiple of 2π. These vortex lines either terminate at a boundary, or form a closed ring. The evolution of vortex lines is well described by the vortex filament model of Schwarz [220]. In this model, the component of the superfluid velocity which is due phase winding about the vortex lines is given by

$$\mathbf{v}(\mathbf{r}) = \frac{\hbar}{2m} \int_{\ell_k} \frac{(\mathbf{s}-\mathbf{r})}{|\mathbf{s}-\mathbf{r}|^3} \times d\mathbf{s}, \tag{3.12}$$

where the integral is taken over all of the vortices in the system, labelled ℓ_k. Vortex lines are not necessarily straight parallel tubes [as depicted in Fig. 3.4 (a)]. A consequence of this is that the velocity field described in Eqn. (3.12) contains contributions not only from other vortices, but also other parts of the same vortex line, quickly leading to complex dynamics as more vortices are added to a system. It has been experimentally observed that the onset of turbulence in a BEC is related to the presence of a vortex tangle [72].

A 3D vortex tube is subject to an excitement known as Kelvin waves [221], where the vortex tube "bends" away from its straight resting position. The existence of these excitations have been inferred in the work of Bretin *et al.* [74], who studied the oscillation of a single vortex line in an oblate BEC, and Fonda *et al.* [222] using tracer particles in superfluid Helium. Kelvin waves generate sound in the system through the emission of phonons [76], a cause of energy dissipation [76, 223].

Pairs of 3D vortex tubes may also interact with each other by reconnecting [224]. Initially two well separated vortex tubes act independently [225]. As the vortex tubes get closer, their curvature increases until they collide, forming a cusp (which excites Kelvin waves in the system [222]) at the point of collision. This is the reconnection event, during which the tails of the vortex are spliced together [226]. After colliding, the vortex tubes separate, however the topology of the flow has now changed. Vortex reconnections have been observed in atomic BECs [75, 225], and continue to be a topic of interest given their ability to distribute energy and helicity within the system [227–229].

3.5 2D Point Vortices

By comparison to the 3D case, vortex dynamics in 2D are relatively simple. If the trapping in one spatial direction is sufficiently tight, the vortex lines straighten until they are parallel, and the 3D effects of bending are absent [98]. Without loss of generality we assume that this takes place in the z axis, so that each of the vortices are parallel to $\hat{\mathbf{z}}$. A schematic of this is shown in in Fig. 3.4 (b). Since the vortex lines are parallel, the

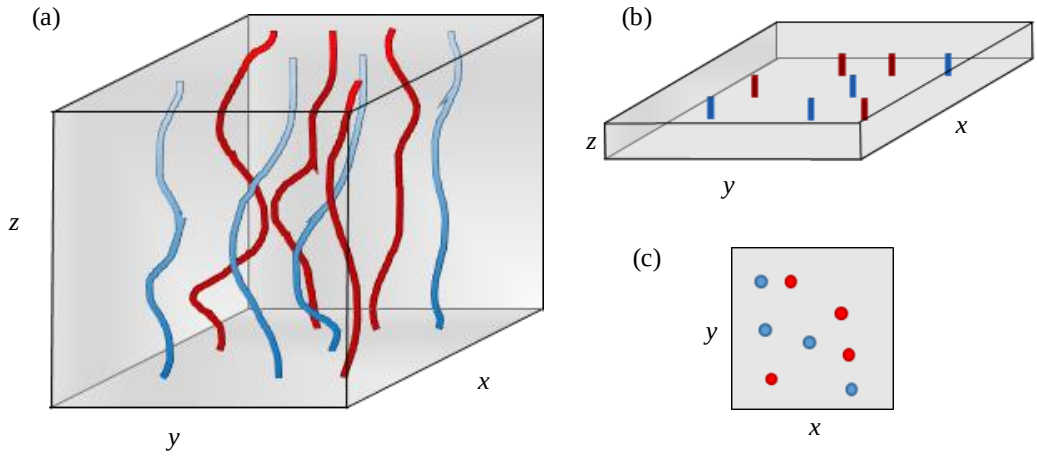

Figure 3.4: A schematic of 3D vortex (blue) and anti-vortex (red) tubes in (a) a 3D system, (b) a highly oblate system where the trapping potential in the z direction is strong enough to "freeze out" bends in the vortex tubes, and (c) the projection of the vortex and anti-vortex tubes in the $z = 0$ plane.

governing dynamics are independent of z and so we can reduce the system to a projection of the vortex positions in the xy-plane, Fig. 3.4 (c).

If we consider a 3 dimensional disk-shaped condensate, a vortex at position $\mathbf{r}_\mathrm{v} = (x_v, y_v)$ with charge n_v has the phase

$$\theta\left(\mathbf{r}\right) = n_v \arctan\left(\frac{y - y_v}{x - x_v}\right), \tag{3.13}$$

which is the azimuthal angle around the shifted origin [230]. Here $n_v \in \mathbb{Z}$ is related to the circulation around the vortex via Eqn. (3.5). We say that a vortex is positively charged if its circulation is in the anti-clockwise direction (i.e., $n_v > 0$), and a vortex is negatively charged if its circulation is in the clockwise direction (i.e., $n_v < 0$). Typically we will refer to a negatively charged vortex as an *anti-vortex*.

As the vortices are advected by the local velocity field, the dynamics of a vortex pair are determined by the sign of the constituent vortices. For a pair of oppositely signed vortices, the flow field which each vortex feels is acting in the same direction, and so the vortices will propagate together. In a uniform system, in the absence of dissipative effects, this vortex anti-vortex pair (also called a vortex dipole pair, or vortex dipole for short) will travel at a constant velocity which is perpendicular to the vector separating the vortices. A vortex dipole can be considered to be a 2D analogy of a 3D vortex ring, whose velocity depends on the radius of the ring. For a pair of same sign vortices, the velocity field is equal and opposite at the coordinates of each vortex, and so the vortices will co-rotate about their mid point.

The dynamics described above rely on the vortices having sufficient separation so that the cores do not overlap. As an isolated pair in a uniform dissipationless system, a vortex dipole pair is a stable configuration. If an external force causes the dipole

length to shorten, eventually the vortex cores will overlap and the pair will annihilate. The exact form of this forcing varies from system to system, but can include dissipation [231], trapping geometries [95], or other vortices [95, 232]. Before the annihilation takes place, the overlapping vortex cores form a crescent-shaped structure [179], which was named *vortexonium* by Groszek *et al.* [95]. During the formation of this structure, the dipole transfers momentum to sound waves [68]. Once the annihilation has taken place, this structure propagates as a dark soliton [68] (similar to a Jones-Roberts solition [233]) before breaking down to release a shock wave. We emphasize that this process is analogous to the shrinking of a vortex ring in 3D [67].

We conclude this section by commenting on the range of values that the charge of a vortex, the integer n_v might take. Thus far we have made no assumptions about the charge n_v. It has been predicted theoretically [234, 235] and confirmed experimentally [236] that a multiply charged vortex will decay into n_v singly charged vortices. Through careful tuning of atomic scattering length, trapping geometry and system rotation, it is possible to stabilize a multiply charged vortex from collapse [234, 237, 238]. However, for the remainder of this thesis we assume that we are not working in such a system, and therefore that the magnitude of the charge of the vortex is unitary, $n_v = \pm 1$.

3.6 Approximate Forms of the Vortex Core

Finally, we consider the form of a vortex core itself. Although there is no exact analytic form for the vortex density profile, in this section we discuss several approximate forms.

3.6.1 Using a Variational Approach

The time-independent wavefunction Ψ representing a system with a charge n vortex whose is core centred at the origin may written in cylindrical polar coordinates as [230, 239, 240]

$$\Psi(\mathbf{r}) = A_n f_n(r) e^{in\phi}. \tag{3.14}$$

Here the constant A_n is calibrated to account for the background density of the fluid, and we have boundary conditions $f_n(r) \to 0$ as $r \to 0$, the vortex core, while $f_n(r) \to 1$ as $r \to \infty$. It has been shown [240], by substituting the vortex solution Eqn. (3.14) into the GPE, Eqn. (2.8), that the function $f_n(r)$ behaves asymptotically as

$$\begin{aligned} f_n(r) &\sim r^{|n|} && \text{as } r \to 0, \\ f_n(r) &\sim 1 - \frac{n^2}{r^2} + \cdots && \text{as } r \to \infty. \end{aligned} \tag{3.15}$$

Rather than find solutions to Eqn. (3.14) analytically, we can find the kinetic energy

per unit length of the vortex [230] which is

$$E_{\rm kin} = \frac{\hbar^2}{2m}\int d^2\mathbf{r}\left|\frac{\partial\Psi}{\partial r}\hat{\boldsymbol{r}} + \frac{1}{r}\frac{\partial\Psi}{\partial\varphi}\hat{\boldsymbol{\varphi}}\right|^2 = \frac{A_n^2\hbar^2}{2m}\int d^2\mathbf{r}\left[\left(\frac{df_n}{dr}\right)^2 + \frac{n^2}{r^2}f_n^2\right]. \tag{3.16}$$

Here the first term is the energy contribution from the density variation near the vortex core, while the second term accounts for the kinetic energy of the flow. Taking a variational approximation, one finds that a vortex with unit charge has the approximate form [197]

$$f_{\rm var}(r) = \frac{r}{\sqrt{r^2+2\xi^2}}. \tag{3.17}$$

It is clear that this form obeys the boundary conditions $f_{\rm var}(r) \to 0$ as $r \to 0$ and $f_{\rm var}(r) \to 1$ as $r \to \infty$.

3.6.2 The Padé Approximation

The next approximate form we present for the shape of a core of a vortex is the so called Padé approximation, studied by Berloff [241]. Due to the zero in density at the core of the vortex, and the requirement that the density recovers the background value of the system far away from the vortex core, it is not possible to express the vortex core as a power series. Berloff [241], on the other hand, used a ratio of truncated power series to construct an improved estimate of the function, where the coefficients are determined recursively by substituting the ansatz into the GPE, Eqn. (2.8). For a singly charged straight line vortex in a uniform condensate, the Padé approximation to the vortex solution is

$$f_{\rm Pa}(r) = \sqrt{\frac{0.6874\left(\frac{r}{\xi}\right)^2 + 0.1144\left(\frac{r}{\xi}\right)^4}{1 + 0.6666\left(\frac{r}{\xi}\right)^2 + 0.1144\left(\frac{r}{\xi}\right)^4}}. \tag{3.18}$$

3.6.3 Numerically Fitting the Variational Ansatz

The final form is the ansatz found by Bradley and Anderson for homogeneous, compressible, quantum fluids in two dimensions [242]. Like Fetter, and others, they write the solution to the GPE which supports a singly charged vortex at the origin in the form of Eqn. (3.14). As before, Bradley and Anderson impose the boundary conditions $f_n(r) \to 0$ as $r \to 0$ and $f_n(r) \to 1$ as $r \to \infty$, however they also impose boundary conditions on the derivative of f_n. Firstly, the derivative $df_n/dr = 0$ as $r \to \infty$, to be consistent with the fact that the density returns to the background value far away from the vortex core. The second condition is that the derivative must match the gradient of the vortex core at the origin. The value

$$\Lambda = \Psi'(0) = \lim_{r\to 0}|A_n\frac{df_n}{dr}| \tag{3.19}$$

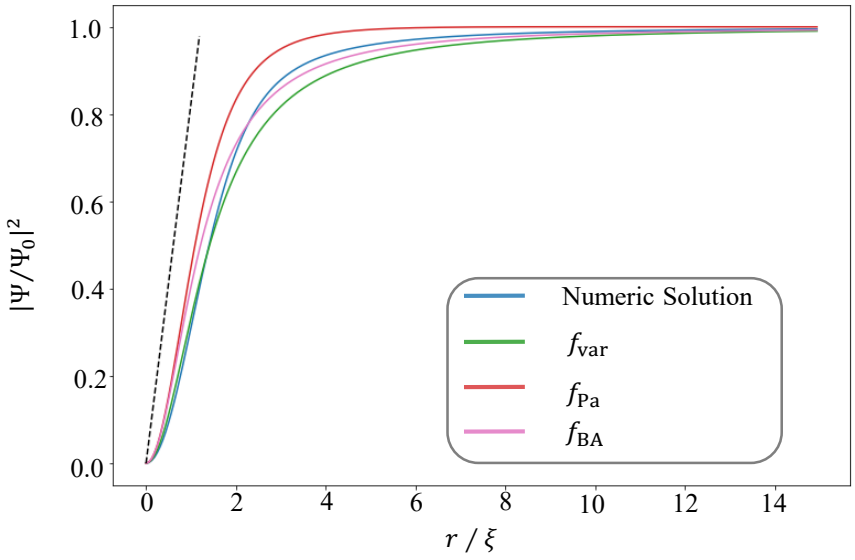

Figure 3.5: A comparison of the approximate analytic vortex cores to a numerically obtained vortex core, plotted in blue. Orange, the variational approximation Eqn. (3.17); red, the Padé approximation Eqn. (3.18); pink, the numerically fitted variational ansatz Eqn. (3.20).

can be found numerically to be $\Lambda = 0.8249...$ [242]. This leads to the approximate form

$$f_{\mathrm{BA}}(r) = \frac{r}{\sqrt{r^2 + \left(\frac{\xi}{\Lambda}\right)^2}}, \tag{3.20}$$

where the length scale $\Lambda^{-1}\xi$ ensures that the functional form matches the vortex at the centre of the core.

Part II

Rotating Bose Einstein Condensates

Chapter 4

Rapidly Rotating Bose Einstein Condensates

Forcing a Bose Einstein Condensate to rotate leads to significantly different physics compared to that of a classical fluid. In this part we present a method for evolving the projected Gross-Pitaevskii equation (PGPE) in an infinite rotating Bose-Einstein Condensate; this allows us to investigate the bulk properties of the system, without needing to worry about edge effects. A key advantage of this is that it allows us to investigate dynamical phase transitions of a rotating superfluid.

4.1 Introduction

The dynamics of rotating 2D Bose gases have been previously studied with the PGPE [178, 243] in finite, harmonically-trapped system using a Laguerre-Gaussian basis. However, in simulations where the condensate has an edge, vortices nucleate at the interface between the condensate and the thermal cloud. These vortices do not penetrate the main bulk of the condensate, rather they remain at the edge of the condensate for considerable time [178]. Between these edge effects, and the tendency of the trapping potential to distort any resulting vortex lattice [244, 245], it difficult to conduct a PGPE simulation of sufficient size to isolate the bulk properties of the system [178].

There are a wide range of numerical methods available for solving the ordinary, non-projected Gross-Pitaevskii Equation (GPE), both with and without rotation. Examples include Crank—Nicolson schemes [147, 173, 246–249], backwards Euler finite difference schemes [250–253], and Sobolov Gradient Methods for a rotating condensate [254–257]. A range of (pseudo-) spectral methods have also been used with Fourier series [258], Chebyshev polynomials [259], and Hermite functions [260]. However, these studies are conducted in a finite trapped system, which will lead to edge effects.

In order to concentrate on the bulk of the system and avoid boundary effects — in a similar way as would be achieved using periodic boundary conditions in the non-rotating case — previous works on rotating 2D systems have used quasi-periodic boundary

conditions to simulate a representative cell of an infinite rotating system. Physically this corresponds to a harmonically trapped gas, rotating rapidly enough that the effective harmonic trapping vanishes. Under such rapid rotation, if the number of vortices in the Bose gas approaches the number of atoms, the gas enters a fractional quantum Hall regime and the classical field approach of the PGPE breaks down. If, however, the number of vortices remains small compared to the number of atoms, the PGPE remains valid. As described by T.-L.Ho, Ref. [261], for sufficiently small interaction strengths, and for a rotation frequency which is approximately equal to the frequency of the harmonic trapping potential, the system is predominantly in the lowest Landau level (LLL) state, due to a large energy gap between the LLL state and higher energy levels. In this regime, at low temperature, the LLL approximation can be used to determine the ground state of a system with good accuracy [261–263]. Such an approximation has led to the studying of vortex lattices [245, 263–270], however, it is necessarily limited to the lowest energy states of the system. Komineas *et al.* [271] investigate the effects of Landau level mixing; we should note, however, that their work concentrates on energy minimisation in a dipolar condensate, and the instability of the lattice to collapse at large values of the chemical potential. They do not undertake dynamic simulations, nor do they investigate finite temperature effects.

Alternatively, Mingarelli *et al.* [272] and Wood *et al.* [273] have implemented quasi-periodic boundary conditions for the Gross–Pitaevskii equation, by using magnetic Fourier transforms and finite difference methods in the symmetric gauge respectively. However, these methods do not operate in a basis of single-particle eigenstates, making it difficult to implement the projection operation needed for the PGPE.

In Chapter 5 we present a numerical method which goes beyond previous work and implements the PGPE in an infinite rotating 2D Bose gas. Our method operates in the Landau gauge, using the correct single-particle basis under quasi-periodic boundary conditions for a representative cell of the system (Fig. 4.1). By establishing a method to integrate the PGPE for such a rotating system, we open the door to study finite-temperature, non-equilibrium dynamics of rotating systems in the bulk, free of edge effects.

In a rotating condensate of finite size, vortices nucleating at the boundary of the condensate and the thermal cloud [178], and the distortion of the lattice due to the trapping potential [244, 245] provide issues when studying vortex lattices.

Non-projected numerical methods will always suffer from pathologies due to boundary conditions, such as mode aliasing issues. Moreover, such methods do not impose a consistent energy cutoff, and so physical quantities in the simulation will depend on this choice of constraining modes. These issues can be solved by using the PGPE.

In the symmetric gauge, in a finite system, Wright *et al.* [178] have studied condensates rotating below the centrifugal limit. However, the upper limit of their energy cutoff is due to the scaling of the Gauss–Laguerre basis which quickly makes the simulations too computationally expensive. This prohibits using a large enough domain that boundary

effects can truly be negated. By operating in the Landau gauge with quasi-periodic boundary conditions, we have successfully removed any issues due to boundary artifacts. Further, by using the correct single particle basis, we are able to implement a projection operator which imposes a consistent energy cutoff.

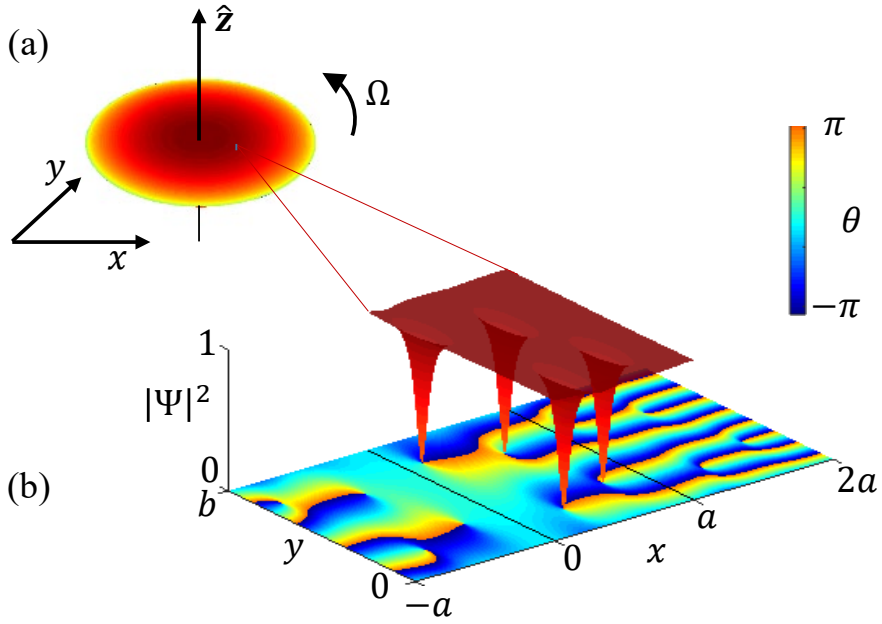

Figure 4.1: A sketch of the system: (a) A large, oblate, harmonically trapped ($\omega_x = \omega_y = \omega_\perp \ll \omega_z = \omega_\parallel$) condensate rotating with angular frequency Ω. (b) In the centrifugal limit ($\Omega \to \omega_\perp$) a small cell in the bulk of the now-infinite condensate can be approximated using the Landau gauge with quasi-periodic (twisted) boundary conditions. The height of the surface represents the density of the wavefunction, while the colour represents the phase of the superfluid.

The remainder of Part II is structured as follows: In Sec. 4.2 we introduce the equation of motion which governs a harmonically trapped Bose gas rotating at the centrifugal limit, as well as introducing the quasi–periodic boundary conditions which we use throughout the following chapters. In Sec. 4.3 we detail the means by which we can choose an arbitrary array of vortices as an initial condition for the PGPE. This requires us to find the Landau gauge expression for the phase of N_v vortices. In Chapter 5 we introduce the PGPE for a infinite rotating system working in the Landau gauge; we also quantify the error which is due to the projection. Sec. 5.2 contains the main results of this part: we consider how the PGPE evolution performs for varying simulation parameters, as well as looking at how our method can be used to find the ground state of a given system. We then investigate the stability of this ground state. Chapter 6 considers the effects of melting the rotating lattice ground state. We describe how the wavefunction may be unwound in order to measure the first order correlation function; this exhibits a transition from algebraic to exponential decay as the amount of noise which is added to the initial condition is increased.

4.2 Rotating Projected Gross-Pitaevskii Equation

4.2.1 The Single–Particle Hamiltonian

In the rotating frame, the Hamiltonian for a particle of mass m rotating with angular momentum $\boldsymbol{\Omega}$ is [274]

$$H_\Omega = \frac{|\boldsymbol{p}|^2}{2m} + \frac{1}{2}m\omega_\perp^2\left(x^2+y^2\right) + \frac{1}{2}m\omega_\parallel^2 z^2 - \boldsymbol{\Omega}\cdot\boldsymbol{r}\times\boldsymbol{p}, \tag{4.1}$$

where $\omega_\parallel$ and $\omega_\perp$ are the trapping frequencies in the z and the radial directions, respectively. Throughout Part II, we will not worry about non-uniform rotation, disturbance to the density of the fluid, or any other effects which would be a direct result of the mechanism used to spin the gas. On choosing the z axis to be the axis of rotation, $\boldsymbol{\Omega} = \Omega\hat{\boldsymbol{z}}$, the Hamiltonian may be written as [126, 275, 276]

$$H_\Omega = \frac{\left(\boldsymbol{p} - m\boldsymbol{\Omega}\times\boldsymbol{r}\right)^2}{2m} + \frac{1}{2}m\left(\omega_\perp^2 - \Omega^2\right)\left(x^2+y^2\right) + \frac{1}{2}m\omega_\parallel^2 z^2. \tag{4.2}$$

In the middle term of Eqn. (4.2) we see that the frequency of rotation Ω reduces the radial trapping frequency. We set $\Omega = \omega_\perp$, which is defined by Cooper [126] as the centrifugal limit[1]. This yields the Hamiltonian

$$H_\Omega = \frac{\left(\boldsymbol{p} - \boldsymbol{A}\right)^2}{2m} + \frac{1}{2}m\omega_\parallel^2 z^2, \tag{4.3}$$

where $H_\Omega\Psi$ is invariant under the transformation

$$\boldsymbol{A} \to \boldsymbol{A} + \nabla\lambda, \qquad \Psi \to \exp\left(\frac{i}{\hbar}\lambda\right)\Psi, \tag{4.4}$$

for a given λ, a function of x and y. Hence we have the gauge freedom to choose any $\boldsymbol{A}$ such that $\nabla\times\boldsymbol{A} = 2m\Omega\hat{\boldsymbol{z}}$. Eqn. (4.2) is implicitly in the symmetric gauge, which is logical outside the centrifugal limit, as the single particle basis functions are the associated Laguerre polynomials [277]. The trapping of a BEC gives rise to several boundary phenomena, including the short lived nucleation and annihilation of vortices which do not penetrate the bulk of the fluid [178]. At the centrifugal limit, it is advantageous to use the Landau gauge,

$$\boldsymbol{A} = \begin{pmatrix} 0 \\ 2m\Omega x \\ 0 \end{pmatrix}, \tag{4.5}$$

as the single particle basis functions with quasi-periodic boundary conditions can be found. This will enable us to study the bulk of the Bose gas using the PGPE, without worrying about edge effects.

[1] Experimentally it is possible to achieve $\Omega = 0.99\omega_\perp$, see for example [165, 166].

4.2.2 The GPE in Dimensionless Variables

The most common description of an ultracold Bose gas is that of a wavefunction Ψ which obeys the mean–field Gross–Pitaevskii equation (GPE). In a rotating system such as the one described in Sec. 4.2.1, this equation takes the form

$$i\hbar\frac{\partial\Psi}{\partial t} = H_\Omega\Psi + g|\Psi|^2\Psi - \mu\Psi. \tag{4.6}$$

We are interested in the behaviour of vortices in the rotating plane and so we adopt a highly oblate condensate with trapping frequencies $\omega_\perp \ll \omega_\parallel$. With this tight confinement in the z direction, and the condition $\hbar\omega_\parallel \gg \mu$, the excitation of modes in the z direction is prevented. The GPE for our rotating quasi–2D system is therefore

$$i\hbar\frac{\partial\Psi}{\partial t} = \left(-\frac{\hbar^2}{2m}\nabla^2 + \frac{i\hbar}{m}\boldsymbol{A}\cdot\nabla + 2m\Omega^2x^2 + g_{2D}|\Psi|^2 - \mu_{2D}\right)\Psi. \tag{4.7}$$

This equation is fundamentally different to those of Refs. [147, 173] as we are in the Landau gauge, given by Eqn. (4.5). One can convert from the Landau gauge to the symmetric gauge [272, 273] by substituting

$$\lambda = -m\Omega xy \tag{4.8}$$

into Eqn. (4.4). We adopt natural units for the system, based on the healing length $\xi = \hbar/\sqrt{m\mu_{2D}}$. This leads to dimensionless distances $x' = x/\xi$ and $y' = y/\xi$, a dimensionless time $t' = \mu_{2D}t/\hbar$, and a dimensionless wavefunction $\Psi' = \Psi\sqrt{g_{2D}/\mu_{2D}}$. Using these units we write Eqn. (4.7) in dimensionless form (dropping the prime notation)

$$i\frac{\partial\Psi}{\partial t} = H_\Omega\Psi + |\Psi|^2\Psi - \Psi, \tag{4.9}$$

where the one-body Hamiltonian can be written as

$$H_\Omega = -\frac{1}{2}\nabla^2 + i\Gamma^2x\frac{\partial}{\partial y} + \frac{1}{2}\Gamma^4x^2, \tag{4.10}$$

with $\Gamma = \xi/\ell$ the ratio of the healing length ξ to the "magnetic length" ℓ by [126, 278] defined

$$\ell^2 = \frac{\hbar}{2m\Omega}. \tag{4.11}$$

In the case of the rotating Bose gas, ℓ is a characteristic distance between vortices.

4.2.3 Quasi-Periodic Boundary Conditions

We now wish to consider a representative cell of an infinite rotating system, by introducing quasi-periodic boundary conditions, and to establish the corresponding single-particle basis functions. This cell will have physical dimensions $0 \le x \le a\xi$, $0 \le y < b\xi$, with

aspect ratio $\kappa = a/b$.

As discussed in Chapter 3, a conventional fluid rotating with angular momentum $\mathbf{\Omega}$ has velocity $\mathbf{v} = \mathbf{\Omega} \times \mathbf{r}$, giving a uniform vorticity field [69], $\nabla \times \mathbf{v} = 2\mathbf{\Omega}$. On making a Madelung transform, the superfluid velocity is $\mathbf{v} = m^{-1}\hbar\nabla\theta$, implying that vortices appear as point-like singularities in the phase, about which θ winds by 2π. From the superfluid velocity, in the cell $\mathcal{R}$ of area ab, one may use Stokes' theorem to compute

$$\int_{\mathcal{R}} \nabla \times \mathbf{v} \cdot d^2\mathbf{r} = \oint_{\partial\mathcal{R}} \mathbf{v} \cdot d\mathbf{r} = \frac{2\pi\hbar}{m} N_{\mathrm{v}} \tag{4.12}$$

where N_{v} is the number of vortices in the cell, and $\partial\mathcal{R}$ is the closed curve bounding the cell. Similarly, one can use the result for solid-body rotation to compute

$$\int_{\mathcal{R}} \nabla \times \mathbf{v} \cdot d^2\mathbf{r} = \int_0^a dx \int_0^b dy\; 2\mathbf{\Omega} \cdot \hat{\boldsymbol{z}}\; dx\, dy = 2\Omega ab. \tag{4.13}$$

Comparing Eqn. (4.12) and Eqn. (4.13) implies the Feynmann relation for areal vortex density [198],

$$\frac{2\pi\hbar}{m} N_{\mathrm{v}} = 2\Omega ab, \tag{4.14}$$

which, using the definition of "magnetic length" from Eqn. (4.11), leads us to a quantisation condition

$$ab\Gamma^2 = 2\pi N_{\mathrm{v}}, \tag{4.15}$$

which relates the area of the cell to the net number of vortices N_{v} [197]. With this quantisation condition, we set the net number of vortices N_{v} and the size of the box a, b, which determines the rotation Ω.

For the representative cell, we define the boundary conditions to be (working in dimensionless variables)

$$\mathrm{Arg}\left[\Psi\left(x + a, y\right)\right] = \mathrm{Arg}\left[\Psi\left(x, y\right)\right] + \frac{2\pi y}{b}, \tag{4.16}$$

$$\mathrm{Arg}\left[\Psi\left(x, y + b\right)\right] = \mathrm{Arg}\left[\Psi\left(x, y\right)\right]. \tag{4.17}$$

Unlike standard periodic boundary conditions, these boundary conditions provide the wavefunction with a winding in the phase. Such boundary conditions were discovered to be necessary in the work of Byers and Yang [279], who considered the physical principles behind the quantization of magnetic flux in a superconducting ring. Working with vortices in a rotating superfluid in the *symmetric* gauge, Wood *et al.*, [273], has shown that analogous quasi-periodic boundary conditions are necessary to ensure that the relative superfluid velocity is periodic. The boundary conditions Eqns. (4.16) and (4.17) are therefore required in our system as a direct result of the quantisation condition in Eqn. (4.15), and the fact that we work in the Landau gauge, Eqn. (4.5). Throughout this part, we will refer to these boundary conditions as quasi-periodic, or 'twisted' [272] boundary conditions.

We now consider the appropriate basis functions needed to implement a projected Gross-Pitaevskii equation. Previous work [166, 245, 263, 265–268, 270, 278] has investigated rapidly rotating 2D systems which depend only on the Lowest Landau Level (LLL). This is accurate for a system of dense vortices, however where the typical vortex spacing is much larger than the healing length, interactions in the Bose gas lead to contributions from higher Landau levels [126]. Ref. [278] gives the LLL eigenfunction of the Hamiltonian in Eqn. (4.10), which can be extended to describe higher Landau levels. These eigenfunctions take the form

$$\phi_{n,k} = \sqrt{a\Gamma}\sum_{p=-\infty}^{\infty}\chi_n\left[\Gamma a\left(\frac{k}{N_\mathrm{v}}+p\right)-\Gamma x\right]\exp\left[i\Gamma^2 a\left(\frac{k}{N_\mathrm{v}}+p\right)y\right], \tag{4.18}$$

where

$$\chi_n(x) = \frac{1}{\sqrt{2^n n!\sqrt{\pi}}}H_n(x)\exp\left(-\frac{1}{2}x^2\right). \tag{4.19}$$

Here, $H_n(\cdot)$ is the n^{th} physicists' Hermite polynomial [280], and the Landau levels are indexed by $n = 0, 1, \ldots$. Without loss of generality, we choose to normalise the basis functions to ab (see Appendix B.1.1 for details). The eigenenergies corresponding to the eigenfunctions of Eqn. (4.18) are

$$E_{n,k} = \Gamma^2\left(n+\frac{1}{2}\right). \tag{4.20}$$

Expanding the wavefunction Ψ in terms of all eigenstates below an energy cutoff $E_\mathrm{cut} = \Gamma^2(M+1/2)$ and solving Eqn. (4.9) for the expansion coefficients constitutes the PGPE for this system. The choice of cutoff M will be discussed further in Secs. 5.1 and 5.2.

4.3 Vortex Ansatz For Initial Condition

In this section we describe the process by which we prepare an initial configuration of N_v vortices placed within the cell. This allows us to investigate a number of scenarios involving free vortices, clustered vortices and dipole pairs.

It is known that it is possible to express the phase of a vortex using the zeros of a Weirstrass function [201]. Further, in the Landau gauge it is appropriate to use Jacobi Theta functions to describe the phase. The 3rd Jacobi Theta Function is defined as [280]

$$\vartheta_3(z,\tau) = 1+2\sum_{n=1}^{\infty}q^{n^2}\cos(2nz), \tag{4.21}$$

where z is a complex coordinate, and $\tau \in \mathbb{C}$ is the lattice parameter with nome $q = \exp(i\pi\tau)$. We restrict ourselves to the case of a rectangular domain, requiring $\Re(\tau) = 0$

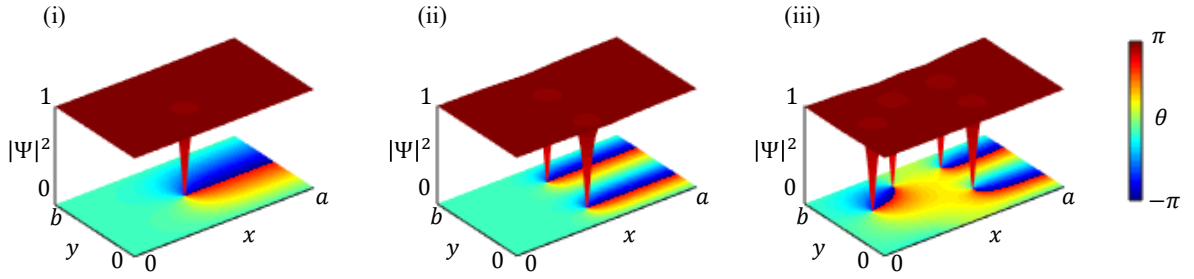

Figure 4.2: Example configuration of vortices using the method described in Sec. 4.3. The colour bar indicates the phase of the superfluid. (a) A single, positively charged, vortex is placed at the centre of the cell. (b) Two positively charged vortices are placed at $(a/2, 3b/4)$ and $(a/2, b/4)$. (c) Three positively charged and one negatively charged vortices create a dipole pair in the cell.

and $\Im(\tau) > 0$, so that ϑ_3 has quasi-periodicity relation

$$\mathrm{Arg}\left[\vartheta_3\left(z + f\pi + g\tau\pi; \tau\right)\right] = \mathrm{Arg}\left[\vartheta_3\left(z; \tau\right)\right] - 2g\Re(z), \tag{4.22}$$

for integers f and g (see Appendix B.2 for further information). In order to describe a domain which is arbitrary sized, we introduce L then by re-scaling $z \to \pi z/L$, and defining the lattice parameter τ to be purely imaginary, the Jacobi theta function ϑ_3 is quasi periodic on $0 \leq \Re(z) < L$ and $0 \leq \Im(z) < L\Im(\tau)$. In this case, the quasi-periodicity relation of Eqn. (4.22) becomes

$$\mathrm{Arg}\left[\vartheta_3\left(\frac{\pi}{L}\left(z + L\tau\right); \tau\right)\right] = \mathrm{Arg}\left[\vartheta_3\left(\frac{\pi z}{L}; \tau\right)\right] - \frac{2\pi}{L}\Re(z). \tag{4.23}$$

By comparison with the quasi-boundary conditions of Eqn. (4.16), it follows that $L = b$, $\tau = i\kappa$ and $z = ix - y$. Consequently, it is possible to determine that the fundamental solution for the phase θ of a vortex centred in the box at $(a/2, b/2)$, is

$$\theta(z) = c\mathrm{Arg}\left[\vartheta_3\left(\frac{\pi}{b}z\,;\, i\kappa\right)\right], \tag{4.24}$$

where c is the integer charge of the vortex. This fundamental solution is shown in the phase plot of Fig. 4.2 (i). By the use of a suitable gauge transformation, it can be shown that this is equivalent to expressions obtained for quasi-periodic boundary conditions in the symmetric gauge in Ref. [273].

Suppose that we wish to obtain the phase of the kth vortex, of charge c_k, which is shifted from the centre of the cell, to the position (x_k, y_k). Then we define the effective vortex coordinate

$$z_k = i\left(x_k - \frac{a}{2}\right) - \left(y_k - \frac{b}{2}\right), \tag{4.25}$$

so that the phase of the kth vortex is given by

$$\theta_k\left(z\,;\,z_k\right) = c_k \mathrm{Arg}\left[\vartheta_3\left(\frac{\pi}{b}[z-z_k];i\kappa\right)\right]. \tag{4.26}$$

The density profile of a vortex was found numerically in Ref. [242]. Non-dimensionalising this function, and setting the background density to be one, we have

$$\rho_k\left(z\,;\,z_k\right) = \left[\frac{\left|z-z_k+\frac{1}{2}(ia-b)\right|^2}{\left|z-z_k+\frac{1}{2}(ia-b)\right|^2+\Lambda^{-2}}\right]^{1/2}, \tag{4.27}$$

where $\Lambda \approx 0.8249$ is a universal constant.

Combining phase and density profiles of the individual vortices, our ansatz wavefunction for N_v vortices is

$$\Psi\left(z\,|\,\{z_k\}\right) = \prod_{k=0}^{N_\mathrm{v}-1} \rho_k\left(z;z_k\right)\exp\left[i\theta_k\left(z;z_k\right)\right], \tag{4.28}$$

where $\{z_k\} = \{z_0,\ldots,z_{N_\mathrm{v}-1}\}$. In order to determine the symmetry conditions of this ansatz, let us consider the transformation $x \to x+a$. In this case, we have

$$\mathrm{Arg}\left[\Psi\left(z+ia\,|\,\{z_k\}\right)\right] = \sum_{k=0}^{N_\mathrm{v}-1} c_k \mathrm{Arg}\left[\vartheta_3\left(\frac{\pi}{b}\{z-z_k\}+i\frac{\pi a}{b};i\kappa\right)\right], \tag{4.29}$$

which, using the quasi-periodicity relation of Eqn. (4.22), is

$$\mathrm{Arg}\left[\Psi\left(z+ia\,|\,\{z_k\}\right)\right] = \mathrm{Arg}\left[\Psi\left(z\,|\,\{z_k\}\right)\right] \quad + \quad \frac{2\pi N y}{b} + \frac{\pi}{b}\sum_{k=0}^{N_\mathrm{v}-1}\left(y_k-\frac{b}{2}\right), \tag{4.30}$$

where N_v is the net number of vortices (the sum of c_k). The first two terms on the right hand side of Eqn. (4.30) are in direct agreement with the quasi-periodic boundary conditions of Eqns. (4.16) and (4.17). However, to match the boundary conditions the third term must vanish. This means that the vortex positions y_k must satisfy

$$\bar{y_v} = \frac{1}{N_\mathrm{v}}\sum_{k=0}^{N_\mathrm{v}-1} c_k y_k = \frac{b}{2}, \tag{4.31}$$

placing the center of vorticity at $b/2$ in the y-direction. This condition is related to the fact that the ground state vortex lattice breaks the translational symmetry of the system. Adding a constant to our boundary conditions [Eqn. (4.17)] would trivially shift the center of vorticity within the cell. An equivalent connection between boundary conditions and the center of vorticity is found for quasi-periodic boundary conditions in the symmetric gauge [273]. Fig. 4.2 shows a small selection of initial vortex configurations which can be created using the ansatz wavefunction of Eqn. (4.28).

Chapter 5

Numerically Implementing the Projected Gross-Pitaevskii Equation in an Infinite Rotating BEC

5.1 Numerical Method For Basis Transformation

5.1.1 PGPE Implementation

To implement the PGPE for the quasi-periodic system introduced in Sec. 4.2, we follow the same approach as used for the uniform system in Ref. [281], but using the quasi-periodic one-body eigenstates. As described by Ref. [134], defining an orthonormal projector with respect to the one-body Hamiltonian is convenient due to the fact the many-body spectrum is well approximated by the single-body spectrum when in the high energy limit. However, in our case there is no known exact numerical quadrature rule for the basis functions with which to implement the projection to numerical precision. Instead we introduce an approximate projection operation that can be made sufficiently accurate for our purposes.

Our basis functions are given by Eqn. (4.18), and we define the wavefunction Ψ to be

$$\Psi(x,y,t) = \sum_{n=0}^{M-1} \sum_{k=0}^{N_\mathrm{v}-1} c_{n,k}(t)\, \phi_{n,k}(x,y), \tag{5.1}$$

where our energy cutoff is prescribed by the value of M. The summation over p contained within the basis functions, Eqn. (4.18), is truncated so that $-p_{max} \leq p \leq p_{max}$. It is critical that we choose a large enough p_{max} that the quasi–periodic basis functions are approximately orthogonal, and we discuss the validity of this truncation in Sec. 5.1.2. We use the orthonormality conditions of the basis functions (see Appendix B.1.1 for details),

to derive an evolution equation for the coefficients $c_{n,k}$

$$i\frac{dc_{n,k}}{dt} = (E_{n,k}-1)\,c_{n,k} + \sum_{n',m,,m'=0}^{M-1}\sum_{k',j,j'=0}^{N_{\rm v}-1} c_{n',k'}c_{m,j}c_{m',j'}\mathcal{I}_{n,n',m,m';k,k',j,j'} \tag{5.2}$$

where

$$\mathcal{I}_{n,n',m,m';k,k',j,j'} = \int_0^a\int_0^b \phi^*_{n,k}\phi^*_{n',k'}\phi_{m,j}\phi_{m',j'}\,dydx. \tag{5.3}$$

There is no known quadrature rule for the integral in Eqn. (5.3), and so we instead will use an approximate pseudospectral method [282]. We write Eqn. (5.1) as

$$\boldsymbol{\Psi} = T\boldsymbol{c}, \tag{5.4}$$

where $\boldsymbol{\Psi}$ is a real space representation of the wavefunction with Q^2 elements indexed by $\boldsymbol{r}_i = (x,y)_i$, and $\boldsymbol{c}$ is a representation of the wave function in the 'coefficient space' of the basis functions, with $MN_{\rm v}$ elements indexed by $\boldsymbol{\sigma}_j = (n,k)_j$. The matrix T is written in terms of the basis functions as

$$T_{ij} = \phi_{\boldsymbol{\sigma}_j}(\boldsymbol{r}_i). \tag{5.5}$$

We must also define the matrix U, which is the inverse transformation of Eqn. (5.4), i.e. $U = T^\dagger/Q^2$, and the diagonal 'energy matrix' E, which contains the eigenvalues of the basis functions, $E_{jj} = E_{\boldsymbol{\sigma}_j}$. The resultant equation for the evolution of the coefficients is

$$i\frac{d\boldsymbol{c}}{dt} = (E - I_{MN_{\rm v}})\,\boldsymbol{c} + U|T\boldsymbol{c}|^2\,(T\boldsymbol{c}), \tag{5.6}$$

the evolution of which will be discussed in Sec. 5.2.

We now consider two sources of error which are unavoidable when performing numerical simulations: the projection error, which arises on choosing the number of grid-points Q for a given M, and the error associated with truncating the summation over p, which comes from our choice in p_{max}.

5.1.2 Projection Error

As discussed in Sec. 4.2, the energy cutoff in our simulations is defined as M, which is the number of Landau levels which are included in our basis functions. We are also working with a system which does not have a quadrature rule, hence there is no clear cut way of selecting a value of Q for a given M. The cubic term in the GPE may lead to aliasing in any grid representation of the wavefunction [133]. In our system, this corresponds to the non-linear term of the GPE producing polynomials of order $3M$, which are outside the c–field region and hence not energy conserving. It is therefore necessary to check the validity of any given values of Q and M, which we do with the following algorithm.

Assume that our system has $N_{\rm v}$ states[1], Q grid points in each of the x and y directions,

[1]Mathematically, the number of states, $N_{\rm v}$ represents the net number of vortices within the funda-

and M Landau levels; for these parameters there is a transformation matrix T, and its inverse U, the construction of which is described in Eqn. (5.4). We generate the matrix $\tilde{T}$ which also has $N_{\rm v}$ states and Q grid-points, but has $3M$ Landau levels (on account of the nonlinear term in Eqn. (4.9) being cubic). For the remainder of this section, we use a tilde to denote a coefficient space which has $3M$ Landau levels.

We create a test vector $\tilde{\boldsymbol{c}}$ which is

$$\tilde{\boldsymbol{c}} = \frac{1}{\sqrt{2MN_{\rm v}}}(\overbrace{0,\ldots,0}^{M\times N_{\rm v}},\overbrace{1,\ldots,\ldots,1}^{2M\times N_{\rm v}}), \tag{5.7}$$

which is a vector where the first $M \times N_{\rm v}$ elements (which are the coefficients for the basis functions with the lowest M Landau levels) are zero, while the other elements are identical, and normalised so that $|\tilde{\boldsymbol{c}}|^2 = 1$. From here, we compute

$$\boldsymbol{c} = U \left[\tilde{T}\tilde{\boldsymbol{c}}\right]. \tag{5.8}$$

This transforms the test vector $\tilde{\boldsymbol{c}}$ from the enlarged basis in coefficient space, into the $Q \times Q$ basis in real space, and then back to the smaller, $M \times N_{\rm v}$, coefficient space.

Using $\boldsymbol{c}$, the $M \times N_{\rm v}$ array of coefficients, we can now quantify the error in the projection. If the projection was perfect, the array $\boldsymbol{c}$ would be precisely zero. That is to say: we would have recovered the coefficients of the lowest M Landau levels from the test array $\tilde{\boldsymbol{c}}$ without alias.

If, however, there are non-zero elements in $\boldsymbol{c}$, then there has been some "leakage" of higher order modes into the M lowest modes which we have defined as our c-field. Numerically we define this error to be

$$\delta = \max\{c^*_{n,k}c_{n,k}\}, \tag{5.9}$$

where this "leakage" corresponds directly to momentum aliasing.

The results of this analysis are presented in Fig. 5.1. We see that, for any given M, there is a threshold value of Q for which the projection error δ becomes negligible. Below these threshold values, the error decreases at a rate which depends on M: for small M, the error decreases very quickly, while larger M requires more grid-points. Above the threshold value, the projection error converges to a characteristic error for the given set of simulation parameters. This means that increasing the number of points serves only to slow the simulation, and offers no numerical advantage.

We note that the analysis above was conducted with a cell where $a = b = 64$, the truncation $p_{max} = 10$, and $N_{\rm v} = 4$ vortices. A similar analysis can be conducted for a different size cell, and for a different number of states in the system, however we note that the results are qualitatively the same: for higher M one must increase the number of grid-points in order to reduce the projection error.

mental cell.

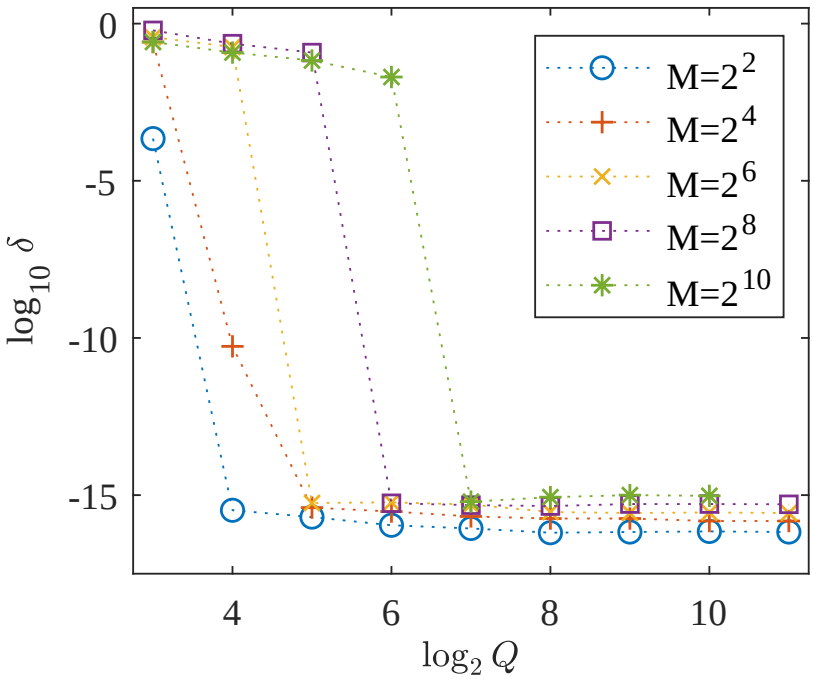

Figure 5.1: The projection error, δ as a function of Q for varying values of M. We have set $a = b = 2^6$ to be the cell size, fixed $p_{max} = 10$, and set $N_v = 4$. The dotted lines are added as a guide to the eye.

5.1.3 Truncation Error

Clearly, when calculating the matrix T from the basis functions defined in Eqn. (4.18) it is necessary to truncate the summation over p. We must, however, ensure that we have chosen a large enough value of p_{max} that significant contributions to the wavefunction from neighbouring cells are not erroneously ignored. It is also critical to choose a large enough value of p_{max}, as the infinite sum over p is responsible for transforming an integration over a finite domain, into an integration over an infinite domain, which is how the orthonormality of the Hermite polynomials is defined (see Appendix B.1.1 for further details).

There are several well known bounds for the zeros of Hermite polynomials, however the eigenfunctions in Eqn. (4.18) are a sum over a product of a Hermite function $\chi_n(x)$, and the complex exponential in y. Although Hermite functions decay exponentially quickly after their most extreme zeros, there is still an imaginary part of these eigenfunctions which must be taken into account. The presence of p in both the x and y components of the basis functions mean that truncating the summation over p is not as simple as using a bound for the Hermite polynomials, and we must be cautious that the value of p_{max} is chosen correctly.

We perform the same analysis as in Sec. 5.1.2 in order to quantify the error δ, however in each case we fix Q and M and instead vary p_{max}. The results can be found in Fig. 5.2. For each Q and M, we note there is a threshold value of p_{max} above which the truncation error becomes negligible (this is indicated by the sharp cusp in the graph). Initially there

is an increase in the error (for $p_{max} = 1$), however this is because the basis functions do not converge to the correct value for this choice in truncation. Above the threshold value, there is a convergence in the error for a given M and Q.

Informed by the analysis of Sec. 5.1.2, we note that for values of M which were greater than 2^{10}, it was necessary to use $Q = 2^8$, grid points in each direction to get a meaningful result.

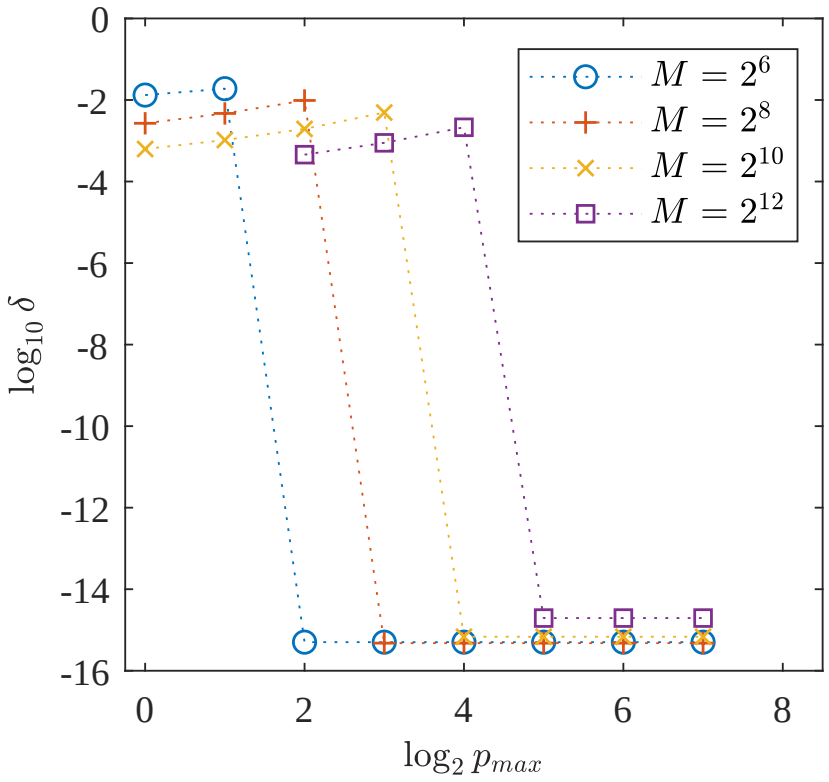

Figure 5.2: The truncation error δ, for varying p_{max} with fixed M and Q. For $M \in \{2^6, 2^8, 2^{10}\}$ we used $Q = 2^7$ grid-points, while for $M > 2^{10}$, it is necessary to use $Q = 2^8$ grid-points to achieve a meaningful result. Note that $a = b = 2^6$ and $N_v = 4$ in this analysis. The dotted lines are added as a guide to the eye.

5.2 Convergence and Testing of the Method

5.2.1 Overview of Numerical Procedure

Here we briefly outline how the pseudospectral method described above can be implemented numerically. In order to perform the transformations between real and coefficient space required by Eqn. (5.4), we begin by creating the matrix described in Eqn. (5.5). Note that this fixes the dimensions of the fundamental cell, a, b (and therefore κ), the number of Landau levels, M, the number of grid-points, Q, and the net number of vortices, N_v. Once this is complete, we evolve Eqn. (5.6) from an initial condition. Numerically, we compute the time evolution using an adaptive 8th order Dormand Prince (DP8) method

[283] with adaptive time stepping subject to an error tolerance ϵ. This method, based on a RK8(7) procedure in which the principal truncation error of the 8^{th} order estimate is minimised, is advantageous in that it is highly accurate and is shown to be efficient even for non-linear equations. Since the majority of the memory requirements lie in the storing of the T and U matrices, the extra memory required to use such a high order time-stepping scheme is inconsequential. The high order of the method reduces the total number of time derivative evaluations required while maintaining sufficiently stringent tolerance to preserve the conserved quantities to good accuracy over long time. The most computationally demanding step in the procedure is performing the basis transformations needed to evaluate the time derivative; this amounts to performing multiplication by the matrices T and U, which have a large size of $MN_{\text{v}}Q^2$ elements (about 2^{27} for typical parameters). Owing to the large size and high condition number of the T and U matrices, numerical rounding errors in these matrix-vector multiplications can become non-negligible with standard double-precision arithmetic. We find that performing a stabilized matrix-vector multiplication, using the techniques to extend precision described in Ref. [284] and parallelized using OpenMP, effectively eliminates these problems without significantly increasing computation times[2].

There are two kinds of initial conditions that we may use. In the first instance, we can control the occupation of the modes in coefficient space, in a manner similar to the simulations of Ref. [285]. More conveniently, we can produce an ansatz wavefunction whereby we prescribe the position and charge of N_{v} vortices, using the method described in Sec. 4.3. The only difference is that we must transform this ansatz into coefficient space before evolving.

5.2.2 Conserved Quantities

There are three quantities which should be conserved by any numerical treatment of Eqn. (4.9). They are the real-space norm $\mathcal{N}_R$ of the wavefunction,

$$\mathcal{N}_R(t) = \int_0^a \int_0^b \Psi^*(x,y,t)\Psi(x,y,t)\,dydx, \tag{5.10}$$

the norm of the coefficients, $\mathcal{N}_C$, defined as

$$\mathcal{N}_C(t) = \sum_{j=0}^{MN_{\text{v}}-1} c^*_{\boldsymbol{\sigma}_j}(t)\,c_{\boldsymbol{\sigma}_j}(t), \tag{5.11}$$

and the energy of the system,

$$\mathcal{E}(t) = \frac{1}{\mathcal{N}_C(0)} \sum_{j=0}^{MN_{\text{v}}-1} E_{\boldsymbol{\sigma}_j} c^*_{\boldsymbol{\sigma}_j}(t)\,c_{\boldsymbol{\sigma}_j}(t) + \frac{1}{\mathcal{N}_R(0)} \int_0^a \int_0^b \frac{1}{2}|\Psi(x,y,t)|^4\,dydx. \tag{5.12}$$

[2]Note that a generic Fortran code to implement this stabilized matrix-vector multiplication, as well as an outline DP8 code, was provided by Thomas Billam.

In both Eqns. (5.10) and (5.12) we have discretized real space, and so the integrals will be replaced with summations, with $dx \to a/Q$ (likewise $dy \to b/Q$). Due to numerical error, these quantities will not be conserved by our evolution scheme. Tracking their changes, however, provide a key insight as to how accurate our scheme is.

5.2.3 Evolution of Vortex Ansatz States

In Fig. 5.3, column (i), we calculate the evolution error for varying values of M, while the tolerance in the numerical timestepping is fixed, $\epsilon = 10^{-10}$. We do this whilst varying the number of grid points: $Q = 2^6$, blue crosses; $Q = 2^7$, red circles; $Q = 2^8$, yellow squares; $Q = 2^9$, purple asterisks. We note that the curves have a characteristic bow shape; initially increasing the number of Landau levels decreases the error in the evolution. For each value of Q, however, there comes a point where projection error dominates the increase in M, and the evolution error increases. This is particularly noticeable in the regime of low Q and high M in the plot of $\Delta\mathcal{N}_R$, Fig. 5.1 (a)(i).

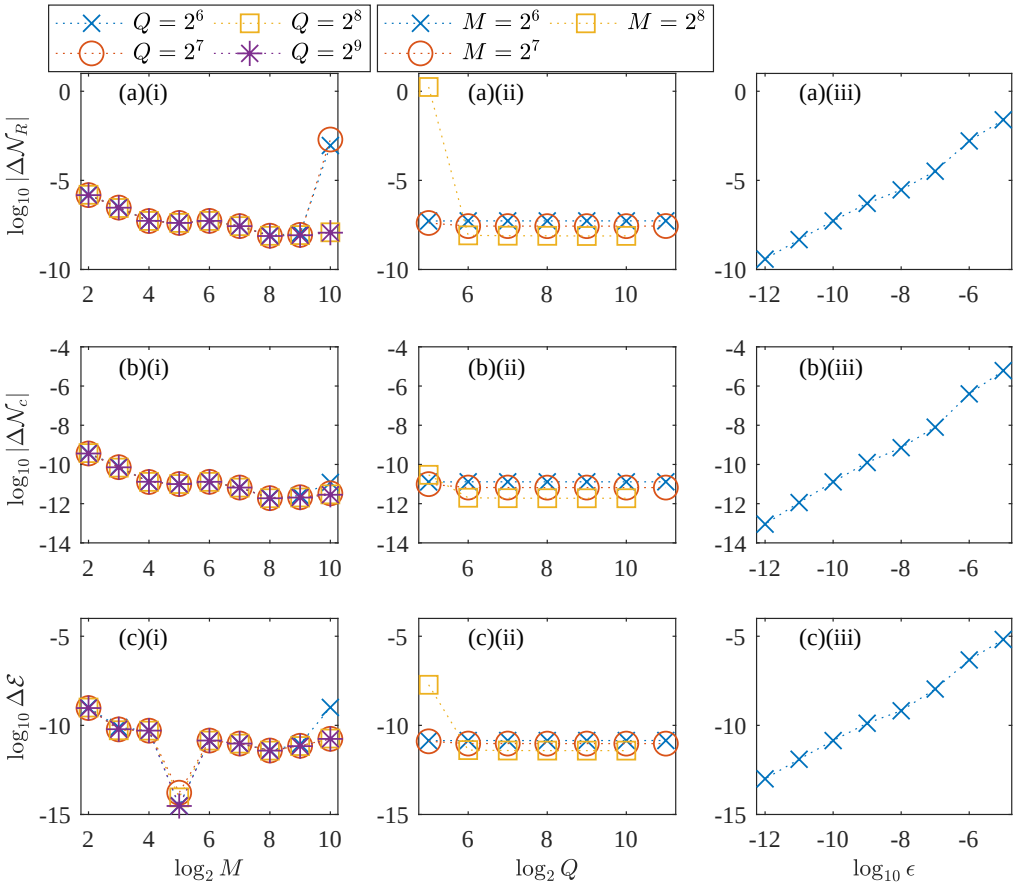

Figure 5.3: Evolution error for the quantities $\mathcal{N}_R$, row (a); $\mathcal{N}_C$, row (b); and $\mathcal{E}$, row (c). Column (i): varying M for $Q = 2^6$, blue crosses; $Q = 2^7$, red circles; $Q = 2^8$, yellow squares; $Q = 2^9$, purple asterisks. Column (ii): varying Q for $M = 2^6$, blue crosses; $M = 2^7$, red circles; $M = 2^8$, yellow squares. For columns (i) and (ii), $\epsilon = 10^{-10}$. Column (iii): varying ϵ for $M = 2^6$ and $Q = 2^8$. In all cases, $a = b = 2^6$.

In column (a)(ii)–(c)(ii), we calculate the evolution error for varying values of Q for

a fixed tolerance of $\epsilon = 10^{-10}$, with $M = 2^6$, blue crosses; $M = 2^7$, red circles; $M = 2^8$, yellow squares. We observe that increasing the number of grid points Q leads to a monotonic decrease in the evolution error. Initially projection error dominates, however this is in a regime where we have one or fewer grid points per healing length. As Q increases beyond approximately 4 grid points per healing length, we note that the error converges for each value of M; it it also apparent that once the error has converged, a higher value of M leads to a better conservation in the quantities of interest.

In column (a)(iii)–(c)(iii), we calculate the evolution error for varying values of ϵ, where $M = 2^6$ and $Q = 2^8$. We see that there is a very good agreement between the tolerance size, and the expected error of the DP8 method.

It should be noted that although this demonstrates the evolution error of one initial state, it is qualitatively representative of all initial states. That is to say, the results of the evolution error testing presented here are a realisation of a single (randomly chosen) initial condition, but we note that this is indicative of all initial conditions.

5.2.4 Stability of the Ground State

As well as performing the dynamical evolutions described in the previous sections, we want to be able to find the ground state of N_v vortices. In order to do this, we add a dimensionless damping parameter γ to the governing equation [147, 274]. This parameter describes the diffusion of thermal atoms from the system, a key physical process in relaxing the system to a ground state [88]. This means that Eqn. (4.9) becomes

$$i\frac{\partial\Psi}{\partial t} = (1 - i\gamma)\left[H_\Omega\Psi + |\Psi|^2\Psi - \Psi\right], \tag{5.13}$$

and hence we will numerically simulate

$$\frac{d\boldsymbol{c}}{dt} = -(\gamma + i)\left[(E - I_{MN_\mathrm{v}})\,\boldsymbol{c} + U|T\boldsymbol{c}|^2(T\boldsymbol{c})\right]. \tag{5.14}$$

For a domain with aspect ratio $\kappa = \sqrt{3}$, the ground state has been shown to be a hexagonal lattice [200, 201, 276]. We will show in the rest of this section that this damped PGPE will cause the system to relax into a vortex lattice ground state.

The procedure is as follows: We initially seed all of the coefficients so that

$$c_{n,k}(0) = \frac{(1+i)}{\sqrt{2MN_\mathrm{v}}}, \tag{5.15}$$

and evolve this state using the damped GPE in Eqn. (5.14), with the parameter $\gamma = 1$. This leads to the ground state $\boldsymbol{c}^{(g)}$. In Fig. 5.4 we plot the ground state for $N_\mathrm{v} = 6$, $N_\mathrm{v} = 8$ and $N_\mathrm{v} = 18$.

A lattice is characterised by a pair of primitive lattice vectors $\boldsymbol{L}_1$ and $\boldsymbol{L}_2$, from which we can infer the shape of a lattice (i.e. square, hexagonal, etc.). In Fig. 5.4 we add

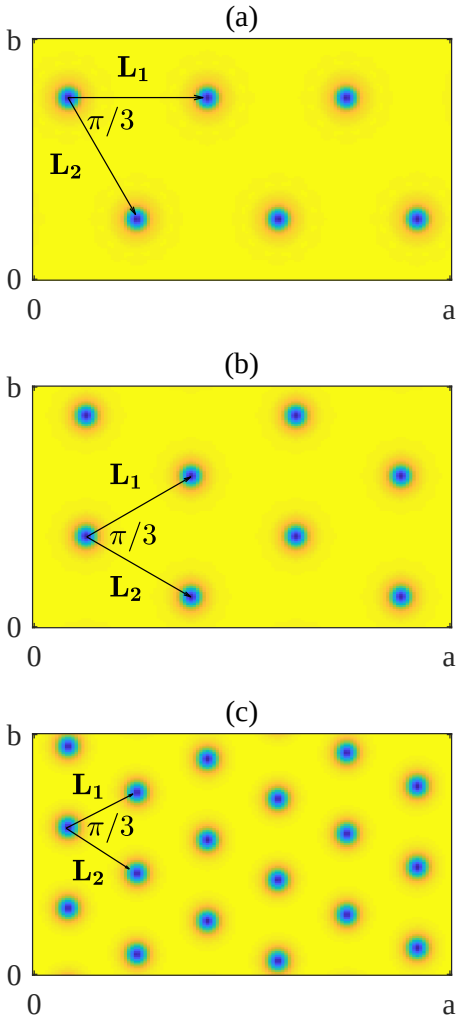

Figure 5.4: The hexagonal lattice ground states. (a) a system with $N_\mathrm{v} = 6$ vortices, (b) a system with $N_\mathrm{v} = 8$ vortices, and (c) a system with $N_\mathrm{v} = 18$ vortices. The primitive vectors of a hexagonal lattice, $\boldsymbol{L}_1$ and $\boldsymbol{L}_2$, are added as a guide to the eye. In each case, $a = 32\sqrt{3}$ and $b = 32$.

the primitive vectors of a hexagonal lattice, such that $|\boldsymbol{L}_1| = |\boldsymbol{L}_2|$ and $\hat{\boldsymbol{L}}_1 \cdot \hat{\boldsymbol{L}}_2 = 1/2$, confirming that the ground state is a hexagonal lattice. Further, we observe that in the long term the energy of the system is monotonically decreasing when evolving Eqn. (5.13) with $\gamma = 1$, and that the energy converges. For the parameters in Fig. 5.4, $|\mathcal{E}(t+\delta t) - \mathcal{E}(t)|$ has converged to within at least 2×10^{-7}.

Chapter 6

Phase Transitions in a Rotating 2D Bose Einstein Condensate

The physics of a Bose Einstein Condensate changes as the dimensionality of the system is reduced, since fluctuations play a greater role in such reduced-dimensionality settings. A consequence of this is that a condensate can not exist in 2 dimensions, except at zero temperature [286, 287]. If we add rotation to a 2D system, then we have a trade off between the effects of reduced dimensionality and the non-trivial effects of forcing a superfluid to rotate.

In this chapter we perturb the ground state of the rotating system found in Chapter 5, in order to investigate how the lattice responds to melting. We then discuss the means by which one may extend this work to investigate phase transitions in a rotating 2D Bose gas. This remains an ongoing topic of investigation.

6.1 The Berezinskii–Kosterlitz–Thouless Transition

In a 3D system, it has been predicted and observed that a BEC phase exists, irrespective the trapping that the condensate is subjected to. In fewer dimensions however, the picture becomes counter-intuitively more complicated. It has been shown by Mermin and Wagner [286] that a finite temperature phase transition to a Long Range Order state in not possible in either 1D or 2D due to thermal fluctuations. Hohenberg [287] later showed that this result extends to ultra-cold gases. These results are collectively known as the *Mermin–Wagner–Hohenberg Theorem*, and show that a BEC transition does not occur in 2D Bose gases.

For a homogeneous 2D system the normalised first order spatial correlation function is defined as [111]

$$G^{(1)}\left(\mathbf{x},\mathbf{x}+\mathbf{r}\right)=\frac{\left\langle \Psi^{*}\left(\mathbf{x}\right)\Psi\left(\mathbf{x}+\mathbf{r}\right)\right\rangle }{\sqrt{\left\langle \left|\Psi\left(\mathbf{x}\right)\right|^{2}\right\rangle \left\langle \left|\Psi\left(\mathbf{x}+\mathbf{r}\right)\right|^{2}\right\rangle }}. \tag{6.1}$$

Large systems have many vortices, and at low temperature it becomes energetically

more favourable for vortices to exist in tightly bound vortex-antivortex pairs. At these low temperatures, thermal fluctuations are dominated by spin wave excitations. This causes the correlation function to decay algebraically with distance,

$$G^{(1)}(r) \propto |\mathbf{r}|^{-\alpha}, \tag{6.2}$$

a phenomenon dubbed "topological order", or quasi-long-range-order [288].

At high temperature, vortex pairs unbind, resulting in the destruction of topological order, and the correlation function decays exponentially with distance,

$$G^{(1)}(r) \propto \exp\left(-\frac{|\mathbf{r}|}{\ell_c}\right), \tag{6.3}$$

for some characteristic length ℓ_c . A schematic of this vortex-unbinding can be found in Fig. 6.1.

This phase transition, known as the Berezinskii-Kosterlitz-Thouless (BKT) transition [289, 290], describes a finite critical temperature, T_{BKT}, at which the system sharply changes from quasi-long-range-order to an absence of long range order. The difference between these regimes indicates that there must be a break in the analicity between high and low temperatures [289] (i.e., a cross-over from an algebraic to an exponential decay of the correlation function). In fact, the 1st order correlation function vanishes at any finite temperature [290]. This is in stark contrast to the smooth transition seen in three dimensions.

Since the BKT transition was experimentally verified in thin films of Helium [291], it has remained an active area of experimental [115–118, 120–124, 292, 293] and theoretical [56, 294–311] research. Importantly, these results on the BKT transition do not necessarily apply to the case of a trapped, rotating system. An interesting and challenging open problem in 2D gases remains: how is the BKT transition affected in a system which is forced to rotate? In the remainder of this chapter we present some preliminary results on this question.

6.2 Lattice Melting

Using the methodology described in Chapter 5, we evolve an initial configuration of 6 vortices using the damped GPE, which leads to a lattice ground state $\boldsymbol{c}^{(g)}$, as reported in Sec. 5.2.4. We then add noise to the ground state, by taking

$$c_{n,k} = \eta c^{(g)}_{n,k} + (1-\eta)\exp\left[i\varpi\right] \tag{6.4}$$

for $n = 1, \ldots, (M-1)$, where the parameter η controls the amount of noise which is injected into the lattice ground state, and ϖ is sampled from a uniform distribution $U(0, 2\pi)$. It should be noted that noise should be added in coefficient space, and not in

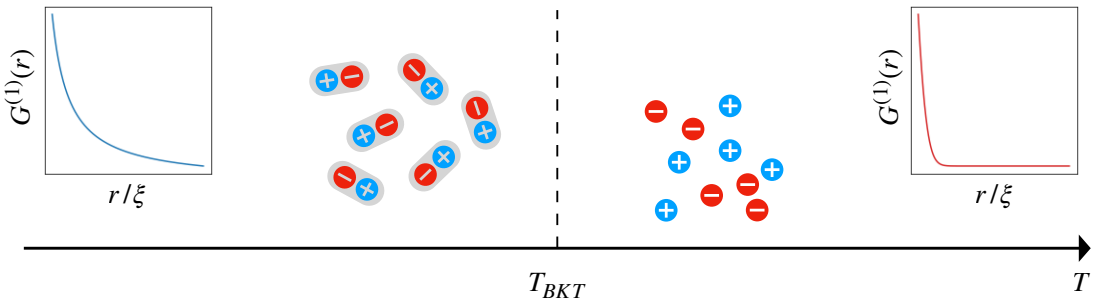

Figure 6.1: A schematic showing the binding and un-binding of dipole pairs in a homogeneous gas across the BKT transition. Left inset: the first order correlation function $G^{(1)}(r)$ decays algebraically for $T < T_{BKT}$; right inset: the first order correlation function decays exponentially for $T > T_{BKT}$.

real space, to ensure that the wavefunction is representable in terms of the basis functions.

Adding noise to the coefficients of the ground state will increase the presence of higher Landau levels in the system, and hence effect the thermal properties of the system. Here we take 5 values of η, so that the initial configuration is 98.2%, 98.6%, 99%, 99.4% and 99.8% of the lattice ground state. For each of these configurations, we simulate 10 different realisations of noise added to the coefficients of the ground state, evolved to dimensionless time $t_f = 10^4$. In addition to the individual trajectories, we compute the time and ensemble averaged density,

$$\bar{\rho} = \frac{1}{t_f - t_i} \int_{t_i}^{t_f} \left\langle \left| \Psi\left(x, y, t\right) \right|^2 \right\rangle dt, \tag{6.5}$$

and the time and ensemble averaged phase,

$$\bar{\theta} = \frac{1}{t_f - t_i} \int_{t_i}^{t_f} \left\langle \mathrm{Arg}\left[\Psi\left(x, y, t\right) - \mathrm{Arg}\left[\Psi\left(0, 0, t\right)\right]\right] \right\rangle dt. \tag{6.6}$$

We compute these averages over an ensemble of 10 trajectories, averaging in time from $t_i = 5 \times 10^3$ to $t_f = 10^4$, numerically integrated over 500 equally-spaced outputs. Although we do not compute the temperatures that these energies correspond to in the microcanonical ensemble, in principle these can be determined as described by Ref. [132].

Fig. 6.2 shows the instantaneous and averaged density and phase profiles for the different values of η. For reference, the energy of the lattice ground state is $\mathcal{E}_g = -0.7135$. Due to the degeneracy of eigenenergies, the parameter η is not a versatile measure of the injected energy for systems with different numbers of vortices. Further, the initial energy of each realisation is different, and so we compare different values of noise in the system

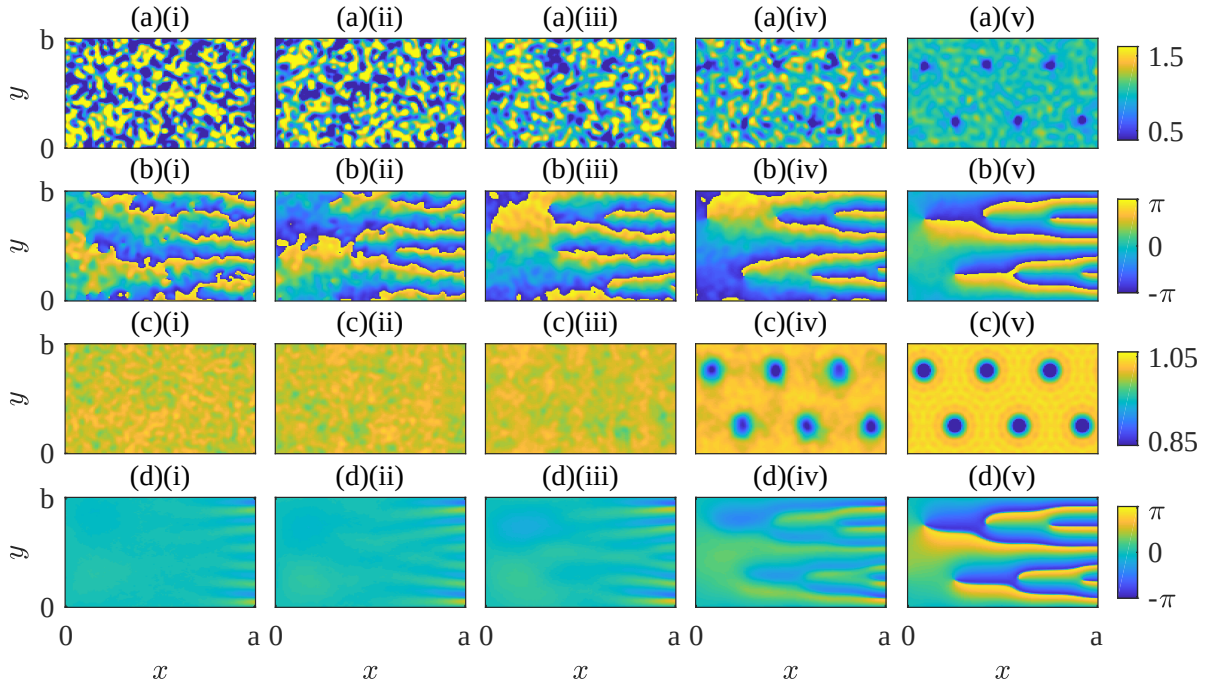

Figure 6.2: Row (a)(i)–(a)(v): instantaneous density profile at $t = 5000$. Row (b)(i)–(b)(v): instantaneous phase profile at $t = 5000$. Row (c)(i)–(c)(v): time and ensemble averaged density profile, $\bar{\rho}$. Row (d)(i)–(d)(v): time and ensemble averaged phase profile, $\bar{\theta}$. The initial configurations are given by: Column (a)(i)–(d)(i): $\eta = 0.982$, column (a)(ii)–(d)(ii): $\eta = 0.986$, column (a)(iii)–(d)(iii): $\eta = 0.990$, column (a)(iv)–(d)(iv): $\eta = 0.994$, and column (a)(v)–(d)(v): $\eta = 0.998$. See Supplemental Material [312] which contains movies of the time evolution.

by computing the added energy,

$$\mathcal{E}_A = \langle \mathcal{E}_0 \rangle - \mathcal{E}_g, \tag{6.7}$$

where $\langle \mathcal{E}_0 \rangle$ is the energy of the system after one time step, so that the wavefunction and vector of coefficients is correctly normalised. In Fig. 6.2, column (i) corresponds to $\mathcal{E}_A = 0.8107\,|\mathcal{E}_g|$, column (ii) corresponds to $\mathcal{E}_A = 0.6688\,|\mathcal{E}_g|$, column (iii) corresponds to $\mathcal{E}_A = 0.5361\,|\mathcal{E}_g|$, column (iv) corresponds to $\mathcal{E}_A = 0.4267\,|\mathcal{E}_g|$, and column (v) corresponds to $\mathcal{E}_A = 0.3638\,|\mathcal{E}_g|$.

It is clear to see that as the energy of the system increases, stronger fluctuations destroy the regular vortex lattice. In Fig. 6.2 (a)(i)–(b)(i) we see that fluctuations have led to the creation of short–lived dipole pairs, which in turn means that there is no recognisable structure to the time and ensemble avearged profiles, Fig. 6.2 (c)(i)–(d)(i). Similarly, fluctuations in Fig. 6.2 (a)(ii)–(b)(ii) prevent the formation of a lattice in Fig. 6.2 (c)(ii)–(d)(ii)

In Fig. 6.2 (a) (iv)–(d)(iv), we see that while the instantaneous density profile, Fig. 6.2 (a)(iv), contains sharp fluctuations, a hexagonal vortex lattice endures in the averaged density profile, Fig. 6.2 (c)(iv). Here the edges of the vortex cores appear fainter than in the lattice of Fig. 6.2 (c)(v), due to oscillations in the position of the vortices in individual trajectories. Indeed, the main difference between the averaged density profiles of Figs. 6.2 (c)(i) – (c)(v) is that the lattice melts as the system becomes dominated by fluctuations, which is the component of the thermal cloud that exists within the classical region [281].

In the ensemble with the smallest additional energy, Fig. 6.2 (a)(v)–(d)(v), we see that even in instantaneous profiles, Figs. 6.2 (a)(v) and (b)(v), the vortex lattice is preserved. Indeed, the fluctuations due to this small amount of injected energy are highly smoothed out by time and ensemble averaging [Figs. 6.2 (c)(v) and (d)(v)] so that we recover profiles similar to the ground state of Fig. 5.4 (a).

In Fig. 6.3 we plot the time and ensemble averaged occupation of the Landau levels. Here we define

$$\bar{n_n} = \frac{1}{t_f - t_i} \int_{t_i}^{t_f} \sum_{k=0}^{N_v - 1} \left\langle |c_{n,k}(t)|^2 \right\rangle dt, \tag{6.8}$$

as the index of the state (vortex) does not enter into the expression of eigenenergies. We notice that, by adding enough noise to the ground state (corresponding to a low value of η), the distribution of Landau level occupation is proportional to $1/E$, which corresponds to classical equi-partition of energy over the modes. For a high value of η, although the majority of the Landau level occupation is centered around the lowest Landau levels, the effects of rotation on the system cause the formation of some structure in the filling of higher modes corresponding to the vortex lattice. The value of $\eta = 0.990$ represents a crossover between these limits. A large proportion of the filling is in the Lowest Landau levels, suggesting the presence of a condensate. However, higher modes

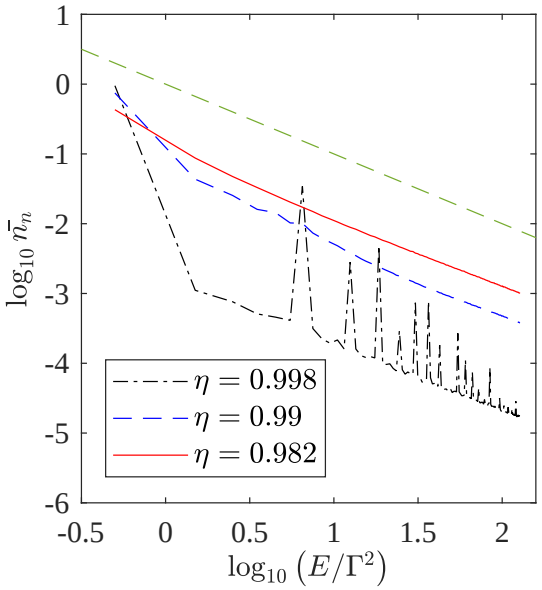

Figure 6.3: The time and ensemble averaged occupation of $c_{n,k}$ as a function of Landau levels for $\eta = 0.982$, solid red line, $\eta = 0.990$, dashed blue line, and $\eta = 0.998$, dot-dashed black line. The equi-partition of energy, $1/E$, green dashed line, is added as a guide to the eye.

are still significantly occupied, destroying the lattice structure, and indicating the presence of thermal effects.

6.3 Evidence of Transitions in Rotating 2D Bose Gases

6.3.1 First Order Correlation Functions

In a superfluid which is rotating at zero temperature, we expect to see an ordered hexagonal lattice of vortices. Thus we expect N_v points at which the phase winds by 2π. We also expect to see N_v points at which the density vanishes (numerically this leads to several computational grid points where the wavefunction is significantly different to the average of the system). Although these vortices are real, and are present in the system due to the rotation of the gas, their existence may cause spurious results in directly calculating $G^{(1)}$. In order to overcome these difficulties we do the following: The ground state of the system is a pure BEC at zero temperature, with a regular hexagonal lattice and wavefunction $\Psi^{(g)}(\mathbf{r})$. We note that the ground state is fixed, as evolving the damped PGPE from different initial conditions leads to the same lattice state. A system which has evolved from some initial condition [as given by Eqn. (6.4)] has a wavefunction $\Psi(\mathbf{r}, t)$ at some time t. Since the ground state is fixed, we can compute the "unwound" wavefunction

$$\Xi(\mathbf{r}, t) = \Psi(\mathbf{r}, t)\, \Psi^{(g)*}(\mathbf{r}), \tag{6.9}$$

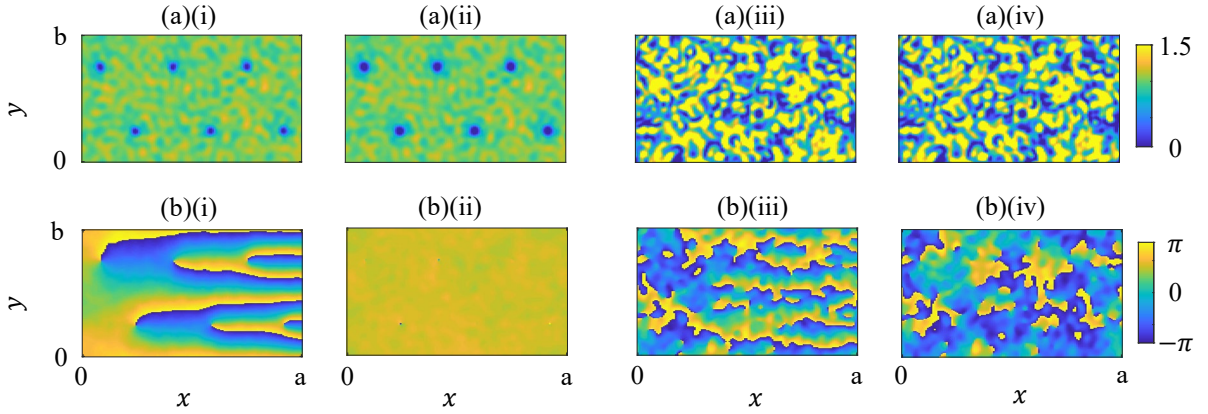

Figure 6.4: An example of the unwinding procedure given by Eqn. (6.9). Row (a) plots the density of the wavefunction and row (b) plots the phase of the wavefunction. Column (i) is the wavefunction at time t_i for $\eta = 0.998$ with (ii) the corresponding unwound wavefunction. Column (iii) is wavefunction at time t_i for $\eta = 0.982$ with (iv) the corresponding unwound wavefunction.

which has the advantage that there is no phase winding when $\Psi = \Psi^{(g)}$. This means that when the deviation from the ground state is small, such as when $\eta \approx 1$, only a small area of the cell will contain a non-zero phase, leading to $G^{(1)}(r) \approx 1$ uniformly across the system. A sketch of this can be found in Fig. 6.4. It is also advantageous to use Eqn. (6.9) to unwind the wavefunction, rather than simply subtracting the lattice ground state from the phase profile $\Psi' = |\Psi| \exp\left[i\mathrm{Arg}\left\{\Psi\right\} - i\mathrm{Arg}\left\{\Psi^{(g)}\right\}\right]$, as unwinding prevents artificially adding "naked singularities" to the system when $\Psi(\mathbf{r}, t) \neq \Psi^{(g)}(\mathbf{r})$; these singularities would be points where the phase has multiple values but the density does not vanish.

Computationally, the first order correlation function of Eqn. (6.9) is relatively straightforward to compute. The function becomes

$$\begin{aligned} G^{(1)}(\mathbf{r}) &= \frac{\langle \Xi^*(\mathbf{x}, t)\, \Xi(\mathbf{x}+\mathbf{r}, t)\rangle}{\sqrt{\langle |\Xi(\mathbf{x}, t)|^2\rangle \langle |\Xi(\mathbf{x}+\mathbf{r}, t)|^2\rangle}} \\ &= \frac{\left\langle \left[\Psi(\mathbf{x}, t)\, \Psi^{(g)*}(\mathbf{x})\right]^* \left[\Psi(\mathbf{x}+\mathbf{r}, t)\, \Psi^{(g)*}(\mathbf{x}+\mathbf{r})\right]\right\rangle}{\sqrt{\left\langle \left|\Psi(\mathbf{x}, t)\, \Psi^{(g)*}(\mathbf{x})\right|^2\right\rangle \left\langle \left|\Psi(\mathbf{x}+\mathbf{r}, t)\, \Psi^{(g)*}(\mathbf{x}+\mathbf{r})\right|^2\right\rangle}}. \end{aligned} \tag{6.10}$$

Since $\Xi(\mathbf{x})$ is periodic (having unwound the phase) it is possible to compute the numerator of Eqn. (6.10) using the Wiener-Khinchin theorem for autocorrelations,

$$\langle \Xi^*(\mathbf{x})\, \Xi(\mathbf{x}+\mathbf{r})\rangle = \mathcal{F}^{-1}\left\{\mathcal{F}\left[\Xi(\mathbf{x})\right]^* \mathcal{F}\left[\Xi(\mathbf{x})\right]\right\}, \tag{6.11}$$

which is easily computed using Fast Fourier Transforms (a result which can be found using the convolution theorem). The two terms in the denominator are easily computed as the ensemble averaged norm at $\mathbf{x}$ and $\mathbf{x}+\mathbf{r}$ respectively.

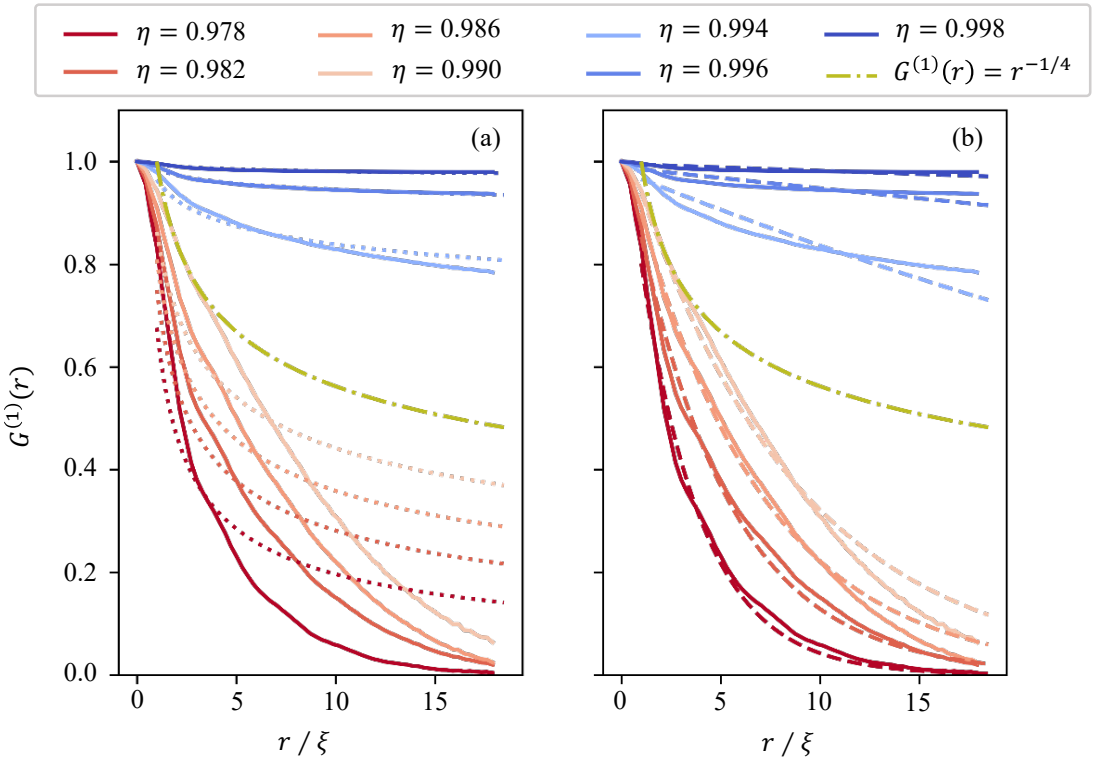

Figure 6.5: The first order correlation function given by Eqn. (6.10) for different values of η. In panel (a), the dotted curves plot the fit to the algebraic decay in Eqn. (6.2) for each value of η. In panel (b), the dashed curves plot the fit to the exponential decay in Eqn. (6.3). In each case, the olive dot-dash curve is the algebraic decay at T_{BKT}, given by $G^{(1)}(r) = r^{-1/4}$. The point $G^{(1)}(0) = 1$ is added for consistency.

For each of the curves in Fig. 6.5, the first order correlation function, Eqn. (6.10), is calculated at a given time with an ensemble of 10 different realisations of initial conditions, and the result of this is averaged over the latter half of the simulation. By construction, $G^{(1)}(0) = 1$.

It is clear from Fig. 6.5 (a) that there is a good agreement between the "coldest" three systems ($\eta \in \{0.994, 0.996, 0.998\}$) and the algebraic fits. Such fits indicate that the systems are below the BKT transition temperature, and therefore posses quasi-long-range-order. There is a small discrepancy between the observed decay and the fit to Eqn. (6.2) in the system where $\eta = 0.994$, we suggest that this is due to the relatively small size of the system [306, 310, 313]. The algebraic fits fail for systems where $\eta \leq 0.990$; as can be see in in Fig. 6.5 (b), these curves are well suited to fitting an exponential curve, implying that the curves are above the BKT transition, and long-range-order has been destroyed. This is further supported by the fact that, for these values of η, the first order correlation function clearly decays faster than the alegbraic decay with the universal exponent 1/4 at the BKT critical temperature.

6.3.2 Vortex Behaviour

A second key characteristic of the BKT transition is the behaviour of vortices. As we have discussed in the introduction to this chapter, the idealised picture of the homogeneous system in the absence of rotation is that for $T < T_{BKT}$ vortices live in tightly bound dipole pairs, while for $T > T_{BKT}$ these pairs un-bind, and the system becomes a free sea of vortices. In our system, however, not only will there always be a net number of vortices, the ground state of the system at $T = 0$ contains $N_{\rm v}$ positively charged vortices, meaning that the dipole distance is not well defined, in contrast to the typical BKT picture.

In Fig. 6.6 (a) we measure the average distance between nearest same-sign vortices, d_{ss}. In order to do this, we locate the position of the vortices by using a vortex tracking method, similar to the one described in Appendix C. Vortices which are positioned on a lattice should be separated from their nearest like-sign neighbours by a constant distance, shown by the black dashed line in Fig. 6.6 (a), which depends on the size of the system and the number of vortices. As we decrease the value of η, we note that d_{ss} starts to fluctuate, which corresponds to the lattice melting and the vortices moving from their lattice position [see Fig. 6.2]. As the noise increases, the size of the fluctuations also increases until eventually there is enough noise that enough short lived vortex-antivortex pairs are injected into the system, so the size of the fluctuations in d_{ss} decreases but d_{ss} continues to decrease, $\eta \in \{0.978, 0982\}$.

In order to calculate the distance between the nearest opposite-sign vortices, d_{os}, without this distance diverging in the lattice ground state, we must do more than just detect the locations of the vortices. Inspired by the approach above, our solution is to find the vortices as previously described, and then add an antivortex at each of the lattice positions before working out the statistics. This ensures that for $\eta \approx 1$, where we would expect $T \ll T_{BKT}$, the average distance d_{os} is small. We plot the result of this calculation in Fig. 6.6 (b). We see that, while $\eta \geq 0.990$, as the amount of noise in the system increases the average dipole length d_{os} increases. This is due to the movement of the vortices from their lattice positions. As the amount of noise in the system is increased, for $\eta < 0.99$, the value of d_{os} decreases: this is due to the nucleation of short-lived vortex-antivortex pairs in the system [see Fig. 6.6, panel (c)] which "washed out" the ability to identify vortex dipole pairs and vortex clusters [301].

In Fig. 6.6 (c) we plot the total number of vortices, $N_{\rm v}$. It should be noted that in the cooler systems, short lived vortex-antivortex pairs do not proliferate. In fact, as is shown in the inset, on average we require that $\eta \leq 0.99$ for additional vortices to be detected in the system.

6.4 Conclusions and Outlook

In this part we have presented an efficient method for simulating a harmonically trapped Bose gas, which is rotating at the centrifugal limit. We have shown that it is possible

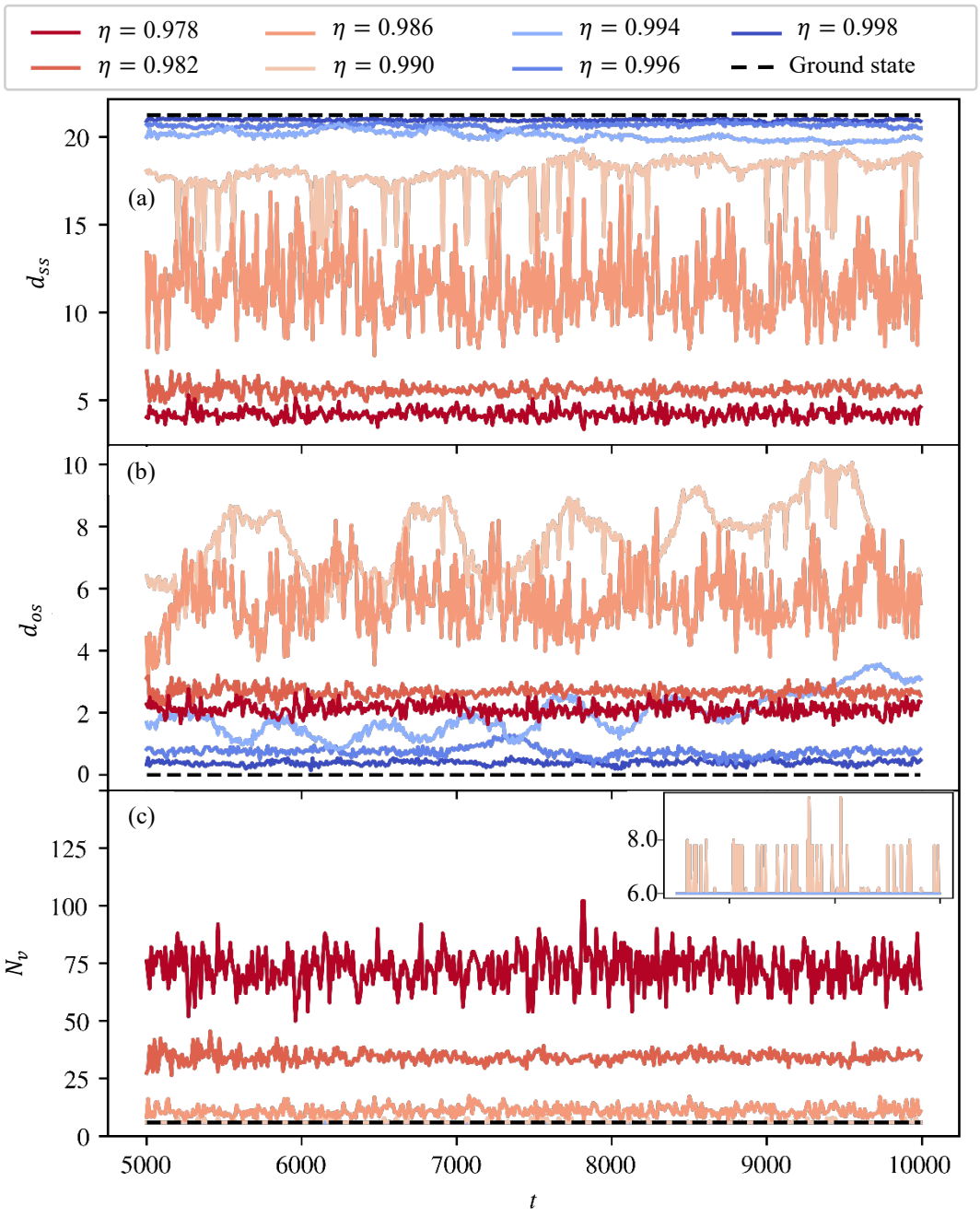

Figure 6.6: Vortex statistics as the strength of the noise η varies. Panel (a) gives the average distance from one vortex to the nearest vortex with the same sign, d_{ss}; the black dashed line gives the value which we measure in the ground state of the vortex lattice. Panel (b) gives the average distance from one vortex to the nearest vortex with opposite sign, d_{os}, after anti-vortices have been imposed at the lattice positions. Panel (c) gives the number of vortices in the system; the inset shows that, on average, short-lived vortex-antivortex pairs are only nucleated as $\eta \leq 0.990$.

to do so without the issue of edge effects by choosing suitable quasi-periodic boundary conditions. We have used the single particle basis functions with these quasi-periodic boundary conditions to expand the wavefunction below an energy cutoff, thus implementing the PGPE for this rotating system. There are two primary sources of error which arise from such a pseudospectral method in this case; these are the error in projection caused by choosing an energy cut-off, M, and the error associated with truncating an infinite summation appearing in the basis functions themselves. We have quantified these errors, and have shown that for suitable choices of simulation parameters it is possible to reduce these errors to an acceptably small value.

On adding damping to the equation of motion, the PGPE method which we present relaxes from non-equilibrium initial conditions to the expected regular lattice ground state, Fig. 5.4. It is also useful to be able to set up an initial condition of $N_{\rm v}$ vortices with arbitrary integer charge placed at any point in the domain (subject to symmetry conditions).

In Chapter 6 we have investigated the melting of a vortex lattice by perturbing the ground state of the system. We observed that for a small amount of added noise the vortices are able to move away from lattice positions, while for larger amounts of noise there are short-lived vortex-antivortex pairs injected into the system. We also calculated the distribution of Landau level occupation as the amount by which the lattise ground state is perturbed increases, and found that for large perturbations this distribution is approximated by the equipartition of energy.

Finally, in a significant additional development to the results presented in our Physical Review E paper [101], we have explored the link between the lattice melting (described above) and the BKT phase transition. For the rotating system, it is not straightforward to calculate the first order correlation function or vortex statistics as is in the homogeneous system. Instead, we formulate a way in which to calculate the first order correlation function whereby the wavefunction is unwound about the lattice ground state. We observe clear evidence of a transition from an algebraic decay in $G^{(1)}$ for small amounts of noise (suggesting $T < T_{BKT}$), to an exponential decay (suggesting $T > T_{BKT}$) for larger amounts of noise, indicating the validity of the "unwinding" technique. We have also conducted preliminary calculations of vortex statistics, although more complex methods are required to determine the exact vortex unbinding point in this system.

Future work in this area will be concerned with identifying T_{BKT} in a rotating system. Significant progress has been made in calculating $G^{(1)}$ in the PGPE which we describe, however a next step will require that we compute temperatures from the microcanonical ensemble [132, 314–318]. In order to identify the role of vortices and vortex pair unbinding in the rotating system, it is likely that a coarse-graining procedure (such as the one employed by Foster *et al.*, [301]) may be utilised to accurately identify free vortices, and therefore vortex pair unbinding. Alternatively, a recursive clustering algorithm such as the one presented in Ref. [87], might be employed to detect vortex dipoles or clusters of

same-sign vortices. As a final hallmark of the BKT transition, it would be desirable to calculate the superfluid fraction of the system at a given temperature; such a calculation, based on the derivations presented in Refs. [111, 301, 310, 319, 320] (see Appendix. A.5), will be modified by the fact that our system is in the Landau gauge and rotating at the centrifugal limit, but is in principle possible.

Part III

The Dirty Boson Problem

Chapter 7

Critical Velocity of a Disordered Potential

7.1 Disorder in a Superfluid

A prototypical study of turbulence in fluids is that of the wake behind a cylinder in a flow [321]. As we discussed in Section 1.4.2, in classical fluids, the degree of turbulence in the flow can be encoded by the dimensionless Reynolds number $\mathrm{Re} = UL/\nu$, where U is the velocity of the uniform flow, L is the size of an obstacle in the flow, and ν is the kinematic viscosity of the fluid. Dynamical similarity allows us to map flows with different U, L and ν to the same flow pattern, so long as the combination UL/ν is the same. In a superfluid flow, although $\nu = 0$, it has been shown that quantum fluids exhibit dynamic similarities in the same way classical fluids do [99].

A superfluid is characterized by frictionless flow in the absence of viscous effects. For a sufficiently small velocity, the flow around an obstacle is steady laminar flow and no vortices are nucleated [186]. Above a critical velocity, the flow around an obstacle creates a drag force which is responsible for the nucleation of quantized vortices [51, 182]. These vortices signal the breakdown of superfluidity in the system at zero temperature [51, 57, 60, 215, 322, 323]. Immediately above the critical velocity, pairs of oppositely charged vortices are shed periodically from opposite sides of the obstacle [184]. As the velocity of the flow around the obstacle increases, there is a transition from the regular shedding of vortex dipole pairs to an irregular shedding of larger clusters of same-sign vortices, indicating that the system has become turbulent [100, 186]. The transition to turbulence in superfluid flow past a potential obstacle has been the focus of recent theoretical [87, 99, 181, 183, 186, 324] and experimental [100, 179, 184, 216] work. These works have investigated the effect of obstacle shape [183, 185, 325] and finite temperature effects [181, 324] on the critical velocity for vortex nucleation past a single obstacle.

As no real system is truly free of imperfections, disorder is an important consideration in interacting Bose systems, with the interplay between disorder and particle-particle interactions providing a rich test bed for many-body quantum physics. Studies into disorder

in BECs have employed impurities [326], rough boundaries [203, 327] and optical speckle patterns [328–336]; the latter playing a role in the prediction of a lowered superfluid transition temperature in 2D [332] and 3D [329, 330, 332]. The realisation of Anderson localization [333], and the transition to an exotic Bose glass [334, 336]. While disorder is an important consideration, few studies have considered the case of a superfluid flow in the presence of a point-like disordered potential. Such a disorder potential is now experimentally realisable, as new optical techniques employing digital micromirror devices (DMDs) allow experiments to have an unprecedented level of control in creating arbitrary shaped potentials [23–25].

Forcing a quasi-two-dimensional superfluid through a disordered potential faster than the critical velocity is a process which injects vortices into the system. These then decay by a process of vortex-antivortex annihilation, which is similar to the coarsening process which takes place after a thermal quench. Such coarsening is a current topic in 2D Bose gases, with investigations into the phase-ordering kinetic taking place in conservative [88, 93, 308, 313, 337–339] and dissipative [88, 93, 308, 309, 313, 339] simulations, as well as in systems of binary BECs [340], spinor BECs [341, 342], and exciton-polariton condensates [343–346]. Previous works on single component Bose gases have conducted quenches by starting from non-equilibrium initial conditions which tend to rapidly seed an approximately isotropic distribution of vortex dipoles [152, 181, 232, 313, 324], while other studies have imprinted a random distribution of vortices with unit charge [196, 339] or multiple charges [308]. Here, we also observe a system which transitions from a non-equilibrium state containing many vortices to an equilibrium state, and use an energy- and number-conserving description similar to the conservative systems mentioned above. Our system, however, has several key differences. Firstly, the vortex injection in our system is different; unlike the initial conditions discussed above, the vortices which are created by a series of barriers have an anisotropic initial position which depends on the details of the barriers (the location, shape, size, etc.), and the speed of the superfluid. Secondly, the vortex injection is not instantaneous; rather vortices are shed over time from the barrier as the barrier moves through the superfluid above the critical velocity. Despite these differences, the system we describe provides a relatively simple way to generate non-equilibrium conditions which can be used to study related coarsening behaviour in a BEC.

In this part we investigate the dynamics of dense superfluid flow through a point-like disorder potential: a scenario which combines disorder, turbulence and coarsening in a 2D Bose gas. We impose the point-like disorder potential through an external trapping which is taken to be zero everywhere, apart from at a series of points where a localised repulsive barrier is placed . These repulsive barriers, which are Gaussian in shape, may be thought of as a set of blue detuned laser beams whose intensity can be controlled at any point in space [23–25]. Unlike the disorder which is imposed by an optical speckle pattern, a key feature of this work is that the barriers which comprise the disorder potential are

sufficiently separated (i.e. several healing lengths apart) so that the fluid is homogeneous away from the centre of the barrier. This ensures that it is possible to have a global superfluid phase, since localization of the condensate does not play a role [333], and we can treat quantities such as the speed of sound and the healing length as constant across the system.

The rest of this part is structured as follows. In Sec. 7.2 we introduce the equation of motion for a system which has a disordered point-like potential dragged through it. In Sec. 7.3 we calculate the critical velocity for vortex nucleation for different potentials, formed by randomly arranging collections of point-like barriers. We begin by placing two identical point-like barriers in a superfluid flow, and study the interplay between relative separation and the incident angle of the barriers on the critical velocity. We then look at a system with many point like barriers, and investigate the link between the density of these point-like barriers and the critical velocity of the system. In Chapter 8, we study the long term behaviour of an initially non-equilibrium superfluid flowing through a disordered potential at varying initial velocities. We measure the condensate fraction, the superfluid fraction, and the superfluid velocity during this process. This illustrates how at short times the superflow breaks down, accompanied by vortex generation and depletion of the condensate fraction. At intermediate times, the momentum of the Bose gas continues to be arrested by interaction with the barriers, as vortex-antivortex annihilation begins. Over longer times, vortices continue to annihilate and thermalization takes place; the gas recondenses and superfluidity is restored. In Sec. 8.2, we investigate the effect of varying the effective barrier width on the vortex decay rate. For small point-like barriers (the radius of which is on the order of a single healing length), the vortex decay rate follows the expected rate which follows a thermal quench. We show that for sufficiently large barriers this changes, and at the same time vortex pinning becomes an important effect in the dynamics of the system.

7.2 System and Numerical Implementation

We consider an obstacle which is moving at a steady velocity $\mathbf{v}$ through a superfluid which is otherwise uniform in the xy plane, and trapped strongly enough in the z direction that all excitations are suppressed in this direction. Such a 2D system, when comprised of a weakly interacting atomic Bose gas at finite temperature, can be described by a wavefunction Ψ which obeys the projected Gross-Pitaevskii equation (PGPE), Eqn. (2.34),

$$i\hbar\frac{\partial\Psi}{\partial t} = \mathcal{P}\left\{\left[-\frac{\hbar^2}{2m}\nabla^2 + V_{\rm obj}(\mathbf{r}) + g_{\rm 2D}|\Psi|^2 - \mu_{\rm 2D}\right]\Psi\right\}.$$

As before, $\mu_{\rm 2D}$ is the chemical potential and the strength of the atomic interactions is parameterized by $g_{\rm 2D} = \sqrt{8\pi}\hbar^2 a_s/ml_z$, where m is the atomic mass, a_s is the s-wave scattering length, and $l_z = \sqrt{\hbar/m\omega_z}$ is the harmonic oscillator length in the z direction.

We impose a uniform flow with velocity $\mathbf{v}$ in the $\hat{\boldsymbol{x}}$ direction by multiplying the initial wavefunction by a phase gradient (see, for example, Ref. [325]). The crucial feature of the PGPE, beyond the ordinary non-projected Gross-Pitaevskii equation, is the projection operator $\mathcal{P}$ which implements an energy cutoff in the basis of non-interacting single particle modes. When working at finite temperature, this allows one to set the cutoff so that modes below the cutoff are highly occupied. In this regime quantum fluctuations are relatively small and the classical field description is accurate [133].

Alternatively, we can consider the system in which the obstacles are dragged through the fluid at some velocity $\mathbf{v}$. In this system, the coordinate of the obstacle reference frame is $\mathbf{r} = \mathbf{r}_L + \mathbf{v}t$, and the lab-frame wavefunction $\Psi(\mathbf{r}, t) = \Psi_L(\mathbf{r}_L, t)$. The PGPE governing the lab-frame wavefunction is given by

$$i\hbar\frac{\partial\Psi}{\partial t} = \mathcal{P}\left\{\left[-\frac{\hbar^2}{2m}\nabla^2 + V_{\rm obj}(\mathbf{r}) + g_{\rm 2D}|\Psi|^2 - \mathbf{v}\cdot\mathbf{p} - \mu_{\rm 2D}\right]\Psi\right\}, \tag{7.1}$$

where the Gallilean shift to the obstacle frame (from the lab-frame) is given by the $\mathbf{v}\cdot\mathbf{p}$ term, with $\mathbf{p} = -i\hbar\nabla$ the usual quantum momentum operator[1] [127]. Eqn. (7.1) is the result of applying the projection operator to the GPE which has had a Gallilean shift applied to it, Eqn. (2.31).

To simulate an obstacle which is a collection of point-like barriers, we use the sum of N_B repulsive Gaussian potentials,

$$V_{\rm obj}(\mathbf{r}) = V_0\sum_{k=0}^{N_B}\exp\left[-\frac{(x-x_k)^2}{a^2} - \frac{(y-y_k)^2}{a^2}\right], \tag{7.2}$$

which have their centers at (x_k, y_k). These barriers each have an effective cylinder width which can be estimated from the zero density region of the Thomas-Fermi approximation, $2a\sqrt{\ln(V_0/\mu_{\rm 2D})}$. In contrast to previous works which use hard-walled barriers [183, 186], we use soft-walled barriers [with $V_0 = \mu_{\rm 2D}\exp(1)$] where the critical velocity is lower [325]. Unless otherwise stated, we take barriers to have a narrow waist, $a = \xi$, thus providing a point like potential with an effective cylinder width 2ξ.

In what follows, we take $\mathbf{v} = -v_{\rm obst}\hat{\boldsymbol{x}}$. The single-particle modes for this system are plane waves satisfying $|\mathbf{k}| < k_{\rm cut}$, for some wave-number cutoff $k_{\rm cut}$. To implement the cut-off, we ignore $V_{\rm obj}$ as it will not affect the potential on the scale of $1/k_{\rm cut}$, and hence does not affect our choice of basis functions. The PGPE is evolved numerically, with doubly periodic boundary conditions, using an adaptive Runge-Kutta method (implemented using XMDS2 [348]) on a $L_x \times L_y$ grid with $N_x \times N_y$ grid points. We take the energy cutoff to be $k_{\rm cut} = \pi N_x/(2L_x) - \pi/L_x$. In the rest of this part, we typically express quantities with reference to energy $\mu_{\rm 2D}$, healing length, $\xi = \hbar/\sqrt{m\mu_{\rm 2D}}$, density, $\rho_0 = \mu_{\rm 2D}/g_{\rm 2D}$, and the speed of sound, $c = \sqrt{\mu_{\rm 2D}/m}$. Consequently, times are expressed in units of

[1] Note that any aliasing problems which may have arisen when computing the first derivative term in Eqn. (7.1) using Fast Fourier Transforms are corrected by the cut-off implemented by the projection operator [347].

$\tau = \hbar/\mu_{2D}$. The number of grid points in our simulations is chosen such that there are two computational grid points per healing length.

7.3 Critical Velocity of Point-Like Disordered Potentials

7.3.1 Method for calculating the critical velocity

In order to find the critical velocity, we first find the ground state of the condensate in the presence of the point-like potentials. To do this, we evolve the damped PGPE, found by multiplying the right hand side of Eqn. (2.31) by $(1 - i\gamma)$, where γ is a phenomenological damping parameter [144], with stationary barriers $v_{\text{obst}} = 0$, and for $\gamma = 1$, up to $t = 5000\tau$. This converges to a wavefunction which is approximately the ground state of the system, and which will be the initial condition for all of the following simulations. We then set $\gamma = 0$ and evolve Eqn. (2.31), with $\mathbf{v} = -v_{\text{obst}}(t)\hat{\boldsymbol{x}}$, whilst smoothly ramping up the velocity [183] according to

$$v_{\text{obst}}(t) = v_f \tanh\left(\frac{t}{200\tau}\right). \tag{7.3}$$

Smoothly increasing the velocity in this way prevents the generation of sound which would be caused by instantaneously setting $v_{\text{obst}} = v_f$. This simulation is run for 1000τ so that the barriers have moved through the fluid with speed v_f for some time, but not so long that thermal effects caused by numerical noise begin to lower the critical velocity [324]. The value of v_f is increased discretely until vortices are observed to be shed from the potential. For reference, the critical velocity of a single point-like barrier is $v_{\text{crit}}/c = 0.5625 \pm 0.0025$.

7.3.2 A Pair of Point-like Barriers

We begin by finding the critical velocity of two point-like barriers, as we vary the relative distance and angle between these barriers. Without loss of generality, we place one barrier at the origin, and one barrier at $(-R\cos\alpha, -R\sin\alpha)$. The results of this are plotted in Fig. 7.1.

When α, the angle between the barriers in the direction of the flow, is small, the system has an increased critical velocity as the barriers are behind each other in the direction of the flow, becoming streamlined. As α increases, the critical velocity decreases since the barriers become a more like an effective elliptical obstacle, causing a denser wake [183]. An important observation which we make is that for the case where $R = 4\xi$, the two barriers act as one larger (essentially elliptical) barrier, and for $v \gtrapprox v_{\text{crit}}$ will shed only one dipole pair of vortices. In the cases where $R \geq 8\xi$, the barriers act independently and both of the point-like potentials will emit a dipole pair, for flow speeds just above v_{crit}.

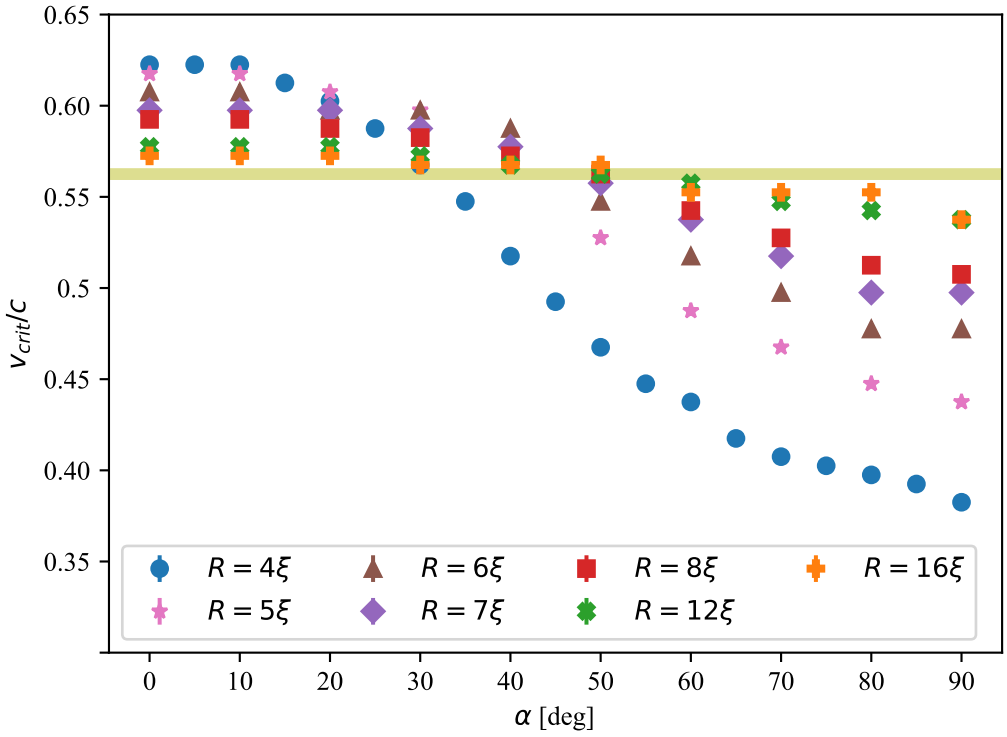

Figure 7.1: The critical velocity of two point-like barriers, with separation distance R, and angle α incident to the direction of the flow. Blue circles represent barriers with separation $R = 4\xi$, red squares represent barriers with separation $R = 8\xi$, green crosses represent barriers with separation $R = 12\xi$, and orange pluses represent barriers with separation $R = 16\xi$. The olive region is the critical velocity of a single point-like barrier, plotted as a guide to the eye (the width indicates numerical uncertainty). The error from the the systematic uncertainty due to increasing v_x in discrete steps is smaller than the symbols used.

The flattening of the curves indicates that, as we would expect, $v_{\rm crit}$ tends towards the single barrier limit as $R \to \infty$.

7.4 Multiple Barriers

Having found the critical velocity for a pair of point-like barriers, we now find the critical velocity for N_B barriers which are placed at random in the cell[2], subject to a minimum separation of 4ξ. The process is the same as before, in that the "overdamped" GPE is used to find the ground-state of the potential in the absence of velocity. We then ramp the flow velocity using the tanh profile in Eqn. (7.3) for discretely increasing values of v_f. A vortex detection algorithm similar to Ref. [301] is used to automate the search.

In Fig. 7.2 we plot the critical velocity of a disordered system, as a function of the angle between the nearest neighbour pair of point-like potentials in the particular disorder realization, n.n. α. We choose this measure because we expect that the critical velocity of a particular potential will be most sensitive to the configuration of the pair of barriers with the smallest separation, as shown by the range of values in the blue curve of Fig. 7.1. The panels of Fig. 7.2 correspond to the binning of the nearest neighbour distance between the closest two point-like barriers in each realization, while the type of marker represents the total number of barriers in the system, N_B. The gray shaded area indicates the region which contains the critical velocity of a system of 2 point-like barriers whose separation distance corresponds to the separation distance of the panel. For larger n.n.α, the nearest neighbour interactions of the closest pair of point-like barriers dominate the critical velocity, as can be seen by the points lying within the gray shaded region. Where the closest nearest neighbour barriers form a streamlined barrier, given by smaller n.n.α, the critical velocity is smaller than the two barrier case; this is due to two factors. Firstly as N_B increases, so does the probability that other (non-closest) pairs of nearest-neighbour barriers are separated by a similar distance but have a large angle against the flow, creating an efficient vortex emitter. Secondly, given that there are multiple barriers in the system, the critical velocity is limited by the single barrier case – any barrier which is sufficiently separated ($\gtrapprox 20\xi$) from the other barriers will act independently, and cause vortices to be present in the system as soon as the flow velocity is greater than the critical velocity for a single point-like barrier. Indeed, we observe that the critical velocity of a point-like disordered potential is bounded above by the lowest of: (a) the critical velocity of a single barrier; (b) the highest critical velocity of the two barrier test case for equivalent nearest-neighbour separation of the closest two barriers.

[2]For a small number of barriers and a small minimum separation, relative to the size of the cell, the coordinates of the centres of the obstacles could be found by sampling x_k x_k from a uniform $U(-L_x/2, L_x/2)$ distribution and sampling y_k from a uniform $U(-L_y/2, L_y/2)$ distribution N_B times. The potential would be rejected, and the process repeated, if a pair of coordinates were closer than the required minimum separation. For a much larger number of barriers, or for a minimum separation which is large relative to the size of the cell, it would be necessary to use a random-walk algorithm to efficiently position the obstacles.

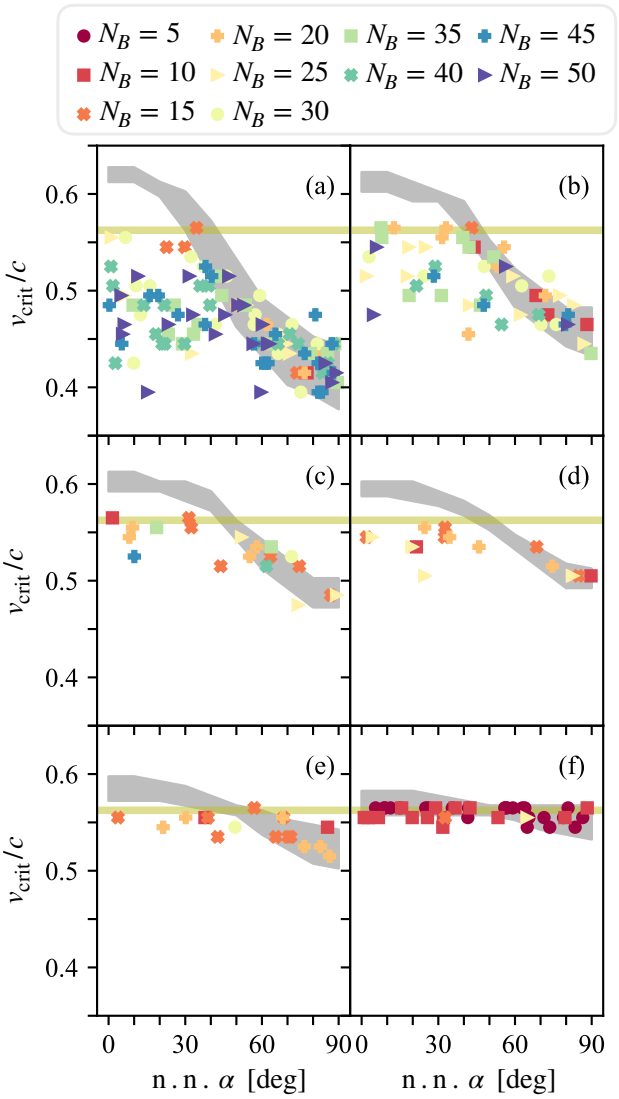

Figure 7.2: The critical velocity of a disordered potential with N_B point-like barriers. Organised by nearest neighbour distance (n.n. R) between the barriers, panel (a) has $4\xi \leq$ n.n. $R < 5\xi$, (b) has $5\xi \leq$ n.n. $R < 6\xi$, (c) has $6\xi \leq$ n.n. $R < 7\xi$, (d) has $7\xi \leq$ n.n. $R < 8\xi$, (e) has $8\xi \leq$ n.n. $R < 12\xi$, (f) has $12\xi \leq$ n.n. R. Different markers represent varying barrier density. The gray shaded area indicates the region containing the critical velocity of an isolated pair of point-like barriers when their separation distance lies within the range of nearest neighbour distances for the panel. The olive shaded area is the critical velocity of one point-like barrier (the width indicates numerical uncertainty).

Chapter 8

Arrest of a Superflow

8.1 Velocity Dependence

Driving a superfluid through a disordered potential faster than the critical velocity injects vortices into the system. The resulting non-equilibrium dynamics are a key object of study in two dimensional quantum turbulence, and have been employed as the initial conditions of studies into quenches both in the highly turbulent clustered case [308], and the dipole dominated case [152, 181, 232, 313, 324]. In this section, we consider a superfluid which is initially flowing through a disordered point-like potential, with an imposed velocity which is greater than the critical velocity of the potential. We observe that the reaction of the fluid is to be arrested by the barriers, suggesting that viscous effects enter the system, before the system equilibrates. The manner in which this disordered system reaches an equilibrium state has connections with quantum turbulence and coarsening in 2D Bose gases.

In this section, we consider one disordered potential with $N_B = 25$ barriers in a system with dimensions $L_x = 256\xi$ by $L_y = 64\xi$. As the system consists of a superfluid initially moving through the point-like barriers above the critical velocity, the formation of elementary excitations causes the system to fall out of equilibrium [349, 350]. To investigate the turbulence in such a system, we measure the condensate and non-condensate fractions, the velocity of the condensate and non-condensate fractions, and the number of vortices which are nucleated by the obstacle.

In order to perform ensemble averaging we add a small amount of complex white noise to the groundstate of the wavefunction, (approximately equal to 1% of the background density). This small amount of initial noise ensures that the system dynamics, and in particular vortex motion, differs in each realization, such that statistics are not dominated by particular vortex trajectories. Averaging over this ensemble allows us to reliably calculate condensate fractions, condensate velocities, and superfluid fractions.

In order to perform an analysis of this system in the long time limit, we evolve the PGPE prescribed in Eqn. (2.38). This is expressed in the frame where the barriers are at

rest and the wavefunction is given an instantaneous initial boost,

$$\Psi\left(\mathbf{r},0\right)=\left[\left(1-\eta\right)\Psi^{(g)}\left(\mathbf{r}\right)+\eta\varpi(\mathbf{r})e^{i\varphi(\mathbf{r})}\right]\exp\left(-\frac{2\pi i v_{\mathrm{int}}x}{cL_x}\right), \tag{8.1}$$

where $\Psi^{(g)}(\mathbf{r})$ is the wavefunction in the ground-state of the system, η is the amount of noise to be added,

$$v_{\mathrm{int}}=\left\lceil\frac{v_{\mathrm{obst}}}{\Delta v}\right\rceil\Delta v, \tag{8.2}$$

where $\lceil\cdot\rceil$ is the ceiling function, and $\Delta v=2\pi c\xi/L_x$ is the smallest velocity representable on the grid in the x direction. The random variables are $\varpi(\mathbf{r})\sim U[0,1]$ and $\varphi(\mathbf{r})\sim U[0,2\pi)$, and we renormalize such that the initial condition has the same normalisation as the ground state. We choose to evolve Eqn. (2.38) as it keeps the late-time, close-to-equilibrium momentum distribution of the system close to symmetric about $\mathbf{k}=0$. Since the k-space cut-off imposed by the projector is symmetric about $\mathbf{k}=0$, this choice helps ensure that the system is evolving towards a well-defined PGPE equilibrium, and hence that the calculation of the momentum-momentum correlations required to compute the superfluid fraction (Sec. 8.1.3) may be performed without the need to perform a gauge transformation.

8.1.1 The Condensate and Non-Condensate Fractions

Where obstacles are dragged through a system at a speed sufficiently above v_{crit}, a large number of vortex-antivortex pairs are nucleated, forming a complicated phase field [100]. Annihilation events between the vortex-antivortex pairs lead to the generation of sound in the system, which causes a depletion to the condensate fraction; this marks the onset of a dissipative regime.

Using the criterion of Penrose and Onsager [15], within the c-field formalism [133], we calculate the condensate and non-condensate fractions from the one body density matrix

$$G^{1B}\left(\mathbf{r},\mathbf{r}'\right)=\left\langle\Psi^{*}\left(\mathbf{r}\right)\Psi\left(\mathbf{r}'\right)\right\rangle_{\mathcal{T}}, \tag{8.3}$$

where $\langle\,\cdot\,\rangle_{\mathcal{T}}$ indicates short time averaging[1]. This fraction is calculated for each of the trajectories before averaging over all trajectories. The condensate number can be identified as the largest magnitude eigenvalue of the one-body density matrix, while the corresponding eigenvector, ψ_0, is the condensate mode. Under this formalism, we deconstruct the wavefunction into contributions from the condensate mode and the non-condensate,

$$\Psi=n_0\psi_0+n_{\mathrm{nc}}\psi_{\mathrm{nc}}, \tag{8.4}$$

[1]In the simulations presented here, we averaged over windows of 10τ. We can compare this to the timescale in which a particle of the fluid might travel between two barriers: $\tau_B=L_B/v_{\mathrm{obst}}$, where $L_B=4\xi$ is the minimum separation of two barriers, and $v_{\mathrm{obst}}\in\{1.0,1.2,1.4,1.6\}c$ is the initial relative speed of the barriers. Thus the sampling window is between $\tau_B=5\xi/(2c)$ and $\tau_B=4\xi/c$.

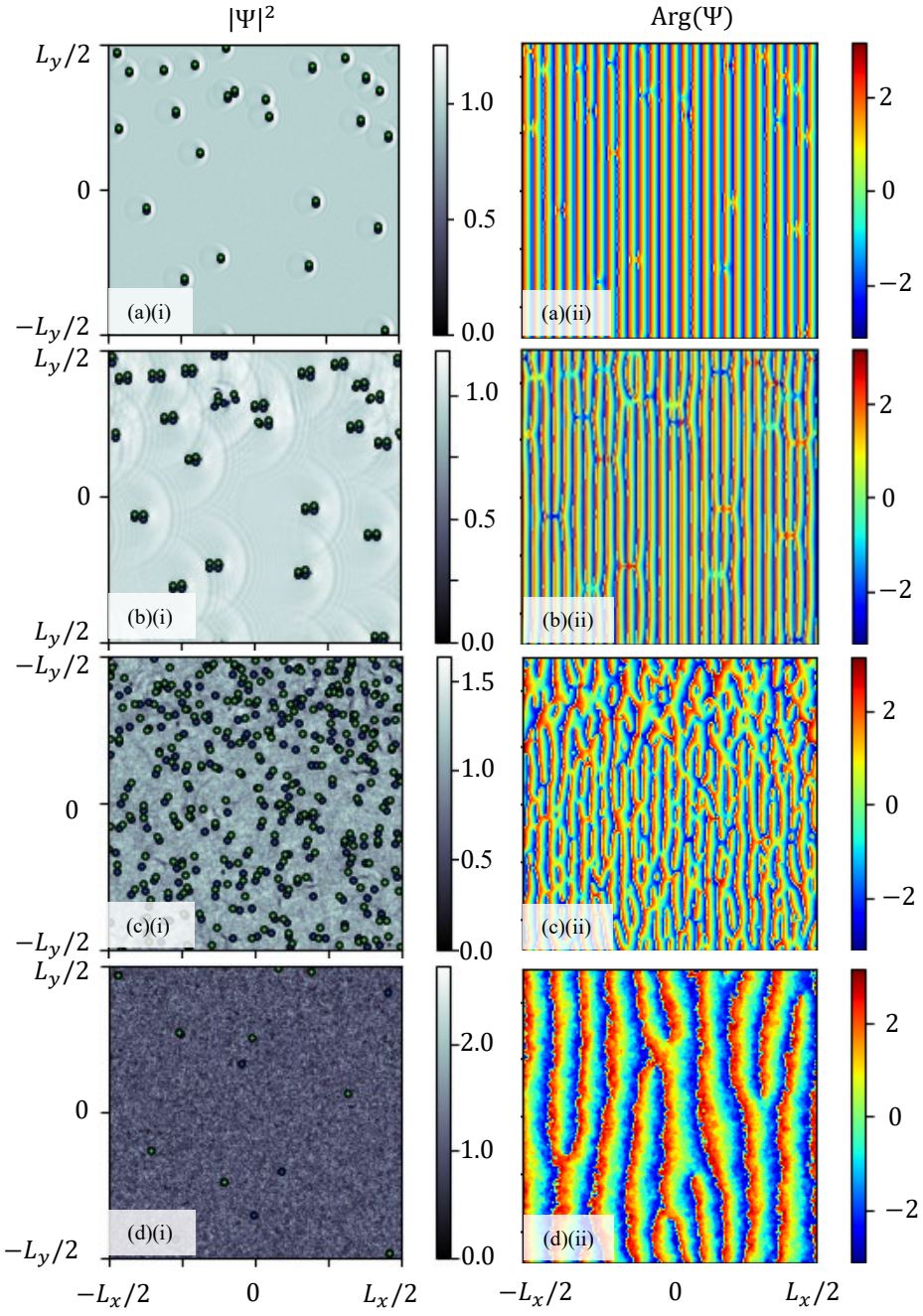

Figure 8.1: Snapshots of a flow past a disordered point-like potential at (a) $t = 10\tau$, (b) $t = 40\tau$, (c) $t = 470\tau$ and (d) $t = 20000\tau$. The flow speed is $v_{\text{obst}} = 1.2v_{\text{crit}}$.

where n_0 is the condensate fraction and $n_{\rm nc}$ is the non-condensate fraction, so that $n_0 + n_{\rm nc} = 1$. The non-condensate mode, $\psi_{\rm nc}$, is the sum of the eigenvectors of G^{1B} excluding ψ_0. Within the c-field formalism, the condensate and non-condensate modes are orthogonal. Further details of this process are given in Appendix A.4.

The average condensate fractions for obstacles which are dragged through the fluid with velocity $v_{\rm obst} \geq v_{\rm crit}$ are plotted in Fig. 8.2, row (a). In systems where $v_{\rm obst} \geq v_{\rm crit}$, there is an initial depletion of the condensate fractions as the barrier sheds vortices which are subsequently annihilated, ultimately heating the system [215]. We observe that the size of the depletion of the condensate fraction (and therefore the spike in the non-condensate fraction) monotonically increases with the velocity of the obstacle which is consistent with the finding of Refs. [51, 325]. Eventually, the energy which is injected into the system by annihilation events is carried away by phonons [51, 350], and the system relaxes to a uniform flow. This is shown by the increases and then plateauing of the condensate fraction, indicating that the system has reached equilibrium and no further vortices are shed. We see that the long term behaviour of the condensate fraction depends on the speed of the obstacles; in the system where $v_{\rm obst} = v_{\rm crit}$ the average condensate fraction over the last 20% of the simulation is $n_0 = 0.8343$, where as for $v_{\rm obst} = 1.6 v_{\rm crit}$ the same average is $n_0 = 0.6160$. This is to be expected, as the faster initial boost injects more energy into the system creating a hotter final state.

8.1.2 The Velocity of the Condensate and Non-Condensate Modes

As the shedding of vortices causes the depletion of the condensate fraction, we would expect the presence of thermal effects to lower the critical velocity [324] which in turn would lead to the nucleation of more vortices, until the condensate is depleted. In fact, since the long term behaviour of the condensate fraction is to equilibriate, we deduce that the system stops shedding vortices. This indicates that the system dynamically reacts to the obstacle velocity.

In dimensionless form, the velocity of the condensate mode ψ_0 and the non-condensate mode ψ_{nc}, is [13]

$$\frac{\mathbf{v}_k}{c} = \frac{1}{2i} \frac{\left(\psi_k^* \tilde{\nabla} \psi_k - \psi_k \tilde{\nabla} \psi_k^*\right)}{|\psi_k|^2}, \tag{8.5}$$

where $k \in \{0, \mathrm{nc}\}$ and $\tilde{\nabla} = \xi \nabla$. We calculate the average velocities of the condensate,

$$v_0(t) = \frac{1}{L_x L_y} \int d^2\mathbf{r} \; \frac{\mathbf{v}_0}{c} \cdot \hat{\boldsymbol{x}}, \tag{8.6}$$

and non-condensate,

$$v_{\rm nc}(t) = \frac{1}{L_x L_y} \int d^2\mathbf{r} \; \frac{\mathbf{v}_{\rm nc}}{c} \cdot \hat{\boldsymbol{x}}, \tag{8.7}$$

and plot them in the barrier reference frame in Fig. 8.2, row (b).

In the presence of the barriers, the fluid nucleates vortices where $v_{\rm obst} \geq v_{\rm crit}$. As these

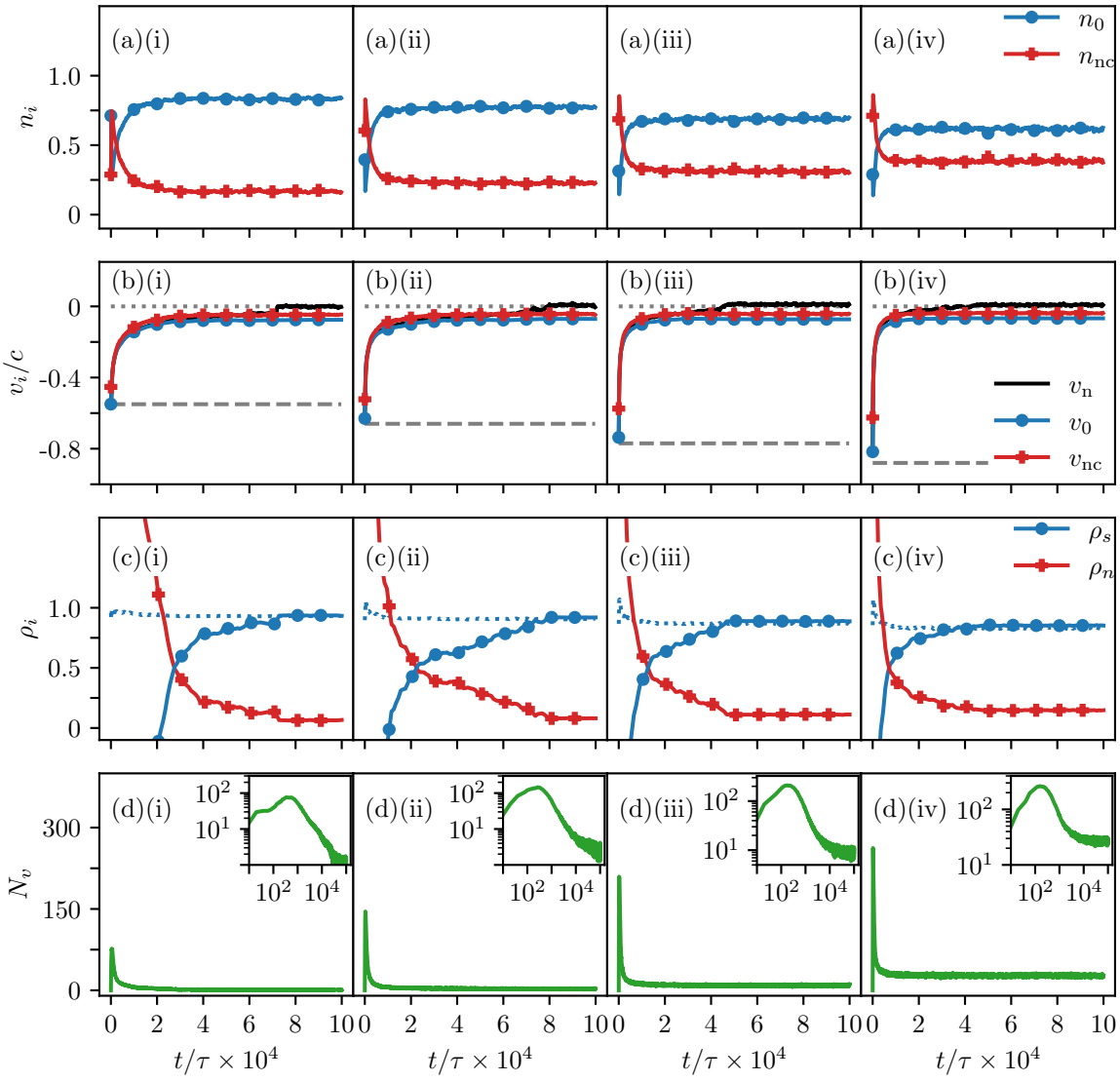

Figure 8.2: Evolution of statistics at different obstacle speeds for column (i) $v_{\text{obst}} = v_{\text{crit}}$, column (ii) $v_{\text{obst}} = 1.2v_{\text{crit}}$, column (iii) $v_{\text{obst}} = 1.4v_{\text{crit}}$, and column (iv) $v_{\text{obst}} = 1.6v_{\text{crit}}$. Row (a) displays the condensate (blue circles) and non-condensate (red pluses) fractions. Row (b) is the velocity of the condensate mode (blue circles), the velocity of the the non-condensate mode (red pluses), and the approximate velocity of the normal fluid (black curve) given by Eqn. (8.13); the grey dashed line indicates v_{obst}, while the grey dotted line indicates zero velocity. Row (c) shows the superfluid fraction computed using the current–current correlations (blue circles), the approximated superfluid fraction described in the text (blue dotted line), and the normal fluid fraction (red pluses). Row (d) plots the vortex number; insets show the vortex number on a log-log scale. The markers are added to help distinguish between curves, rather than indicating individual data points.

vortices nucleate, a phase winding is imparted on the wavefunction, which causes the fluid to decelerate as it attempts to match the speed of the obstacle. In the long time limit, we observe that the velocity of the condensate and non-condensate modes is arrested by the barrier, suppressing further vortex nucleation. The drag force which is exerted on the obstacle potential by the fluid can also be measured, [186], and we find that this vanishes as the system evolves.

We note that we also expect to see a variation in the velocity in the y direction, as different configurations of the barriers act as airfoils, [185], causing a lift effect. In our simulations, since $\mathbf{u} = v_{\mathrm{obst}}\hat{\boldsymbol{x}}$, this variation depends on the configuration of the barrier, but it is always small in comparison to the velocity change in the x direction.

8.1.3 The Superfluid and Normal Fluid Fractions

In order to understand the mechanism by which the velocity of the condensate and non-condensate modes are arrested by the barrier, we calculate the superfluid and normal fluid fractions. We calculate these fractions in two different ways, further details of which can be found in Appendix A.5.

Firstly, we assume that the current, $\mathbf{J}$, of the wavefunction can be decomposed into contributions from a superfluid component (which flows without energy loss) and a normal fluid component (which is subject to viscous effects). We expect that the normal fluid will move with the barriers, and so in the frame of reference where the barriers are stationary, the velocity of the normal fluid will vanish once the system is in equilibrium. Since the superfluid velocity is locked to the condensate velocity [351, 352], assuming that the velocity of the normal fluid is zero leads to an estimate of the superfluid fraction ρ_s using

$$\mathbf{J} = \rho_{\mathbf{s}}\rho_{\mathbf{0}}\mathbf{v_0}, \tag{8.8}$$

where $\mathbf{v_0}$ is the condensate velocity introduced in the previous section.

Secondly, one can compute the superfluid fraction by noting that the (α, β) element of the current-current correlations of the system in thermal equilibrium can be written as

$$\left\langle \left\langle \left[\mathcal{F}\left(\mathbf{J}\right)\right]_{\alpha} \left[\mathcal{F}\left(\mathbf{J}\right)\right]^{*}_{\beta} \right\rangle_{\mathcal{T}} \right\rangle_{\mathcal{R}} \propto \rho_s \frac{k_\alpha k_\beta}{k^2} + \rho_n \delta_{\alpha\beta} \tag{8.9}$$

in the limit of vanishing momentum [111], where $\alpha, \beta \in \{x, y\}$. Here ρ_s and ρ_n are the superfluid and normal fluid fractions, and $\mathcal{F}(\mathbf{J})$ is the Fourier transform of the current of the wavefunction. The angled brackets $\langle\langle \cdot \rangle_{\mathcal{T}}\rangle_{\mathcal{R}}$ indicate that the correlations are found by short time averaging and by averaging over the ensemble of initial conditions. It is then possible to extract the superfluid and normal fluid fractions by fitting the current-current correlations of the wavefunction to the right hand side of Eqn. (8.9), [301]. Formally this method is only valid at equilibrium. Here we employ it with ensemble- and short-time-averaging to give a dynamic measure. We expect this measure to be quantitatively accurate at late times as equilibrium is approached, since we observe the current-current

$v_{\rm obst}$	$\langle n_0\rangle_\mathcal{T}$	$\langle v_0\rangle_\mathcal{T}$	$\langle v_{\rm nc}\rangle_\mathcal{T}$	$\langle \rho_s\rangle_\mathcal{T}$	approximate $\langle \rho_s\rangle_\mathcal{T}$
$0.8v_{\rm crit}$	0.9986	-0.4353	-0.3569	——	0.9974
$v_{\rm crit}$	0.8343	-0.0756	-0.0468	0.9356	0.9303
$1.2v_{\rm crit}$	0.7721	-0.0704	-0.0431	0.9194	0.9072
$1.4v_{\rm crit}$	0.6916	-0.0726	-0.0424	0.8880	0.8668
$1.6v_{\rm crit}$	0.6160	-0.0671	-0.0381	0.8532	0.8296

Table 8.1: A summary of the observables averaged over the last 20% of the simulation. Column 1, the initial velocity of the fluid relative to the barriers; column 2, the condensate fraction n_0; column 3, the condensate velocity v_0; column 4, the non-condensate velocity $v_{\rm nc}$; column 5, the superfluid fraction ρ_s found using current–current correlations; column 6, the approximate superfluid fraction found by decomposing the momentum, $\mathbf{J}$.

correlations remain well fitted by the expected functional form here. At earlier times, further from equilibrium, fits to the expected functional form of the correlations fail, and the measure only provides a qualitative indication of the lack of superfluidity.

The superfluid fraction of the system is plotted in Fig. 8.2, row (c). Where the superfluid fraction (computed using the current–current correlations) is negative, or the normal fluid fraction is greater than 1, it is clear that the condition of vanishing momentum is not met. This condition is better fulfilled at later times, where the velocity of the fluid has been arrested by the barrier [see Fig. 8.2 row (b)]. The fluid must respond to the boost which is initially imposed, and so the velocity of the normal fluid at $t = 0$ is not necessarily zero. This explains why, at very early times, the superfluid fraction computed by decomposing the momentum of the wavefunction is greater than 1.

At earlier times, there is a jump in the normal fluid fraction which equates to the absence of superfluidity. It is this mechanism which forces the fluid to be arrested by the barrier: the appearance of many vortices is associated with a rise in the normal fluid component which is subject to viscous effects, causing the fluid to be decelerated by the barrier. At later times, the superfluid fraction grows and equilibrates with the fluid velocity now approximately zero. By the end of the simulation, both measures of the superfluid fraction are in good agreement with each other, as can be seen in the final two columns of Table 8.1.

As the velocity of the barriers is increased, the final superfluid fraction decreases. In the system where $v_{\rm obst} = v_{\rm crit}$ the average superfluid fraction over the last 20% of the simulation is $\rho_s = 0.9356$ using current–current correlations, and $\rho_s = 0.9303$ by decomposing the current of the wavefunction; in the system where $v_{\rm obst} = 1.6v_{\rm crit}$ these values are $\rho_s = 0.8532$ and $\rho_s = 0.8296$ respectively. This is an analogous result to the depletion of the final condensate fraction as $v_{\rm obst}$ increases.

8.1.4 The Superfluid and Normal Fluid Velocities

While a slow but non-zero final velocity of the superfluid (i.e., a small remnant superfluid velocity) is not physically unexpected, it is interesting that we do not observe the non-

condensate velocity $v_{\rm nc}$ reaching zero over the timescale of our simulations. However, as noted above and as can be seen in Table 8.1 columns 5 and 6, while the superfluid fractions found by current-current correlations and found by assuming that the normal fluid components give similar answers, these two quantities are not equal. This suggest that part of the non-condensate fraction contributes to the superflow.

We now approximate the velocity of the normal fluid in the system. The expected total momentum of the fluid can be written in terms of the condensate and non-condensate fraction

$$\frac{\mathbf{J}}{\rho_0} = n_0 \mathbf{v}_0 + n_{\rm nc} \mathbf{v}_{\rm nc}, \tag{8.10}$$

or, in terms of the superfluid and normal fluid fractions

$$\frac{\mathbf{J}}{\rho_0} = \rho_s \mathbf{v}_s + \rho_n \mathbf{v}_n \tag{8.11}$$

Therefore, for the average velocities in the x-direction we should have

$$\rho_s v_s + \rho_n v_n = n_0 v_0 + n_{\rm nc} v_{\rm nc}, \tag{8.12}$$

where v_s and v_n are the average superfluid and normal fluid velocities [an analogous result to Eqns. (8.6) and (8.7)]. In this analysis, we no longer assume that $v_n = 0$, the velocity of the normal fluid is zero. Instead, since the superfluid velocity is locked to the condensate velocity, $v_s = v_0$, we can use our estimates of n_0, $n_{\rm nc}$, v_0 and $v_{\rm nc}$ from the Penrose–Onsager analysis and our estimates of ρ_s and ρ_n from the current-current correlation analysis to extract the normal fluid velocity from Eqn. (8.12) as

$$v_n = \frac{(n_0 - \rho_s)\, v_0 + n_{\rm nc} v_{\rm nc}}{\rho_n}. \tag{8.13}$$

The value of normal fluid velocity v_n obtained from Eqn. (8.13) is plotted as the black curve in Fig. 8.2 row (b). At late times, the value of v_n is approximately zero; the small fluctuations are due to the combination of uncertainties from the Penrose-Onsager calculations, section 8.1.1, and the calculations of the current-current correlations, section 8.1.3. We also note that v_n found in Eqn. (8.13) is much closer to zero than $v_{\rm nc}$, suggesting that a significant amount of the non-condensate fraction is contained within the superfluid.

This measurement of v_n suggests that the results of our condensate and superfluid analysis are consistent. During our simulations, the interaction between the initial superflow and the barriers has resulted in a normal fluid velocity which is approximately zero, which coexists with a superfluid which has a remaining velocity which is significantly smaller than the critical velocity of the system.

8.1.5 The Vortex Number

Since the reaction of the fluid is to accelerate to catch up with the barriers, vortex anti-vortex pairs are shed from the barrier only at the beginning of the simulation. This leads to a peak in the vortex number as seen in row (d) of Fig. 8.2. It is evident that the amplitude of the peak in $N_{\rm v}$ increases as $v_{\rm obst}$ increases, this is because the vortex shedding frequency increases with the velocity of the obstacle [325].

At the end of the simulation it is possible that a small number of vortices remain in the system. The average number of such vortices at late times increases as the late-time condensate and superfluid fractions decrease. Typically, for the barriers considered in this section, this small number of vortices are not pinned to barriers but are free to move, and hence consistent with thermal vortices in the fluid. We will discuss the role of free vortices and vortices which become pinned to the barriers in more detail in the next section.

It should be emphasized that, while the results presented in this section are measurements of one disordered potential averaged over an ensemble of ten initial conditions, these results are applicable to other disordered point-like potentials. We have checked that the results presented in Fig. 8.2 are qualitatively the same for other N_B, so long as $v_{\rm crit}$ is the same (within error bars). The effect of simulating a system which has a higher (lower) $v_{\rm crit}$ is simply to steepen (flatten) the curves seen in Fig. 8.2, while the long-term behaviour is unchanged.

8.2 Scaling and Turbulence

8.2.1 Overview

Until now we have only considered disordered potentials which consist of a number of point-like barriers, with an effective radius of 1ξ, randomly placed in a periodic cell. We now extend our parameter space to consider disordered potentials consisting of barriers with a greater effective radius, and focus on analyzing vortex decay processes. In this section we consider a square domain with dimensions $L_x = L_y = 256\xi$.

The numerical simulations which are carried out in this section can be related to practical experiments. Periodic boundary conditions, such as those imposed in our simulations, can be realised in one direction in experiments using ring traps [353] It is possible to impose a persistent superflow current in such a geometry by stirring [354] or optical methods [353], creating a superflow in the periodic direction. Technology such as DMDs could be used to paint the stationary disordered potential in part or all of the ring trap [25]. For a large, annular (i.e., tightly confined in the z-direction) ring trap, the main difference from our simulations here would be the lack of periodic boundary conditions perpendicular to the flow. We do not expect that difference to play a crucial role in the dynamics as long as the difference between inner and outer radii of the annulus is a large number of healing lengths. Interestingly, in addition to the studies performed here, in

such a system one could switch off the disorder potential after the initial burst of vortex injections; this could be used as a controllable way to inject a vortex distribution and study the resulting coarsening dynamics *without* the point-like disorder.

In what follows, we will consider the number of *mobile* vortices, $N_{\rm v}$, which are outside the low-density regions at the centres of the barriers, and the number of *pinned* vortices, $\mathcal{W}$, which are contained within the zero-density regions at the centres of the barriers.

8.2.2 Vortex Decay Rate

The rate at which a gas of vortex dipoles decays has been the subject of much discussion over the last decade [95, 179, 232, 338, 355]. The vortex decay rate has connections with the growth of the correlation length of a system, L_c. As the system relaxes after a quench, L_c should become the only relevant length scale, and it is predicted that L_c grows as

$$L_c(t) \sim t^{1/z}, \tag{8.14}$$

where z is the dynamical critical exponent [217]. It is also predicted that, for randomly distributed defects, the vortex number and the correlation length are linked as $N_{\rm v} \sim L_c^{-2}$. Based on experimental observations, the suggested phenomenological rate equation for $N_{\rm v}$ is [179]

$$\frac{dN_{\rm v}}{dt} = -\Gamma_1 N_{\rm v} - \Gamma_2 N_{\rm v}^2. \tag{8.15}$$

Single vortex annihilations are prohibited as vortices are topologically protected quantities, meaning that $\Gamma_1 N_{\rm v}$ describes the drifting of vortices out of the condensate (a one-vortex mechanism), while $\Gamma_2 N_{\rm v}^2$ represents the rate of vortex-antivortex annihilations (a two-vortex mechanism, in this model). However, the decay rate given by Eqn. (8.15) does not match with the results of zero-temperature GPE simulations [95, 232, 338, 355]. This has led to the proposal of a corrected idealized decay rate [355]

$$\frac{dN_{\rm v}}{dt} = -\Gamma_1 N_{\rm v}^{3/2} - \Gamma_4 N_{\rm v}^4, \tag{8.16}$$

where it is argued that the drift and annihilation processes have a $N_{\rm v}^{3/2}$ and $N_{\rm v}^4$ dependence respectively. It has since been shown [95, 232, 355] that for a homogeneous system at zero temperature $N_{\rm v} \sim t^{-1/3}$ which is indicative of a four-vortex process, while the addition of dissipation (finite temperature effects) or trapping potentials removes the need for a fourth vortex (the $N_{\rm v}^4$ scaling which describes a four-vortex annihilation process was also observed numerically in Ref. [338]).

Due to the large proportion of our simulations which occur after the peak in vortex number, it is possible to study the long-time behaviour of vortex decay in our disordered potential systems in a similar fashion. As discussed earlier, we use the plaquette technique [301] to enable vortex detection. Unlike before, where we focused on barriers with effective radii 1ξ, for barriers which have an effective radii $\gtrsim 2\xi$ there is a significant zero density

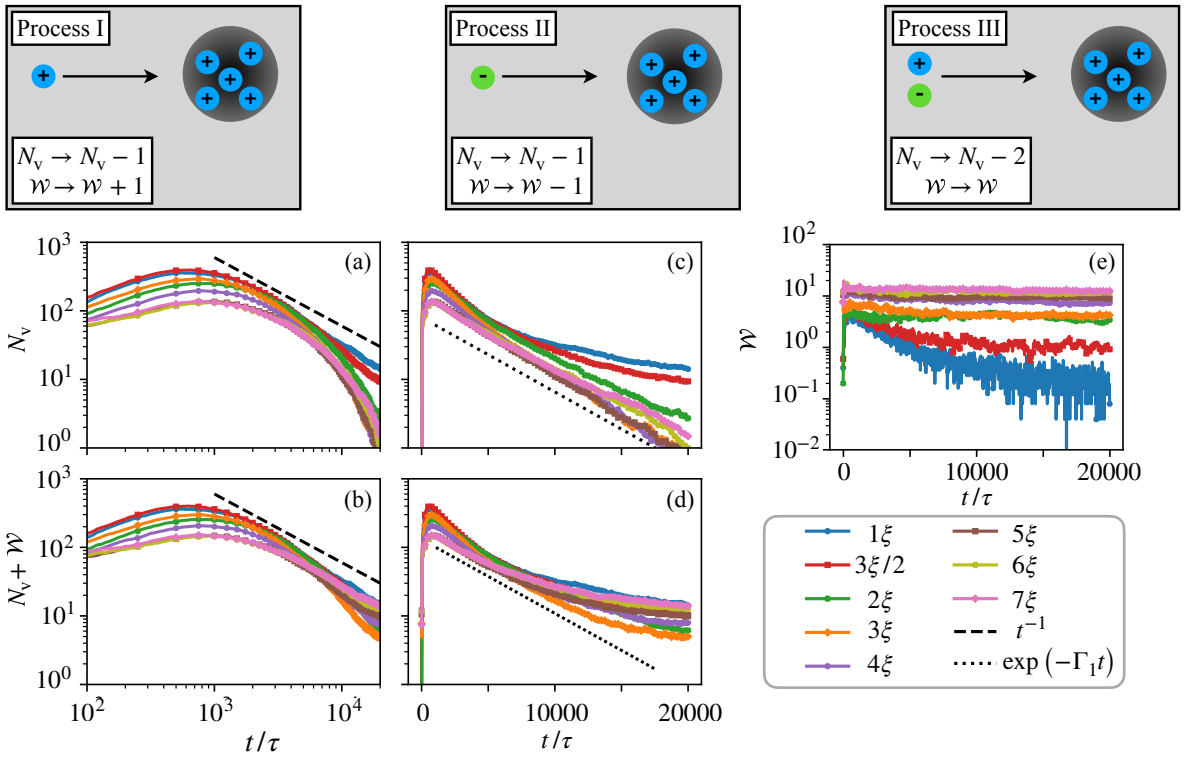

Figure 8.3: The decay of the number of vortices in a system as the barrier width varies. Panels (a) and (c), the decay of the number of mobile vortices, N_v. Panel (e), the decay of the number of pinned vortices, $\mathcal{W}$. Panels (b) and (c), the decay of the total number of vortices, $(N_v + \mathcal{W})$. Panels (a) and (b) are plotted on a log-log scale, while panels (c)–(e) are plotted on a semi-log scale. The power law $N_v \propto t^{-1}$, black dashed line, and the exponential decay $N_v \propto \exp(-\Gamma_1 t)$, black dotted line, are added as guides to the eye. The markers are added to help distinguish between curves, rather than indicating individual data points.
Above: a sketch of the 3 processes by which the number of *mobile* vortices decays. Process I, a vortex collides with a barrier which has a number of like-sign vortices pinned to it. Process II, a vortex collides with a barrier which has a number of opposite-sign vortices pinned to it. Process III, a dipole pair collides with a barrier which has a number of vortices pinned to it.

region where the phase of the condensate is ill-defined. Naively applying the plaquette technique here leads to the detection of spurious vortices. However, it is also possible for a net number of quanta of circulation to genuinely be present at this low density region: we define this number of quanta as the *winding number* of the barrier $\mathcal{W}_k$ (for the kth barrier). The winding number can also be interpreted as a number of *pinned* vortices. Hence, when computing the vortex number we detect both the number of *mobile* vortices N_v, using the plaquette technique and excluding the density-depleted regions, and the total number of *pinned* vortices

$$\mathcal{W} = \sum_{k=1}^{N_v} |\mathcal{W}_k|, \tag{8.17}$$

which is computed using a loop integral technique described in the next section.

The evolution of the vortex numbers for a system with $N_B = 25$ barriers of varying

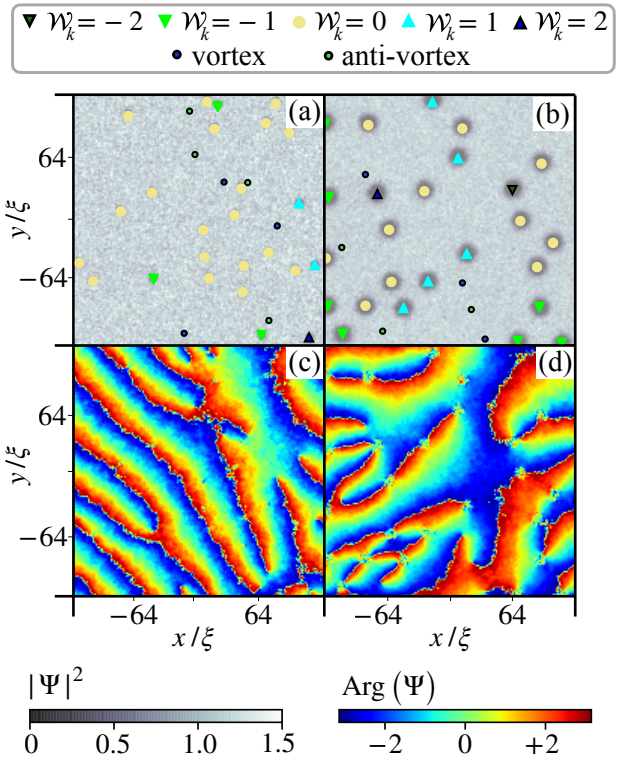

Figure 8.4: A still, taken at time $t = 14460\tau$, from the simulations of barriers with an effective radius of 3ξ, (a) and (c), and simulations of barriers with an effective radius of 7ξ, (b) and (d). In panels (a) and (b), the density of the wavefunction is shown, while different markers indicate the winding number $\mathcal{W}$ of a barrier, and the position of a vortex or anti-vortex. The phase of the wavefunction is shown in panels (c) and (d).

effective radii is shown in Fig. 8.3 (a)–(d). In Fig. 8.3(a) and (c) we plot only the number of mobile vortices N_v. In Fig. 8.3(b) and (d) we plot the total number of vortices (mobile and pinned), $N_v + \mathcal{W}$. For the narrowest barriers we consider, the vortex decay rate appears to follow a $t^{-1.1}$ power law for effective barrier radii of ξ, and a $t^{-1.2}$ power law for effective barrier radii of $3\xi/2$, as can be seen in panel (a). In a system where the vortex number only decays via vortex-antivortex annihilations, Eqn. (8.15) predicts that $N_v \propto t^{-1}$. The fact that the observed power laws are relatively close to t^{-1} for the narrowest barriers is indicative of the fact that vortex decay is a two-vortex process in this system. For barriers which are larger than the typical size of a vortex core (i.e., have an effective width which is greater than a few healing lengths), the vortex number appears to decay exponentially, as can be seen in panel (c). This is consistent with a solution to Eqn. (8.15) where a one-vortex mechanism is dominant, i.e., $N_v \propto \exp(-\Gamma_1 t)$. This suggests that for wider barriers, at late times in the simulation, vortices are colliding with a barrier more often than they are colliding and annihilating with a vortex of the opposite sign. We discuss the effects of vortices colliding with barriers in the following section.

8.2.3 Pinning to Barriers

As well as measuring the rate at which the number of vortices decay, we have also measured the number of vortices which become pinned to the barriers. The pinning and un-pinning of superfluid vortices is an important physical process for understanding the mechanism of neutron star glitches [356–360], and is also of interest in systems with macroscopic container defects [361–363], as well as spin-down experiments with helium [364, 365], and laboratory BECs [366]. The microscopic process by which a vortex becomes pinned to a density depleted region has recently been studied by Ref. [192]. For systems where impurities exist, it is energetically favourable for a vortex to be contained within the zero-density region, as there is no cost in energy to create a vortex core [367].

As described above, we define *pinned* vortices in terms of the net quanta of circulation around a barrier, which is well defined as the branch cut representing a discontinuity in the phase extends into the non-zero density region of the condensate (i.e., it is not a spurious vortex caused by the phase not being well defined in the zero density region at the centre of the barrier). For each barrier in a given potential, we can measure the winding number $\mathcal{W}_k$ by integrating around a loop containing the barrier (see Appendix C for details of the numerical method). Examples of the phase of a barrier with no pinned vortices, one pinned vortex, and two pinned vortices are shown in Fig. 8.5 panels (i), (j) and (k). Also shown is the approximate location of the radius of the circular "exclusion zone" which we choose when counting the number of mobile vortices. A slightly larger circular loop is used to measure the winding number. It should be noted that in any one trajectory the time-dependent values of the numbers of mobile and pinned vortices may display fluctuations in time that depend on the precise choice of radii for these circles, especially when two or more barriers are close together. While we were unable to find choices that eliminate these fluctuations in any one trajectory, we find the averaged results are relatively insensitive to the choice of radii.

At early times, the system is in a highly non-equilibrium state, and many vortices are periodically shed by the barriers. However, by $t \gtrapprox 10^3\tau$, shedding from each of the barriers has almost completely stopped, and the winding number of each barrier is steady. This can be seen in Fig. 8.3 panel (e). For larger barriers, the number of mobile vortices in the system decays as $N_\mathrm{v} \propto \exp(-\Gamma_1 t)$, suggesting that the vortices are annihilating with the barriers. From our observations of the simulations, we suggest that there are 3 processes taking place here. Process I: a vortex collides with a barrier which has a number of vortices with the same sign pinned to it. Here the number of mobile vortices decays, $N_\mathrm{v} \to N_\mathrm{v} - 1$, while the number of pinned vortices increases, $\mathcal{W} \to \mathcal{W} + 1$. Process II: a vortex collides with a barrier which has a number of vortices with the opposite sign pinned to it. Here the number of mobile vortices decays, $N_\mathrm{v} \to N_\mathrm{v} - 1$, but the number of pinned vortices also decays since the mobile vortex annihilates with one of the pinned vortices, $\mathcal{W} \to \mathcal{W} - 1$. Process III: a dipole pair collides with a barrier which has a number of vortices pinned to it. Here, the number of mobile vortices decreases by two, $N_\mathrm{v} \to N_\mathrm{v} - 2$,

however the number of pinned vortices remains the same, since one of the dipole pair will annihilate with the vortices of opposite sign in the barrier, while the other vortex in the dipole pair will remain and will become pinned to the barrier, $\mathcal{W} \to \mathcal{W}$. As, on average, each barrier sheds an equal number of vortices and anti-vortices, Processes I and II take place with approximately the same frequency, conserving the pinning number $\mathcal{W}$. Process III, which also conserves the winding number, happens far less frequently. However, this process may perhaps explain the slight modifications to the exponential decay which we see in Fig. 8.3. We assume that collisions between three or more vortices and a barrier are so rare as to be negligible.

The probability of observing a given winding number can be seen in the histograms in Fig. 8.5, where the data is taken from $10^4\tau \leq t \leq 2 \times 10^4\tau$. As we can see, for narrow barriers vortex pinning is not an important feature. However, for barriers which are significantly larger than a vortex core, a significant number of the barriers do have a vortex or anti-vortex pinned to them ($\mathcal{W}_k = \pm 1$), and the largest barriers which we consider support the pinning of multiple vortices ($|\mathcal{W}_k| > 1$). Examples of this behaviour can be seen in Fig. 8.4.

It can be seen in Fig. 8.3 that the rate at which the number of mobile vortices decays becomes quicker as the effective radius is increased past 2ξ, and is at its fastest for barriers which have an effective radius of $\approx 5\xi$. This may be attributed to the fact that for barriers with an effective radius greater than 2ξ we have observed that is is more likely for a barrier to support the pinning of vortices; this provides a mechanism to lose mobile vortices via Process I, above. For barriers which have a larger effective radius than 5ξ, we have observed that it is possible to have multiple vortices pinned to a barrier. Multiple pinning creates a stronger velocity field around the barrier than single pinning does; this could explain why the rate at which the number of mobile vortices decays slows slightly as the effective barrier radius increases above 5ξ.

8.3 Conclusion

In this part we have studied the effect of dragging a disordered point-like potential through a superfluid which is initially in the ground state. We have seen how the critical velocity of two point like barriers depends on the relative distance and angle between the barriers. We have then determined the critical velocity for a system which has up to 50 point like barriers at randomized locations, and shown that the critical velocity of such a system can be mapped on to the two-barrier case by considering the separation and angle with respect to the flow of the closest nearest-neighbour pair of barriers in the disorder potential.

Using PGPE simulations, we investigated the evolution of a system in which an initial superflow, moving at or above the critical velocity, is disturbed by a stationary point-like disorder potential. This strongly non-equilibrium initial condition causes the nucleation of vortices and depletion of the condensate and superfluid fractions. We observe that

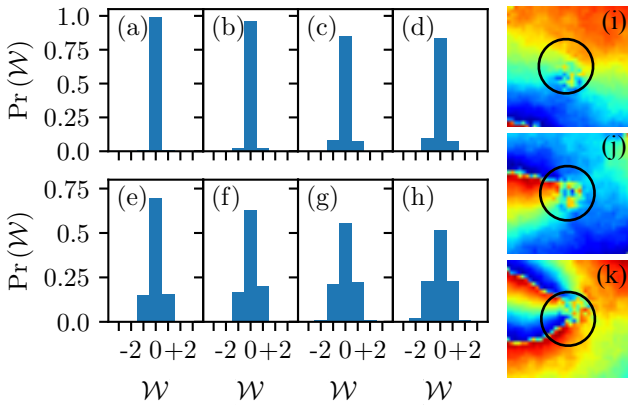

Figure 8.5: Normalized histogram of the winding number, $\mathcal{W}$, for barriers with effective radius (a) 1ξ, (b) $3\xi/2$, (c) 2ξ, (d) 3ξ, (e) 4ξ, (f) 5ξ, (g) 6ξ and (h) 7ξ. Right: examples the phase of the wavefunction, $\mathrm{Arg}\,(\Psi)$, around a barrier with (i) no pinning, $\mathcal{W} = 0$, (j) one pinned vortex, $\mathcal{W} = +1$, and (k) two pinned vortices, $\mathcal{W} = +2$; the black circle is approximately the boundary of the zero-density region of the barrier. A slightly larger circular loop is used to compute the integral required to calculate $\mathcal{W}$.

the reaction of the fluid is to accelerate to a final velocity closer to the obstacle velocity. This suppresses the nucleation of further vortices, and the fluid re-condenses and some superfluidity is restored.

We extended our parameter space to consider the effect of larger barriers in the system, and investigated the way in which this affects the decay of the number of vortices in the system. It is clear that the presence of randomly placed barriers that have an effective width which is larger than the characteristic size of a vortex core, modifies the form of the vortex number decay from the behaviour identified in previous theoretical works without a disordered potential. Within the limits of our numerical analysis, it appears as though the vortex decay rate no longer follows a t^{-1} power-law scaling which is indicative of vortex-antivortex annihilations, but rather the vortices collide with the barriers which make up the potential, causing an exponential decay. This one-vortex decay process is confirmed with our observations of the simulations. Finally, we observe that for these larger barriers vortex pinning becomes a relevant phenomenon, with the largest barriers which we consider supporting the pinning of multiple vortices.

With an appropriate trapping geometry, it may be possible to experimentally study a system equivalent to the one studied here in which the disordered potential arrests a superflow.

Part IV

Point Vortex Models

Chapter 9

The Point Vortex Model

In this part we consider the dynamics of a system of vortices using the Point Vortex Model, rather than the PGPE. As the name implies, this model considers the vortices as a series of points, whose dynamics are governed by a set of coupled, first order, ordinary differential equations. We begin by introducing the standard Point Vortex Model, and consider some of the ways in which it may be extended. We end this chapter by deriving a Point Vortex Model which takes into account fluctuations in the density of the fluid in which the vortices live. In Chapter 10 we apply this updated model to a system with a continuously varying disordered potential.

9.1 Introduction to the Point Vortex Model

The concept of using a point vortex model to describe the dynamics of an ideal 2D fluid containing vortices (or a 3D fluid which contains straight, parallel, vortex filament tubes) was originally introduced by Helmholtz [368] and Kirchoff [369]. In classical fluids, this is a highly idealized model, since a vortex may have an arbitrary sized core, and the circulation is continuous. Superfluids, on the other hand, are immediately more amenable to a point vortex model, as the size of the vortex core is fixed, and the circulation is quantized [370, 371], as seen in Chapter 3. The key idea of point vortex model is that, in the absence of other forces, a vortex will move with the local velocity field, which is imposed by other nearby vortices. In a 3D superfluid, the motion of a vortex line is due to velocity contributions both from other vortex lines, and also (if the vortex line is not straight) from other parts of the same vortex line [224]. In a 2D superfluid, the effects of vortex bending are "frozen-out" [98], and so the dynamics of the pure point vortex model depend only on the relative positions and charges of the vortices [230], and not on other parts of the vortex line.

The point vortex model has been sucessfully used to study a diverse range of physics in superfluids [57, 88, 89, 91, 93, 96, 339, 371–386], including vortex dynamics [372, 373, 382, 385, 387] and clustering [88, 96], the prediction of negative temperature states [88, 388], the direct enstrophy cascade [91], and the inverse energy cascade [88, 389]. The

advantage of the point vortex model is that it is a conceptually simple model which correctly describes the dynamics of the vortices in a fluid [390]. It has been shown that, for a system of well separated vortices, the point vortex model for a superfluid [230] is in good agreement with GPE simulations [88, 89, 339, 374, 382, 386, 391] and experimental observations [57, 375, 379, 383, 391]. The point vortex model is also numerically cheaper to implement than the GPE, since at any one time one only needs to compute the position and velocities of $N_{\rm v}$ vortices, rather than compute mean-field dynamics on a $N_x \times N_y$ grid[1].

Unfortunately, there are some processes which must be artificially added to the point vortex model to make it physically realistic. The primary ingredient which must be added is the annihilation of vortex anti-vortex pairs which takes place in quantum turbulence [93, 179, 232, 389]. This can be achieved "by hand" in the point vortex model, by removing pairs of vortices of opposite sign when they are below a threshold distance of each other; typically this distance is one or two healing lengths [88, 89, 392]. A related phenomena, is the presence of damping in the system, which is due to the friction between the superfluid and normal fluid components [57, 379]. A dissipative term can be rigorously added to the point vortex model, by addition of a Peach-Koehler term [231, 393].

Given recent experimental advances in controlling the trapping geometry of a condensate [25], it is necessary to consider the role of the geometry of the system on vortex dynamics. If the condensate is of finite size, the boundary of a condensate must play a role in modifying the dynamics of a vortex. In classical fluids, the method of image vortices to account for a hard boundary is well established [69]. However, within the context of the point vortex model, a debate exists on the necessity of imposing image vortices in condensates which have a soft boundary [197, 339, 373, 394–397]. In order to avoid such ambiguities, the work on the point vortex model in this thesis will be in a regime where there are no regions where the fluid density vanishes, and therefore the system has no boundary.

Aside from boundaries, the point vortex model introduced by Fetter [230] is only strictly valid in a uniform system. It has been predicted and observed that variations in the background density of the fluid will affect the motion of a vortex [244, 375–377, 394, 398–401]. There has been some progress in simulating point vortex models where the density of the fluid varies, such as the work by Groszek *et al.* [339] on few vortices in a trapped system. Studies of a system with a large number of vortices on a varying background density using the point vortex model in are in their infancy, however.

The remainder of this part is structured as follows. In the following sections we introduce the vanilla point vortex model, as well as recent advances in adding dissipation and compressible effects to this equation. We conclude this chapter by introducing an

[1]Typically, point vortex simulations initially have fewer than $N_{\rm v}(0) = 2^{15}$ vortices [91], a number which decreases as simulations progress and vortices are removed after annihilation. In order to numerically simulate the Povint Vortex Model, one must calculate the distance between each of the vortices, Eqn. (9.3); with symmetries, r_{jk} is a $N_{\rm v}(N_{\rm v}-1)/2$ matrix. On the other hand, the complexity of computing the Fast Fourier Transform (an operation which can be used to calculate the derivative terms in the GPE) scales like $N_x N_y \log(N_x N_y)$.

outline of the derivation of a point vortex model which correctly accounts for dissipation and fluctuations in the background density of the fluid. A full derivation can be found in Appendix. D. In Chapter 10 we present preliminary results on the dynamics of vortices both in a simple non-uniform potential, and then in a continuously varying disorder potential. We end this part with a discussion of future avenues of research.

9.2 The Point Vortex Equation of Motion

The equation of motion found by Fetter [230] is for the position $\mathbf{r}_j$ of the j-th vortex in the system. This position depends on the gradient of the phase field which is due to the other vortices in the system. For a system containing N_v vortices, the phase field of the j-th vortex is given by

$$\mathcal{S}_j(x,y) = \sum_{\substack{k=1 \\ k\neq j}}^{N_\mathrm{v}} n_k \arctan\left(\frac{y-y_k}{x-x_k}\right), \tag{9.1}$$

where the vortices may be described by a coordinate (x_k, y_k) and a charge n_k. Recalling that the superfluid velocity is $\mathbf{v} = (\hbar/m)\nabla\mathcal{S}$, the gradient of this phase field gives the velocity of the j-th vortex [230],

$$\frac{d}{dt}\mathbf{r}_j = \mathbf{v}_j, \tag{9.2}$$

where

$$\mathbf{v}_j = \sum_{\substack{k=1 \\ k\neq j}}^{N_\mathrm{v}} \frac{n_k}{r_{jk}^2}\begin{pmatrix} -y_{jk} \\ x_{jk}\end{pmatrix}, \tag{9.3}$$

the distances $x_{jk} = x_j - x_k$, $y_{jk} = y_j - y_k$, and $r_{jk}^2 = x_{jk}^2 + y_{jk}^2$, with $n_j = \pm 1$ the sign of the jth vortex. The $j = k$ term is omitted from the sum, as the motion of a given vortex depends only on the velocity field of *other* vortices. We will refer to this equation as the "pure" Point Vortex Model, as it simply treats each of the vortices as a point (based on the vortex's position) and states that the vortex moves with the local superfluid velocity with no other corrections.

It should be noted that, in an unbounded system, the problem can also be formulated as a Hamiltonian system [402]

$$\mathcal{H}_\mathrm{PV} = -\sum_{j=1}^{N_\mathrm{v}}\sum_{\substack{k=1 \\ k\neq j}}^{N_\mathrm{v}} n_j n_k \ln|\mathbf{r}_j - \mathbf{r}_k|, \tag{9.4}$$

where the vortex dynamics are governed by

$$\frac{dx_j}{dt} = \frac{\partial\mathcal{H}_\mathrm{PV}}{\partial y_j}, \qquad \frac{dy_j}{dt} = -\frac{\partial\mathcal{H}_\mathrm{PV}}{\partial x_j}. \tag{9.5}$$

In systems where boundaries are present, it is necessary to replace to logarithmic term in Eqn. (9.4) with appropriate Green's functions which depend on the geometry of the system [371, 402]. It can be seen in Eqn. (9.5) that the variables x and y, which represent the coordinates of the vortices, are canonically conjugate; we also note that Eqn. (9.4) does not describe a typical Hamiltonian system, since the conjugate variables are the x and y positions rather than position and momentum. In addition to the Hamiltonian, the vortex momentum

$$\mathbf{P} = \sum_{j=1}^{N_\mathrm{v}} n_j \left(y_j \hat{\mathbf{x}} - x_j \hat{\mathbf{y}}\right) \tag{9.6}$$

must be conserved due to translational symmetry, and the angular momentum,

$$P_L = \sum_{j=1}^{N_\mathrm{v}} n_j \left(x_j^2 + y_j^2\right), \tag{9.7}$$

is conserved in an open domain due to rotational symmetry.

In a periodic square domain of size $L \times L$ is it possible to write [403]

$$\mathbf{v}_j = \frac{\pi c}{L} \sum_{\substack{k=1 \\ k \neq j}}^{N_\mathrm{v}} n_k \begin{bmatrix} -f\left(\tilde{y}_{jk}, \tilde{x}_{jk}\right) \\ f\left(\tilde{x}_{jk}, \tilde{y}_{jk}\right) \end{bmatrix}, \tag{9.8}$$

where

$$f(x, y) = \frac{1}{2} \sum_{p=-\infty}^{\infty} \frac{\sin(x)}{\cosh(y - 2\pi p) - \cos(x)}, \tag{9.9}$$

c is the speed of sound of the fluid, and the re-scaled coordinates are given by $(\tilde{x}_{jk}, \tilde{y}_{jk}) = 2\pi \left(x_{jk}, y_{jk}\right) / L\xi$, [403] . More generally, an expression can be derived for point vortices within an arbitrarily sized periodic parallelogram [404], although we will not consider such a set up within this thesis.

9.2.1 Adding Dissipation

It is possible to add dissipation to the system, by means of the phenomenological damping parameter γ. The equation becomes

$$\frac{d}{dt}\mathbf{r}_j = \mathbf{v}_j - \gamma n_j \hat{\mathbf{z}} \times \mathbf{v}_j, \tag{9.10}$$

where the second term is a perpendicular Peach–Koelher term [393], which typically describes the force which acts upon a line element in a stress field. In the case of Eqn. (9.10), the line element is the vortex filament (point vortex in 2D), and the stress field is the velocity vield induced by the other votices. This term was introduced by Kawasaki [405].

Typically, damping is added to the system as a uniform parameter (see, for example, [379]) in a similar sense to the addition of damping to the (S)(P)GPE, where γ paramaterises the rate at which the system relaxes [144]. Some models, on the other hand, add

damping as a spatially dependent function in order to mimic the sound waves which are generated when two vortices annihilate in a mean-field simulation [91]. In the dissipative point vortex model, the effect of damping depends on the mutual sign of the interacting vortices, as can be seen by the second term in Eqn. (9.10). For a constant value of γ, the result of adding damping is to shorten the distance between oppositely signed vortex pairs, or lengthen the distance between like-sign vortex pairs over time (see Appendix D.3).

9.2.2 Adding Compressible Effects

Some progress has been made in modifying a simple point vortex model to be able to consider the role of sound and thermal fluctuations. This model, proposed by Reeves *et al.*, [406], combines a dissipative point vortex model with a noise term, thus forming a Langevin equation. The dynamics are modeled as

$$d\mathbf{r}_j = (\mathbf{v}_j - \gamma n_j \hat{\mathbf{z}} \times \mathbf{v}_j)\, dt + \sqrt{2\eta}\, d\mathbf{W}_j, \tag{9.11}$$

where η is the vortex diffusion rate, and the noise term $d\mathbf{W}_j$ components are independent Gaussian random variables with

$$\left\langle dW_j^\alpha dW_k^\beta \right\rangle = \delta_{jk}\delta_{\alpha\beta} \tag{9.12}$$

with all other correlations vanishing (much like the approach of the SPGPE [133]).

This model represents a significant stepping stone in correcting for sound in the point vortex model at the single vortex level. Unfortunately, however, Reeves *et al.* [406] found that the value of η is highly sensitive to the geometry of the system, and the means by which vortices are injected into the system.

9.3 Taking Account of Background Fluctuations

Previous works [230, 239, 240] have derived equations of motion for a system of vortices, assuming that the vortices are dilute within the system. This assumption, equivalent to the assumption that the average inter-vortex distance is large compared to the healing length of the system, means that the equation of motion does not take into account variations in the background density of the field. In a dilute system of vortices in a uniform BEC it is reasonable to assume that the effect of density gradients is negligible, it can be shown that in a trapped system the trapping potential distorts the position of the vortex [244], and so the vortex dynamics will be modified by gradients in the density.

In the remainder of this chapter, we will discuss a dissipative point vortex model which takes into account the effects of the background density of the fluid [231]. This equation of motion is applicable to a non-relativistic dissipative system, and can be derived from a Ginzburg-Landau equation with complex coefficients. The derivation is based on that

of Törnkvist and Schröder, Ref. [231], and a full derivation of the model can be found in Appendix D.

Consider a general Ginzburg-Landau equation,

$$\frac{d\Psi}{dt} = P\left(\Psi, \Psi^*\right)\Psi + b\nabla^2\Psi, \tag{9.13}$$

where Ψ is a complex field, the function P is given by

$$P\left(\Psi, \Psi^*\right) = \varsigma - a|\Psi|^2, \tag{9.14}$$

and $a, b, \varsigma \in \mathbb{C}$. The complex Ginzburg-Landau equation has a number of special cases; if a, b, ς are purely imaginary, then we recover the non-linear Schrödinger equation, which in this context may also be called the Ginzburg-Pitaevskii-Gross equation. This equation is conservative, and may be derived from a Lagrangian formalism [407]. In general, the complex Ginzburg-Landau equation is a dissipative system from which the damped GPE may be recovered on setting $a = g(\gamma + i)/\hbar$, $b = \hbar(\gamma + i)/(2m)$ and $\varsigma = \mu(\gamma + i)/\hbar$, by comparison with Eqn. (2.38).

We adopt a coordinate system for a one-dimensional string, which is the vortex filament [231]. At any time t, the position of the filament of the vortex is given by $\boldsymbol{X}(s,t)$, where s parameterises the arclength of the filament. In differential geometry, the Frenet-Serret formulas [408] describe the dynamical properties of a particle moving along a smooth, continuous curve, as well as intrinsic properties of the curve itself. From here, an orthonormal coordinate system may be derived from the Frenet frame which describes any position $\mathbf{r}$ in the neighbourhood of the string as

$$\mathbf{r} = \boldsymbol{X}(s,t) + r\cos\varphi\boldsymbol{N}(s,t) + r\sin\varphi\boldsymbol{B}(s,t), \tag{9.15}$$

where $\boldsymbol{N}$ is vector normal to $\boldsymbol{X}$, the binormal vector $\boldsymbol{B}$ can be found by taking the vector product of the tangent and normal vectors, and $r\cos\varphi$, $r\sin\varphi$ are polar coordinates introduced in this local region. In this coordinate system, it is possible to write the Laplacian term of Eqn. (9.13) as

$$\begin{aligned}\nabla^2 \;=\; & \frac{\partial^2}{\partial r^2} + \frac{1}{r}\frac{\partial}{\partial r} + \frac{1}{r^2}\frac{\partial^2}{\partial\varphi^2} - \frac{\kappa}{1-\kappa r\cos\varphi}\left(\cos\varphi\frac{\partial}{\partial r} - \kappa\sin\varphi\frac{\partial}{\partial\varphi}\right) \\ & + \left[\frac{1}{1-\kappa r\cos\varphi}\left(\frac{\partial}{\partial s} - \tau\frac{\partial}{\partial\varphi}\right)\right]^2\end{aligned} \tag{9.16}$$

where κ is is the curvature of the vortex filament, and τ is the torsion of the vortex filament (a measure of how quickly the curve is twisting out of the plane).

Suppose that we write the complex field in Eqn. (9.13) as

$$\Psi = |\Psi|\exp\left(iS\right), \tag{9.17}$$

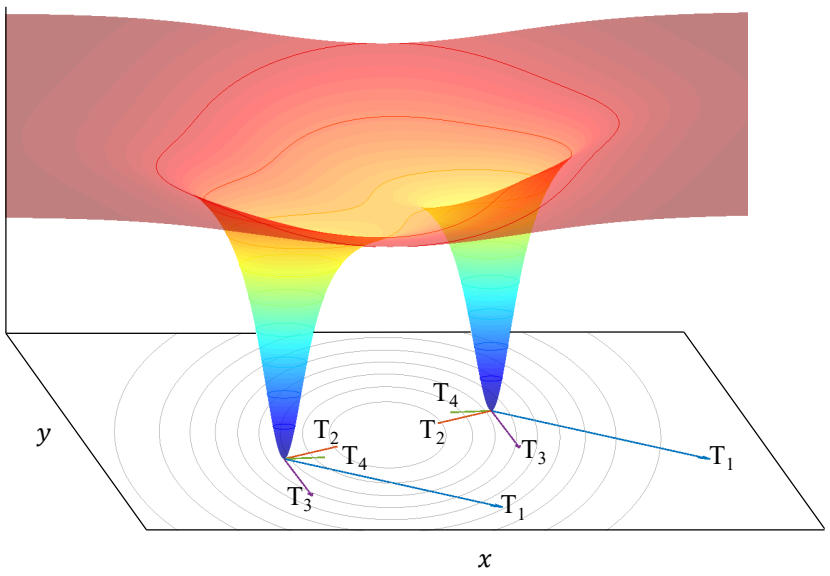

Figure 9.1: A schematic of the Törnkvist and Schröder model, applied to a vortex dipole ($n_1 = 1$, $n_2 = -1$) in an inhomogeneous background. The surface represents a sketch of the background fluid density for a system that contains two vortices (shown as the two density minima). The gray lines show the contours of the trapping potential. The arrows represent each term in Eqn. (9.29); blue, the point vortex velocity, $\mathrm{T}_1 = \mathbf{v}_j$; red, the damped term from the point vortex model, $\mathrm{T}_2 = -\gamma n_j \times \mathbf{v}_j$; purple, the perpendicular Peach-Koehler term, $\mathrm{T}_3 = -n_j \times \nabla \ln w|_{\mathbf{r}_j}$; green, the background dissipative term $\mathrm{T}_4 = -\gamma \nabla \ln w|_{\mathbf{r}_j}$. The length of each arrow is proportional to the modulus of each of the terms.

by virtue of a Madelung transform. The multivalued nature of the phase of a vortex will cause problems with the continuity and differentiability of $|\Psi|$ and S as $r \to 0$. To counter this, we split the modulus and phase of Ψ as follows: let

$$|\Psi| = R(r,\varphi)\, w(r,\varphi), \tag{9.18}$$

$$S = \chi(r,\varphi) + \theta(r,\varphi) \tag{9.19}$$

where $\ln R$ depends on the filament position and contains any contribution to the modulus which is non-differentiable at $r = 0$. Similarly, we absorb into χ any part of the phase field which is multivalued at any point, or non-differentiable at $r = 0$. We note that is important to allow the amplitude, $|\Psi|$ of the complex field to vary, as this will include the contributions from the background fluid density in our model. Since R and χ only occur in the combinations described in Eqns. (9.18) and (9.19), they are non-unique which in 3D provides a gauge freedom. In 2D, we set

$$R = r^{|n|}, \qquad \chi = n\varphi, \tag{9.20}$$

and we note that the curvature and torsion of the vortex filaments vanish, so $\kappa \to 0$ and $\tau \to 0$. Physically this is equivalent to assuming that the vortex filaments are straight and parallel [98], and taking a cut in the xy plane.

The result of Eqn. (9.20) and Eqn. (9.16) is that we can write the real and imaginary

parts of the complex Ginzburg-Landau equation as

$$\frac{d}{dt}\left(\ln R + \ln w\right) = \mathrm{Re}\left[P\left(\Psi,\Psi^*\right)\right] + b_R Q_1 - b_I Q_2, \tag{9.21}$$

$$\frac{d}{dt}\left(\theta + \chi\right) = \mathrm{Im}\left[P\left(\Psi,\Psi^*\right)\right] + b_R Q_1 + b_I Q_2, \tag{9.22}$$

where the coefficient b has been divided into real, $\mathrm{Re}(b) = b_R$, and imaginary, $\mathrm{Im}(b) = b_I$, parts, and

$$Q_1 = \nabla^2 \ln w + \frac{2|n|}{r}\hat{\boldsymbol{r}}\cdot\nabla\ln w - \frac{2n}{r}\hat{\boldsymbol{\varphi}}\cdot\nabla\theta + \left(\nabla\ln w\right)^2 - \left(\nabla\theta\right)^2, \tag{9.23}$$

$$Q_2 = \nabla^2\theta + \frac{2|n|}{r}\hat{\boldsymbol{r}}\cdot\nabla\theta + \frac{2n}{r}\hat{\boldsymbol{\varphi}}\cdot\nabla\ln w + 2\nabla\ln w\cdot\nabla\theta. \tag{9.24}$$

It is possible to link the time derivative in the lab-frame to the time derivative in the moving reference frame of the local segment of the vortex filament by

$$\frac{d}{dt} = \frac{\partial}{\partial t} - \frac{d\boldsymbol{X}}{dt}\cdot\nabla. \tag{9.25}$$

Applying this to Eqns. (9.23) and (9.24) leads to two more coupled equations which describe the evolution of the four variables R, w, θ, and χ. In each of these equations [as one can see in Eqns. (9.23) and (9.24)], there are terms which are proportional to r^{-1}, which will lead to singularities as $r \to 0$. We must, therefore, derive regularity conditions for these equations, so that the singularities cancel term by term. The form of the function $P\left(\Psi,\Psi^*\right)$ does not enter into the remainder of the derivation, as it is globally differentiable. Recall that $\ln w$ and θ are continuous and differentiable everywhere; the regularity conditions are

$$0 = \frac{d\boldsymbol{X}}{dt}\cdot\hat{\boldsymbol{r}} + 2b_R\left[\hat{\boldsymbol{r}}\cdot\nabla\ln w - \frac{n}{|n|}\hat{\boldsymbol{\varphi}}\cdot\nabla\theta\right] - 2b_I\left[\hat{\boldsymbol{r}}\cdot\nabla\theta + \frac{n}{|n|}\hat{\boldsymbol{\varphi}}\cdot\nabla\ln w\right], \tag{9.26}$$

$$0 = \frac{d\boldsymbol{X}}{dt}\cdot\hat{\boldsymbol{\varphi}} + 2b_R\left[\frac{n}{|n|}\hat{\boldsymbol{r}}\cdot\nabla\theta + \hat{\boldsymbol{\varphi}}\cdot\nabla\ln w -\right] + 2b_I\left[\frac{n}{|n|}\hat{\boldsymbol{r}}\cdot\nabla\ln w - \hat{\boldsymbol{\varphi}}\cdot\nabla\theta\right]. \tag{9.27}$$

We now have equations for the two perpendicular components of $d\boldsymbol{X}/dt$. We can combine these into one equation, using the fact that $\hat{\boldsymbol{r}}\times\hat{\boldsymbol{\varphi}} = \hat{\boldsymbol{z}}$. Since the tangential velocity is devoid of physical meaning, it is possible to set $\hat{\boldsymbol{z}}\cdot d\boldsymbol{X}/dt = 0$, by means of a time dependent reparameterization [231]; the resulting equation for the velocity of the vortex filament is therefore

$$\frac{d\boldsymbol{X}}{dt} = 2b_I\nabla\theta - 2b_R\frac{n}{|n|}\hat{\boldsymbol{z}}\times\nabla\theta - 2b_I\frac{n}{|n|}\hat{\boldsymbol{z}}\times\nabla\ln w - 2b_R\nabla\ln w. \tag{9.28}$$

It is now possible to write down an equation of motion for a dissipative point vortex

model which takes into account the background density fluctuations of the fluid in which the vortices exist. By comparison with the dissipative GPE, Eqn. (2.38), we have the constants $b_R = \gamma\hbar/2m$ and $b_I = \hbar/2m$ (or, in adimensional form, $b_R = \gamma/2$ and $b_I = 1/2$). For a system which has only unit vortices, $n_j = \pm 1$, the non-dimensional equation of motion of the position $\mathbf{r}_j$ of the j-th defect is

$$\frac{d}{dt}\mathbf{r}_j = \mathbf{v}_j - \gamma n_j \hat{\boldsymbol{z}} \times \mathbf{v}_j - n_j \hat{\boldsymbol{z}} \times \nabla \ln w\big|_{\mathbf{r}_j} - \gamma \nabla \ln w\big|_{\mathbf{r}_j}, \tag{9.29}$$

where $\mathbf{v}_j$ is given by Eqn. (9.3).

This is a modified form Eqn. (9.10). The third term has the same formulation as the second term: a perpendicular Peach-Koehler term. In this case, the term depends on the natural logarithm of the background density, and so this term generates a force on the vortex filament which is due to the gradient of the density of the superfluid. The final term is proportional to the gradient of the background fluid; the strength of this term depends on the dissipation of the system. A sketch of how Eqn. (9.29) applies to a vortex dipole in an inhomogeneous background can be found in Fig. 9.1. The advantages of solving Eqn. (9.29), rather than the full GPE, are similar to those of the vanilla point vortex model: it is numerically cheaper to implement, and the coordinates of the vortices are readily available. In addition, the Törnkvist and Schröder model, Eqn. (9.29), is an exact equation for a system of vortices where dissipation is present, and the velocity of the vortices depends on local gradients in the background density of the fluid.

Chapter 10

Vortex Dynamics in the Presence of Disorder

In this chapter we present some preliminary results on vortex dynamics, found using Eqn. (9.29). The chapter is in two halves, the first half dealing with the motion of a few vortices moving in a simple non-uniform 2D condensate, and the latter half is dedicated to investigating the decay of many vortices which are in a continuously varying disordered potential with some scale cut-off.

10.1 A Simple non-Uniform Potential

We begin by examining the effects of Eqn. (9.29) by looking at the dynamics of a single vortex-antivortex pair on a varying background. This provides a useful prototype on which to test our numerical procedure. In the simplest case, we do this by imposing a slowly varying periodic potential given by

$$V_{\text{ext}}(\mathbf{r}) = V_0 \sin\left(\frac{2\pi x}{L_x}\right), \tag{10.1}$$

on a periodic cell which has dimensions $L_x \times L_y$. In order to determine the background density, w, of the fluid, we use the Thomas-Fermi approximation. This means that the background density is given by

$$w(\mathbf{r}) = \sqrt{\frac{V_0}{g}}\left[\frac{\mu}{V_0} - \sin\left(\frac{2\pi x}{L_x}\right)\right]^{1/2}. \tag{10.2}$$

We substitute this into Eqn. (9.29) and numerically evolve the equations of motion using a 4th order Runge-Kutta time stepping scheme with a fixed step size of $\delta t = 0.1$. We have ensured that this time step is small enough by comparing the vortex dynamics for a system where the time step is one tenth of the size. We impose a cut-off distance of 1 healing length, so that if a vortex anti-vortex pair is separated by less than this distance they are deemed to have annihilated and are removed from the system. Note that, in

the simulations presented in Fig. 10.1, we directly apply Eqn. (9.29) in a rectangular ($L_x \neq L_y$) domain, with the velocity $\mathbf{v}_j$ as it appears in Eqn. (9.3). This is a first order approximation, as it does not take into account the image vortices which are due to the periodic boundary conditions; for a square domain this is corrected by Eqn. (9.8), which we will use in the next section. We do not expect that this will make a qualitative difference to the dynamics in Fig. 10.1.

The evolution of a vortex-antivortex pair on a non-uniform background is plotted in Fig. 10.1 column (a). It is evident that the strength of the background potential (and thus the variation in the density of the background fluid) has an effect on the dynamics of the vortices. As the vortices enter a denser region of fluid, indicated by the darker shaded region in Fig. 10.1, the dipole length $r_{12}(t) = |\mathbf{r}_1(t) - \mathbf{r}_2(t)|$ decreases, and so the velocity of the dipole pair increases. As the vortices enter a region where the density of the fluid is depleted, indicated by the lighter shaded region of Fig. 10.1, the dipole length increases and the velocity of the dipole pair is reduced. By making the potential function strong enough, it is possible to have steep enough density gradients that the dipole length becomes shorter than the cut-off distance for annihilations, and the dipole is removed from the system. Note that to avoid the issue of image vortices at a boundary, we have chosen $\mu/V_0 > 1$ so that there isn't a region where the density of the background fluid vanishes. In Fig. 10.1 column (b) we vary the strength of the dissipation γ in the system. As expected, the distance between the vortices in the dipole pair decreases according to the strength of γ. This distance evolves as

$$[r_{12}(t)]^2 = [r_{12}(0)]^2 - 4\gamma t \tag{10.3}$$

where $\mathbf{r}_1$ and $\mathbf{r}_2$ are the coordinates of the dipole pair.

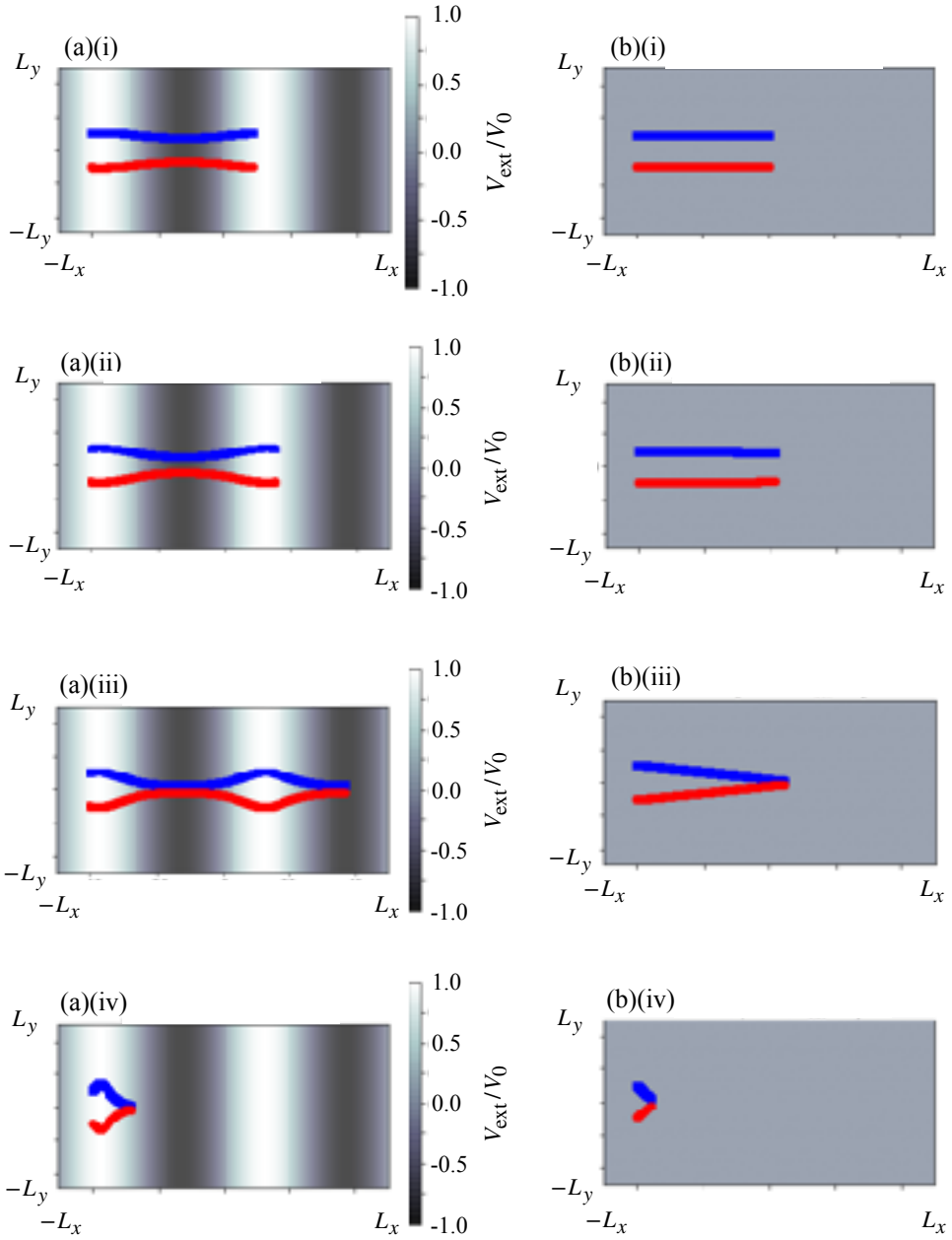

Figure 10.1: The dynamics of a vortex (blue) anti-vortex (red) pair, governed by the dissipative point vortex model with background fluctuations. In column (a) the non-uniform background potential given in Eqn. (10.1) is imposed; the background colour gives the relative height of the potential, V_{ext}/V_0; panel (a)(i) has $\mu/V_0 = 10.0$, panel (a)(ii) has $\mu/V_0 = 5.0$, panel (a)(iii) has $\mu/V_0 = 2.5$, and panel (a)(iv) has $\mu/V_0 = 1.25$. In column (b) the background is uniform while the value of dissipation varies; panel (b)(i) has $\gamma = 10^{-3}$, panel (b)(ii) has $\gamma = 10^{-2}$, panel (b)(iii) has $\gamma = 10^{-1}$, panel (b)(iv) has $\gamma = 10^{0}$. Markers are placed at equal time steps.

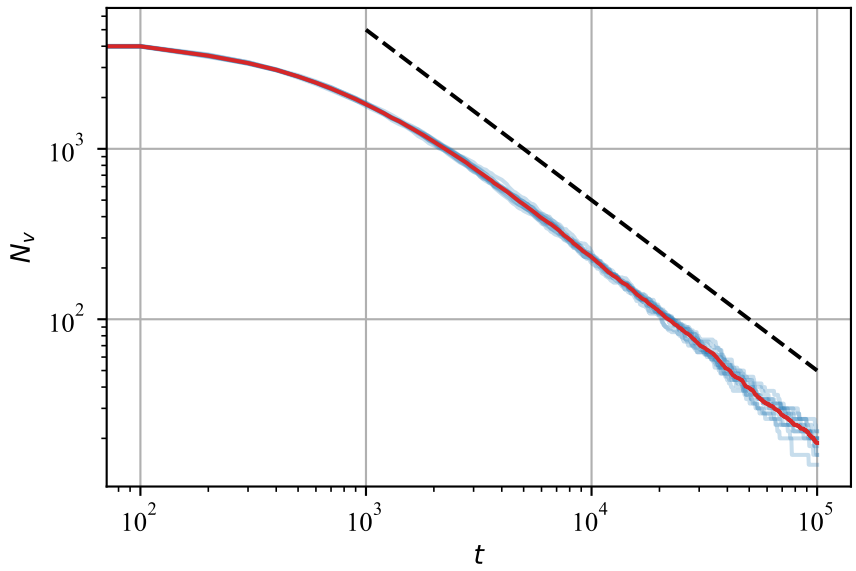

Figure 10.2: The decay of N_v vortices in a homogeneous background. Initially there are $N_\mathrm{v} = 2^{12}$ vortices, with an equal number of positive and negative unit charges, randomly placed within a $256\xi \times 256\xi$ periodic cell, where the value of damping is $\gamma = 0.01$. Light blue lines show the trajectory of individual simulations, while the solid red line shows the ensemble average. The line $N_\mathrm{v} \sim t^{-1}$ is added as a guide to the eye.

10.2 A Continuously Varying Disordered Potential

We are primarily interested in determining the effect which a varying density of the background fluid has on the rate at which vortices decay. As a benchmark, we evolved a system which initially has $N_\mathrm{v} = 2^{12}$ vortices all within a spatially homogeneous, w =constant, fluid. In order to speed up the dynamics of the vortex coarsening, a small amount of damping is added to the system. The results of these simulations are shown in Fig. 10.2. As there are no boundaries in this simulation, we would expect that the vortex decay rate is given by

$$\frac{dN_\mathrm{v}}{dt} = -\Gamma_2 N_\mathrm{v}^2, \tag{10.4}$$

as in Ref. [232], and indeed this is the result which we recover.

In Part. III we considered a point-like disordered potential which consisted of N_B Gaussian peaks, randomly distributed in the domain, which is otherwise uniform. By tuning the height and width of these peaks, we were able to form barriers in the flow, which had a regular (effectively cylindrical) cross section. In this part, however, we consider a potential which is continuously varying throughout the domain. In order to efficiently implement Eqn. (9.29), we choose a potential which has a relatively simple analytic form,

$$V_\mathrm{ext}(\mathbf{r}) = \sum_{\mathbf{k}\in\mathcal{K}} A_\mathbf{k} \cos\left(\frac{2\pi}{L}\mathbf{k}\cdot\mathbf{r} + \varphi_\mathbf{k}\right), \tag{10.5}$$

where

$$\mathcal{K} = \left\{ \mathbf{k} = (k_x, k_y) \ : \ k_{min}^2 \leq k_x^2 + k_y^2 \leq k_{max}^2 \right\}, \tag{10.6}$$

and the random variables $A_{\mathbf{k}}$ and $\varphi_{\mathbf{k}}$ are sampled from uniform $U[0,1]$ and $U[0,2\pi)$ distributions respectively. The set of modes, $\mathcal{K}$ represents an annulus in $\mathbf{k}$ space, and by controlling the parameters k_{min} and k_{max}, we are able to control the deviations of V_{ext} from a uniform potential: a low k_{max} represents a slowly varying potential landscape, while increasing k_{max} leads to sharp peaks in the potential. A third parameter to control is the Root Mean Square (RMS) value of the potential, V_{RMS}. The RMS value of the trap is related to the maximum value of the trap (see Appendix. D.4 for details), and is a good indicator of the strength of the potential.

In order to calculate the terms in Eqn. (9.29) which depend on the gradient of the background density, we approximate the background density using the Thomas-Fermi density profile. For the remainder of this section we write any variables in dimensionless form, where the chemical potential μ and the interaction strength g are both set to one. We also ensure that the coefficients $A_{\mathbf{k}}$ are chosen so that the maximum of the potential is less than one. This ensures that there are no regions in the cell where the background density vanishes, removing the need to worry about image vortices, or how to deal with vortex pinning. The resulting expression for the background density is, in dimensionless form,

$$w = \sqrt{1 - V_{\text{ext}}(\mathbf{r})}. \tag{10.7}$$

To ensure that this is a valid approximation to the background density, in Fig. 10.3 we compare the Thomas-Fermi density profile given in Eqn. (10.7) to the density ground state which is found by numerically evolving the damped GPE, Eqn. (2.38). We find that when the ratio k_{max}/L is small, there is a good agreement between the Thomas-Fermi approximation and the exact state. As the ratio increases, however, the discrepancy between the Thomas-Fermi profile and the numerically obtained density profile grows; this is due to the fact that the derivatives of the wavefunction become more significant, meaning that the Thomas-Fermi approximation becomes weaker.

In the remainder of this section we will work in the region of $(k_{max}, V_{\text{RMS}})$ parameter space where the Thomas-Fermi profile, Eqn. (10.7), is a good approximation of background density, as can be seen in Fig. 10.3. This has the advantage that there is a simple analytical form for the gradient of the densities,

$$\nabla \ln w = \frac{1}{2}\left[1 - \sum_{\mathbf{k}\in\mathcal{K}} A_{\mathbf{k}} \cos\left(\frac{2\pi}{L}\mathbf{k}\cdot\mathbf{r} + \varphi_{\mathbf{k}}\right)\right]^{-1} \sum_{\mathbf{k}\in\mathcal{K}} A_{\mathbf{k}}\ \mathbf{k} \sin\left(\frac{2\pi}{L}\mathbf{k}\cdot\mathbf{r} + \varphi_{\mathbf{k}}\right). \tag{10.8}$$

We note that μ/g does not enter Eqn. (10.8) since w invariant to scaling by a constant, Eqn. (9.18). As in the previous section, we substitute this analytic expression for the gradient into Eqn. (9.29) and numerically evolve the equations of motion using a 4th order Runge-Kutta time stepping scheme with a fixed step size of $\delta t = 0.1$. We continue

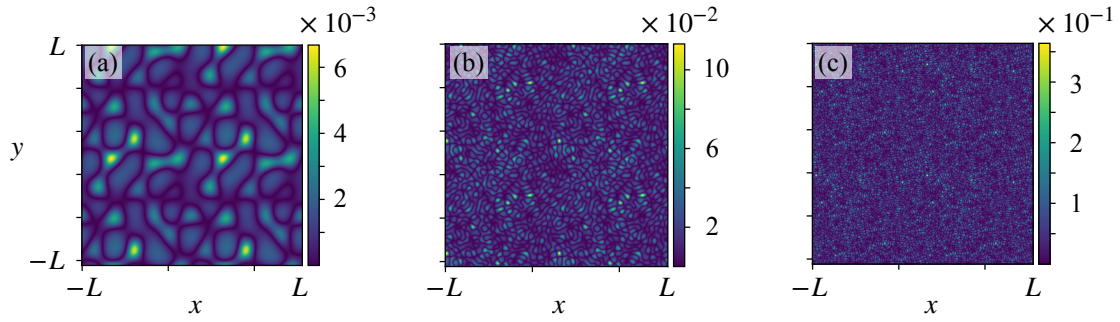

Figure 10.3: The absolute difference between the Thomas Fermi density profile, given by Eqn. (10.7), and the numerically obtained ground state of a system subjected to a continuously varying disordered potential, Eqn. (10.5), found by evolving the damped GPE. In panel (a) $k_{max} = 4$, in panel (b) $k_{max} = 16$, and in panel (c) $k_{max} = 32$; in each case $k_{min} = 2$, $V_{\mathrm{RMS}} = 0.25$, and $L = 128\xi$.

to use a small value of damping in order to speed up the dynamics of the system, while imposing an cut-off length for vortex anti-vortex annihilation of one healing length.

The results of this simulation can be found in Fig. 10.4. For small values of k_{max} and V_{RMS}, there is no significant difference between the decay of the homogeneous system, where $N_{\mathrm{v}} \propto t^{-1}$, and the vortex decay rate observed in the system with a varying background fluid density. It is clear, however, that as the values of k_{max} and V_{RMS} are increased, that there is a deviation between the vortex decay rate in the homogeneous case and in the case where the background of the fluid varies. In the case of the strongest and fastest varying disorder, panel (c)(v), the rate at which the vortex number decreases is significantly different to the homogeneous case, indicating that if $N_{\mathrm{v}} \sim t^{-\beta}$ then $\beta < 1$. As we discussed in Chapter 8, for randomly distributed vortices in a homogeneous system the vortex decay rate is connected to the correlation length, $L_c(t)$ of the system via $N_{\mathrm{v}}(t) \sim L_c^{-2}$. Since we observe that the vortex decay rate is slower than in a the homogeneous case, the correlation length of the system is growing more slowly than in the homogeneous case, indicating that the value of the dynamical critical exponent in Eqn. (8.14) has changed [217]. This could be suggestive of vortex localisation [308], or possibly the transition of the system to an exotic phase.

10.3 Outlook

In this part, we have introduced a dissipative point vortex model which correctly accounts for fluctuations of the background density in the fluid. We have began by applying a conceptually simple disordered potential to the system, and measuring the rate at which

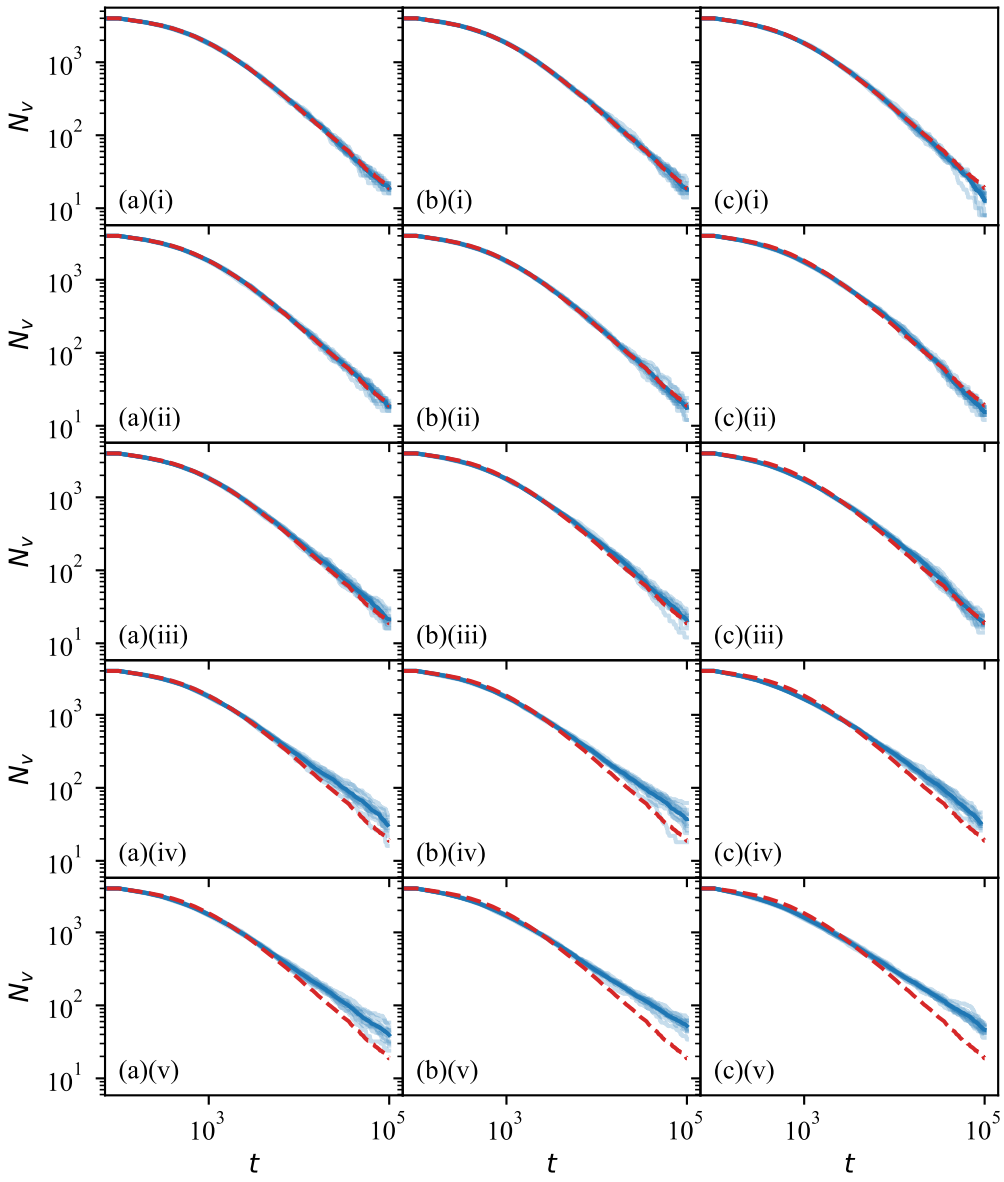

Figure 10.4: The decay of N_v point vortices in a system which has a varying background density. Different columns correspond to different values of k_{max}; in column (a) $k_{max} = 4$, in column (b) $k_{max} = 8$, and in column (c) $k_{max} = 16$. Different rows correspond to different imposed values of V_RMS; in row (i) $V_\mathrm{RMS} = 0.05$, in row (ii) $V_\mathrm{RMS} = 0.10$, in row (iii) $V_\mathrm{RMS} = 0.15$, in row (iv) $V_\mathrm{RMS} = 0.20$, and in row (v) $V_\mathrm{RMS} = 0.25$. Light blue curves show individual trajectories, while the dark blue curve shows the ensemble average. The red dashed curve is the averaged decay of a homogeneous system of the same size, given in Fig. 10.2.

the vortex number decays. We have shown that, for strong enough disorder, there is a clear divergence from the known results of vortex decay in a homogeneous system. Future work on this model will involve calculating the mobility of remaining vortices in the system, and investigating the possibility of finding a phenomenological rate equation which links the parameters controlling the disorder potential ($k_{max}, V_{\mathrm{RMS}}$) and the number of vortices in the system $N_{\mathrm{v}}(t)$. There is a fundamental link between the rate at which the number of vortices decays and the coherence length of the system [217]; in this model, both of these quantities differ from the homogeneous system, and so it is a potentially fruitful to investigate whether the energy spectra or the enstrophy of the system are similarly affected in the presence of disorder.

At present, the parameters which control the disordered potentials (k_{max} and V_{RMS}) used in our numerical simulations have been chosen so that background density of the fluid is well described by the Thomas-Fermi approximation. In future work, in order to extend the parameter space of disordered potentials available to us, we would look to find the ground state of the system by numerically evolving the damped GPE, and then calculating the background density terms in Eqn. (9.29) using interpolation. Even for a large system, the computational time required to calibrate the model by evolving the GPE to the system's ground state before investigating the dynamics using the point vortex model is shorter than simulating everyting using the GPE.

To further extend the parameter space of disordered potentials available, we could also consider strongly disordered potentials, where there are zero density regions in the fluid. In this regime, we would have to consider to need to add image vortices to our governing equations, as well as considering the means by which we would add pinning to the model. Such strongly disordered potentials may lead to vortex dynamics in exotic phases; at zero temperature, a BEC that is subject to subject to a disorder stronger than a critical value undergoes a quantum phase transition to an exotic "Bose glass" [308, 409]. It remains an open question as to how the Bose glass phase is connected to the normal fluid phase [330, 335, 410]. Using the model which we have developed in this part, and by expanding the parameter space available, it may be possible to rigorously address this question. In order to present a comprehensive picture of the interplay between disorder, vortex dynamics and phase transitions, it will also be necessary to compare the results of this model to a sample of (S)PGPE simulations.

A final topic to explore would be to attempt to derive a hydrodynamic model from Eqn. (9.29). This would be similar to the studies carried out by Refs. [381, 384, 411], who have shown that a coarse-grained description of small patches of vortex distributions behaves as an inviscid non-Eulerian fluid on scales which are much larger than the scale of the patches. Such a model would enable the study of very large numbers of vortices, over long time scales, in a 2D fluid with a varying background density.

Part V

Conclusions, Future Work and Appendices

Chapter 11

Conclusions

11.1 Conclusions

This thesis has considered the vortex dynamics in a variety of 2D BEC systems, encompassing systems which are rotating at the centrifugal limit, as well as systems which are subjected to disorder.

In Part I we introduced Bose Einstein Condensation as well as the Gross-Pitaevskii Equation, which is a non-linear partial differential equation that has been successfully used to model a condensed gas. We also provided a comprehensive introduction to the *projected* Gross-Pitaevskii Equation, an extension to the ordinary GPE that simulates a weakly interacting Bose gas at finite temperature. We ended this part with a theoretical description of quantized vortices and their properties, as well as the means by which they might be created in an experiment.

In Part II we studied a 2D Bose gas that is subjected to a harmonic trapping potential, rotating at the centrifugal limit so that the effective trapping potential vanishes. This allows us to probe the behaviour of the bulk of the system, as there are no boundaries or edge effects.

We work in the Landau gauge, which is advantageous at the centrifugal limit since we can write down quasi-periodic boundary conditions that allow us to consider a representative cell of the infinite system. We also present the analytic expression for the phase of a Bose gas subjected to these boundary conditions; this allows us to prepare the system with an initial configuration of N_{v} vortices placed within the cell (subject to symmetry considerations).

It is possible to evolve the PGPE for this system by using a pseudo-spectral method, using the eigenfunctions of the single particle Hamiltonian as basis functions. This has the advantage in that the projection operator can be implemented exactly; the number of basis functions which describe the wavefunction is controlled by the energy cut-off. Despite the fact that there is no known quadrature rule for these basis functions, we show that by suitable choice of the simulation parameters it is possible to make the resulting error of the evolution negligible.

By adding a dimensionless damping parameter to the PGPE, we were able to confirm that the system relaxes to the expected ground state: for a cell with aspect ratio $\sqrt{3}$ this is a hexagonal lattice of vortices. Adding noise to the ground state increases the contribution of higher energy levels, and hence affects the thermal properties of the state. We evolved this perturbed ground state in the absence of damping and observed that the vortex lattice "melts" for sufficiently large amounts of noise.

The absence of boundaries and edge effects of the infinite system provides an excellent test-bed in which to study phase transitions in a rotating 2D system. After evolving a perturbed ground state, we were able to measure the first-order correlation function of the system; the nature of the decay of this function is a hallmark of the Berezinskii-Kosterlitz-Thouless transition. We observed a clear transition from algebraic to exponential decay as the amount of noise added to the ground state increases, suggesting that a transition analogous to the BKT transition has taken place.

In Part III we investigated the dynamics of a 2D Bose gas which is forced to flow through a point-like disordered potential. We begin by determining the critical velocity for vortex nucleation as the flow passes a system of two point-like barriers, and see that this velocity depends on both the relative separation of the barriers, and the angle between the barriers and the direction of the flow. Having determined the critical velocity for a pair of point-like barriers, we obtain the critical velocity for a system of N_B point like barriers. We find that the critical velocity of the system can be inferred from the positioning of the closest two barriers: for relatively close barriers the critical velocity is bounded above by the highest critical velocity of the two barrier test case for equivalent nearest-neighbour separation, while for well separated barriers the critical velocity is bounded above by the single barrier case.

Having carried out a detailed study of the critical velocities of point-like disorder potentials, we moved to look at the resulting non-equilibrium dynamics of the system. Initially forcing the fluid to flow through the potential faster than the critical velocity, we observed that the reaction of the fluid was to be arrested by the barrier. This is due to the non-equilibrium initial conditions causing a dip in the superfluid fraction.

Finally, we explored the behaviour of the system as the effective width of the barriers is increased. Measuring the number of vortices in the system as the width varies, we observed a significant departure from the vortex decay rate that we would expect. We also observed that vortex pinning becomes more relevant as the size of the barriers increases, with the largest barriers which we considered supporting the pinning of multiple vortices.

In Part IV we considered the application of a Point Vortex Model to a 2D system with a continuously varying background potential. Unlike typical Point Vortex Models which are unsuitable for studying disordered potentials as they neglect background density gradients, we have simulated a Point Vortex Model which correctly accounts for these fluctuations [231].

Initially we consider the motion of a dipole pair in a fluid with a non-uniform back-

ground density. We observe that the dynamics of the dipole are altered by the background. In fact, for strong enough variations in the background density, the dipole pair can be forced to annihilate in the absence of damping.

Applying the model to a system which initially has a large number of vortices, we confirm that in a uniform system the expected scaling of the vortex number is recovered. We then move to consider the dynamics of a large number of vortices in a continuously varying trapping potential. We achieve this by using a Thomas-Fermi profile to approximate the background density of the fluid when the disorder is weak and slowly varying. Such a system displays a clear departure from the expected scaling law as the disorder strength increases, suggesting that this is an interesting area of research to pursue.

11.2 Future Work

Future research will consider two main avenues. Using the numerical method from Part II, we have an excellent framework in which to study vortex dynamics and phase transitions of Bose gases in a rotating system. Furthermore, based on the findings presented in Part III and the methodology of Part IV, there is a wide scope to investigate vortex dynamics in a system which is subject to disorder. In the remaining sub-sections we propose some of the initial work to be carried out.

11.2.1 A BKT-like Transition in a Rotating BEC

The possibility of a phase transition in a 2D rotating BEC which is analogous to the BKT transition was probed in Chapter 6, and this remains an exciting future direction of research.

The work presented in Chapter 6 takes place in a $64\xi \times 64\xi/\sqrt{3}$ cell, which means that the range in which the first order correlation function can be reliably calculated is $0 < r < 32\xi/\sqrt{3}$. In order to ensure that a comprehensive picture of the BKT-like transition is presented, similar statistics should be calculated for larger systems. As with any PGPE simulation, it will also be necessary that we perform these simulations with a different number of energy levels included in the c-field region, to ensure that our calculations are insensitive to our choice of cut-off.

In order to explore the vortex pair unbinding which is a characteristic of the BKT transition, further work is needed to analyse the spatial distribution of vortices. To fully understand the effect that rotation has on the BKT transition temperature, we must find a correspondence between the amount of noise which is added to the ground state, and the temperature and superfluid fraction of the system. Such a calculation is highly non-trivial as our system is in a non-inertial frame and in the Landau gauge. Relating these physical observables, however, will undoubtedly unearth rich results in condensed matter physics.

11.2.2 Flow through disordered potentials

Adding disorder to a system vastly increases the parameter space which may be explored. In our investigation, we only considered identical soft walled circular potentials; in principle one could observe different physics by using hard walled potentials, or by changing the shape of the individual barriers. We were also limited in the effective widths of the barrier which we could study due to the size of the system. An immediate next step in the work which we carried out would be to increase the size of the barriers still further, and determine the possibility of the pinning number becoming saturated. Beyond this, the minimum separation could be altered so that eventually the system consists of small isolated "pools" of non-zero density.

Inspired by the experimental works of Andronikashvili *et al.* [365] who measured the period of closely stacked disks in rotating Helium, an interesting system to simulate would be that of a disordered point-like potential which oscillates linearly in a superfluid which is initially at rest. This would be similar to the experimental set up of Inouye [60]. Further, perhaps the most experimentally realisable geometry in which to operate would be that of a toroidal trap which has point-like potentials randomly distributed throughout.

In classical fluids, Darcy's Law [412] relates the discharge of a fluid which flows through a porous medium to the difference in pressure before and after the porous medium. With a subtle adaptation to the point-like disorder potential which we have studied, it may be relatively straight-forward to realise an effective superfluid version of Darcy's law. Since the law for classical fluids can be related to Ohm's law, this could be an exciting stepping-stone to relating superfluid flows in disordered potentials to the emerging field of atomtronics [413].

11.2.3 Extended Point Vortex Models

The work carried out in Chapter 10 is carried out in the limit of weak, slowly varying, disordered potentials. This is due to the fact that the Thomas-Fermi approximation fails as the potentials vary quickly. Future work should proceed by using a background density field which is calibrated by numerically finding the ground state of the system using the GPE. It is also unclear whether, if the potential is strong enough that there are regions of zero background density, image vortices would be needed in the model. Resolving these two issues will immediately lead to a huge parameter space of disordered potentials which may be explored in a numerically inexpensive way.

Recently, it has been possible to access a huge number of point vortices in simulations by re-casting the point vortex model as a hydrodynamical equation for vortex fluid density [381, 384, 411]. This is obtained by considering a large number of well separated vortices as a fluid in their own right. As an added flourish, it may be possible to derive a similar hydrodynamical equation for a dissipative point vortex model which accounts for fluctuations in the background density of the superfluid.

Appendix A

Derivation of Mean–Field Results

A.1 Derivation of the GPE

We begin with the second quantised Hamiltonian for Bose field operators is

$$\begin{aligned}\hat{\mathcal{H}}(t) &= \int d^3\mathbf{r}\hat{\Psi}^\dagger(\mathbf{r},t)\,\hat{\mathcal{H}}_{\text{s.p.}}(\mathbf{r},t)\,\hat{\Psi}(\mathbf{r},t) \\ &+ \frac{1}{2}\int d^3\mathbf{r}\int d^3\mathbf{r}'\hat{\Psi}^\dagger(\mathbf{r},t)\,\hat{\Psi}^\dagger(\mathbf{r}',t)\,V_{\text{int}}(\mathbf{r},\mathbf{r}')\,\hat{\Psi}(\mathbf{r}',t)\,\hat{\Psi}(\mathbf{r},t), \qquad \text{(A.1)}\end{aligned}$$

where the operator $\hat{\Psi}(\mathbf{r},t)$ annihilates a boson located at $\mathbf{r}$ at time t. The first integral in Eqn. (A.1) corresponds to a non-interacting ideal gas, whose single-particle Hamiltonian is

$$\hat{\mathcal{H}}_{\text{s.p.}}(\mathbf{r},t) = -\frac{\hbar^2}{2m}\nabla^2 + V_{\text{ext}}(\mathbf{r},t), \qquad \text{(A.2)}$$

for some external (trapping) potential, V_{ext}. We assume that the gas is sufficiently dilute that 3-body collisions are rare, so V_{int} encapsulates the interactions between two bosons (the two-body interaction potential).

The Bose field operators obey the equal time commutation relations

$$\left[\hat{\Psi}(\mathbf{r},t),\hat{\Psi}^\dagger(\mathbf{r}',t)\right] = \delta(\mathbf{r}-\mathbf{r}'), \qquad \text{(A.3)}$$

$$\left[\hat{\Psi}(\mathbf{r},t),\hat{\Psi}(\mathbf{r}',t)\right] = 0, \qquad \text{(A.4)}$$

$$\left[\hat{\Psi}^\dagger(\mathbf{r},t),\hat{\Psi}^\dagger(\mathbf{r}',t)\right] = 0, \qquad \text{(A.5)}$$

The Heisenberg equation of motion for this system is

$$i\hbar\frac{\partial}{\partial t}\hat{\Psi}(\mathbf{r},t) = \left[\hat{\Psi}(\mathbf{r},t),\hat{\mathcal{H}}(t)\right], \qquad \text{(A.6)}$$

and we can expand the right hand side of this equation to get

$$\begin{aligned} i\hbar\frac{\partial}{\partial t}\hat{\Psi}\left(\mathbf{r},t\right) &= \hat{\Psi}\left(\mathbf{r},t\right)\hat{\mathcal{H}}(t) - \hat{\mathcal{H}}(t)\hat{\Psi}\left(\mathbf{r},t\right) \\ &= \hat{\Psi}\left(\mathbf{r},t\right)\hat{\mathcal{H}}(t) - \int d^3\mathbf{r}'\hat{\Psi}^\dagger\left(\mathbf{r}',t\right)\hat{\mathcal{H}}_{\text{s.p.}}\left(\mathbf{r}',t\right)\hat{\Psi}\left(\mathbf{r}',t\right)\hat{\Psi}\left(\mathbf{r},t\right) \\ &- \frac{1}{2}\int d^3\mathbf{r}'\int d^3\mathbf{r}''\hat{\Psi}^\dagger\left(\mathbf{r}',t\right)\hat{\Psi}^\dagger\left(\mathbf{r}'',t\right)V_{\text{int}}\left(\mathbf{r}',\mathbf{r}''\right)\hat{\Psi}\left(\mathbf{r}'',t\right)\hat{\Psi}\left(\mathbf{r}',t\right)\hat{\Psi}\left(\mathbf{r},t\right). \end{aligned}$$

Using Eqn. (A.4), one moves the $\hat{\Psi}\left(\mathbf{r},t\right)$ term towards the left of both integrands resulting in

$$\begin{aligned} i\hbar\frac{\partial}{\partial t}\hat{\Psi}\left(\mathbf{r},t\right) &= \hat{\Psi}\left(\mathbf{r},t\right)\hat{\mathcal{H}}(t) - \int d^3\mathbf{r}'\hat{\Psi}^\dagger\left(\mathbf{r}',t\right)\hat{\Psi}\left(\mathbf{r},t\right)\hat{\mathcal{H}}_{\text{s.p.}}\left(\mathbf{r}',t\right)\hat{\Psi}\left(\mathbf{r}',t\right) \\ &- \frac{1}{2}\int d^3\mathbf{r}'\int d^3\mathbf{r}''\hat{\Psi}^\dagger\left(\mathbf{r}',t\right)\hat{\Psi}^\dagger\left(\mathbf{r}'',t\right)\hat{\Psi}\left(\mathbf{r},t\right)V_{\text{int}}\left(\mathbf{r}',\mathbf{r}''\right)\hat{\Psi}\left(\mathbf{r}'',t\right)\hat{\Psi}\left(\mathbf{r},t\right). \end{aligned}$$

The commutation relation in Eqn. (A.3) is slightly more complicated, as $\hat{\Psi}^\dagger\left(\mathbf{r}',t\right)\hat{\Psi}(\mathbf{r},t) = \hat{\Psi}(\mathbf{r},t)\hat{\Psi}^\dagger\left(\mathbf{r}',t\right) - \delta\left(\mathbf{r}-\mathbf{r}'\right)$. Applying this to the previous equation, one can rearrange expand both integrands as

$$\begin{aligned} i\hbar\frac{\partial}{\partial t}\hat{\Psi}\left(\mathbf{r},t\right) &= \hat{\Psi}\left(\mathbf{r},t\right)\hat{\mathcal{H}}(\mathbf{r},t) - \int d^3\mathbf{r}'\left[\hat{\Psi}\left(\mathbf{r},t\right)\hat{\Psi}\left(\mathbf{r}',t\right) - \delta\left(\mathbf{r}-\mathbf{r}'\right)\right]\hat{\mathcal{H}}_{\text{s.p.}}\left(\mathbf{r}',t\right)\hat{\Psi}\left(\mathbf{r}',t\right) \\ &- \frac{1}{2}\int d^3\mathbf{r}'\int d^3\mathbf{r}''\hat{\Psi}^\dagger\left(\mathbf{r}'\right)\left[\hat{\Psi}\left(\mathbf{r}\right)\Psi^\dagger\left(\mathbf{r}''\right) - \delta\left(\mathbf{r}-\mathbf{r}''\right)\right]V_{\text{int}}\left(\mathbf{r}',\mathbf{r}''\right)\hat{\Psi}\left(\mathbf{r}''\right)\hat{\Psi}\left(\mathbf{r}'\right), \end{aligned} \tag{A.7}$$

where the t dependence of the operators in the second integrand is implied for brevity. Expanding this and applying the delta functions gives

$$\begin{aligned} i\hbar\frac{\partial}{\partial t}\hat{\Psi}\left(\mathbf{r},t\right) &= \hat{\Psi}\left(\mathbf{r},t\right)\hat{\mathcal{H}}(\mathbf{r},t) - \hat{\Psi}\left(\mathbf{r},t\right)\int d^3\mathbf{r}'\hat{\Psi}\left(\mathbf{r}',t\right)\hat{\mathcal{H}}_{\text{s.p.}}\left(\mathbf{r}',t\right) + \hat{\mathcal{H}}_{\text{s.p.}}\left(\mathbf{r},t\right)\hat{\Psi}\left(\mathbf{r},t\right) \\ &- \frac{1}{2}\int d^3\mathbf{r}'\int d^3\mathbf{r}''\hat{\Psi}^\dagger\left(\mathbf{r}',t\right)\hat{\Psi}\left(\mathbf{r},t\right)\hat{\Psi}^\dagger\left(\mathbf{r}'',t\right)V_{\text{int}}\left(\mathbf{r}',\mathbf{r}''\right)\hat{\Psi}\left(\mathbf{r}'',t\right)\hat{\Psi}\left(\mathbf{r}',t\right), \\ &+ \frac{1}{2}\int d^3\mathbf{r}'\hat{\Psi}^\dagger\left(\mathbf{r}',t\right)V_{\text{int}}\left(\mathbf{r}',\mathbf{r}\right)\hat{\Psi}\left(\mathbf{r},t\right)\hat{\Psi}\left(\mathbf{r}',t\right), \end{aligned}$$

which may then be written as

$$\begin{aligned} i\hbar\frac{\partial}{\partial t}\hat{\Psi}\left(\mathbf{r},t\right) &= \hat{\Psi}\left(\mathbf{r},t\right)\hat{\mathcal{H}}(\mathbf{r},t) - \hat{\Psi}\left(\mathbf{r},t\right)\int d^3\mathbf{r}'\hat{\Psi}\left(\mathbf{r}',t\right)\hat{\mathcal{H}}_{\text{s.p.}}\left(\mathbf{r}',t\right) + \hat{\mathcal{H}}_{\text{s.p.}}\left(\mathbf{r},t\right)\hat{\Psi}\left(\mathbf{r},t\right) \\ &- \frac{1}{2}\int d^3\mathbf{r}'\int d^3\mathbf{r}''\hat{\Psi}(\mathbf{r},t)\hat{\Psi}^\dagger\left(\mathbf{r}',t\right)\hat{\Psi}^\dagger\left(\mathbf{r}'',t\right)V_{\text{int}}\left(\mathbf{r}',\mathbf{r}''\right)\hat{\Psi}\left(\mathbf{r}'',t\right)\hat{\Psi}\left(\mathbf{r}',t\right), \\ &+ \int d^3\mathbf{r}'\hat{\Psi}^\dagger\left(\mathbf{r}',t\right)V_{\text{int}}\left(\mathbf{r}',\mathbf{r}\right)\hat{\Psi}\left(\mathbf{r},t\right)\hat{\Psi}\left(\mathbf{r}',t\right), \end{aligned}$$

Collecting terms, this is

$$i\hbar\frac{\partial}{\partial t}\hat{\Psi}\left(\mathbf{r},t\right) = \hat{\mathcal{H}}\left(\mathbf{r},t\right)\hat{\Psi}\left(\mathbf{r},t\right) + \int d^3\mathbf{r}''\hat{\Psi}^\dagger\left(\mathbf{r}'',t\right)V_{\text{int}}\left(\mathbf{r},\mathbf{r}''\right)\hat{\Psi}\left(\mathbf{r}'',t\right)\hat{\Psi}\left(\mathbf{r},t\right). \tag{A.8}$$

Assuming that the temperature of the gas is sufficiently low, the interactions between particles are low energy s-wave collisions. Mathematically, we can model these interactions as collisions between atoms which are elastic collisions of two hard spheres,

$$V_{\text{int}}\left(\mathbf{r},\mathbf{r}'\right) = g\delta\left(\mathbf{r}-\mathbf{r}'\right), \tag{A.9}$$

where

$$g = \frac{4\pi\hbar^2 N a_s}{m}, \tag{A.10}$$

with a_s, the s-wave scattering length, and m the mass of the atomic species. Since the condensate occupies a single macroscopic state, we may decompose the operator $\hat{\Psi}\left(\mathbf{r},t\right)$ as the sum of a mean field term, $\langle\hat{\Psi}\left(\mathbf{r},t\right)\rangle = \Psi\left(\mathbf{r},t\right)$ and a fluctuation term $\delta\hat{\Psi}\left(\mathbf{r},t\right)$, where $\langle\delta\hat{\Psi}(\mathbf{r},t)\rangle = 0$. This allows us to write

$$\hat{\Psi}\left(\mathbf{r},t\right) = \Psi\left(\mathbf{r},t\right) + \delta\hat{\Psi}\left(\mathbf{r},t\right), \tag{A.11}$$

which we substitute into Eqn. (A.8). Taking the expectation value and ignoring non-linear terms in $\delta\hat{\Psi}$, we have the Gross-Pitaevskii Equation

$$i\hbar\frac{\partial\Psi}{\partial t} = -\frac{\hbar^2}{2m}\nabla^2\Psi + V_{\text{ext}}\left(\mathbf{r},t\right)\Psi + g|\Psi|^2\Psi. \tag{A.12}$$

In order to conserve particle number in the grand canonical system, we must use the modified Hamiltonian $\hat{\mathcal{H}}' = \hat{\mathcal{H}} - \mu\hat{\mathcal{N}}$, where

$$\hat{\mathcal{N}} = \int d^3\mathbf{r} \quad \hat{\Psi}^\dagger(\mathbf{r},t)\hat{\Psi}(\mathbf{r},t) \tag{A.13}$$

is the total number operator, and μ is the chemical potential. It is relatively straightforward to repeat the analysis above with $\hat{\mathcal{H}}'$ and one obtains

$$i\hbar\frac{\partial\Psi}{\partial t} = -\frac{\hbar^2}{2m}\nabla^2\Psi + V_{\text{ext}}\left(\mathbf{r},t\right)\Psi + g|\Psi|^2\Psi - \mu\Psi. \tag{A.14}$$

This is exactly the same as Eqn. (A.12), with the addition of a chemical potential term.

A.2 The GPE in lower dimensions

The energy functional of the 3D GPE given in Eqn. (2.8), and derived in the previous section, is

$$\mathcal{E}\left[\Psi\right] = \frac{\hbar^2}{2m}|\nabla\Psi|^2 + V_{\text{ext}}|\Psi|^2 + \frac{1}{2}g|\Psi|^4 - \mu|\Psi|^2 \tag{A.15}$$

where the total energy is

$$E\left[\Psi\right] = \int \mathcal{E}\left[\Psi\right] d^2\mathbf{r} = E_{\text{kin}} + E_{\text{pot}} + E_{\text{int}} - E_{\text{chem}}. \tag{A.16}$$

Suppose we have a harmonically trapped condensate, whose trapping potential is given by

$$V_{\text{ext}}(\mathbf{r}) = \frac{1}{2}m\omega_\perp^2\left(x^2+y^2\right) + \frac{1}{2}m\omega_\parallel^2 z^2. \tag{A.17}$$

A highly oblate condensate may be formed with trapping frequencies $\omega_\perp \ll \omega_\parallel$. The condensate is quasi-2D when the confinement in the z direction is sufficiently strong to prevent excitations in this direction. Typically, this is given by the condition $\hbar\omega_\parallel \gg \mu$. In the quasi 2D regime, the system may be described by the 3D wavefunction

$$\Psi_{\text{3D}}(\mathbf{r},t) = \pi^{-1/4}l_z^{-1/2}\Psi_\perp\left(x,y,t\right)\exp\left(-\frac{z^2}{2l_z^2}\right), \tag{A.18}$$

where the z dependence is a Gaussian ground state, and l_z is the oscillator length in the z direction, $l_z = \sqrt{\hbar/\left(m\omega_\parallel\right)}$. The numerical factors in Eqn. (A.18) are chosen so that $\int d^2\mathbf{r}\ |\Psi_\perp|^2 = N$. In what follows we will derive a two-dimensional Gross-Pitaevskii equation, by integrating out the z dependence. Throughout this derivation, we will make use of the identities [280]

$$\int_{-\infty}^{\infty} e^{-az^2}\ dz = \sqrt{\frac{\pi}{a}} \tag{A.19}$$

$$\int_{-\infty}^{\infty} z^2\, e^{-az^2}\ dz = \frac{1}{2}\sqrt{\frac{\pi}{a^3}}. \tag{A.20}$$

We begin by calculating

$$|\nabla\Psi_{\text{3D}}|^2 = \pi^{-1/2}l_z^{-1}\left|\nabla_\perp\Psi_\perp\right|^2 e^{-z^2/l_z^2} + \pi^{-1/2}l_z^{-5}\left|\Psi_\perp\right|^2 z^2 e^{-z^2/l_z^2},$$

where $\nabla_\perp = \left(\frac{\partial}{\partial x}, \frac{\partial}{\partial y}\right)$, and substitute this into the kinetic energy term. Thus

$$\begin{aligned} E_{\text{kin}} &= \frac{\hbar^2}{2m}\int d^3\mathbf{r}\ \left|\nabla\Psi_{\text{3D}}\right|^2 \\ &= \frac{\hbar^2}{2m}\int d^2\mathbf{r}\ \left|\nabla_\perp\Psi_\perp\right|^2 \int_{-\infty}^{\infty}\pi^{-1/2}l_z^{-1}e^{-z^2/l_z^2}\ dz \\ &+ \frac{\hbar^2}{2m}\int d^2\mathbf{r}\ \left|\Psi_\perp\right|^2 \int_{-\infty}^{\infty}\pi^{-1/2}l_z^{-5}z^2e^{-z^2/l_z^2}\ dz, \end{aligned}$$

and by applying the identities in Eqn. (A.19) and (A.20), this becomes

$$E_{\rm kin} = \frac{\hbar^2}{2m}\int d^2\mathbf{r}\ \left|\nabla_\perp \Psi_\perp\right|^2 + \frac{\hbar^2}{4ml_z^2}\int d^2\mathbf{r}\ \left|\Psi_\perp\right|^2. \tag{A.21}$$

Next we compute the potential energy term, $E_{\rm pot}$ which is given by

$$\begin{aligned} E_{\rm pot} &= \int d^3\mathbf{r}\ V_{\rm ext}\left|\Psi_{\rm 3D}\right|^2 \\ &= \frac{1}{2}m\omega_\perp^2\int d^2\mathbf{r}\ \left(x^2+y^2\right)\left|\Psi_\perp\right|^2\ \int_{-\infty}^{\infty}\pi^{-1/2}l_z^{-1}e^{-z^2/l_z^2}\,dz \\ &+ \frac{1}{2}m\omega_\parallel^2\int d^2\mathbf{r}\ \left|\Psi_\perp\right|^2\ \int_{-\infty}^{\infty}\pi^{-1/2}l_z^{-1}z^2e^{-z^2/l_z^2}\,dz. \end{aligned}$$

Using the identities in Eqn. (A.19) and (A.20), this is

$$E_{\rm pot} = \int d^2\mathbf{r}\ V_\perp\left|\Psi_\perp\right|^2 + \frac{1}{4}m\omega_\parallel^2 l_z^2\int d^2\mathbf{r}\ \left|\Psi_\perp\right|^2, \tag{A.22}$$

where $V_\perp$ represents the components of the trap in the xy plane. Finally, we compute the interaction term

$$E_{\rm int} = \frac{1}{2}g_{\rm 3D}\int d^3\mathbf{r}\ \left|\Psi_{\rm 3D}\right| = \frac{1}{2}g_{\rm 3D}\int d^2\mathbf{r}\ \left|\Psi_\perp\right|\ \int_{-\infty}^{\infty}\pi^{-1}l_z^{-2}e^{-2z^2/l_z^2}\,dz$$

to be

$$E_{\rm int} = \frac{1}{\sqrt{2\pi}l_z}\frac{1}{2}g_{\rm 3D}\int d^2\mathbf{r}\ \left|\Psi_\perp\right| \tag{A.23}$$

and the chemical potential term to be

$$E_{\rm chem} = \mu\int d^2\mathbf{r}\left|\Psi_\perp\right|^2. \tag{A.24}$$

Combining the results of Eqns. (A.21)–(A.24) we get

$$\begin{aligned} E\left[\Psi\right] &= \frac{\hbar^2}{2m}\int d^2\mathbf{r}\ \left|\nabla_\perp\Psi_\perp\right|^2 + \int d^2\mathbf{r}\ V_\perp\left|\Psi_\perp\right|^2 + \frac{1}{\sqrt{2\pi}l_z}\frac{1}{2}g\int d^2\mathbf{r}\ \left|\Psi_\perp\right| \\ &- \left(\mu - \frac{\hbar^2}{4ml_z^2} - \frac{1}{4}m\omega_\parallel^2 l_z^2\right)\int d^2\mathbf{r}\left|\Psi_\perp\right|^2 \end{aligned}$$

which is exactly the same functional form as in Eqn. (A.16). All that remains is to identify the new constants,

$$g_{\rm 2D} = \frac{g_{\rm 3D}}{\sqrt{2\pi}l_z} = \frac{\sqrt{8\pi}\hbar^2 a_s}{ml_z}, \tag{A.25}$$

and

$$\mu_{\rm 2D} = \mu_{\rm 3D} - \frac{1}{2}\hbar\omega_\parallel, \tag{A.26}$$

which is recovered by using the definition of the harmonic oscillator length.

We note that it is possible to further constrain the system to a quasi 1D "cigar". To

do so follows similar arguments to the derivation above, integrating over the y dimension, and one finds the one-dimensional interaction parameter and one-dimensional chemical potential. The results of this calculation are omitted from this thesis.

A.3 Derivation of the Hydrodynamic Equations of Motion

In this section we derive Eqns. (2.27) and (2.23), presented in Sec. 2.3.

The Hydrodynamic equations of motion can be derived form the GPE by substituting the Madelung transform,

$$\Psi(\mathbf{r},t) = \sqrt{\rho(\mathbf{r},t)}\exp\left[i\theta(\mathbf{r},t)\right]$$

into the Gross–Pitaevskii Equation, Eqn. (2.8), which yields (cancelling $e^{i\theta}$ terms)

$$\begin{aligned} i\hbar\left(\frac{1}{2\sqrt{\rho}}\frac{\partial\rho}{\partial t} + i\sqrt{\rho}\frac{\partial\theta}{\partial t}\right) &= -\frac{\hbar^2}{2m}\left[\nabla^2\sqrt{\rho} + 2i\left(\nabla\sqrt{\rho}\right)\cdot\left(\nabla\theta\right) - \sqrt{\rho}\left(\nabla\theta\right)\cdot\left(\nabla\theta\right) + i\sqrt{\rho}\nabla^2\theta\right] \\ &+ V_{\text{ext}}\sqrt{\rho} + g\rho^{3/2}. \end{aligned} \tag{A.27}$$

We can then separate this equation into real,

$$-\hbar\sqrt{\rho}\frac{\partial\theta}{\partial t} = -\frac{\hbar^2}{2m}\left[\nabla^2\sqrt{\rho} - \sqrt{\rho}\left(\nabla\theta\right)\cdot\left(\nabla\theta\right)\right] + V_{\text{ext}}\sqrt{\rho} + g\rho^{3/2}, \tag{A.28}$$

and imaginary,

$$\frac{\hbar}{2\sqrt{\rho}}\frac{\partial\rho}{\partial t} = -\frac{\hbar^2}{2m}\left[2\left(\nabla\sqrt{\rho}\right)\cdot\left(\nabla\theta\right) + \sqrt{\rho}\nabla^2\theta\right] \tag{A.29}$$

parts. If we consider Eqn. (A.28), we can write

$$\frac{\partial}{\partial t}\left(\frac{\hbar}{m}\theta\right) = \frac{\hbar^2}{2m^2}\frac{1}{\sqrt{\rho}}\nabla^2\sqrt{\rho} - \frac{1}{2}\left(\frac{\hbar}{m}\nabla\theta\right)\cdot\left(\frac{\hbar}{m}\nabla\theta\right) - \frac{1}{m}V_{\text{ext}} - \frac{g}{m}\rho. \tag{A.30}$$

Recalling the fact that $\mathbf{v} = (\hbar/m)\nabla\theta$, this can be written

$$\frac{\partial\mathbf{v}}{\partial t} = \nabla\left[\frac{\hbar^2}{2m^2}\left(\frac{1}{\sqrt{\rho}}\nabla^2\sqrt{\rho}\right) - \frac{1}{2}\mathbf{v}\cdot\mathbf{v} - \frac{1}{m}V_{\text{ext}} - \frac{g}{m}\rho\right]. \tag{A.31}$$

Rearranging terms, and noticing that $\nabla\left(\mathbf{v}\cdot\mathbf{v}\right) = 2\left(\mathbf{v}\cdot\nabla\right)\mathbf{v}$ and $2\rho\nabla\rho = \nabla\rho^2$, we arrive at

$$\rho\left[\frac{\partial\mathbf{v}}{\partial t} + \left(\mathbf{v}\cdot\nabla\right)\mathbf{v}\right] = -\frac{1}{2}\frac{g}{m}\nabla\rho^2 + \frac{\hbar^2}{2m^2}\rho\nabla\left(\frac{1}{\sqrt{\rho}}\nabla^2\sqrt{\rho}\right) - \frac{\rho}{m}\nabla V_{\text{ext}}, \tag{A.32}$$

which is similar in form to the Euler equation for an inviscid fluid. We introduce $P =$

$g\rho^2/(2m)$ which is a pressure term, and the quantum pressure term

$$\Pi = \frac{\hbar^2}{2m^2}\frac{1}{\sqrt{\rho}}\nabla^2\sqrt{\rho} \tag{A.33}$$

in which case the equation reads

$$\frac{\partial \mathbf{v}}{\partial t} + (\mathbf{v}\cdot\nabla)\,\mathbf{v} = -\frac{1}{\rho}\nabla P + \nabla\Pi - \frac{1}{m}\nabla V_{\text{ext}}. \tag{A.34}$$

On the other hand, we may write Eqn. (A.29) as

$$\frac{1}{\sqrt{\rho}}\frac{\partial \rho}{\partial t} + 2\left(\nabla\sqrt{\rho}\right)\cdot\left(\frac{\hbar}{m}\nabla\theta\right) + \sqrt{\rho}\nabla\cdot\left(\frac{\hbar}{m}\nabla\theta\right) = 0, \tag{A.35}$$

which, on using $(\hbar/m)\nabla\theta = \mathbf{v}$, is

$$\frac{1}{\sqrt{\rho}}\frac{\partial \rho}{\partial t} + 2\left(\nabla\sqrt{\rho}\right)\cdot\mathbf{v} + \sqrt{\rho}\nabla\cdot\mathbf{v} = 0. \tag{A.36}$$

Using the fact that $\nabla\sqrt{\rho} = (\nabla\rho)\,/\left(2\sqrt{\rho}\right)$, this can be written as

$$\frac{\partial \rho}{\partial t} + (\nabla\rho)\cdot\mathbf{v} + \rho\nabla\cdot\mathbf{v} = 0, \tag{A.37}$$

where the second and third terms may be combined to get the continuity equation,

$$\frac{\partial \rho}{\partial t} + \nabla\cdot(\rho\mathbf{v}) = 0. \tag{A.38}$$

A.4 Identifying the Condensate Fraction

In this section we detail the means by which we compute the condensate fraction of a system[1]. This derivation is based on the criterion of Penrose and Onsager [15], which is cast into the c-field methodology by Blakie *et al.* [133].

According to the criterion of Penrose and Onsager [15], the condensate number of a system is identified as the largest eigenvalue of the one-body density matrix. We write the one-body density matrix as

$$G^{1B}(\mathbf{r},\mathbf{r}') = \langle\Psi^*(\mathbf{r})\,\Psi(\mathbf{r}')\rangle_{\mathcal{T}}, \tag{A.39}$$

where $\langle\cdot\rangle_{\mathcal{T}}$ indicates short time averaging. Following the procedure of Blakie *et al.* [133], it is more efficient to compute G^{1B} in the spectral basis in this problem. Suppose the

[1]Note that an outline version of this code, based on the procedure in Ref. [133], was provided by Andrew Groszek.

wavefunction Ψ can be expanded as

$$\Psi(\mathbf{r}) = \sum_{\alpha} c_\alpha \phi_\alpha(\mathbf{r}),$$

then we write

$$G^{1B}_{\alpha\beta} = \langle c^*_\alpha c_\beta \rangle. \tag{A.40}$$

This means that, in spectral space the condensate mode $\tilde{\psi}_0$ is given by

$$\sum_{\beta} G^{1B}_{\alpha\beta} \tilde{\psi}_{0\beta} = n_0 \tilde{\psi}_0 \tag{A.41}$$

where α, β index the modes within the c-field region.

In Part III, we use a Fourier spectral basis. This means the c_α are readily computed by taking the Fast Fourier Transform (FFT) of the wavefunction, $\mathcal{F}[\Psi]$, and α indexes the modes in the projection region, given by $|\mathbf{k}| < k_{\text{cut}}$. In order to numerically implement the result in Eqn. (A.41), we do the following: Firstly, we compute the FFT of the wavefunction, which is $\tilde{\Psi} = \mathcal{F}[\Psi]$. We repeat this for the samples of the wavefunction in some window of time, so that we can use short time averaging. This allows us to compute $G^{1B}_{\alpha\beta}$ in Eqn. (A.40). We then compute the eigenvalues and eigenvectors of $G^{1B}_{\alpha\beta}$, using the `eigs` function in Matlab. By the Penrose and Onsager criterion, the largest eigenvalue is the condensate number; as the background of the wavefunction is normalised to be one, we can calculate the condensate fraction n_0. The condensate mode in Fourier space is the eigenvector which corresponds to this eigenvalue, $\tilde{\psi}_0$. From here it is relatively straight forward to compute the non-condensate fraction, $n_{\text{nc}} = 1 - n_0$, and the non-condensate mode (in Fourier space), which is the sum of the remaining eigenvectors. All that then remains is to take inverse FFTs of the condensate and non-condensate modes.

A.5 Identifying the Superfluid Fraction

It is possible to extract the superfluid fraction of a system using the current–current correlations of the wavefunction. This result is derived in Refs. [301, 319], and may also be derived using the theory of hydrodynamics in a superfluid [111, 320]. Throughout this section we will assume that we are working in a box B containing both superfluid and normal fluid fractions, with dimensions $L_x \times L_y$.

Suppose that we are able to accelerate the walls until they are moving with a small velocity $\mathbf{v}$, which without loss of generality we take to be in the $\hat{\mathbf{x}}$ direction. If the box is filled with a normal fluid, which is subject to viscous effects between itself and the wall, the momentum density at equilibrium will be

$$\langle \hat{\mathbf{p}} \rangle_{\mathbf{v}} = n\mathbf{v} \tag{A.42}$$

where n is the number density of the fluid. We assume that the fraction of fluid in the box which is superfluid remains stationary in the laboratory frame, even at equilibrium; this is due to the fact that the velocity $\mathbf{v}$ is not enough to force a fluid which has no viscosity to flow. According to Landau's two fluid model [50], we have $n = \rho_s + \rho_n$. As described in Chapter 8, ρ_n is the normal fluid density, ρ_s is the superfluid density, and by our choice of dimensionless variables ρ_s (equivalently ρ_n) is both the superfluid (normal fluid) *density* and the superfluid (normal fluid) *fraction*. As a result, the observed momentum density of the fluid at equilibrium will be

$$\rho_n \mathbf{v} \leq (\rho_n + \rho_s)\,\mathbf{v} = n\mathbf{v}. \tag{A.43}$$

We must now consider two frames of reference: in the *laboratory* frame, the walls move with velocity $\mathbf{v}$ in the $\hat{\mathbf{x}}$ direction and the Hamiltonian of the system is $\mathcal{H}_L$; in the *wall* frame (the frame of reference which is moving with the walls), the walls are at rest and the Hamiltonian of the system is $\mathcal{H}_{\mathbf{v}}$. These Hamiltonians are related by a Galilean transformation, so that

$$\mathcal{H}_{\mathbf{v}} = \mathcal{H}_L - \mathbf{v}\cdot\hat{\mathbf{P}} + \frac{1}{2}mN|\mathbf{v}|^2, \tag{A.44}$$

where the total momentum is given by

$$\hat{\mathbf{P}} = \int_0^{L_y} dy \int_0^{L_x} dx\ \hat{\mathbf{p}}(\mathbf{r}), \tag{A.45}$$

and $\hat{\mathbf{p}}(\mathbf{r})$ is the momentum at point $\mathbf{r}$.

If we assume that the fluid is in thermal equilibrium with the walls, then we may employ a standard result from Statistical Mechanics to write down the expectation value of the momentum density (see, for example, [288]). The expectation value of the momentum density reads

$$\langle\hat{\mathbf{p}}(\mathbf{r})\rangle_{\mathbf{v}} = \frac{\mathrm{Tr}\left[\exp\left(-\beta\mathcal{H}_L + \beta\hat{\mathbf{P}}\cdot\mathbf{v} - \frac{1}{2}\beta m|\mathbf{v}|^2N + \beta\mu N\right)\hat{\mathbf{p}}(\mathbf{r})\right]}{\mathrm{Tr}\left[\exp\left(-\beta\mathcal{H}_L + \beta\hat{\mathbf{P}}\cdot\mathbf{v} - \frac{1}{2}\beta m|\mathbf{v}|^2N + \beta\mu N\right)\right]}, \tag{A.46}$$

which we can expand this equation to terms which are linear in $\mathbf{v}$. Beginning by writing

$$\exp\left(\hat{H}\right) = \exp\left(-\beta\mathcal{H}_L - \frac{1}{2}\beta m|\mathbf{v}|^2N + \beta\mu N\right) \tag{A.47}$$

we can write the expectation value as

$$\langle\hat{\mathbf{p}}(\mathbf{r})\rangle_{\mathbf{v}} = \frac{\mathrm{Tr}\left[\exp\left(\hat{H}\right)\exp\left(\beta\hat{\mathbf{P}}\cdot\mathbf{v}\right)\hat{\mathbf{p}}(\mathbf{r})\right]}{\mathrm{Tr}\left[\exp\left(\hat{H}\right)\exp\left(\beta\hat{\mathbf{P}}\cdot\mathbf{v}\right)\right]} \approx \frac{\mathrm{Tr}\left[\exp\left(\hat{H}\right)\left(1+\beta\hat{\mathbf{P}}\cdot\mathbf{v}\right)\hat{\mathbf{p}}(\mathbf{r})\right]}{\mathrm{Tr}\left[\exp\left(\hat{H}\right)\left(1+\beta\hat{\mathbf{P}}\cdot\mathbf{v}\right)\right]} \tag{A.48}$$

where the approximation comes from using the first two terms of the Maclaurin series of

the exponential function. Using the linearity of the trace of a matrix, we can perform on a binomial expansion on the denominator of the expectation to get

$$\begin{aligned}\left\langle \hat{\mathbf{p}}(\mathbf{r})\right\rangle_{\mathbf{v}} &= \left\{ \frac{\mathrm{Tr}\left[\exp\left(\hat{H}\right)\hat{\mathbf{p}}(\mathbf{r})\right]}{\mathrm{Tr}\left[\exp\left(\hat{H}\right)\right]} + \beta \frac{\mathrm{Tr}\left[\exp\left(\hat{H}\right)\left(\hat{\mathbf{P}}\cdot\mathbf{v}\right)\hat{\mathbf{p}}(\mathbf{r})\right]}{\mathrm{Tr}\left[\exp\left(\hat{H}\right)\right]} \right\} \\ &\times \left\{ 1 - \beta \frac{\mathrm{Tr}\left[\exp\left(\hat{H}\right)\hat{\mathbf{P}}\cdot\mathbf{v}\right]}{\mathrm{Tr}\left[\exp\left(\hat{H}\right)\right]} + \mathcal{O}\left(\mathbf{v}^2\right) \right\}, \end{aligned} \tag{A.49}$$

which is

$$\left\langle \hat{\mathbf{p}}(\mathbf{r})\right\rangle_{\mathbf{v}} = \left\langle \hat{\mathbf{p}}(\mathbf{r})\right\rangle + \beta\left\langle \left(\hat{\mathbf{P}}\cdot\mathbf{v}\right)\hat{\mathbf{p}}(\mathbf{r})\right\rangle - \beta\left\langle \hat{\mathbf{p}}(\mathbf{r})\right\rangle\left\langle \hat{\mathbf{P}}\cdot\mathbf{v}\right\rangle + \mathcal{O}\left(\mathbf{v}^2\right). \tag{A.50}$$

The expectation values on the right hand side of Eqn. (A.50) are taken at equilibrium in the frame where the walls are at rest.

We now make the assumption that the infinite system is homogeneous, which means that

$$\left\langle \hat{\mathbf{p}}(\mathbf{x})\hat{\mathbf{p}}\left(\mathbf{x}'\right)\right\rangle_{\infty} = \left\langle \hat{\mathbf{p}}(\mathbf{x}+\mathbf{r})\hat{\mathbf{p}}\left(\mathbf{x}'+\mathbf{r}\right)\right\rangle_{\infty} \tag{A.51}$$

$$\left\langle \hat{\mathbf{p}}(\mathbf{x})\right\rangle_{\infty}\left\langle \hat{\mathbf{p}}\left(\mathbf{x}'\right)\right\rangle_{\infty} = \left\langle \hat{\mathbf{p}}(\mathbf{x}+\mathbf{r})\right\rangle_{\infty}\left\langle \hat{\mathbf{p}}\left(\mathbf{x}'+\mathbf{r}\right)\right\rangle_{\infty} \tag{A.52}$$

for all $\mathbf{r}$, where the subscript on the angle brackets suggests that the average is taken over an infinite system. Setting $\mathbf{r} = -\mathbf{x}$ we recover

$$\begin{aligned}\left\langle \hat{\mathbf{p}}(\mathbf{x})\hat{\mathbf{p}}\left(\mathbf{x}'\right)\right\rangle_{\infty} &= \left\langle \hat{\mathbf{p}}(0)\hat{\mathbf{p}}\left(\mathbf{x}'-\mathbf{x}\right)\right\rangle_{\infty} \\ &= \frac{1}{(2\pi)^2}\int d^2\mathbf{k} e^{i\mathbf{k}\cdot\left(\mathbf{x}'-\mathbf{x}\right)}\int d^2\mathbf{r} e^{-i\mathbf{k}\cdot\mathbf{r}}\left\langle \hat{\mathbf{p}}(0)\hat{\mathbf{p}}(\mathbf{r})\right\rangle_{\infty}, \end{aligned} \tag{A.53}$$

and

$$\begin{aligned}\left\langle \hat{\mathbf{p}}(\mathbf{x})\right\rangle_{\infty}\left\langle \hat{\mathbf{p}}\left(\mathbf{x}'\right)\right\rangle_{\infty} &= \left\langle \hat{\mathbf{p}}(0)\right\rangle_{\infty}\left\langle \hat{\mathbf{p}}\left(\mathbf{x}'-\mathbf{x}\right)\right\rangle_{\infty} \\ &= \frac{1}{(2\pi)^2}\int d^2\mathbf{k} e^{i\mathbf{k}\cdot\left(\mathbf{x}'-\mathbf{x}\right)}\int d^2\mathbf{r} e^{-i\mathbf{k}\cdot\mathbf{r}}\left\langle \hat{\mathbf{p}}(0)\right\rangle_{\infty}\left\langle \hat{\mathbf{p}}(\mathbf{r})\right\rangle_{\infty}, \end{aligned} \tag{A.54}$$

where in each case the second equality is found by Fourier transforming the average, and then inverse Fourier transforming to the relative coordinate $(\mathbf{x}'-\mathbf{x})$.

We now make the approximation that we are in a very large system, so that the expectation values $\left\langle \hat{\mathbf{p}}(\mathbf{x})\hat{\mathbf{p}}\left(\mathbf{x}'\right)\right\rangle \approx \left\langle \hat{\mathbf{p}}(\mathbf{x})\hat{\mathbf{p}}\left(\mathbf{x}'\right)\right\rangle_{\infty}$ and $\left\langle \hat{\mathbf{p}}(\mathbf{x})\right\rangle\left\langle \hat{\mathbf{p}}\left(\mathbf{x}'\right)\right\rangle \approx \left\langle \hat{\mathbf{p}}(\mathbf{x})\right\rangle_{\infty}\left\langle \hat{\mathbf{p}}\left(\mathbf{x}'\right)\right\rangle_{\infty}$. Using the above identities, and considering only terms which are linear in $\mathbf{v}$, this means

that we can write Eqn. (A.50) as

$$\begin{aligned}\langle\hat{\mathbf{p}}(\mathbf{x})\rangle_{\mathbf{v}} &\approx \langle\hat{\mathbf{p}}(\mathbf{x})\rangle_{\infty} \\ &+ \frac{\beta}{(2\pi)^2}\int_B d^2\mathbf{x}'\int d^2\mathbf{k}e^{i\mathbf{k}\cdot(\mathbf{x}'-\mathbf{x})}\int d^2\mathbf{r}e^{-i\mathbf{k}\cdot\mathbf{r}}\langle\hat{\mathbf{p}}(0)\hat{\mathbf{p}}(\mathbf{r})\rangle_{\infty}\cdot\mathbf{v} \\ &- \frac{\beta}{(2\pi)^2}\int_B d^2\mathbf{x}'\int d^2\mathbf{k}e^{i\mathbf{k}\cdot(\mathbf{x}'-\mathbf{x})}\int d^2\mathbf{r}e^{-i\mathbf{k}\cdot\mathbf{r}}\langle\hat{\mathbf{p}}(0)\rangle_{\infty}\langle\hat{\mathbf{p}}(\mathbf{r})\rangle_{\infty}\cdot\mathbf{v},\end{aligned} \tag{A.55}$$

where the integrals are carried out over the box, B.

We now introduce the nascent delta function, which is defined as

$$\Delta(\mathbf{k},B) = \frac{1}{(2\pi)^2}\int_B d^2\mathbf{x}'e^{i\mathbf{k}\cdot\mathbf{x}'} \tag{A.56}$$

where, again, the integral on the right hand side is performed over the box B with dimensions $L_x \times L_y$. We introduce this function because it has the properties $\Delta(\mathbf{k},B) \to \delta(\mathbf{k},0)$ as $B\to\infty$, and it can be factorised so that $\Delta(\mathbf{k},B) = \Delta(k_x,L_x)\Delta(k_y,L_y)$ where each of the factors $\Delta(k_j,L_j)\to\delta(k_j)$ as $L_j\to\infty$, for $j\in\{x,y\}$.

Since we have assumed that the superfluid fraction remains stationary in the laboratory frame in equilibrium is zero, $\langle\hat{\mathbf{p}}(\mathbf{x})\rangle_{\infty} = 0$. Changing the order of integration in Eqn. (A.55), we write

$$\langle\hat{\mathbf{p}}(\mathbf{x})\rangle_{\mathbf{v}} \approx \beta\int d^2\mathbf{k}\left[\frac{1}{(2\pi)^2}\int_B d^2\mathbf{x}'e^{i\mathbf{k}\cdot\mathbf{x}'}\right]e^{-i\mathbf{k}\cdot\mathbf{x}}\int d^2\mathbf{r}e^{-i\mathbf{k}\cdot\mathbf{r}}\langle\hat{\mathbf{p}}(0)\hat{\mathbf{p}}(\mathbf{r})\rangle_{\infty}\cdot\mathbf{v} \tag{A.57}$$

where the quantities in the square brackets can be identified as nascent delta functions, Enq. (A.56). Inserting this function allows us to write

$$\langle\hat{\mathbf{p}}(\mathbf{x})\rangle_{\mathbf{v}} \approx \beta\int d^2\mathbf{k}\Delta(\mathbf{k},B)\,e^{-i\mathbf{k}\cdot\mathbf{x}}\int d^2\mathbf{r}e^{-i\mathbf{k}\cdot\mathbf{r}}\langle\hat{\mathbf{p}}(0)\hat{\mathbf{p}}(\mathbf{r})\rangle_{\infty}\cdot\mathbf{v}. \tag{A.58}$$

Following Foster *et al.* [301], we now introduce the dyad

$$\chi(\mathbf{k}) = \int d^2\mathbf{r}e^{-i\mathbf{k}\cdot\mathbf{r}}\langle\hat{\mathbf{p}}(0)\hat{\mathbf{p}}(\mathbf{r})\rangle_{\infty}, \tag{A.59}$$

which is essentially a current-current correlation term. We now approximate the finite system with the calculations we have performed above for the infinite system, and along with the dyad in Eqn. (A.59) we recover

$$\langle\hat{\mathbf{p}}(\mathbf{x})\rangle_{\mathbf{u}} = \beta\int d^2\mathbf{k}\Delta(\mathbf{k},B)e^{-i\mathbf{k}\cdot\mathbf{x}}\chi(\mathbf{k})\cdot\mathbf{v}. \tag{A.60}$$

We now introduce an equivalent form to Eqn. (A.59), which is more tractable for the

numerical simulations which we consider in Part III. In the limit of vanishing momentum, we write the current–current correlations of a system with volume V in equilibrium at temperature T as

$$J_{\alpha\beta}(\mathbf{k}) = \left\langle \left\langle \left[\mathcal{F}\left(\boldsymbol{J}\right)\right]_{\alpha} \left[\mathcal{F}\left(\boldsymbol{J}\right)\right]^{*}_{\beta} \right\rangle_{t} \right\rangle_{r} = \left(\rho_s \frac{k_\alpha k_\beta}{k^2} + \rho_n \delta_{\alpha\beta} \right) \frac{k_B T V}{m^2}, \tag{A.61}$$

where $\mathcal{F}\left(\boldsymbol{J}\right)$ indicates that the momentum is calculated using Eq. (2.26) and then transformed into Fourier space [310]. The angled brackets $\langle\langle\cdot\rangle_t\rangle_r$ indicate that the correlations are found by short time averaging and by averaging over the ensemble of initial conditions. The current–current correlations in the system are captured by

$$\chi\left(\mathbf{k}\right) = \begin{bmatrix} J_{xx} & J_{xy} \\ J_{yx} & J_{yy} \end{bmatrix} = \left[\left(\rho_s + \rho_n\right) \hat{\boldsymbol{k}}\hat{\boldsymbol{k}} + \rho_n \left(I - \hat{\boldsymbol{k}}\hat{\boldsymbol{k}} \right) \right] \frac{k_B T V}{m^2} \tag{A.62}$$

where we introduce the dyad

$$\hat{\boldsymbol{k}}\hat{\boldsymbol{k}} = \frac{1}{k^2} \begin{bmatrix} k_x^2 & k_x k_y \\ k_y k_x & k_y^2 \end{bmatrix}, \tag{A.63}$$

and I is the identity. We now introduce transverse, $\chi_t(k)$, and longitudinal, $\chi_l(k)$, functions which are scalars depending only on k so that

$$\chi\left(\mathbf{k}\right) = \chi_l(k) \hat{\boldsymbol{k}}\hat{\boldsymbol{k}} + \chi_t(k) \left(I - \hat{\boldsymbol{k}}\hat{\boldsymbol{k}} \right). \tag{A.64}$$

As suggested by Eqn. (A.64), it is possible to identify the transverse and longitudinal parts of χ since $\chi_l(k) = \hat{\boldsymbol{k}} \cdot \chi(\mathbf{k}) \cdot \hat{\boldsymbol{k}}$ and $\chi_t(k) = \hat{\boldsymbol{k}_\perp} \cdot \chi(\mathbf{k}) \cdot \hat{\boldsymbol{k}_\perp}$, where $\hat{\boldsymbol{k}}$ and $\hat{\boldsymbol{k}_\perp}$ are mutually orthogonal unit vectors. This means that we can write the matrix χ in terms of the dyad as

$$\left(\frac{k_B T V}{m^2} \right)^{-1} \chi(\mathbf{k}) = \frac{1}{k_x^2 + k_y^2} \begin{pmatrix} k_x^2 & k_x k_y \\ k_x k_y & k_y^2 \end{pmatrix} \chi_l(k) + \frac{1}{k_x^2 + k_y^2} \begin{pmatrix} k_y^2 & -k_x k_y \\ -k_x k_y & k_x^2 \end{pmatrix} \chi_t(k). \tag{A.65}$$

The results which we have obtained so far are heavily reliant on the ability to switch between the finite box B with dimensions $L_x \times L_y$, and the infinite system. This is only mathematically robust if we are able to take limits $L_x, L_y \to \infty$, although doing so simultaneously may cause a divergence in Eqn. (A.65). In fact, it is not trivial to take the limits $L_x, L_y \to \infty$, as the order of the limits represent completely different physical situations.

Suppose that we begin by taking the limit $L_x \to \infty$. Physically, this corresponds to making the box infinitely long in the direction in which the walls are moving. In this limit, the superfluid continues to be stationary, while the normal fluid moves with the

walls with velocity $\mathbf{v}$ in the $\hat{\mathbf{x}}$ direction. Mathematically, this is

$$\rho_n \mathbf{v} = \lim_{L_y \to \infty} \left[\lim_{L_x \to \infty} \langle \hat{\mathbf{p}}(\mathbf{r}) \rangle_{\mathbf{v}} \right]. \tag{A.66}$$

Suppose, on the other hand, that we begin by taking the limit $L_y \to \infty$. This corresponds to making the box infinitely long in the direction which is perpendicular to the direction in which the walls are moved; all of the fluid, both normal and super-, is swept along with the walls at with velocity $\mathbf{v}$. Mathematically, this is

$$(\rho_n + \rho_s)\,\mathbf{v} = n\mathbf{v} = \lim_{L_x \to \infty} \left[\lim_{L_y \to \infty} \langle \hat{\mathbf{p}}(\mathbf{r}) \rangle_{\mathbf{v}} \right]. \tag{A.67}$$

We are now in a position to take limits. In doing so we assume that we take $\lim_{k_x \to 0} \chi(\mathbf{k})$ by setting $k_x = 0$ in Eqn. (A.65) and requiring $k_y \neq 0$, and similarly for $\lim_{k_y \to 0} \chi(\mathbf{k})$. Then, using the fact that the nascant delta function implies that

$$\lim_{L_y \to \infty} \lim_{L_x \to \infty} \int d^2\mathbf{k} \Delta(\mathbf{k}, B) e^{-i\mathbf{k}\cdot\mathbf{x}} \chi(\mathbf{k}) = \lim_{k_y \to 0} \lim_{k_x \to 0} \chi(\mathbf{k}), \tag{A.68}$$

we arrive at

$$\rho_n \mathbf{v} = \lim_{k_y \to 0} \lim_{k_x \to 0} \chi(\mathbf{k}) = \begin{pmatrix} 0 & 0 \\ 0 & 1 \end{pmatrix} \lim_{k_y \to 0} \lim_{k_x \to 0} \chi_l(k) + \begin{pmatrix} 1 & 0 \\ 0 & 0 \end{pmatrix} \lim_{k_y \to 0} \lim_{k_x \to 0} \chi_t(k) \tag{A.69}$$

$$(\rho_n + \rho_s)\,\mathbf{v} = \lim_{k_x \to 0} \lim_{k_y \to 0} \chi(\mathbf{k}) = \begin{pmatrix} 1 & 0 \\ 0 & 0 \end{pmatrix} \lim_{k_y \to 0} \lim_{k_x \to 0} \chi_l(k) + \begin{pmatrix} 0 & 0 \\ 0 & 1 \end{pmatrix} \lim_{k_y \to 0} \lim_{k_x \to 0} \chi_t(k). \tag{A.70}$$

Making use of the decomposition in Eqn. (A.64) we find

$$\rho_n = \frac{k_B T V}{m^2} \lim_{k_y \to 0} \lim_{k_x \to 0} \chi_t(k), \tag{A.71}$$

$$\rho_n + \rho_s = \frac{k_B T V}{m^2} \lim_{k_x \to 0} \lim_{k_y \to 0} \chi_l(k). \tag{A.72}$$

At this juncture, we note that χ_l and χ_t are functions depend only on k, so our final result is

$$\rho_n = \frac{\rho_n}{\rho_n + \rho_s} = \frac{\lim_{k \to 0} \chi_t(k)}{\lim_{k \to 0} \chi_l(k)}. \tag{A.73}$$

We are able to evaluate χ at all points in our system, and use the decomposition described above to find χ_l and χ_t, while projecting azimuthally so that the functions depend only on k. Once this has been obtained, we fit each of $\ln[\chi_t(k)]$ and $\ln[\chi_l(k)]$ to a quadratic [301]

$$f(k; a, b, c) = a + bk + ck^2. \tag{A.74}$$

As our simulations are computed on a square grid, the density of points increases with k; to account for this in our curve fitting procedure, we set the uncertainty to be proportional to k.

Finding the normal fluid density corresponds to taking the limit as $k \to 0$ of the transverse component of χ, while the same limit of the longitudinal component of χ gives the sum of the superfluid and normal fluid densities. Taking the limit as $k \to 0$ for the parameters fitted to Eqn. (A.74) allows us to calculate the normal fluid fraction as

$$\rho_n = \frac{\lim_{k\to 0} \chi_t(k)}{\lim_{k\to 0} \chi_l(k)}, \tag{A.75}$$

and $\rho_s = 1 - \rho_n$. This allows us to relate the superfluid ad normal fluid fractions to correlations from our simulations, in a similar manner to the condensate and non-condensate fractions which are determined using G^{1B}.

A.5.1 Decomposing the Momentum of the Wavefunction

A second, "rougher" approximation to the superfluid fraction may be calculated by decomposing the momentum of the wavefunction. The momentum Ψ can be calculated using the relationship in Eqn. (2.26),

$$\mathbf{J} = \frac{\hbar}{2mi} \left(\Psi^* \nabla \Psi - \Psi \nabla \Psi^* \right).$$

Using Landau's two–fluid model [50] we may assume that the wavefunction comprises of a superfluid component, which flows without energy loss, and a normal fluid component, which is subject to viscous effects. In this framework, the superfluid component has velocity $\mathbf{v}_s$, the normal fluid component has velocity $\mathbf{v}_n$, and we may write

$$\boldsymbol{J} = \rho_s \mathbf{v}_s + \rho_n \mathbf{v}_n, \tag{A.76}$$

where ρ_s and ρ_n are the superfluid and normal fluid fractions respectively. We now assume that the normal fluid moves with the barriers [414], so that in the barrier frame of reference $\mathbf{v}_n = 0$ and $\boldsymbol{J} = \rho_s \mathbf{v}_s$. Since the superfluid velocity is locked to the condensate velocity [351, 352], it is then relatively straight forward to calculate the average momentum of the wavefunction $\boldsymbol{J}$, calculate the velocity of the condensate mode, $\mathbf{v}_0$, as described in Eqn. (8.5), and extract an estimate for ρ_s.

Appendix B

The GPE in a Rotating Frame of Reference

B.1 Eigenfunctions and Eigenenergies of the One–Body Hamiltonian

Here we show that the basis functions given in Eqn. (4.18) are the correct eigenfunctions of the single particle Hamiltonian.

The one-body Hamiltonian is given in dimensionless form in Eqn. (4.10) as

$$H_\Omega = -\frac{1}{2}\nabla^2 + i\Gamma^2 x\frac{\partial}{\partial y} + \frac{1}{2}\Gamma^4 x^2,$$

and we claim that the eigenfunctions take the form

$$\phi_{n,k} = \sqrt{a\Gamma}\sum_{p=-\infty}^{\infty}\chi_n\left[\Gamma a\left(\frac{k}{N_\mathrm{v}}+p\right)-\Gamma x\right]\exp\left[i\Gamma^2 a\left(\frac{k}{N_\mathrm{v}}+p\right)y\right],$$

where the Hermite functions are given by

$$\chi_n(x) = \frac{1}{\sqrt{2^n n!\sqrt{\pi}}}H_n(x)\exp\left(-\frac{1}{2}x^2\right).$$

For the sake of compactness, we set

$$A_n = \frac{\sqrt{a\Gamma}}{\sqrt{2^n n!\sqrt{\pi}}}, \qquad \square = \frac{k}{N_\mathrm{v}}+p, \tag{B.1}$$

so that

$$\phi_{n,k} = A_n\sum_p H_n\left(\Gamma a\square - \Gamma x\right)\exp\left[-\frac{1}{2}\left(\Gamma a\square-\Gamma x\right)^2\right]\exp\left(i\Gamma^2 a\square y\right). \tag{B.2}$$

Then, using the relationship

$$\frac{d}{dx}H_n(x) = 2nH_{n-1}(x), \tag{B.3}$$

we can calculate

$$\begin{aligned}
\frac{\partial\phi_{n,k}}{\partial y} &= A_n\sum_p i\Gamma^2 a\Box H_n\left(\Gamma a\Box-\Gamma x\right)\exp\left[-\frac{1}{2}\left(\Gamma a\Box-\Gamma x\right)^2\right]\exp\left(i\Gamma^2 a\Box y\right),\\
\frac{\partial^2\phi_{n,k}}{\partial y^2} &= -A_n\sum_p \Gamma^4 a^2\Box^2 H_n\left(\Gamma a\Box-\Gamma x\right)\exp\left[-\frac{1}{2}\left(\Gamma a\Box-\Gamma x\right)^2\right]\exp\left(i\Gamma^2 a\Box y\right),
\end{aligned} \tag{B.4}$$

along with

$$\begin{aligned}
\frac{\partial\phi_{n,k}}{\partial x} &= A_n\sum_p \exp\left[-\frac{1}{2}\left(\Gamma a\Box-\Gamma x\right)^2\right]\exp\left(i\Gamma^2 a\Box y\right)\\
&\qquad\times\left[\Gamma\left(\Gamma a\Box-\Gamma x\right)H_n\left(\Gamma a\Box-\Gamma x\right)-2n\Gamma H_{n-1}\left(\Gamma a\Box-\Gamma x\right)\right],
\end{aligned} \tag{B.5}$$

and

$$\begin{aligned}
\frac{\partial^2\phi_{n,k}}{\partial x^2} &= A_n\sum_p \exp\left[-\frac{1}{2}\left(\Gamma a\Box-\Gamma x\right)^2\right]\exp\left(i\Gamma^2 a\Box y\right)\\
&\quad\times\ \Gamma^2\Big[4n(n-1)H_{n-2}\left(\Gamma a\Box-\Gamma x\right)+2n\left(\Gamma a\Box-\Gamma x\right)H_{n-1}\left(\Gamma a\Box-\Gamma x\right)\\
&\qquad\qquad+\left[\left(\Gamma a\Box-\Gamma x\right)^2-1\right]H_n\left(\Gamma a\Box-\Gamma x\right)\Big].
\end{aligned} \tag{B.6}$$

From here we can substitute Eqn. (4.18) and its derivatives into Eqn. (4.10) to get

$$\begin{aligned} H_\Omega \phi_{n,k} &= A_n \sum_p \exp\left[-\frac{1}{2}\left(\Gamma a\Box - \Gamma x\right)^2\right] \exp\left(i\Gamma^2 a\Box y\right) \\ &\times \left[\left[\frac{1}{2}\Gamma^2 - \frac{1}{2}\Gamma^2\left(\Gamma a\Box - \Gamma x\right)^2 + \frac{1}{2}\Gamma^4 a^2\Box^2 - x\Gamma^4 a\Box + \frac{1}{2}\Gamma^4 x^2\right] H_n\left(\Gamma a\Box - \Gamma x\right)\right. \\ &\qquad \left. + 2n\Gamma^2\left(\Gamma a\Box - \Gamma x\right) H_{n-1}\left(\Gamma a\Box - \Gamma x\right) - 2n(n-1) H_{n-2}\left(\Gamma a\Box - \Gamma x\right)\right], \\ &= A_n \sum_p \exp\left[-\frac{1}{2}\left(\Gamma a\Box - \Gamma x\right)^2\right] \exp\left(i\Gamma^2 a\Box y\right) \left[\frac{1}{2}\Gamma^2 H_n\left(\Gamma a\Box - \Gamma x\right)\right. \\ &\qquad \left. + 2n\Gamma^2\left(\Gamma a\Box - \Gamma x\right) H_{n-1}\left(\Gamma a\Box - \Gamma x\right) - 2n(n-1) H_{n-2}\left(\Gamma a\Box - \Gamma x\right)\right]. \end{aligned} \tag{B.7}$$

We must now make use of the recurrence relation for Hermite polynomials,

$$H_n(x) = 2xH_{n-1}(x) - 2(n-1)H_{n-2}(x). \tag{B.8}$$

The result is

$$H_\Omega \phi_{n,k} = \frac{1}{2}\Gamma^2\left(2n+1\right) A_n \sum_p H_n\left(\Gamma a\Box - \Gamma x\right) \exp\left[-\frac{1}{2}\left(\Gamma a\Box - \Gamma x\right)^2\right] \exp\left(i\Gamma^2 a\Box y\right), \tag{B.9}$$

and hence we have an eigenfunction

$$H_\Omega \phi_{n,k} = \Gamma^2\left(n + \frac{1}{2}\right)\phi_{n,k}. \tag{B.10}$$

B.1.1 Normalisation and Orthonormality of the Eigenfunction

In this section we calculate the normalisation factor A_n of the the wavefunction given in Eqn. (4.18), such that

$$ab = \int_0^a \int_0^b \phi^*_{m,j}\phi_{n,k}\, dy\, dx. \tag{B.11}$$

We need to assume that the summation converges in such a way that we may interchange the order of summation and integration. Then, the y–integral is

$$\begin{aligned} I_y &= \int_0^b \exp\left[-i\Gamma^2 a\left(\frac{j}{N_\mathrm{v}} + q\right) y\right] \exp\left[i\Gamma^2 a\left(\frac{k}{N_\mathrm{v}} + p\right) y\right]\, dy \\ &= \int_0^b \exp\left[i\Gamma^2 a y\left(\frac{k-j}{N_\mathrm{v}} + p - q\right)\right]\, dy. \end{aligned} \tag{B.12}$$

We make the substitution $2\pi y = b\tilde{y}$ so that for $\tilde{y} \in [0, 2\pi)$ we have

$$\begin{aligned} I_y &= \frac{b}{2\pi}\int_0^{2\pi} d\tilde{y}\ \exp\left[i\Gamma^2\frac{ab}{2\pi}\tilde{y}\left(\frac{k-j}{N_\mathrm{v}}+p-q\right)\right] \\ &= \frac{b}{2\pi}\int_0^{2\pi} d\tilde{y}\ \exp\left[i\tilde{y}\left(k-j+N_\mathrm{v}p-N_\mathrm{v}q\right)\right]. \end{aligned} \tag{B.13}$$

We are now in a position where, since $j, k, p, q, N_\mathrm{v} \in \mathbb{Z}$, we can apply the identity

$$\int_0^{2\pi} e^{inx} = \begin{cases} 2\pi & n = 0, \\ 0 & \text{otherwise.} \end{cases} \tag{B.14}$$

In order that I_y doesn't vanish, we have the requirement $[k - j + N_\mathrm{v}(p - q)] = 0$. This condition is separable , however, as $k, j \in \{0, 1, \ldots, N_\mathrm{v} - 1\}$, thus

$$I_y = b\,\delta_{j,k}\,\delta_{p,q}. \tag{B.15}$$

The result for I_y now reduces Eqn. (B.11) to

$$\begin{aligned} &\int_0^a\int_0^b \phi^*_{m,j}\phi_{n,k}\ dx\,dy = A^*_m A_n b \times \\ &\sum_{p=-\infty}^{\infty}\int_0^a \chi^*_m\left[\Gamma a\left(\frac{k}{N_\mathrm{v}}+p\right)-\Gamma x\right]\chi_n\left[\Gamma a\left(\frac{k}{N_\mathrm{v}}+p\right)-\Gamma x\right]\ dx. \end{aligned} \tag{B.16}$$

We note that the Hermite functions, χ_m are real, and that the summation over p, imposed to provide the periodic boundary conditions of the solution, essentially transforms the integral into an infinite domain, such that

$$\int_0^a\int_0^b \phi^*_{m,j}\phi_{n,k}\,dxdy = A^*_m A_n\frac{b}{\Gamma}\int_{-\infty}^{\infty}\chi_m(\tilde{x})\,\chi_n(\tilde{x})\ d\tilde{x}.$$

The Hermite polynomials, $H_n(x)$ are orthogonal over $(-\infty, \infty)$ with respect to the weight function e^{-x^2}, so the Hermite functions $\chi_n(x)$, defined in Eqn. (4.19), are orthonormal over this interval. This leaves

$$ab = A^*_m A_n\frac{b}{\Gamma}\,\delta_{m,n} \tag{B.17}$$

so

$$\phi_{n,k} = \sqrt{a\Gamma}\sum_{p=-\infty}^{\infty}\chi_n\left[\Gamma a\left(\frac{k}{N_\mathrm{v}}+p\right)-\Gamma x\right]\exp\left[i\Gamma^2 a\left(\frac{k}{N_\mathrm{v}}+p\right)y\right]. \tag{B.18}$$

B.1.2 Quasi-Periodicity of the Eigenfunction

We can also show that $\phi_{n,k}$ obeys the quasi-periodic boundary conditions given in Eqns. (4.16) – (4.17). The y–direction is trivial, as taking $y \to y + b$ gives

$$\begin{aligned}\phi_{n,k}(x, y+b) &= A_n \sum_{p=-\infty}^{\infty} \chi_n \left[\Gamma a\left(\frac{k}{N_\mathrm{v}} + p\right) - \Gamma x\right] e^{i\Gamma^2 a\left(\frac{k}{N_\mathrm{v}}+p\right)y} e^{i\Gamma^2 \frac{ab}{N_\mathrm{v}}(k+N_\mathrm{v}p)} \\ &= A_n \sum_{p=-\infty}^{\infty} \chi_n \left[\Gamma a\left(\frac{k}{N_\mathrm{v}} + p\right) - \Gamma x\right] e^{i\Gamma^2 a\left(\frac{k}{N_\mathrm{v}}+p\right)y} e^{2\pi i(k+N_\mathrm{v}p)}, \quad \text{(B.19)}\end{aligned}$$

which is in agreement with Eqn. (4.17). On setting $x \to x + a$ we get

$$\begin{aligned}&\phi_{n,k}(x, y+b) \\ =\ & A_n \sum_{p=-\infty}^{\infty} \chi_n \left[\Gamma a\left(\frac{k}{N_\mathrm{v}} + p\right) - \Gamma x - \Gamma a\right] \exp\left[i\Gamma^2 a\left(\frac{k}{N_\mathrm{v}} + p\right) y\right] \\ =\ & A_n \sum_{p'=-\infty}^{\infty} \chi_n \left[\Gamma a\left(\frac{k}{N_\mathrm{v}} + p'\right) - \Gamma x\right] \exp\left[i\Gamma^2 a\left(\frac{k}{N_\mathrm{v}} + p'\right) y\right] e^{i\Gamma^2 a y} \\ =\ & \phi_{n,k}(x, y) \exp\left(i\frac{2\pi N_\mathrm{v} y}{b}\right), \quad \text{(B.20)}\end{aligned}$$

where $p' = p - 1$. Taking the principal value of the argument of this, we recover

$$\mathrm{Arg}\left[\phi_{n,k}\left(x + a, y\right)\right] = \mathrm{Arg}\left[\phi_{n,k}\left(x, y\right)\right] + \frac{2\pi y}{b},$$

which is Eqn. (4.16).

B.2 The Jacobi Theta Functions

The 3rd Jacobi theta function is defined as [280]

$$\vartheta_3\left(z;\tau\right) = \vartheta_3\left(z|q\right) = 1 + 2\sum_{k=1}^{\infty} q^{k^2} \cos\left(2kz\right) \quad \text{(B.21)}$$

where z is a complex number, τ is the lattice parameter (which, in general, is also a complex number), and the nome, q, is related to the lattice parameter by

$$q = \exp(i\pi\tau). \quad \text{(B.22)}$$

To ensure that $\vartheta_3\left(z;\tau\right)$ is an analytic function, the lattice parameter τ should be chosen so that $0 < |q| < 1$, and to avoid issues of multi-valuedness we take $q^{k^2} = \exp\left(ik^2\pi\tau\right)$, where $k \in \mathbb{R}$. In general the domain is a parallelogram in the complex plane, with vertices 0, π, $\tau\pi$ and $\pi + \tau\pi$, and so, as discussed in the main text, we take τ to be purely imaginary, so that we are describing a rectangular domain.

As well as the Fourier series representation of the 3rd Jacobi Theta function given in Eqn. (B.21), we can express the function as

$$\vartheta_3(z;\tau) = \sum_{k=-\infty}^{\infty} \exp\left(i\pi\tau k^2 + 2ikz\right). \tag{B.23}$$

To prove this, one simply uses the identity $\cos(2kz) = \left(e^{2ikz} + e^{-2ikz}\right)/2$ and manipulates the infinite sum.

B.2.1 Periodic and Quasi-Periodic Boundary Conditions

In the main text, we use the periodic and quasi-periodic boundary conditions of the 3rd Jacobi Theta function. In this sub-section we will prove these properties.

We claim that

$$\vartheta_3[z + (m + n\tau)\pi;\ \tau] = e^{-2inz}e^{-\pi\tau n^2}\vartheta_3(z;\ \tau),$$

where $m, n \in \mathbb{Z}$. To prove this, we consider the form of the 3rd Jacobi Theta function given in Eqn. (B.23). This gives

$$\vartheta_3[z + (m + n\tau)\pi;\ \tau] = \sum_{k=-\infty}^{\infty} \exp\left(i\pi\tau k^2\right)\exp\left[2ikz + 2ik(m + n\tau)\pi\right] \tag{B.24}$$

which, noting that $e^{2ikm\pi} = 1$ for integers k and m, reduces to

$$\vartheta_3[z + (m + n\tau)\pi;\ \tau] = \sum_{k=-\infty}^{\infty} \exp\left(i\pi\tau k^2\right)\exp\left(2ikz + 2ikn\tau\pi\right). \tag{B.25}$$

The trick now is to note that

$$i\pi\tau k^2 + 2ikn\tau\pi = i\pi\tau(k + n)^2 - i\pi\tau n^2,$$

so that we can write

$$\vartheta_3[z + (m + n\tau)\pi;\ \tau] = \exp\left(-i\pi\tau n^2\right)\sum_{k=-\infty}^{\infty} \exp\left[i\pi\tau(k + n)^2\right]\exp(2ikz), \tag{B.26}$$

or equivalently

$$\begin{aligned}&\vartheta_3[z + (m + n\tau)\pi;\ \tau] = \\ &\exp\left(-i\pi\tau n^2\right)\exp(-2inz)\sum_{k=-\infty}^{\infty} \exp\left[i\pi\tau(k + n)^2\right]\exp(2ikz)\exp(-2inz).\end{aligned} \tag{B.27}$$

Since the sum over k is infinite, we can introduce the dummy variable $k' = k + n$ so that the expression above becomes

$$\vartheta_3 \left[z + (m + n\tau)\, \pi;\ \tau \right] = \exp\left(-i\pi\tau n^2\right) \exp\left(-2inz\right) \sum_{k'=-\infty}^{\infty} \exp\left(i\pi\tau k'^2\right) \exp\left(2ik'z\right), \tag{B.28}$$

which (dropping primes) proves that

$$\vartheta_3 \left[z + (m + n\tau)\, \pi;\ \tau \right] = e^{-2inz} e^{-\pi\tau n^2} \vartheta_3 \left(z;\ \tau \right). \tag{B.29}$$

Appendix C

Identifying Vortices and Vortex Pinning

Throughout this thesis we have been concerned with the dynamics of quantized vortices. In Part IV, we have considered different point vortex models, where the dynamics of the system are described by the position of the vortices. In Parts II and III, however, we have modelled the system using the PGPE, where the vortex positions enter the system implicitly through the velocity field of the wavefunction Ψ. In these cases, it is necessary to be able to detect the location and charges of quantized vortices, and vortices which are pinned to barriers. In a similar calculation to the vortex detection method described in Ref. [301], in this section we describe the method used to detect the winding number, $\mathcal{W}$, about a given barrier.

Using the Madelung transformation, we write the wavefunction as $\Psi = |\Psi| \exp(i\theta)$, where $|\Psi|^2$ is the particle density, and θ is proportional to the velocity potential. The circulation of a quantum fluid is quantized, so that around any closed contour the change in the phase, $\Delta\theta$ is given as

$$\Delta\theta = \oint_{\mathcal{C}} \nabla\theta \cdot d\mathbf{r} = 2\pi\mathcal{W} \tag{C.1}$$

for some integer $\mathcal{W}$ which we shall refer to as the winding number. A vortex with non-zero charge $\mathcal{W}$ (which may also be called a charge $\mathcal{W}$ vortex) is detected when the contour $\mathcal{C}$ contains the vortex core and the phase changes continuously from 0 to $2\pi n$ around this curve. In order to detect a vortex which is pinned to a barrier (that is to say – the vortex is contained within the zero density region of the barrier but the branch-cut which represents the singularity in the phase extends into the non-zero density region of the condensate) we compute the winding number $\mathcal{W}$ about some contour which contains the barrier centre.

In our simulations, the wavefunction Ψ is computed at discrete grid points and so we calculate the line integral in Eqn. (C.1) numerically. For a barrier with centre (x_B, y_B) and effective width a, we create an annulus which has inner radius r_{in} and outer radius r_{out}. A sketch of this set-up is given in Fig. C.1. The inner and outer radii are chosen

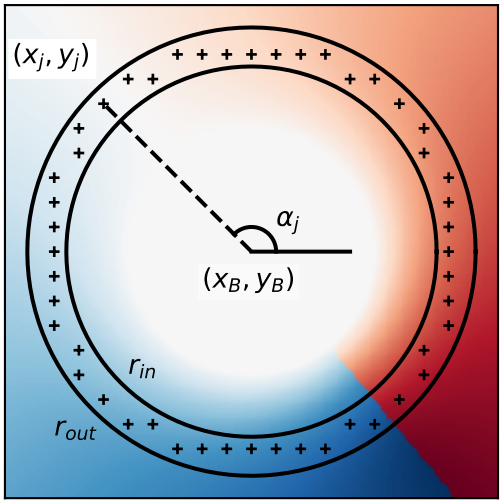

Figure C.1: A schematic of the numerical method used to compute the winding number in each barrier. The contour integral in Eqn. (C.1) is performed by evaluating the phase at the grid points (indicated with pluses) located within the annulus with inner radius r_{in} and outer radius r_{out}, shown. The angle α_j at each grid point can be computed by $\alpha_j = \arctan2\,(y_B - y_j, x_B - x_j)$. The colour plot represents a density weighted plot of the phase, $\theta|\Psi|^2$, where $\Psi = |\Psi|e^{i\theta}$; the white central region represents the area within the barrier where the density of the fluid vanishes. In this case, the barrier supports a winding number $\mathcal{W} = 1$.

so that the computational grid points contained within the annulus are outside the zero density region of the barrier, but do not overlap with the annulii enclosing other barriers. Once the grid points contained within the anulus have been identified, they are sorted in order of increasing α_j and the phase of the wave function is evaluated at each point. We then calculate the unwrapped phase difference between neighbouring points,

$$\Delta\theta_{j,j+1} = \theta\,\big|_{\alpha_j} - \theta\,\big|_{\alpha_{j+1}}. \tag{C.2}$$

It is necessary to unwrap the phase in this way to ensure that the phase is continuous between neighbouring points [301], however working on a discrete grid this continuity is poorly defined as there may be jumps in the phase of 2π; to correct for this we add multiples of 2π so that $|\Delta\theta_{j,j+1}| < \pi$. The winding number is then computed as a sum of $\Delta\theta_{j,j+1}$.

Fortunately we must only consider singly charged vortices, as it has been predicted theoretically [234, 235] and confirmed experimentally [236] that multiply charged vortices are unstable and will split into n singly charged vortices.

The process of vortex detection in the bulk of a superfluid (away from boundaries) is a simplified version of this calculation. In this case, rather than the circular array of grid points used in Eqn. (C.2), the calculation uses four neighbouring grid points which form a square around the centre of the vortex[1].

[1]Note that the code for this vortex detection was kindly provided by Andrew Groszek

Appendix D

Derivation of the 2D Point Vortex Model with Background Fluctuations

In this appendix we present a full derivation of the Point Vortex Model with the addition of a varying background density field. This derivation is based on the work of Törnkvist and Schröder, Ref. [231], although it focuses on the case of a two dimensional system.

D.1 The Filament Coordinate System

We adopt the coordinate system of [231] for a one-dimensional string, which is the filament of a defect. At any time t, we say that the position of the filament of a vortex is given by $\boldsymbol{X}(s,t)$, where s is the natural parameterisation of the vortex filament (i.e., it parameterises the arc length of the filament). At this position, we can develop an orthonormal coordinate basis using the so-called Frenet frame.

We define the tangent vector

$$\boldsymbol{T}(s,t) = \frac{\partial \boldsymbol{X}}{\partial s} \tag{D.1}$$

and the normal vector $\boldsymbol{N}(s,t)$ as usual. This is sometimes known as the Osculating plane. A sketch of this system is in Fig. D.1. To make an orthonormal basis we define the binormal vector to be $\boldsymbol{B}(s,t) = \boldsymbol{T} \times \boldsymbol{N}$, which completes the Frenet frame. In differential geometry, the Frenet-Serret formulas [408] describe both the dynamic properties of a particle moving along a continuous smooth curve, as well as the intrinsic properties of the curve itself. The formulas are stated as

$$\frac{\partial \boldsymbol{T}}{\partial s} = \kappa \boldsymbol{N}, \tag{D.2}$$

$$\frac{\partial \boldsymbol{N}}{\partial s} = -\kappa \boldsymbol{T} + \tau \boldsymbol{B}, \tag{D.3}$$

$$\frac{\partial \boldsymbol{B}}{\partial s} = -\tau \boldsymbol{N}, \tag{D.4}$$

where κ is the curvature of the curve, and τ is the torsion of the curve which is the measure of how quickly the curve is twisting out of the plane of curvature (torsion can

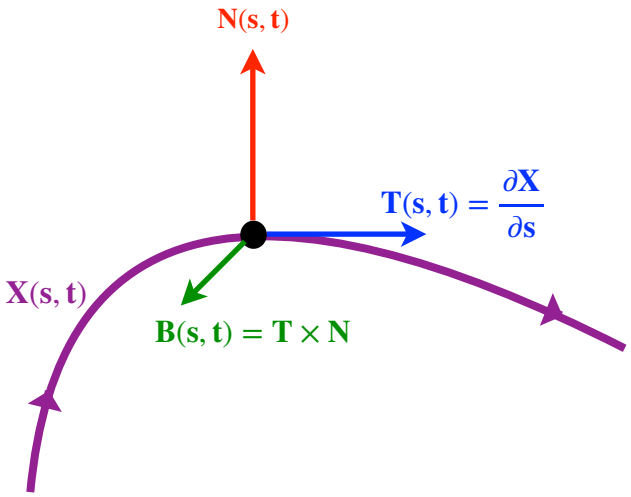

Figure D.1: The osculating plane.

also be thought of as the measure of the turn-around of the binormal vector). In this frame, we can describe any position $\boldsymbol{x}$ in the neighbourhood of the string can be expressed as

$$\boldsymbol{x} = \boldsymbol{X}(s,t) + x\boldsymbol{N}(s,t) + y\boldsymbol{B}(s,t). \tag{D.5}$$

We note that the coordinate representation (s, x, y) is unique, so long as $x, y < \kappa^{-1}$ where κ^{-1} is the radius of curvature. The approach of [231] is to then introduce polar coordinates in this local region, defined as $x = r\cos\varphi$, $y = r\sin\varphi$. The representation in Eqn. (D.5) now reads

$$\boldsymbol{x} = \boldsymbol{X}(s,t) + r\cos\varphi\boldsymbol{N}(s,t) + r\sin\varphi\boldsymbol{B}(s,t). \tag{D.6}$$

Note that for the representation in Eqn. (D.6), since (r, φ) define plane-polar coordinates and the vectors $\boldsymbol{N}$ and $\boldsymbol{B}$ are orthogonal by construction, we have basis vectors

$$\hat{\boldsymbol{r}} = \cos\varphi\boldsymbol{N} + \sin\varphi\boldsymbol{B}, \tag{D.7}$$

$$\hat{\boldsymbol{\varphi}} = -\sin\varphi\boldsymbol{N} + \cos\varphi\boldsymbol{B}. \tag{D.8}$$

From this coordinate representation, we are left to derive expressions for the gradient and then the Laplacian.

D.1.1 The Gradient of the Filament Coordinate System

The metric tensor (assuming the Einstein summation convention where appropriate) in orthogonal curvilinear coordinates is defined as

$$g_{\mu\nu} = \frac{\partial\boldsymbol{x}}{\partial q^\mu}\frac{\partial\boldsymbol{x}}{\partial q^\nu}, \tag{D.9}$$

where

$$d\boldsymbol{x}\cdot d\boldsymbol{x}=\frac{\partial x_\lambda}{\partial q^\mu}\frac{\partial x^\lambda}{\partial q^\nu}dq^\mu dq^\nu. \tag{D.10}$$

So we can calculate

$$\begin{aligned} d\boldsymbol{x} &= \left(\frac{\partial \boldsymbol{X}}{\partial s}+r\cos\varphi\frac{\partial \boldsymbol{N}}{\partial s}+r\sin\varphi\frac{\partial \boldsymbol{B}}{\partial s}\right)ds+\left(\cos\varphi\boldsymbol{N}+\sin\varphi\boldsymbol{B}\right)dr \\ &+ \left(-r\sin\varphi\boldsymbol{N}+r\cos\varphi\boldsymbol{B}\right)d\varphi \\ \\ &= \boldsymbol{T}\left(1-\kappa r\cos\varphi\right)ds+\tau\left(-r\sin\varphi\boldsymbol{N}+r\cos\varphi\boldsymbol{B}\right)ds+\left(\cos\varphi\boldsymbol{N}+\sin\varphi\boldsymbol{B}\right)dr \\ &+ \left(-r\sin\varphi\boldsymbol{N}+r\cos\varphi\boldsymbol{B}\right)d\varphi, \end{aligned}$$

where we have used Eqns. (D.1), (D.3) and (D.4) on the terms in the first bracket. From here, using the fact that $\{\boldsymbol{T},\boldsymbol{N},\boldsymbol{B}\}$ are pairwise orthonormal, we compute

$$d\boldsymbol{x}\cdot d\boldsymbol{x} = \left[\left(1-\kappa r\cos\varphi\right)^2+\tau^2r^2\right]dsds+drdr+r^2d\varphi d\varphi+2\tau r^2dsd\varphi. \tag{D.11}$$

The metric tensor can then be written as

$$g_{\mu\nu}=\begin{bmatrix}\left(1-\kappa r\cos\varphi\right)^2+\tau^2r^2 & 0 & \tau r^2\\ 0 & 1 & 0\\ \tau r^2 & 0 & r^2\end{bmatrix} \tag{D.12}$$

where q^μ, $q^\nu\in\{s,r,\varphi\}$. We can calculate the determinant of this to be

$$\det\left(g_{\mu\nu}\right)=r^2\left(1-\kappa r\cos\varphi\right)^2 \tag{D.13}$$

We can invert the metric tensor in three steps: firstly we find the matrix of minors which is given by

$$\begin{bmatrix} r^2 & 0 & -\tau r^2\\ 0 & r^2\left(1-\kappa r\cos\varphi\right)^2 & 0\\ -\tau r^2 & 0 & \left(1-\kappa r\cos\varphi\right)^2+\tau^2r^2\end{bmatrix}.$$

Secondly, we apply the alternate sign rule, which in this case is trivial. Hence the matrix of minors is also the matrix of cofactors. Finally, using $\det\left(g_{\mu\nu}\right)$ as found in Eqn. (D.13), we have

$$g^{\mu\nu}=\begin{bmatrix}\dfrac{1}{\left(1-\kappa r\cos\varphi\right)^2} & 0 & \dfrac{-\tau}{\left(1-\kappa r\cos\varphi\right)^2}\\ 0 & 1 & 0\\ \dfrac{-\tau}{\left(1-\kappa r\cos\varphi\right)^2} & 0 & \dfrac{1}{r^2}+\dfrac{\tau^2}{\left(1-\kappa r\cos\varphi\right)^2}\end{bmatrix}. \tag{D.14}$$

We now define "basis-vectors" as $\boldsymbol{b}_\mu = \boldsymbol{x}_{,\mu} = \partial\boldsymbol{x}/\partial q^\mu$. So

$$\begin{aligned}
\boldsymbol{b}_s &= \boldsymbol{T}\left(1-\kappa r\cos\varphi\right)+\tau\left(-r\sin\varphi\boldsymbol{N}+r\cos\varphi\boldsymbol{B}\right), && \text{(D.15)}\\
\boldsymbol{b}_r &= \cos\varphi\boldsymbol{N}+\sin\varphi\boldsymbol{B}=\hat{\boldsymbol{r}}, && \text{(D.16)}\\
\boldsymbol{b}_\varphi &= -r\sin\varphi\boldsymbol{N}+r\cos\varphi\boldsymbol{B}=r\hat{\boldsymbol{\varphi}}, && \text{(D.17)}
\end{aligned}$$

and using this we can use the inverse metric tensor, Eqn. (D.14), in the definition of the gradient,

$$\nabla = \boldsymbol{b}^\mu\frac{\partial}{\partial q^\mu} = g^{\mu\nu}\boldsymbol{b}_\nu\frac{\partial}{\partial q^\mu}. \tag{D.18}$$

In order to use this definition, we calculate

$$\begin{aligned}
\boldsymbol{b}^s &= g^{ss}\boldsymbol{b}_s+g^{sr}\boldsymbol{b}_r+g^{s\varphi}\boldsymbol{b}_\varphi\\
&= \frac{1}{1-\kappa r\cos\varphi}\boldsymbol{T}, && \text{(D.19)}\\
\boldsymbol{b}^r &= g^{rr}\boldsymbol{b}_r=\cos\varphi\boldsymbol{N}+\sin\varphi\boldsymbol{B}, && \text{(D.20)}\\
\boldsymbol{b}^\varphi &= g^{\varphi s}\boldsymbol{b}_s+g^{\varphi\varphi}\boldsymbol{b}_\varphi\\
&= -\frac{\tau}{1-\kappa r\cos\varphi}\boldsymbol{T}+\frac{1}{r^2}\left[-r\sin\varphi\boldsymbol{N}+r\cos\varphi\boldsymbol{B}\right]. && \text{(D.21)}
\end{aligned}$$

So, substituting Eqns. (D.19) – (D.21) into the definition given by Eqn. (D.18), we arrive at

$$\nabla = \boldsymbol{T}\left[\frac{1}{\left(1-\kappa r\cos\varphi\right)}\frac{\partial}{\partial s}-\frac{\tau}{\left(1-\kappa r\cos\varphi\right)}\frac{\partial}{\partial\varphi}\right]+\hat{\boldsymbol{r}}\frac{\partial}{\partial r}+\frac{1}{r}\hat{\boldsymbol{\varphi}}\frac{\partial}{\partial\varphi}. \tag{D.22}$$

D.1.2 The Laplacian of the Filament Coordinate System

To calculate the Laplacian of this coordinate system we use the definition for general curvilinear coordinates q^μ,

$$\nabla^2 = \frac{1}{\sqrt{g}}\frac{\partial}{\partial q^\mu}\left(\sqrt{g}g^{\mu\nu}\frac{\partial}{\partial q^\nu}\right). \tag{D.23}$$

The non-zero elements of the inverse metric tensor we found in Eqn. (D.14) are

$$\begin{aligned}
g^{ss} &= \frac{1}{\left(1-\kappa r\cos\varphi\right)^2}, && \text{(D.24)}\\
g^{rr} &= 1, && \text{(D.25)}\\
g^{\varphi\varphi} &= \frac{1}{r^2}+\frac{\tau^2}{\left(1-\kappa r\cos\varphi\right)^2}, && \text{(D.26)}\\
g^{s\varphi} &= -\frac{\tau}{\left(1-\kappa r\cos\varphi\right)^2} = g^{\varphi s}. && \text{(D.27)}
\end{aligned}$$

Then, as $\sqrt{\det\left(g_{\mu\nu}\right)} = r\left(1-\kappa r\cos\varphi\right)$ does not depend on s, substituting Eqns. (D.24) – (D.27) into Eqn. (D.23), we find

$$
\begin{aligned}
\nabla^2 &= g^{ss}\frac{\partial^2}{\partial s^2} + g^{s\varphi}\frac{\partial^2}{\partial s\partial\varphi} + \frac{1}{\sqrt{g}}\frac{\partial}{\partial r}\left[r\left(1-\kappa r\cos\varphi\right)\frac{\partial}{\partial r}\right] \\
&\quad + \frac{1}{\sqrt{g}}\frac{\partial}{\partial\varphi}\left[-\frac{\tau r\left(1-\kappa r\cos\varphi\right)}{\left(1-\kappa r\cos\varphi\right)^2}\frac{\partial}{\partial s} + \left(\frac{\left(1-\kappa\cos\varphi\right)}{r} + \frac{\tau^2 r}{\left(1-\kappa r\cos\varphi\right)}\right)\frac{\partial}{\partial\varphi}\right] \\
&= \frac{1}{\left(1-\kappa r\cos\varphi\right)^2}\frac{\partial^2}{\partial s^2} - \frac{\tau}{\left(1-\kappa r\cos\varphi\right)^2}\frac{\partial^2}{\partial s\partial\varphi} + \left[\frac{1-\kappa r\cos\varphi}{r\left(1-\kappa r\cos\varphi\right)} - \frac{\kappa\cos\varphi}{\left(1-\kappa r\cos\varphi\right)}\right]\frac{\partial}{\partial r} \\
&\quad + \frac{\partial^2}{\partial r^2} \\
&\quad + \frac{1}{r\left(1-\kappa r\cos\varphi\right)}\frac{\partial}{\partial\varphi}\left[-\frac{\tau r}{\left(1-\kappa r\cos\varphi\right)}\frac{\partial}{\partial s} + \left(\frac{\left(1-\kappa\cos\varphi\right)}{r} + \frac{\tau^2 r}{\left(1-\kappa r\cos\varphi\right)}\right)\frac{\partial}{\partial\varphi}\right] \\
&= \frac{1}{\left(1-\kappa r\cos\varphi\right)^2}\frac{\partial^2}{\partial s^2} - \frac{2\tau}{\left(1-\kappa r\cos\varphi\right)^2}\frac{\partial^2}{\partial s\partial\varphi} + \frac{1}{r}\frac{\partial}{\partial r} - \frac{\kappa\cos\varphi}{\left(1-\kappa\cos\varphi\right)}\frac{\partial}{\partial r} + \frac{\partial^2}{\partial r^2} \\
&\quad + \frac{1}{r\left(1-\kappa r\cos\varphi\right)}\left[\frac{\tau\kappa r^2\sin\varphi}{\left(1-\kappa r\cos\varphi\right)^2}\frac{\partial}{\partial s} + \left(\frac{\left(1-\kappa r\cos\varphi\right)}{r} + \frac{\tau^2 r}{\left(1-\kappa r\cos\varphi\right)}\right)\frac{\partial^2}{\partial\varphi^2}\right] \\
&\quad + \frac{1}{r\left(1-\kappa r\cos\varphi\right)}\left(\kappa\sin\varphi - \frac{\tau^2\kappa r^2\sin\varphi}{\left(1-\kappa r\cos\varphi\right)^2}\right)\frac{\partial}{\partial\varphi} \\
&= \frac{\partial^2}{\partial r^2} + \frac{1}{r}\frac{\partial}{\partial r} + \frac{\left(1-\kappa r\cos\varphi\right)^2 + \tau^2 r^2}{r^2\left(1-\kappa r\cos\varphi\right)^2}\frac{\partial^2}{\partial\varphi^2} - \frac{\kappa}{1-\kappa r\cos\varphi}\left(\cos\varphi\frac{\partial}{\partial r} - \kappa\sin\varphi\frac{\partial}{\partial\varphi}\right) \\
&\quad + \frac{1}{\left(1-\kappa r\cos\varphi\right)^2}\frac{\partial^2}{\partial s^2} - \frac{2\tau}{\left(1-\kappa r\cos\varphi\right)^2}\frac{\partial^2}{\partial s\partial\varphi} + \frac{\tau\kappa r^2\sin\varphi}{r\left(1-\kappa r\cos\varphi\right)^3}\frac{\partial}{\partial s} \\
&\quad - \frac{\tau^2\kappa r\sin\varphi}{\left(1-\kappa r\cos\varphi\right)^3}\frac{\partial}{\partial\varphi} \\
&= \frac{\partial^2}{\partial r^2} + \frac{1}{r}\frac{\partial}{\partial r} + \frac{1}{r^2}\frac{\partial^2}{\partial\varphi^2} - \frac{\kappa}{1-\kappa r\cos\varphi}\left(\cos\varphi\frac{\partial}{\partial r} - \kappa\sin\varphi\frac{\partial}{\partial\varphi}\right) \\
&\quad + \frac{1}{\left(1-\kappa r\cos\varphi\right)^2}\frac{\partial^2}{\partial s^2} - \frac{2\tau}{\left(1-\kappa r\cos\varphi\right)^2}\frac{\partial^2}{\partial s\partial\varphi} + \frac{\tau\kappa r^2\sin\varphi}{r\left(1-\kappa r\cos\varphi\right)^3}\frac{\partial}{\partial s} \\
&\quad - \frac{\tau^2\kappa r\sin\varphi}{\left(1-\kappa r\cos\varphi\right)^3}\frac{\partial}{\partial\varphi} + \frac{\tau^2}{\left(1-\kappa r\cos\varphi\right)^2}\frac{\partial^2}{\partial\varphi^2}
\end{aligned}
$$

At this point, we employ some clever factorisation for the terms on the second and third lines to recover

$$\begin{aligned}\nabla^2 &= \frac{\partial^2}{\partial r^2}+\frac{1}{r}\frac{\partial}{\partial r}+\frac{1}{r^2}\frac{\partial^2}{\partial\varphi^2}-\frac{\kappa}{1-\kappa r\cos\varphi}\left(\cos\varphi\frac{\partial}{\partial r}-\kappa\sin\varphi\frac{\partial}{\partial\varphi}\right)\\ &+ \left[\frac{1}{1-\kappa r\cos\varphi}\left(\frac{\partial}{\partial s}-\tau\frac{\partial}{\partial\varphi}\right)\right]^2. \end{aligned} \tag{D.28}$$

D.2 The Vortex Equation of Motion

The multivalued nature of the phase of a vortex will cause problems with continuity and differentiability as $r\to 0$. To counter this, we split the modulus and phase of Ψ as follows: let

$$|\Psi| = Rw, \tag{D.29}$$
$$S = \chi+\theta \tag{D.30}$$

where $\ln R$ depends on the filament position and contains any contribution to the modulus which is non-differentiable at $r=0$. Similarly, we absorb into χ any part of the phase field which is multivalued at any point, or non-differentiable at $r=0$. As R and χ only occur in the combinations described in Eqns. (D.29) and (D.30), they are non-unique subject to the independent symmetries

$$\chi\to\chi+\delta, \qquad \theta\to\theta-\delta, \tag{D.31}$$
$$R\to Rf, \qquad w\to wf^{-1}, \tag{D.32}$$

for suitably differentiable arbitrary functions δ and $\ln f$. Using this definition, Eqn. (9.13) becomes

$$\begin{aligned}\frac{d\Psi}{dt} &= \frac{d}{dt}\left(\ln R+\ln w+i\chi+i\theta\right)\\ &= P\left(\Psi,\Psi^*\right)\Psi+b\nabla^2\left(\ln R+\ln w+i\chi+i\theta\right).\end{aligned}$$

We now follow [231] and write a set of coupled PDEs for this system. On substituting

$$\Psi = Rw\exp\left[i\left(\theta+\chi\right)\right] \tag{D.33}$$

into Eqn. (9.13) we have

$$\begin{aligned}
\text{LHS} &= \frac{d\Psi}{dt} = \frac{d}{dt}\left[Rw\right]e^{i(\theta+\chi)} + Rw\frac{d}{dt}e^{i(\theta+\chi)} \\
&= \frac{dR}{dt}we^{i(\theta+\chi)} + R\frac{dw}{dt}e^{i(\theta+\chi)} + iRw\frac{d\theta}{dt}e^{i(\theta+\chi)} + iRw\frac{d\chi}{dt}e^{i(\theta+\chi)} \\
&= Rwe^{i(\theta+\chi)}\left[\frac{1}{R}\frac{dR}{dt} + \frac{1}{w}\frac{dw}{dt} + i\frac{d\theta}{dt} + i\frac{d\chi}{dt}\right] \\
&= Rwe^{i(\theta+\chi)}\frac{d}{dt}\left[\ln R + \ln w + i\theta + i\chi\right]. \qquad \text{(D.34)}
\end{aligned}$$

As an aside, we make note of several vector calculus identities for scalar fields ψ, ϕ. Mainly

$$\begin{aligned}
\nabla\cdot(\phi\nabla\psi) &= \phi\nabla^2\psi + \nabla\phi\cdot\nabla\psi \qquad \text{(D.35)} \\
\nabla^2(\psi\phi) &= \phi\nabla^2\psi + 2\nabla\psi\cdot\nabla\phi + \psi\nabla^2\phi \qquad \text{(D.36)} \\
\nabla^2\ln\phi &= \nabla\cdot\left(\frac{1}{\phi}\nabla\phi\right) \\
&= \frac{1}{\phi}\nabla^2\phi - \frac{1}{\phi^2}\nabla\phi\cdot\nabla\phi. \qquad \text{(D.37)}
\end{aligned}$$

Then,

$$\nabla^2\Psi = \underbrace{\nabla^2\left(Rw\right)e^{i(\theta+\chi)}}_{1} + \underbrace{2\nabla(Rw)\cdot\nabla e^{i(\theta+\chi)}}_{2} + \underbrace{Rw\nabla^2 e^{i(\theta+\chi)}}_{3} \qquad \text{(D.38)}$$

and so term by term:

$$\text{Term 1} = \nabla^2\left(Rw\right)e^{i(\theta+\chi)} = \left[R\nabla^2 w + 2\nabla R\cdot\nabla w + w\nabla^2 R\right]e^{i(\theta+\chi)}, \qquad \text{(D.39)}$$

$$\text{Term 2} = iRwe^{i(\theta+\chi)}\left(\frac{1}{w}\nabla w + \frac{1}{R}\nabla R\right)\cdot\left(\nabla\theta + \nabla\chi\right), \qquad \text{(D.40)}$$

and

$$\begin{aligned}
&\text{Term 3} = \\
&Rw\Big[ie^{i(\theta+\chi)}\nabla^2\chi - e^{i(\theta+\chi)}\nabla\chi\cdot\nabla\chi - 2e^{i(\theta+\chi)}\nabla\theta\cdot\nabla\chi + ie^{i(\theta+\chi)}\nabla^2\theta - e^{i(\theta+\chi)}\nabla\theta\cdot\nabla\theta\Big].
\end{aligned}$$

From here, we can write the Laplacian term of Eqn. (9.13) as

$$\begin{aligned}
\nabla^2\Psi &= Rwe^{i(\theta+\chi)}\left[\frac{1}{w}\nabla^2 w + \frac{2}{Rw}\nabla R\cdot\nabla w + \frac{1}{R}\nabla^2 R\right] \\
&+ 2iRwe^{i(\theta+\chi)}\left(\frac{1}{w}\nabla w + \frac{1}{R}\nabla R\right)\cdot\left(\nabla\theta + \nabla\chi\right) \\
&+ Rwe^{i(\theta+\chi)}\left[i\nabla^2\chi - \left(\nabla\chi\right)^2 - 2\nabla\chi\cdot\nabla\theta + i\nabla^2\theta - \left(\nabla\theta\right)^2\right], \qquad \text{(D.41)}
\end{aligned}$$

and then we have [applying the identity in Eqn. (D.37)]

$$\begin{aligned}\frac{1}{A}\nabla^2\Psi &= \left[\frac{1}{w}\nabla^2 w + \frac{2}{Rw}\nabla R\cdot\nabla w + \frac{1}{R}\nabla^2 R\right] + 2i\left(\frac{1}{w}\nabla w + \frac{1}{R}\nabla R\right)\cdot(\nabla\theta+\nabla\chi)\\ &\quad + \left[i\nabla^2\chi - (\nabla\chi)^2 - 2\nabla\chi\cdot\nabla\theta + i\nabla^2\theta - (\nabla\theta)^2\right]\\ &= \nabla^2\ln R + \nabla^2\ln w + (\nabla\ln R + \nabla\ln w)^2 - (\nabla\theta+\nabla\chi)^2\\ &\quad + i\left[\nabla^2\chi + \nabla^2\theta + 2\left(\nabla\ln w + \nabla\ln R\right)\cdot(\nabla\theta+\nabla\chi)\right].\end{aligned}$$

By setting $b = b_R + ib_I$, we can then write this expression in real and imaginary parts

$$\frac{d}{dt}\left(\ln R + \ln w\right) = \mathrm{Re}\left[P\left(A, A^*\right)\right] + b_R Q_1 - b_I Q_2, \tag{D.42}$$

$$\frac{d}{dt}\left(\theta + \chi\right) = \mathrm{Im}\left[P\left(A, A^*\right)\right] + b_I Q_1 + b_R Q_2, \tag{D.43}$$

where we define the quantities

$$Q_1 = \left(\nabla^2\ln R + \nabla^2\ln w\right) + \left(\nabla\ln R + \nabla\ln w\right)^2 - \left(\nabla\chi + \nabla\theta\right)^2, \tag{D.44}$$

$$Q_2 = \left(\nabla^2\chi + \nabla^2\theta\right) + 2\left(\nabla\ln R + \nabla\ln w\right)\cdot\left(\nabla\chi + \nabla\theta\right). \tag{D.45}$$

D.2.1 The 2D System

Up to this point, we have assumed that we are working with a 3D vortex filament which can be modeled as a curve in the Frenet-Serret frame. In order to derive the equation of motion for a 2D system, we assume that the vortex are straight parallel tubes, and that we can take a cut in the xy–plane. The result of this is that the curvature and torsion of the filaments vanish, so $\kappa, \tau \to 0$. In 2D we are also without gauge freedom, so

$$R = r^{|n|}, \tag{D.46}$$

$$\chi = n\varphi. \tag{D.47}$$

From here we can calculate

$$\begin{aligned}\nabla\ln R = \hat{\boldsymbol{r}}\frac{|n|}{r}, \qquad & \nabla\chi = \frac{n}{r}\hat{\boldsymbol{\varphi}},\\ \nabla^2\ln R = 0, \qquad & \nabla^2\chi = 0.\end{aligned} \tag{D.48}$$

Substituting this result into Eqns. (D.44) and (D.45) we arrive at

$$Q_1^{(2D)} = \nabla^2\ln w + 2\frac{|n|}{r}\hat{\boldsymbol{r}}\cdot\nabla\ln w - 2\frac{n}{r}\hat{\boldsymbol{\varphi}}\cdot\nabla\theta + (\nabla\ln w)^2 - (\nabla\theta)^2, \tag{D.49}$$

$$Q_2^{(2D)} = \nabla^2\theta + 2\frac{|n|}{r}\hat{\boldsymbol{r}}\cdot\nabla\theta + 2\frac{n}{r}\hat{\boldsymbol{\varphi}}\cdot\nabla\ln w + 2\ln w\cdot\nabla\theta. \tag{D.50}$$

The time derivative in the lab-frame is related to the time derivative in the moving

reference frame of the local segment of the filament by

$$\frac{d}{dt} = -\dot{\boldsymbol{X}} \cdot \nabla + \frac{\partial}{\partial t}. \tag{D.51}$$

Combining these results, we arrive at two more equations for the real and imaginary parts of the complex field,

$$\begin{aligned}
\frac{\partial}{\partial t}\left(\ln R + \ln w\right) &= \dot{\mathbf{X}} \cdot \hat{\boldsymbol{r}} \frac{|n|}{r} + \dot{\mathbf{X}} \cdot \nabla \ln w + \mathrm{Re}\left(P\right) \\
&+ b_R \left[\nabla^2 \ln w + 2\frac{|n|}{r}\hat{\boldsymbol{r}} \cdot \nabla \ln w - 2\frac{n}{r}\hat{\boldsymbol{\varphi}} \cdot \nabla\theta + \left(\nabla \ln w\right)^2 - \left(\nabla\theta\right)^2\right] \\
&- b_I \left[\nabla^2\theta + 2\frac{|n|}{r}\hat{\boldsymbol{r}} \cdot \nabla\theta + 2\frac{n}{r}\hat{\boldsymbol{\varphi}} \cdot \nabla \ln w + 2\ln w \cdot \nabla\theta\right],
\end{aligned} \tag{D.52}$$

and

$$\begin{aligned}
\frac{\partial}{\partial t}\left(\theta + \chi\right) &= \dot{\mathbf{X}} \cdot \hat{\boldsymbol{\varphi}} \frac{n}{r} + \dot{\mathbf{X}} \cdot \nabla\theta + \mathrm{Im}\left(P\right) \\
&+ b_R \left[\nabla^2\theta + 2\frac{|n|}{r}\hat{\boldsymbol{r}} \cdot \nabla\theta + 2\frac{n}{r}\hat{\boldsymbol{\varphi}} \cdot \nabla \ln w + 2\ln w \cdot \nabla\theta\right] \\
&+ b_I \left[\nabla^2 \ln w + 2\frac{|n|}{r}\hat{\boldsymbol{r}} \cdot \nabla \ln w - 2\frac{n}{r}\hat{\boldsymbol{\varphi}} \cdot \nabla\theta + \left(\nabla \ln w\right)^2 - \left(\nabla\theta\right)^2\right].
\end{aligned} \tag{D.53}$$

Equations (D.52) and (D.53) describe the evolution of the four variables R, w, θ and χ. In both of the equations, there are terms which are proportional to r^{-1}, which will lead to singularities are $r \to 0$. We must therefore derive regularity conditions for these equations, so that these singularities cancel term by term. Recall that $\ln w$ and θ are continuous and differentiable anywhere. The form of the function $P(A)$ does not enter into the remainder of the derivation, as it is globally differentiable.

From Eqns. (D.52) and (D.53), the terms involving an r^{-1} are

$$0 = \dot{\mathbf{X}} \cdot \hat{\boldsymbol{r}} + 2b_R \left[\hat{\boldsymbol{r}} \cdot \nabla \ln w - \frac{n}{|n|}\hat{\boldsymbol{\varphi}} \cdot \nabla\theta\right] - 2b_I \left[\hat{\boldsymbol{r}} \cdot \nabla\theta + \frac{n}{|n|}\hat{\boldsymbol{\varphi}} \cdot \nabla \ln w\right] \tag{D.54}$$

$$0 = \dot{\mathbf{X}} \cdot \hat{\boldsymbol{\varphi}} + 2b_R \left[\frac{n}{|n|}\hat{\boldsymbol{r}} \cdot \nabla\theta + \hat{\boldsymbol{\varphi}} \cdot \nabla \ln w\right] + 2b_I \left[\frac{n}{|n|}\hat{\boldsymbol{r}} \cdot \nabla \ln w - \hat{\boldsymbol{\varphi}} \cdot \nabla\theta\right]. \tag{D.55}$$

where the terms on the right hand side must vanish to ensure regularity. In 2D, the tangent vector $\boldsymbol{T} = \hat{\boldsymbol{z}}$, and we must also note that

$$\begin{aligned}
\hat{\boldsymbol{r}} \times \hat{\boldsymbol{\varphi}} &= \hat{\boldsymbol{z}}, \\
\hat{\boldsymbol{z}} \times \hat{\boldsymbol{r}} &= \hat{\boldsymbol{\varphi}}, \\
\hat{\boldsymbol{z}} \times \hat{\boldsymbol{\varphi}} &= -\hat{\boldsymbol{r}}.
\end{aligned} \tag{D.56}$$

We have equations for the two perpendicular components of $\dot{\mathbf{X}}$, which we can combine

into a vector equation by using the identity

$$\boldsymbol{a} \times (\boldsymbol{b} \times \boldsymbol{c}) = \boldsymbol{b}\,(\boldsymbol{a} \cdot \boldsymbol{c}) - \boldsymbol{c}\,(\boldsymbol{a} \cdot \boldsymbol{b})\,. \tag{D.57}$$

Thus,

$$\begin{aligned}
\hat{\boldsymbol{r}}\left(\dot{\mathbf{X}} \cdot \hat{\boldsymbol{\varphi}}\right) \;&-\; \hat{\boldsymbol{\varphi}}\left(\dot{\mathbf{X}} \cdot \hat{\boldsymbol{r}}\right) = \\
&-\; \hat{\boldsymbol{r}}\left[2b_R\left(\frac{n}{|n|}\hat{\boldsymbol{r}} \cdot \nabla\theta + \hat{\boldsymbol{\varphi}} \cdot \nabla \ln w\right) + 2b_I\left(\frac{n}{|n|}\hat{\boldsymbol{r}} \cdot \nabla \ln w - \hat{\boldsymbol{\varphi}} \cdot \nabla\theta\right)\right] \\
&+\; \hat{\boldsymbol{\varphi}}\left[2b_R\left(\hat{\boldsymbol{r}} \cdot \nabla \ln w - \frac{n}{|n|}\hat{\boldsymbol{\varphi}} \cdot \nabla\theta\right) - 2b_I\left(\hat{\boldsymbol{r}} \cdot \nabla\theta + \frac{n}{|n|}\hat{\boldsymbol{\varphi}} \cdot \nabla \ln w\right)\right]
\end{aligned} \tag{D.58}$$

where the term on the left hand side,

$$\hat{\boldsymbol{r}}\left(\dot{\mathbf{X}} \cdot \hat{\boldsymbol{\varphi}}\right) - \hat{\boldsymbol{\varphi}}\left(\dot{\mathbf{X}} \cdot \hat{\boldsymbol{r}}\right) = \dot{\mathbf{X}} \times (\hat{\boldsymbol{r}} \times \hat{\boldsymbol{\varphi}}) = \dot{\mathbf{X}} \times \hat{\boldsymbol{z}}. \tag{D.59}$$

Taking the vector product of this with $\hat{\boldsymbol{z}}$, and collecting like terms, we get

$$\begin{aligned}
\hat{\boldsymbol{z}} \times \left(\dot{\mathbf{X}} \times \hat{\boldsymbol{z}}\right) \;&=\; -(\hat{\boldsymbol{z}} \times \hat{\boldsymbol{r}})\left[2b_R\left(\frac{n}{|n|}\hat{\boldsymbol{r}} \cdot \nabla\theta + \hat{\boldsymbol{\varphi}} \cdot \nabla \ln w\right) + 2b_I\left(\frac{n}{|n|}\hat{\boldsymbol{r}} \cdot \nabla \ln w - \hat{\boldsymbol{\varphi}} \cdot \nabla\theta\right)\right] \\
&\quad + (\hat{\boldsymbol{z}} \times \hat{\boldsymbol{\varphi}})\left[2b_R\left(\hat{\boldsymbol{r}} \cdot \nabla \ln w - \frac{n}{|n|}\hat{\boldsymbol{\varphi}} \cdot \nabla\theta\right) - 2b_I\left(\hat{\boldsymbol{r}} \cdot \nabla\theta + \frac{n}{|n|}\hat{\boldsymbol{\varphi}} \cdot \nabla \ln w\right)\right] \\
&=\; -2b_R\frac{n}{|n|}\nabla\theta \times (\hat{\boldsymbol{\varphi}} \times \hat{\boldsymbol{r}}) - 2b_R\hat{\boldsymbol{z}} \times [\nabla \ln w \;\times (\hat{\boldsymbol{r}} \times \hat{\boldsymbol{\varphi}})] \\
&\quad -2b_I\frac{n}{|n|}\nabla \ln w \;\times (\hat{\boldsymbol{\varphi}} \times \hat{\boldsymbol{r}}) + 2b_I\hat{\boldsymbol{z}} \times [\nabla\theta \;\times (\hat{\boldsymbol{r}} \times \hat{\boldsymbol{\varphi}})]\,.
\end{aligned}$$

Note that the left hand side is

$$\hat{\boldsymbol{z}} \times \left(\dot{\mathbf{X}} \times \hat{\boldsymbol{z}}\right) = \dot{\mathbf{X}}\;(\hat{\boldsymbol{z}} \cdot \hat{\boldsymbol{z}}) - \hat{\boldsymbol{z}}\;\left(\hat{\boldsymbol{z}} \cdot \dot{\mathbf{X}}\right),$$

and, as the tangential velocity is devoid of physical meaning, it is possible to set $\hat{\boldsymbol{z}} \cdot \dot{\mathbf{X}} = 0$ by a time dependent reparametrization $s \to s(t)$; this is called worldsheet reparametrization invariance in relativistic string theory [231]. Therefore, the resulting equation of motion is

$$\dot{\mathbf{X}} = -2b_R\frac{n}{|n|}\hat{\boldsymbol{z}} \times \nabla\theta + 2b_R\hat{\boldsymbol{z}} \times (\hat{\boldsymbol{z}} \times \nabla \ln w) - 2b_I\frac{n}{|n|}\hat{\boldsymbol{z}} \times \nabla \ln w - 2b_I\hat{\boldsymbol{z}} \times (\hat{\boldsymbol{z}} \times \nabla\theta)\,, \tag{D.60}$$

or, more simply

$$\dot{\mathbf{X}}_j = -2b_R\frac{n_j}{|n_j|}\hat{\boldsymbol{z}} \times \nabla\theta_j - 2b_R\nabla \ln w - 2b_I\frac{n_j}{|n_j|}\hat{\boldsymbol{z}} \times \nabla \ln w + 2b_I\nabla\theta_j \tag{D.61}$$

where the terms involving $\ln w$ on the right hand side are evaluated at the position $\mathbf{r}_j$.

We recall that

$$\theta_j = \sum_{\substack{k=1 \\ k\neq j}}^{N_\mathrm{v}} n_k \arctan\left(\frac{y_{jk}}{x_{jk}}\right),$$

where $x_{jk} = x_j - x_k$ and $y_{jk} = y_j - y_k$. We note that, if the background density $w = U_0$, some constant uniform background density, we exactly recover the equation found by [239, 240]. It is possible to compute that the gradient terms

$$\nabla\theta_j = \sum_{\substack{k=1 \\ k\neq j}}^{N_\mathrm{v}} \frac{1}{r_{jk}^2}\begin{pmatrix} -y_{jk} \\ x_{jk} \end{pmatrix}, \tag{D.62}$$

where $r_{jk}^2 = x_{jk}^2 + y_{jk}^2$. By comparison to the dissipative system

$$i\frac{\partial\Psi}{\partial t} = (1 - i\gamma)\left[\mathcal{H} + g|\Psi|^2 - \mu\right]\Psi, \tag{D.63}$$

we have $b_R = \gamma/2$ and $b_I = 1/2$, therefore

$$\dot{\mathbf{X}}_j = -\gamma\frac{n_j}{|n_j|}\hat{\boldsymbol{z}} \times \nabla\theta_j - \gamma\nabla \ln w - \frac{n_j}{|n_j|}\hat{\boldsymbol{z}} \times \nabla \ln w + \nabla\theta_j. \tag{D.64}$$

i.e., for $n_k = \pm 1$, this is

$$\frac{d}{dt}\mathbf{r}_j = \sum_{\substack{k=1 \\ k\neq j}}^{N_\mathrm{v}} \frac{n_k}{r_{jk}^2}\begin{pmatrix} \gamma n_j x_{jk} - y_{jk} \\ \\ \gamma n_j y_{jk} + x_{jk} \end{pmatrix} - \frac{1}{w\left(\mathbf{r}_j\right)}\begin{pmatrix} \gamma w_x\left(\mathbf{r}_j\right) - n_j w_y\left(\mathbf{r}_j\right) \\ \\ \gamma w_y\left(\mathbf{r}_j\right) + n_j w_x\left(\mathbf{r}_j\right) \end{pmatrix}. \tag{D.65}$$

D.3 Some Simple Analytic Solutions

Consider a point vortex model for a system with two vortices, each with unit charges ($n_{1,2} = \pm 1$), on a homogeneous background, $w = 0$. The coupled equations of motion are

$$\frac{d}{dt}\mathbf{r}_1 = \frac{n_2}{r_{12}^2}\begin{pmatrix} -y_{12} \\ x_{12} \end{pmatrix} + \frac{\gamma n_1 n_2}{r_{12}^2}\begin{pmatrix} x_{12} \\ y_{12} \end{pmatrix}, \tag{D.66}$$

$$\frac{d}{dt}\mathbf{r}_2 = \frac{n_1}{r_{21}^2}\begin{pmatrix} -y_{21} \\ x_{21} \end{pmatrix} + \frac{\gamma n_2 n_1}{r_{21}^2}\begin{pmatrix} x_{21} \\ y_{21} \end{pmatrix}. \tag{D.67}$$

The dynamics of such a system is mainly influenced by the sign of the vortices; we consider this effect in the next two subsections. In both cases, we will assume that the vortices are initially at $\mathbf{r}_1(0) = (x_1(0), y_1(0))$ and $\mathbf{r}_2(0) = (x_2(0), y_2(0))$, where the vector from $\mathbf{r}_1(0)$ to $\mathbf{r}_2(0)$ has length r_0 and subtends an angle $\vartheta_0 = \tan(y_{12}(0)/x_{12}(0))$ with the x axis.

D.3.1 A dipole pair

Suppose that we have a dipole pair, $n_1 = 1$, $n_2 = -1$. We can combine the equations of motion as

$$\begin{aligned}
\frac{d}{dt}\begin{pmatrix} x_{12} \\ y_{12} \end{pmatrix} &= \frac{d}{dt}\mathbf{r}_1 - \frac{d}{dt}\mathbf{r}_2 \\
&= -\frac{1}{r_{12}^2}\begin{pmatrix} -y_{12} \\ x_{12} \end{pmatrix} - \frac{\gamma}{r_{12}^2}\begin{pmatrix} x_{12} \\ y_{12} \end{pmatrix} - \frac{1}{r_{21}^2}\begin{pmatrix} -y_{21} \\ x_{21} \end{pmatrix} + \frac{\gamma}{r_{21}^2}\begin{pmatrix} x_{21} \\ y_{21} \end{pmatrix} \\
&= -\frac{1}{r_{12}^2}\begin{pmatrix} -y_{12} \\ x_{12} \end{pmatrix} - \frac{\gamma}{r_{12}^2}\begin{pmatrix} x_{12} \\ y_{12} \end{pmatrix} + \frac{1}{r_{12}^2}\begin{pmatrix} -y_{12} \\ x_{12} \end{pmatrix} - \frac{\gamma}{r_{12}^2}\begin{pmatrix} x_{12} \\ y_{12} \end{pmatrix},
\end{aligned}$$

by using the symmetry of r_{12}^2 and the anti-symmetry of x_{12} and y_{12}. For convenience we write $x = x_{12}$, $y = y_{12}$, and $r^2 = x^2 + y^2$, so that the equations of motion become

$$\frac{dx}{dt} = -\frac{2\gamma x}{r^2}, \qquad \frac{dy}{dt} = -\frac{2\gamma y}{r^2}. \tag{D.68}$$

We make the substitution to polar coordinates $x = \varpi\cos\vartheta$ and $y = \varpi\sin\vartheta$, where $\varpi^2 = x^2 + y^2$ and $\vartheta = \arctan(y/x)$. In these coordinates, the time derivatives are

$$\frac{d\varpi}{dt} = \frac{x}{\varpi}\frac{dx}{dt} + \frac{y}{\varpi}\frac{dy}{dt}, \qquad \frac{d\vartheta}{dt} = \frac{1}{\varpi^2}\left(x\frac{dy}{dt} - y\frac{dx}{dt}\right) \tag{D.69}$$

so we can write the coupled equations in Eqn. (D.68) as

$$\frac{d\varpi}{dt} = -\frac{2\gamma}{\varpi}, \qquad \frac{d\vartheta}{dt} = 0. \tag{D.70}$$

In the absence of dissipation, $\gamma = 0$, meaning $\varpi(t) = r_0$ and $\vartheta = \vartheta_0$. This solution corresponds to a dipole pair which move together in parallel with fixed translational velocity [402]. When dissipation is present, the solution is $\varpi^2 = r_0^2 - 4\gamma t$. This means that we can write the separation

$$[r_{12}(t)]^2 = x_{12}^2 + y_{12}^2 = [r_{12}(0)]^2 - 4\gamma t, \tag{D.71}$$

indicating that the dipole pair will move together at a rate proportional to the damping parameter γ until they eventually annihilate.

D.3.2 A chiral pair

Suppose that the vortices are of the same sign, $n_1 = n_2$. Without loss of generality, take $n_1 = 1 = n_2$. Now, we can combine the equations of motion as

$$\frac{d}{dt}\begin{pmatrix} x_{12} \\ y_{12} \end{pmatrix} = \frac{2}{r_{12}^2}\begin{pmatrix} -y_{12} \\ x_{12} \end{pmatrix} + \frac{2\gamma}{r_{12}^2}\begin{pmatrix} x_{12} \\ y_{12} \end{pmatrix}, \tag{D.72}$$

For convenience we write $x = x_{12}$, $y = y_{12}$, and $r^2 = x^2 + y^2$, so that the equations of motion become

$$\frac{dx}{dt} = \frac{-2y + 2\gamma x}{r^2}, \qquad \frac{dy}{dt} = \frac{2x + 2\gamma y}{r^2}. \tag{D.73}$$

At this juncture, we again convert to plane polar coordinates and write Eqn. (D.73) as

$$\frac{d\varpi}{dt} = \frac{2\gamma}{\varpi}, \qquad \frac{d\vartheta}{dt} = \frac{2}{\varpi^2}. \tag{D.74}$$

In the absence of dissipation, $\varpi = r_0$ and $\vartheta = \vartheta_0 + 2t/r_0^2$. This corresponds to a pair of vortices which rotate around their centre of vorticity with fixed separation [402]. If, on the other hand, there is dissipation in the system, the solutions take the form

$$\varpi^2(t) = 4\gamma t + r_0^2, \qquad \vartheta(t) = \frac{1}{2\gamma}\ln\left(1 + \frac{4\gamma t}{r_0^2}\right) + \vartheta_0, \tag{D.75}$$

which corresponds to a pair of vortices which follow a modified spiral away from each other.

D.4 A continuous disordered potential

We consider the continuously disordered potential defined in a cell with dimensions $-L \leq x \leq L$ and $-L \leq y \leq L$ by Eqn. (10.5) as

$$V_{\text{ext}}(\mathbf{r}) = \sum_{(k_x,k_y)\in\mathcal{K}} A_{\mathbf{k}} \cos\left[\frac{2\pi}{L}(xk_x + yk_y) + \varphi_{\mathbf{k}}\right],$$

where the random variables $A_{\mathbf{k}} \sim U[0,1]$ and $\varphi_{\mathbf{k}} \sim U[0,2\pi)$, and the modes considered are $\mathcal{K} = \left\{(k_x, k_y) \ : \ k_{min}^2 \leq k_x^2 + k_y^2 \leq k_{max}^2\right\}$. It can be shown that this trap is orthogonal, so that

$$\int d^2\mathbf{r}\ V'(\mathbf{r})\, V(\mathbf{r}) = 2L^2 \sum_{\mathbf{k}\in\mathcal{K}} \sum_{\mathbf{k}'\in\mathcal{K}} A_{\mathbf{k}} A_{\mathbf{k}'} \delta_{\mathbf{k},\mathbf{k}'}. \tag{D.76}$$

For a two-dimensional function, $f(x,y)$, defined in a region $-L \leq x \leq L$ and $-L \leq y \leq L$, it is possible to write the Root Mean Square (RMS) value of this function as

$$f_{\text{RMS}} = \sqrt{\frac{1}{4L^2} \int d^2\mathbf{r}\ \left[f(x,y)\right]^2}. \tag{D.77}$$

If the function $f(x,y)$ is the sum of K known waveforms, and the component waveforms are orthogonal, then the RMS of the resulting function is given by

$$\text{RMS}_{\text{Total}} = \sqrt{\text{RMS}_1^2 + \text{RMS}_2^2 + \cdots + \text{RMS}_K^2}. \tag{D.78}$$

Since the potential defined in Eqn. (10.5) is orthogonal, we calculate that the Root Mean Square of the potential, V_{RMS}, is given by

$$V_{\text{RMS}} = \sqrt{\frac{1}{2} \sum_{\mathbf{k}\in\mathcal{K}} A_{\mathbf{k}}^2}. \tag{D.79}$$

Suppose we wish to put a bound on the maximum value of the trap. The amplitude of each of the component waveforms of the trap is $A_{\mathbf{k}}$, and if we suppose that the all of the waves have a local maximum at the origin[1] then V_{max}, the maximum value of the potential, is given by the sum of the amplitudes, $V_{max} = \sum_{\mathbf{k}\in\mathcal{K}} A_{\mathbf{k}}$. We can rearrange the formula for V_{RMS} to get

$$2V_{\text{RMS}}^2 = \sum_{\mathbf{k}\in\mathcal{K}} A_{\mathbf{k}}^2.$$

Using the Cauchy-Schwarz inequality,

$$\left(\sum_{\mathbf{k}\in\mathcal{K}} A_{\mathbf{k}}\right)^2 \leq \left(\sum_{\mathbf{k}\in\mathcal{K}} A_{\mathbf{k}}^2\right)\left(\sum_{\mathbf{k}\in\mathcal{K}} 1^2\right) = |\mathcal{K}| \sum_{\mathbf{k}\in\mathcal{K}} A_{\mathbf{k}}^2 \tag{D.80}$$

where the number of modes contained in the set $\mathcal{K}$ is given by $|\mathcal{K}|$. This leads to the upper-bound for the maximum of the potential,

$$V_{max}^2 < 2|\mathcal{K}| V_{\text{RMS}}^2. \tag{D.81}$$

[1] Note that we have avoided such "bunching" by adding the random offset $\varphi_{\mathbf{k}}$.

Bibliography

[1] S. N. Bose, "Plancks Gesetz und Lichtquantenhypothese", Z. Phys. **26** (1924).

[2] A. Einstein, "Quantentheorie des einatomigen idealen Gases", Kgl. Preuss. Akad. Wiss. (1924).

[3] A. Einstein, "Quantentheorie des einatomigen idealen Gases. 2. Abhandlung", Kgl. Preuss. Akad. Wiss. (1925).

[4] M. H. Anderson, J. R. Ensherm, R. Matthews, C. E. Wieman, and E. A. Cornell, "Observation of Bose-Einstein Condensation in a Dilute Atomic Vapor", Science **269**, 198–201 (1995).

[5] C. C. Bradley, C. A. Sackett, J. J. Tollett, and R. G. Hulet, "Evidence of Bose-Einstein Condensation in an Atomic Gas with Attractive Interactions", Phys. Rev. Lett. **75**, 1687–1690 (1995).

[6] K. B. Davis, M.-O. Mewes, M. R. Andrews, N. J. van Druten, D. S. Durfee, D. M. Kurn, and W. Ketterle, "Bose-Einstein Condensation in a Gas of Sodium Atoms", Phys. Rev. Lett. **75**, 3969–3973 (1995).

[7] E. A. Cornell and C. E. Wieman, "Nobel Lecture: Bose-Einstein condensation in a dilute gas, the first 70 years and some recent experiments", Rev. Mod. Phys. **74**, 875–893 (2002).

[8] N. S. Ginsberg, S. R. Garner, and L. V. Hau, "Coherent control of optical information with matter wave dynamics", Nature **445**, 623–626 (2007).

[9] D. Becker, M. D. Lachmann, S. T. Seidel, H. Ahlers, A. N. Dinkelaker, J. Grosse, O. Hellmig, H. Müntinga, V. Schkolnik, T. Wendrich, A. Wenzlawski, B. Weps, R. Corgier, T. Franz, N. Gaaloul, W. Herr, D. Lüdtke, M. Popp, S. Amri, H. Duncker, M. Erbe, A. Kohfeldt, A. Kubelka-Lange, C. Braxmaier, E. Charron, W. Ertmer, M. Krutzik, C. Lämmerzahl, A. Peters, W. P. Schleich, K. Sengstock, R. Walser, A. Wicht, P. Windpassinger, and E. M. Rasel, "Space-borne Bose–Einstein condensation for precision interferometry.", Nature **562**, 391–395 (2018).

[10] N. Navon, A. Gaunt, R. Smith, and Z. Hadzibabic, "Emergence of a turbulent cascade in a quantum gas", Nature **539**, 72–75 (2016).

[11] P. J. Mohr and B. N. Taylor, "CODATA recommended values of the fundamental physical constants: 2002", Rev. Mod. Phys. **77**, 1–107 (2005).

[12] C. F. Barenghi and N. G. Parker, *A Primer In Quantum Fluids (Springer Briefs in Physics Series)* (Springer, Berlin, 2016).

[13] C. J. Pethick and H. Smith, *Bose-Einstein Condensation in Dilute Gases* (Cambridge University Press, 2002).

[14] C. Gruber and A. Pelster, "A theory of finite-temperature Bose-Einstein condensates in neutron stars", Eur. Phys. J. D **68**, 341 (2014).

[15] O. Penrose and L. Onsager, "Bose-Einstein Condensation and Liquid Helium", Phys. Rev. **104**, 576–584 (1956).

[16] S. Chu, "Nobel Lecture: The manipulation of neutral particles", Rev. Mod. Phys. **70**, 685–706 (1998).

[17] C. N. Cohen-Tannoudji, "Nobel Lecture: Manipulating atoms with photons", Rev. Mod. Phys. **70**, 707–719 (1998).

[18] W. D. Phillips, "Nobel Lecture: Laser cooling and trapping of neutral atoms", Rev. Mod. Phys. **70**, 721–741 (1998).

[19] H. F. Hess, "Evaporative cooling of magnetically trapped and compressed spin-polarized hydrogen", Phys. Rev. B **34**, 3476 (R) (1986).

[20] F. Schreck and K. van Druten, "Laser cooling for quantum gases.", Nature Physics **17**, 1296–1304 (2021).

[21] T. Lahaye, J. Metz, B. Fröhlich, T. Koch, M. Meister, A. Griesmaier, T. Pfau, H. Saito, Y. Kawaguchi, and M. Ueda, "*d*-Wave Collapse and Explosion of a Dipolar Bose-Einstein Condensate", Phys. Rev. Lett. **101**, 080401 (2008).

[22] C. Chin, R. Grimm, P. Julienne, and E. Tiesinga, "Feshbach resonances in ultracold gases", Rev. Mod. Phys. **82**, 1225–1286 (2010).

[23] C. M. K. Henderson C. Ryu and M. G. Boshier, "Experimental demonstration of painting arbitrary and dynamical potentials for Bose-Einstein condensates", New J. Phys. **11**, 043030 (2009).

[24] A. L. Gaunt, T. F. Schmidutz, I. Gotlibovych, R. P. Smith, and Z. Hadzibabic, "Bose-Einstein Condensation of Atoms in a Uniform Potential", Phys. Rev. Lett. **110**, 200406 (2013).

[25] G. Gauthier, I. Lenton, N. M. Parry, M. Baker, M. J. Davis, H. Rubinsztein-Dunlop, and T. W. Neely, "Direct imaging of a digital-micromirror device for configurable microscopic optical potentials", Optica **3**, 1136–1143 (2016).

[26] D. G. Fried, T. C. Killian, L. Willmann, D. Landhuis, S. C. Moss, D. Kleppner, and T. J. Greytak, "Bose-Einstein Condensation of Atomic Hydrogen", Phys. Rev. Lett. **81**, 3811–3814 (1998).

[27] A. Robert, O. Sirjean, A. Browaeys, J. Poupard, S. Nowak, D. Boiron, C. I. Westbrook, and A. Aspect, "A Bose-Einstein Condensate of Metastable Atoms", Science **292**, 461–464 (2001).

[28] G. Modugno, G. Ferrari, G. Roati, R. J. Brecha, A. Simoni, and M. Inguscio, "Bose-Einstein Condensation of Potassium Atoms by Sympathetic Cooling", Science **294**, 1320–1322 (2001).

[29] Tino Weber and Jens Herbig and Michael Mark and Hanns-Christoph Nögerl and Rudolf Grimm, "Bose-Einstein Condensation of Cesium", Science **299**, 232–235 (2003).

[30] S. Kraft, F. Vogt, O. Appel, F. Riehle, and U. Sterr, "Bose-Einstein Condensation of Alkaline Earth Atoms: ^{40}Ca", Phys. Rev. Lett. **103**, 130401 (2009).

[31] S. Stellmer, M. K. Tey, B. Huang, R. Grimm, and F. Schreck, "Bose-Einstein Condensation of Strontium", Phys. Rev. Lett. **103**, 200401 (2009).

[32] A. Griesmaier, J. Werner, S. Hensler, J. Stuhler, and T. Pfau, "Bose-Einstein Condensation of Chromium", Phys. Rev. Lett. **94**, 160401 (2005).

[33] Y. Takasu, K. Maki, K. Komori, T. Takano, K. Honda, M. Kumakura, T. Yabuzaki, and Y. Takahashi, "Spin-Singlet Bose-Einstein Condensation of Two-Electron Atoms", Phys. Rev. Lett. **91**, 040404 (2003).

[34] M. Lu, N. Q. Burdick, S. H. Youn, and B. L. Lev, "Strongly Dipolar Bose-Einstein Condensate of Dysprosium", Phys. Rev. Lett. **107**, 190401 (2011).

[35] K. Aikawa, A. Frisch, M. Mark, S. Baier, A. Rietzler, R. Grimm, and F. Ferlaino, "Bose-Einstein Condensation of Erbium", Phys. Rev. Lett. **108**, 210401 (2012).

[36] E. T. Davletov, V. V. Tsyganok, V. A. Khlebnikov, D. A. Pershin, D. V. Shaykin, and A. V. Akimov, "Machine learning for achieving Bose-Einstein condensation of thulium atoms", Phys. Rev. A **102**, 011302 (2020).

[37] I. Bloch, J. Dalibard, and S. Nascimbène, "Quantum simulations with ultracold quantum gases", Nature Physics **8**, 267–276 (2012).

[38] C. Gross and I. Bloch, "Quantum simulations with ultracold atoms in optical lattices", Science **357**, 995–1001 (2017).

[39] T. Byrnes, K. Wen, and Y. Yamamoto, "Macroscopic quantum computation using Bose-Einstein condensates", Phys. Rev. A **85**, 040306 (2012).

[40] L. Pezzè, A. Smerzi, M. K. Oberthaler, R. Schmied, and P. Treutlein, "Quantum metrology with nonclassical states of atomic ensembles", Rev. Mod. Phys. **90**, 035005 (2018).

[41] A. Sørensen, L. M. Duan, J. Cirac, and P. Zoller, "Many-particle entanglement with Bose–Einstein condensates.", Nature **409**, 63–66 (2001).

[42] S. Dimopoulos and A. A. Geraci, "Probing submicron forces by interferometry of Bose-Einstein condensed atoms", Phys. Rev. D **68**, 124021 (2003).

[43] T. Berrada, S. van Frank, R. Bücker, T. Schumm, J.-F. Schaff, and J. Schmiedmayer, "Integrated Mach–Zehnder interferometer for Bose–Einstein condensates.", Nature Communications **4** (2013).

[44] T. V. Ngo, D. V. Tsarev, R.-K. Lee, and A. P. Alodjants, "Bose–Einstein condensate soliton qubit states for metrological applications.", Sci. Rep. **11** (2021).

[45] F. London, "The λ-Phenomenon of Liquid Helium and the Bose-Einstein Degeneracy.", Nature **141**, 643–644 (1938).

[46] L. Tisza, "Transport Phenomena in Helium II.", Nature **141**, 913 (1938).

[47] P. Kapitza, "Viscosity of Liquid Helium below the λ-Point.", Nature **141** (1938).

[48] J. Allen and A. Misener, "Flow of Liquid Helium II.", Nature **141**, 75 (1938).

[49] J. Allen and A. Misener, "Flow Phenomena in Liquid Helium II.", Nature **142**, 643–644 (1938).

[50] L. Landau, "Theory of the Superfluidity of Helium II", Phys. Rev. **60**, 356–358 (1941).

[51] T. Frisch, Y. Pomeau, and S. Rica, "Transition to dissipation in a model of superflow", Phys. Rev. Lett. **69**, 1644–1647 (1992).

[52] W. F. Vinen, "Mutual friction in a heat current in liquid helium II I. Experiments on steady heat currents", Proc. Royal Soc. A **240**, 114–127 (1957).

[53] M. R. Matthews, B. P. Anderson, P. C. Haljan, D. S. Hall, C. E. Wieman, and E. A. Cornell, "Vortices in a Bose-Einstein Condensate", Phys. Rev. Lett. **83**, 2498–2501 (1999).

[54] B. P. Anderson, P. C. Haljan, C. E. Wieman, and E. A. Cornell, "Vortex Precession in Bose-Einstein Condensates: Observations with Filled and Empty Cores", Phys. Rev. Lett. **85**, 2857–2860 (2000).

[55] D. L. Feder, A. A. Svidzinsky, A. L. Fetter, and C. W. Clark, "Anomalous Modes Drive Vortex Dynamics in Confined Bose-Einstein Condensates", Phys. Rev. Lett. **86**, 564–567 (2001).

[56] T. P. Simula and P. B. Blakie, "Thermal Activation of Vortex-Antivortex Pairs in Quasi-Two-Dimensional Bose-Einstein Condensates", Phys. Rev. Lett. **96**, 020404 (2006).

[57] G. Moon, W. J. Kwon, H. Lee, and Y.-i. Shin, "Thermal friction on quantum vortices in a Bose-Einstein condensate", Phys. Rev. A **92**, 051601 (2015).

[58] J. Arlt, O. Maragò1, E. Hodby, S. A. Hopkins, G. Hechenblaikner, S. Webster, and C. J. Foot, "Bose-Einstein condensation in a rotating anisotropic TOP trap", J. Phys. B: At. Mol. Opt. Phys. **32**, 5861 (1999).

[59] K. W. Madison, F. Chevy, W. Wohlleben, and J. Dalibard, "Vortex Formation in a Stirred Bose-Einstein Condensate", Phys. Rev. Lett. **84**, 806–809 (2000).

[60] S. Inouye, S. Gupta, T. Rosenband, A. P. Chikkatur, A. Görlitz, T. L. Gustavson, A. E. Leanhardt, D. E. Pritchard, and W. Ketterle, "Observation of Vortex Phase Singularities in Bose-Einstein Condensates", Phys. Rev. Lett. **87**, 080402 (2001).

[61] T. Dauxois and M. Peyrard, *Physics of solitons* (Cambridge University Press).

[62] K. E. Strecker, G. B. Partridge, A. G. Truscott, and R. G. Hulet, "Formation and propagation of matter-wave soliton trains", Nature **417**, 150–153 (2002).

[63] L. Khaykovich, F. Schreck, G. Ferrari, T. Bourdel, J. Cubizolles, L. D. Carr, Y. Castin, and C. Salomon, "Formation of a Matter-Wave Bright Soliton", Science **296**, 1290–1293 (2002).

[64] S. L. Cornish, S. T. Thompson, and C. E. Wieman, "Formation of Bright Matter-Wave Solitons during the Collapse of Attractive Bose-Einstein Condensates", Phys. Rev. Lett. **96**, 170401 (2006).

[65] A. Marchant, T. Billam, T. Wiles, M. M. H. Yu, S. A. Gardiner, and S. L. Cornish, "Controlled formation and reflection of a bright solitary matter-wave.", Nature Communications **4**, 1865 (2013).

[66] T. M. T. Arh, J. Brence, J. Pišljar, K. Gosar, Ž. Gosar, R. Žitko, and E. Z. P. Jeglič, "Cesium bright matter-wave solitons and soliton trains", Phys. Rev. A **99**, 033625 (2019).

[67] B. P. Anderson, P. C. Haljan, C. A. Regal, D. L. Feder, L. A. Collins, C. W. Clark, and E. A. Cornell, "Watching Dark Solitons Decay into Vortex Rings in a Bose-Einstein Condensate", Phys. Rev. Lett. **86**, 2926–2929 (2001).

[68] S. Nazarenko and M. Onorato, "Freely decaying Turbulence and Bose–Einstein Condensation in Gross–Pitaevski Model.", J. Low Temp. Phys. **146**, 31–46 (2007).

[69] D. J. Tritton, *Physical fluid dynamics* (Van Nostrand Reinhold (UK) Co. Ltd., 1977).

[70] O. Reynolds, "An experimental investigation of the circumstances which determine whether the motion of water shall be direct or sinuous, and of the law of resistance in parallel channels", Phil. Trans. R. Soc. **174**, 935–982 (1883).

[71] A. N. Kolmogorov, Dokl. Akad. Nauk SSSR **30**, 301 (1941).

[72] E. A. L. Henn, J. A. Seman, G. Roati, K. M. F. Magalhães, and V. S. Bagnato, "Emergence of Turbulence in an Oscillating Bose-Einstein Condensate", Phys. Rev. Lett. **103**, 045301 (2009).

[73] M. C. Tsatsos, P. E. Tavares, A. Cidrim, A. R. Fritsch, M. A. Caracanhas, F. E. A. dos Santos, C. F. Barenghi, and V. S. Bagnato, "Quantum turbulence in trapped atomic Bose–Einstein condensates", Phys. Rep. **622**, 1–52 (2016).

[74] V. Bretin, P. Rosenbusch, F. Chevy, G. V. Shlyapnikov, and J. Dalibard, "Quadrupole Oscillation of a Single-Vortex Bose-Einstein Condensate: Evidence for Kelvin Modes", Phys. Rev. Lett. **90**, 100403 (2003).

[75] S. Serafini, M. Barbiero, M. Debortoli, S. Donadello, F. Larcher, F. Dalfovo, G. Lamporesi, and G. Ferrari, "Dynamics and Interaction of Vortex Lines in an Elongated Bose-Einstein Condensate", Phys. Rev. Lett. **115**, 170402 (2015).

[76] M. Leadbeater, D. C. Samuels, C. F. Barenghi, and C. S. Adams, "Decay of superfluid turbulence via Kelvin-wave radiation", Phys. Rev. A **67**, 015601 (2003).

[77] M. Leadbeater, T. Winiecki, D. C. Samuels, C. F. Barenghi, and C. S. Adams, "Sound Emission due to Superfluid Vortex Reconnections", Phys. Rev. Lett. **86**, 1410–1413 (2001).

[78] D. Proment, S. Nazarenko, and M. Onorato, "Quantum turbulence cascades in the Gross-Pitaevskii model", Phys. Rev. A **80**, 051603 (2009).

[79] D. Proment, S. Nazarenko, and M. Onorato, "Sustained turbulence in the three-dimensional Gross–Pitaevskii model", Physica D: Nonlinear Phenomena **241**, Special Issue on Small Scale Turbulence, 304–314 (2012).

[80] A. W. Baggaley, J. Laurie, and C. F. Barenghi, "Vortex-Density Fluctuations, Energy Spectra, and Vortical Regions in Superfluid Turbulence", Phys. Rev. Lett. **109**, 205304 (2012).

[81] A. W. Baggaley, C. F. Barenghi, and Y. A. Sergeev, "Quasiclassical and ultraquantum decay of superfluid turbulence", Phys. Rev. B **85**, 060501 (2012).

[82] P. M. Walmsley and A. I. Golov, "Quantum and Quasiclassical Types of Superfluid Turbulence", Phys. Rev. Lett. **100**, 245301 (2008).

[83] T. W. Neely, A. S. Bradley, E. C. Samson, S. J. Rooney, E. M. Wright, K. J. H. Law, R. Carretero-González, P. G. Kevrekidis, M. J. Davis, and B. P. Anderson, "Characteristics of Two-Dimensional Quantum Turbulence in a Compressible Superfluid", Phys. Rev. Lett. **111**, 235301 (2013).

[84] N. Navon, C. Eigen, J. Zhang, R. Lopes, A. L. Gaunt, K. Fujimoto, M. Tsubota, R. P. Smith, and Z. Hadzibabic, "Synthetic dissipation and cascade fluxes in a turbulent quantum gas", Science **366**, 382–385 (2019).

[85] R. H. Kraichnan, "Inertial Ranges in Two-Dimensional Turbulence", The Physics of Fluids **10**, 1417 (1967).

[86] R. H. Kraichnan, "Inertial-range transfer in two- and three-dimensional turbulence", Journal of Fluid Mechanics **47**, 525–535 (1971).

[87] M. T. Reeves, T. P. Billam, B. P. Anderson, and A. S. Bradley, "Inverse Energy Cascade in Forced Two-Dimensional Quantum Turbulence", Phys. Rev. Lett. **110**, 104501 (2013).

[88] T. P. Billam, M. T. Reeves, B. P. Anderson, and A. S. Bradley, "Onsager-Kraichnan Condensation in Decaying Two-Dimensional Quantum Turbulence", Phys. Rev. Lett. **112**, 145301 (2014).

[89] T. P. Billam, M. T. Reeves, and A. S. Bradley, "Spectral energy transport in two-dimensional quantum vortex dynamics", Phys. Rev. A **91**, 023615 (2015).

[90] S. P. Johnstone, A. J. Groszek, P. T. Starkey, C. J. Billington, T. P. Simula, and K. Helmerson, "Evolution of large-scale flow from turbulence in a two-dimensional superfluid", Science **364**, 1267–1271 (2019).

[91] M. T. Reeves, T. P. Billam, X. Yu, and A. S. Bradley, "Enstrophy cascade in decaying two-dimensional quantum turbulence", Phys. Rev. Lett. **119**, 184502 (2017).

[92] L. Onsager, "Statistical hydrodynamics", Il Nuovo Cimento (1943-1954) **6**, 279–287 (1949).

[93] T. Simula, M. J. Davis, and K. Helmerson, "Emergence of Order from Turbulence in an Isolated Planar Superfluid", Phys. Rev. Lett. **113**, 165302 (2014).

[94] M. T. Reeves, T. P. Billam, B. P. Anderson, and A. S. Bradley, "Signatures of coherent vortex structures in a disordered two-dimensional quantum fluid", Phys. Rev. A **89**, 053631 (2014).

[95] A. J. Groszek, T. P. Simula, D. M. Paganin, and K. Helmerson, "Onsager vortex formation in Bose-Einstein condensates in two-dimensional power-law traps", Phys. Rev. A **93**, 043614 (2016).

[96] X. Yu, T. P. Billam, J. Nian, M. T. Reeves, and A. S. Bradley, "Theory of the vortex-clustering transition in a confined two-dimensional quantum fluid", Phys. Rev. A **94**, 023602 (2016).

[97] G. Gauthier, M. T. Reeves, X. Yu, A. S. Bradley, M. A. Baker, T. A. Bell, H. Rubinsztein-Dunlop, M. J. Davis, and T. W. Neely, "Giant vortex clusters in a two-dimensional quantum fluid", Science **364**, 1264–1267 (2019).

[98] S. J. Rooney, P. B. Blakie, B. P. Anderson, and A. S. Bradley, "Suppression of Kelvon-induced decay of quantized vortices in oblate Bose-Einstein condensates", Phys. Rev. A **84**, 023637 (2011).

[99] M. T. Reeves, T. P. Billam, B. P. Anderson, and A. S. Bradley, "Identifying a Superfluid Reynolds Number via Dynamical Similarity", Phys. Rev. Lett. **114**, 155302 (2015).

[100] W. J. Kwon, J. H. Kim, S. W. Seo, and Y. Shin, "Observation of von Kármán Vortex Street in an Atomic Superfluid Gas", Phys. Rev. Lett. **117**, 245301 (2016).

[101] R. Doran and T. P. Billam, "Numerical method for the projected Gross-Pitaevskii equation in an infinite rotating two-dimensional Bose gas", Phys. Rev. E **102**, 033309 (2020).

[102] R. Doran, A. J. Groszek, and T. P. Billam, "Critical Velocity and Arrest of a Superfluid in a Point-Like Disordered Potential", arXiv preprint, 2201.11887 (2022).

[103] M. J. Edmonds, T. Bland, R. Doran, and N. G. Parker, "Engineering bright matter-wave solitons of dipolar condensates", New Journal of Physics **19**, 023019 (2017).

[104] Y. Lim, J. Goo, H. Kwak, and Y. Shin, "Large-area ^{87}Rb Bose-Einstein condensate in a clipped-Gaussian optical dipole trap", Phys. Rev. A **103**, 063319 (2021).

[105] A. J. Leggett, "Bose-Einstein condensation in the alkali gases: Some fundamental concepts", Rev. Mod. Phys. **73**, 307–356 (2001).

[106] J. O. Andersen, "Theory of the weakly interacting Bose gas", Rev. Mod. Phys. **76**, 599–639 (2004).

[107] E. P. Gross, "Structure of a quantized vortex in boson systems", Nuovo Cim **20**, 454–477 (1961).

[108] E. P. Gross, "Hydrodynamics of a Superfluid Condensate", J. Math. Phys. **4** (1963).

[109] L. P. Pitaevskii, Zh. Eksp. Teor. Fiz **40**, 646 (1961).

[110] N. P. Proukakis and B. Jackson, "Finite-temperature models of Bose-Einstein condensation", J. Phys. B: At. Mol. Opt. Phys. **41**, 203002 (2008).

[111] L. Pitaevskii and S. Stringari, *Bose–Einstein Condensation and Superfluidity* (Oxford Science Publications, 2016).

[112] S. L. Cornish, N. R. Claussen, J. L. Roberts, E. A. Cornell, and C. E. Wieman, "Stable ^{85}Rb Bose-Einstein Condensates with Widely Tunable Interactions", Phys. Rev. Lett. **85**, 1795–1798 (2000).

[113] E. Donley, N. Claussen, S. Cornish, J. L. Roberts, E. A. Cornell, and C. E. Weiman, "Dynamics of collapsing and exploding Bose–Einstein condensates", Nature **412** (2001).

[114] A. Görlitz, J. M. Vogels, A. E. Leanhardt, C. Raman, T. L. Gustavson, J. R. Abo-Shaeer, A. P. Chikkatur, S. Gupta, S. Inouye, T. Rosenband, and W. Ketterle, "Realization of Bose-Einstein Condensates in Lower Dimensions", Phys. Rev. Lett. **87**, 130402 (2001).

[115] S. Stock, Z. Hadzibabic, B. Battelier, M. Cheneau, and J. Dalibard, "Observation of Phase Defects in Quasi-Two-Dimensional Bose-Einstein Condensates", Phys. Rev. Lett. **95**, 190403 (2005).

[116] Z. Hadzibabic, P. Krüger, M. Cheneau, B. Battelier, and J. Dalibard, "Berezinskii–Kosterlitz–Thouless crossover in a trapped atomic gas", Nature **441**, 1118–1121 (2006).

[117] P. Krüger, Z. Hadzibabic, and J. Dalibard, "Critical Point of an Interacting Two-Dimensional Atomic Bose Gas", Phys. Rev. Lett. **99**, 040402 (2007).

[118] P. Cladé, C. Ryu, A. Ramanathan, K. Helmerson, and W. D. Phillips, "Observation of a 2D Bose Gas: From Thermal to Quasicondensate to Superfluid", Phys. Rev. Lett. **102**, 170401 (2009).

[119] S. P. Rath, T. Yefsah, K. J. Günter, M. Cheneau, R. Desbuquois, M. Holzmann, W. Krauth, and J. Dalibard, "Equilibrium state of a trapped two-dimensional Bose gas", Phys. Rev. A **82**, 013609 (2010).

[120] S. Tung, G. Lamporesi, D. Lobser, L. Xia, and E. A. Cornell, "Observation of the Presuperfluid Regime in a Two-Dimensional Bose Gas", Phys. Rev. Lett. **105**, 230408 (2010).

[121] C.-L. Hung, X. Zhang, N. Gemelke, and C. Chin, "Observation of scale invariance and universality in two-dimensional Bose gases", Nature **470**, 236–239 (2011).

[122] T. Yefsah, R. Desbuquois, L. Chomaz, K. J. Günter, and J. Dalibard, "Exploring the Thermodynamics of a Two-Dimensional Bose Gas", Phys. Rev. Lett. **107**, 130401 (2011).

[123] L.-C. Ha, C.-L. Hung, X. Zhang, U. Eismann, S.-K. Tung, and C. Chin, "Strongly Interacting Two-Dimensional Bose Gases", Phys. Rev. Lett. **110**, 145302 (2013).

[124] L. Chomaz, L. Corman, T. Bienaimé, R. Desbuquois, C. Weitenberg, S. Nascimbene, J. Beugnon, and J. Dalibard, "Emergence of coherence via transverse condensation in a uniform quasi-two-dimensional Bose gas", Nature Communications **6**, 1–10 (2015).

[125] E. Madelung, "Quantentheorie in hydrodynamischer Form", Zeitschrift für Physik **40** (1927).

[126] N. R. Cooper, "Rapidly rotating atomic gases", Adv. Phys. **57**, 539–616 (2008).

[127] M. Leadbeater, T. Winiecki, and C. S. Adams, "Effect of condensate depletion on the critical velocity for vortex nucleation in quantum fluids", J. Phys. B: At. Mol. Opt. Phys. **36**, L143–L148 (2003).

[128] M. J. Davis, R. J. Ballagh, and K. Burnett, "Dynamics of thermal Bose fields in the classical limit", J. Phys. B: At. Mol. Opt. Phys. **34**, 4487–4512 (2001).

[129] M. J. Davis, S. A. Morgan, and K. Burnett, "Simulations of Bose Fields at Finite Temperature", Phys. Rev. Lett. **87**, 160402 (2001).

[130] M. J. Davis, S. A. Morgan, and K. Burnett, "Simulations of thermal Bose fields in the classical limit", Phys. Rev. A **66**, 053618 (2002).

[131] C. W. Gardiner and M. J. Davis, "The stochastic Gross-Pitaevskii equation: II", J. Phys. B: At. Mol. Opt. Phys. **36**, 4731–4753 (2003).

[132] P. B. Blakie and M. J. Davis, "Projected Gross-Pitaevskii equation for harmonically confined Bose gases at finite temperature", Phys. Rev. A **72**, 063608 (2005).

[133] P. B. Blakie, A. S. Bradley, M. J. Davis, R. J. Ballagh, and C. W. Gardiner, "Dynamics and statistical mechanics of ultra-cold Bose gases using c-field techniques", Adv. Phys. **57**, 363–455 (2008).

[134] A. S. Bradley, C. W. Gardiner, and M. J. Davis, "Bose-Einstein Condensation from a Rotating Thermal Cloud: Vortex Nucleation and Lattice Formation", Phys. Rev. A **77**, 033616 (2008).

[135] P. B. Blakie, C. Ticknor, A. S. Bradley, A. M. Martin, M. J. Davis, and Y. Kawaguchi, "Numerical method for evolving the dipolar projected Gross-Pitaevskii equation", Phys. Rev. E **80**, 016703 (2009).

[136] A. Sinatra, C. Lobo, and Y. Castin, "The truncated Wigner method for Bose-condensed gases: limits of validity and applications", J. Phys. B: At. Mol. Opti. Phys. **35** (2002).

[137] A. S. Bradley, P. B. Blakie, and C. W. Gardiner, "Properties of the stochastic Gross-Pitaevskii equation: finite temperature Ehrenfest relations and the optimal plane wave representation", en, J. Phys. B: At. Mol. Opt. Phys. **38**, 4259 (2005).

[138] T. Sato, Y. Kato, T. Suzuki, and N. Kawashima, "Validity of projected Gross-Pitaevskii simulation: Comparison with quantum Monte Carlo", Phys. Rev. E **85**, 050105 (2012).

[139] M.-O. Mewes, M. R. Andrews, N. J. van Druten, D. M. Kurn, D. S. Durfee, C. G. Townsend, and W. Ketterle, "Collective Excitations of a Bose-Einstein Condensate in a Magnetic Trap", Phys. Rev. Lett. **77**, 988–991 (1996).

[140] D. S. Jin, M. R. Matthews, J. R. Ensher, C. E. Wieman, and E. A. Cornell, "Temperature-Dependent Damping and Frequency Shifts in Collective Excitations of a Dilute Bose-Einstein Condensate", Phys. Rev. Lett. **78**, 764–767 (1997).

[141] K. W. Madison, F. Chevy, V. Bretin, and J. Dalibard, "Stationary States of a Rotating Bose-Einstein Condensate: Routes to Vortex Nucleation", Phys. Rev. Lett. **86**, 4443–4446 (2001).

[142] P. C. Haljan, I. Coddington, P. Engels, and E. A. Cornell, "Driving Bose-Einstein-Condensate Vorticity with a Rotating Normal Cloud", Phys. Rev. Lett. **87**, 210403 (2001).

[143] C. Raman, J. R. Abo-Shaeer, J. M. Vogels, K. Xu, and W. Ketterle, "Vortex Nucleation in a Stirred Bose-Einstein Condensate", Phys. Rev. Lett. **87**, 210402 (2001).

[144] S. Choi, S. A. Morgan, and K. Burnett, "Phenomenological damping in trapped atomic Bose-Einstein condensates", Phys. Rev. A **57**, 4057–4060 (1998).

[145] C. W. Gardiner, P. Zoller, R. J. Ballagh, and M. J. Davis, "Kinetics of Bose-Einstein Condensation in a Trap", Phys. Rev. Lett. **79**, 1793–1796 (1997).

[146] L. P. Pitaevskii and E. M. Lifshitz, *Physical Kinetics: Volume 10*, Vol. 10 (Butterworth-Heinemann, 2012).

[147] M. Tsubota, K. Kasamatsu, and M. Ueda, "Vortex Lattice Formation in a Rotating Bose-Einstein Condensate", Phys. Rev. A **65**, 023603 (2002).

[148] A. A. Penckwitt, R. J. Ballagh, and C. W. Gardiner, "Nucleation, Growth, and Stabilization of Bose-Einstein Condensate Vortex Lattices", Phys. Rev. Lett. **89**, 260402 (2002).

[149] E. J. M. Madarassy and C. F. Barenghi, "Vortex Dynamics in Trapped Bose-Einstein Condensate", J. Low Temp. Phys. **152**, 122–135 (2008).

[150] J. R. Abo-Shaeer, C. Raman, and W. Ketterle, "Formation and Decay of Vortex Lattices in Bose-Einstein Condensates at Finite Temperatures", Phys. Rev. Lett. **88**, 070409 (2002).

[151] N. P. Proukakis, S. A. Gardiner, Matthew. Davis, and M. Szymanska, *Quantum Gases: Finite Temperature And Non-equilibrium Dynamics.* Cold Atoms (Imperial College Press, 2013).

[152] N. G. Berloff and B. V. Svistunov, "Scenario of strongly non equilibriated Bose-Einstein condensation", Phys. Rev. A **66**, 013603 (2002).

[153] M. J. Steel, M. K. Olsen, L. I. Plimak, P. D. Drummond, S. M. Tan, M. J. Collett, D. F. Walls, and R. Graham, "Dynamical quantum noise in trapped Bose-Einstein condensates", Phys. Rev. A **58**, 4824–4835 (1998).

[154] C. W. Gardiner and P. Zoller, *Quantum Noise: A Handbook of Markovian and Non-Markovian Quantum Stochastic Methods with Applications to Quantum Optics* (Springer, Berlin, 2000).

[155] A. Polkovnikov, "Quantum corrections to the dynamics of interacting bosons: Beyond the truncated Wigner approximation", Phys. Rev. A **68**, 053604 (2003).

[156] A. A. Norrie, R. J. Ballagh, and C. W. Gardiner, "Quantum turbulence and correlations in Bose-Einstein condensate collisions", Phys. Rev. A **73**, 043617 (2006).

[157] H. T. C. Stoof and M. J. Bijlsma, "Dynamics of Fluctuating Bose–Einstein Condensates", J. Low Temp. Phys. **124**, 431–442 (2001).

[158] C. W. Gardiner, J. R. Anglin, and T. I. A. Fudge, "The stochastic Gross-Pitaevskii equation", J. Phys. B: At. Mol. Opt. Phys. **35**, 1555–1582 (2002).

[159] S. P. Cockburn and N. P. Proukakis, "The stochastic Gross-Pitaevskii equation and some applications", Laser Phys. **19**, 558–570 (2009).

[160] R. W. Pattinson, N. P. Proukakis, and N. G. Parker, "Equilibration of a finite-temperature binary Bose gas formed by population transfer", Phys. Rev. A **90**, 033625 (2014).

[161] E. Zaremba, T. Nikuni, and A. Griffin, "Dynamics of Trapped Bose Gases at Finite Temperatures", J. Low Temp. Phys. **116**, 277–345 (1999).

[162] A. L. Fetter and A. A. Svidzinsky, "Vortices in a trapped dilute Bose-Einstein condensate", J. Phys.: Condens. Matter **13** (2001).

[163] P. Engels, I. Coddington, P. C. Haljan, V. Schweikhard, and E. A. Cornell, "Observation of Long-Lived Vortex Aggregates in Rapidly Rotating Bose-Einstein Condensates", Phys. Rev. Lett. **90**, 170405 (2003).

[164] P. Engels, I. Coddington, P. C. Haljan, and E. A. Cornell, "Using anisotropic compression to melt a vortex lattice in a Bose-Einstein condensate", Physica B **329**, 7 (2003).

[165] P. Engels, I. Coddington, V. Schweikhard, and E. A. Cornell, "Vortex Lattice Dynamics in a Dilute Gas BEC", J. Low Temp. Phys. **134**, 683 (2004).

[166] V. Schweikhard, I. Coddington, P. Engels, V. P. Mogendorff, and E. A. Cornell, "Rapidly Rotating Bose-Einstein Condensates in and near the Lowest Landau Level", Phys. Rev. Lett. **92**, 040404 (2004).

[167] G. P. Bewley, M. S. Paoletti, K. R. Sreenivasan, and D. P. Lathrop, "Characterization of reconnecting vortices in superfluid helium", Proc. Nat. Acad. Sci. USA. **105**, 13707–13710 (2008).

[168] D. V. Freilich, D. M. Bianchi, A. M. Kaufman, T. K. Langin, and D. S. Hall, "Real-Time Dynamics of Single Vortex Lines and Vortex Dipoles in a Bose-Einstein Condensate", Science **329**, 1182–1185 (2010).

[169] J. R. Anglin and W. Ketterle, "Bose-Einstein condensation of atomic gases", Nature **416**, 211–218 (2002).

[170] T. Aioi, T. Kadokura, T. Kishimoto, and H. Saito, "Controlled Generation and Manipulation of Vortex Dipoles in a Bose-Einstein Condensate", Phys. Rev. X **1**, 021003 (2011).

[171] S. W. Seo, B. Ko, J. H. Kim, and Y.Shin, "Observation of vortex-antivortex pairing in decaying 2D turbulence of a superfluid gas", Sci. Rep. **7**, 4587 (2017).

[172] S. Sinha and Y. Castin, "Dynamic Instability of a Rotating Bose-Einstein Condensate", Phys. Rev. Lett. **87**, 190402 (2001).

[173] K. Kasamatsu, M. Tsubota, and M. Ueda, "Nonlinear dynamics of vortex lattice formation in a rotating Bose-Einstein condensate", Phys. Rev. A **67**, 033610 (2003).

[174] C. Lobo, A. Sinatra, and Y. Castin, "Vortex Lattice Formation in Bose-Einstein Condensates", Phys. Rev. Lett. **92**, 020403 (2004).

[175] N. G. Parker, R. M. W. van Bijnen, and A. M. Martin, "Instabilities leading to vortex lattice formation in rotating Bose-Einstein condensates", Phys. Rev. A **73**, 061603 (2006).

[176] T. Mizushima, Y. Kawaguchi, K. Machida, T. Ohmi, T. Isoshima, and M. M. Salomaa, "Collective Oscillations of Vortex Lattices in Rotating Bose-Einstein Condensates", Phys. Rev. Lett. **92**, 060407 (2004).

[177] N. G. Parker and C. S. Adams, "Emergence and Decay of Turbulence in Stirred Atomic Bose-Einstein Condensates", Phys. Rev. Lett. **95**, 145301 (2005).

[178] T. M. Wright, R. J. Ballagh, A. S. Bradley, P. B. Blakie, and C. W. Gardiner, "Dynamical thermalization and vortex formation in stirred two-dimensional Bose-Einstein condensates", Phys. Rev. A **78**, 063601 (2008).

[179] W. J. Kwon, G. Moon, J.-y. Choi, S. W. Seo, and Y.-i. Shin, "Relaxation of superfluid turbulence in highly oblate Bose-Einstein condensates", Phys. Rev. A **90**, 063627 (2014).

[180] G. Stagg, A. J. Allen, N. G. Parker, and C. F. Barenghi, "Generation and decay of two-dimensional quantum turbulence in a trapped Bose-Einstein condensate", Phys. Rev. A **91**, 013612 (2015).

[181] G. W. Stagg, N. G. Parker, and C. F. Barenghi, "Ultraquantum turbulence in a quenched homogeneous Bose gas", Phys. Rev. A **94**, 053632 (2016).

[182] B. Jackson, J. F. McCann, and C. S. Adams, "Vortex Formation in Dilute Inhomogeneous Bose-Einstein Condensates", Phys. Rev. Lett. **80**, 3903–3906 (1998).

[183] G. W. Stagg, N. G. Parker, and C. F. Barenghi, "Quantum analogues of classical wakes in Bose–Einstein condensates", J. Phys. B: At. Mol. Opt. Phys. **47**, 095304 (2014).

[184] W. J. Kwon, S. W. Seo, and Y.-i. Shin, "Periodic shedding of vortex dipoles from a moving penetrable obstacle in a Bose-Einstein condensate", Phys. Rev. A **92**, 033613 (2015).

[185] S. Musser, D. Proment, M. Onorato, and W. T. M. Irvine, "Starting Flow Past an Airfoil and its Acquired Lift in a Superfluid", Phys. Rev. Lett. **123**, 154502 (2019).

[186] K. Sasaki, N. Suzuki, and H. Saito, "Bénard–von Kármán Vortex Street in a Bose-Einstein Condensate", Phys. Rev. Lett. **104**, 150404 (2010).

[187] K. Xhani, E. Neri, L. Galantucci, F. Scazza, A. Burchianti, K.-L. Lee, C. F. Barenghi, A. Trombettoni, M. Inguscio, M. Zaccanti, G. Roati, and N. P. Proukakis, "Critical Transport and Vortex Dynamics in a Thin Atomic Josephson Junction", Phys. Rev. Lett. **124**, 045301 (2020).

[188] G. Gauthier, S. S. Szigeti, M. T. Reeves, M. Baker, T. A. Bell, H. Rubinsztein-Dunlop, M. J. Davis, and T. W. Neely, "Quantitative Acoustic Models for Superfluid Circuits", Phys. Rev. Lett. **123**, 260402 (2019).

[189] C. F. Barenghi, N. G. Parker, N. P. Proukakis, and C. S. Adams, "Decay of quantised vorticity by sound emission", J. Low Temp. Phys. **138**, 629–634 (2005).

[190] R. M. Caplan, J. D. Talley, R Carretero-González, and P. G. Kevrekidis, "Scattering and leapfrogging of vortex rings in a superfluid", Physics of Fluids **26** (2014).

[191] A. Griffin, G. W. Stagg, N. P. Proukakis, and C. F. Barenghi, "Vortex scattering by impurities in a Bose–Einstein condensate", J. Phys. B: At. Mol. Opt. Phys. **50**, 115003 (2017).

[192] O. R. Stockdale, M. T. Reeves, and M. J. Davis, "Dynamical mechanisms of vortex pinning in superfluid thin films", Phys. Rev. Lett. **127**, 255302 (2021).

[193] L. Galantucci, M. Sciacca, N. Parker, A. Baggaley, and C. Barenghi, "Classical and quantum vortex leapfrogging in two-dimensional channels", Journal of Fluid Mechanics **912** (2021).

[194] D. Proment, M. Onorato, and C. F. Barenghi, "Vortex knots in a Bose-Einstein condensate", Phys. Rev. E **85**, 036306 (2012).

[195] C. Ticknor, V. P. Ruban, and P. G. Kevrekidis, "Quasistable quantum vortex knots and links in anisotropic harmonically trapped Bose-Einstein condensates", Phys. Rev. A **99**, 063604 (2019).

[196] A. J. Groszek, M. J. Davis, and T. P. Simula, "Decaying quantum turbulence in a two-dimensional Bose-Einstein condensate at finite temperature", SciPost Phys. **8**, 39 (2020).

[197] A. L. Fetter, "Rotating trapped Bose-Einstein condensates", Rev. Mod. Phys. **81**, 647–691 (2009).

[198] R. Feynman, *Progress in low temperature physics* (North-Holland, Amsterdam, 1955).

[199] J. R. Abo-Shaeer, C. Raman, J. M. Vogels, and W. Ketterle, "Observation of vortex lattices in Bose-Einstein condensates", Science **292**, 476–479 (2001).

[200] A. A. Abrikosov, "On the magnetic properties of superconductors of the second group", Sov. Phys. JETP **5**, 1174–1182 (1957).

[201] V. K. Tkachenko, "On Vortex Lattices", Sov. Phys. JETP **22** (1966).

[202] E. J. Yarmchuk, M. J. V. Gordon, and R. E. Packard, "Observation of Stationary Vortex Arrays in Rotating Superfluid Helium", Phys. Rev. Lett. **43**, 214–217 (1979).

[203] N. A. Keepfer, G. W. Stagg, L. Galantucci, C. F. Barenghi, and N. G. Parker, "Spin-up of a superfluid vortex lattice driven by rough boundaries", Phys. Rev. B **102**, 144520 (2020).

[204] C. N. Weiler, T. W. Neely, D. R. Scherer, A. S. Bradley, M. J. Davis, and B. P. Anderson, "Spontaneous vortices in the formation of Bose–Einstein condensates", Nature **455**, 958–951 (2008).

[205] T. W. B. Kibble, "Topology of cosmic domains and strings", J. Phys. A: Mat. Gen. **9** (1976).

[206] W. Zurek, "Cosmological experiments in superfluid helium?", Nature **317**, 505–508 (1985).

[207] J. R. Anglin and W. H. Zurek, "Vortices in the Wake of Rapid Bose-Einstein Condensation", Phys. Rev. Lett. **83**, 1707–1710 (1999).

[208] Ł. Dobrek, M. Gajda, M. Lewenstein, K. Sengstock, G. Birkl, and W. Ertmer, "Optical generation of vortices in trapped Bose-Einstein condensates", Phys. Rev. A **60**, R3381–R3384 (1999).

[209] A. E. Leanhardt, A. Görlitz, A. P. Chikkatur, D. Kielpinski, Y. Shin, D. E. Pritchard, and W. Ketterle, "Imprinting Vortices in a Bose-Einstein Condensate using Topological Phases", Phys. Rev. Lett. **89**, 190403 (2002).

[210] R. Onofrio, D. S. Durfee, C. Raman, M. Köhl, C. E. Kuklewicz, and W. Ketterle, "Surface Excitations of a Bose-Einstein Condensate", Phys. Rev. Lett. **84**, 810–813 (2000).

[211] F. Chevy, K. W. Madison, and J. Dalibard, "Measurement of the Angular Momentum of a Rotating Bose-Einstein Condensate", Phys. Rev. Lett. **85**, 2223–2227 (2000).

[212] E. Hodby, G. Hechenblaikner, S. A. Hopkins, O. M. Maragò, and C. J. Foot, "Vortex Nucleation in Bose-Einstein Condensates in an Oblate, Purely Magnetic Potential", Phys. Rev. Lett. **88**, 010405 (2001).

[213] J. Tempere and J. T. Devreese, "Fringe pattern of interfering Bose–Einstein condensates with a vortex", Solid State Communications **108**, 993–996 (1998).

[214] E. L. Bolda and D. F. Walls, "Detection of Vorticity in Bose-Einstein Condensed Gases by Matter-Wave Interference", Phys. Rev. Lett. **81**, 5477–5480 (1998).

[215] T. W. Neely, E. C. Samson, A. S. Bradley, M. J. Davis, and B. P. Anderson, "Observation of Vortex Dipoles in an Oblate Bose-Einstein Condensate", Phys. Rev. Lett. **104**, 160401 (2010).

[216] W. J. Kwon, G. Moon, S. W. Seo, and Y. Shin, "Critical velocity for vortex shedding in a Bose-Einstein condensate", Phys. Rev. A **91**, 053615 (2015).

[217] A. J. Bray, "Theory of phase-ordering kinetics", Adv. Phys. **43**, 357–459 (1994).

[218] H. E. Hall, "An Experimental and theoretical study of torsional oscillations in uniformly rotating liquid helium II", Proc. Royal. Soc. London. A (1958).

[219] Z. Dutton, M. Budde, C. Slowe, and L. V. Hau, "Observation of quantum shock waves created with ultra-compressed slow light pulses in a Bose-Einstein condensate", Science **293**, 663–668 (2001).

[220] K. W. Schwarz, "Three-dimensional vortex dynamics in superfluid ^{4}He: Line-line and line-boundary interactions", Phys. Rev. B **31**, 5782–5804 (1985).

[221] W. Thompson, "XXIV. Vibrations of a columnar vortex", The London, Edinburgh, and Dublin Philosophical Magazine and Journal of Science **10** (1880).

[222] E. Fonda, D. P. Meichle, N. T. Ouellette, S. Hormoz, and D. P. Lathrop, "Direct observation of Kelvin waves excited by quantized vortex reconnection", Proc. Nat. Acad. Sci. **111**, 4707–4710 (2014).

[223] A. Villois, D. Proment, and G. Krstulovic, "Evolution of a superfluid vortex filament tangle driven by the Gross-Pitaevskii equation", Phys. Rev. E **93**, 061103 (R) (2016).

[224] S. Zuccher, M. Caliari, A. W. Baggaley, and C. F. Barenghi, "Quantum vortex Reconnections", Physics of Fluids **24** (2012).

[225] S. Serafini, L. Galantucci, E. Iseni, T. Bienaimé, R. N. Bisset, C. F. Barenghi, F. Dalfovo, G. Lamporesi, and G. Ferrari, "Vortex Reconnections and Rebounds in Trapped Atomic Bose-Einstein Condensates", Phys. Rev. X **7**, 021031 (2017).

[226] D. Kleckner, L. Kauffman, and W. Irvine, "How superfluid vortex knots untie.", Nature Physics **12**, 650–655 (2016).

[227] M. W. Scheeler, D. Kleckner, D. Proment, G. L. Kindlmann, and W. T. M. Irvine, "Helicity conservation by flow across scales in reconnecting vortex links and knots", Proc. Nat. Acad. Sci. **111**, 15350–15355 (2014).

[228] L. Galantucci, A. W. Baggaley, N. G. Parker, and C. F. Barenghi, "Crossover from interaction to driven regimes in quantum vortex reconnections", Proc. Nat. Acad. Sci. **116**, 12204–12211 (2019).

[229] D. Proment and G. Krstulovic, "Matching theory to characterize sound emission during vortex reconnection in quantum fluids", Phys. Rev. Fluids **5**, 104701 (2020).

[230] A. L. Fetter, "Vortices in an Imperfect Bose Gas. IV. Translational Velocity", Phys. Rev. **151**, 100–104 (1966).

[231] O. Törnkvist and E. Schröder, "Vortex Dynamics in Dissipative Systems", Phys. Rev. Lett. **78**, 1908–1911 (1997).

[232] A. W. Baggaley and C. F. Barenghi, "Decay of homogeneous two-dimensional quantum turbulence", Phys. Rev. A **97**, 033601 (2018).

[233] C. A. Jones and P. H. Roberts, "Motions in a Bose condensate. IV. Axisymmetric solitary waves", J. Phys. A: Mat. Gen. **15**, 2599–2619 (1982).

[234] H. Pu, C. K. Law, J. H. Eberly, and N. P. Bigelow, "Coherent disintegration and stability of vortices in trapped Bose condensates", Phys. Rev. A **59**, 1533–1537 (1999).

[235] J. A. M. Huhtamäki, M. Möttönen, T. Isoshima, V. Pietilä, and S. M. M. Virtanen, "Splitting Times of Doubly Quantized Vortices in Dilute Bose-Einstein Condensates", Phys. Rev. Lett. **97**, 110406 (2006).

[236] Y. Shin, M. Saba, M. Vengalattore, T. A. Pasquini, C. Sanner, A. E. Leanhardt, M. Prentiss, D. E. Pritchard, and W. Ketterle, "Dynamical Instability of a Doubly Quantized Vortex in a Bose-Einstein Condensate", Phys. Rev. Lett. **93**, 160406 (2004).

[237] T. P. Simula, S. M. M. Virtanen, and M. M. Salomaa, "Stability of multiquantum vortices in dilute Bose-Einstein condensates", Phys. Rev. A **65**, 033614 (2002).

[238] J. A. M. Huhtamäki, M. Möttönen, and S. M. M. Virtanen, "Dynamically stable multiply quantized vortices in dilute Bose-Einstein condensates", Phys. Rev. A **74**, 063619 (2006).

[239] C. Elphickand and E. Meron, "Dynamics of phase singularities in two-dimensional oscillating systems", Physica D: Nonlinear Phenomena **53**, 385–399 (1991).

[240] S. Rica and E. Tirapegui, "Analytical description of a state dominated by spiral defects in two-dimensional extended systems", Physica D: Nonlinear Phenomena **48**, 396–424 (1991).

[241] N. G. Berloff, "Padé approximations of solitary wave solutions of the Gross-Pitaevskii equation", J. Phys. A: Mat. Gen. **37**, 1617–1632 (2004).

[242] A. S. Bradley and B. P. Anderson, "Energy Spectra of Vortex Distributions in Two-Dimensional Quantum Turbulence", Phys. Rev. X **2**, 041001 (2012).

[243] T. M. Wright, A. S. Bradley, and R. J. Ballagh, "Nonequilibrium dynamics of vortex arrest in a finite-temperature Bose-Einstein condensate", Phys. Rev. A **81**, 013610 (2010).

[244] D. E. Sheehy and L. Radzihovsky, "Vortices in spatially inhomogeneous superfluids", Phys. Rev. A **70**, 063620 (2004).

[245] A. L. Fetter, "Lowest-Landau-level description of a Bose-Einstein condensate in a rapidly rotating anisotropic trap", Phys. Rev. A **75**, 013620 (2007).

[246] A. Aftalion and I. Danaila, "Three-dimensional vortex configurations in a rotating Bose-Einstein condensate", Phys. Rev. A **68**, 023603 (2003).

[247] A. Aftalion and I. Danaila, "Giant vortices in combined harmonic and quartic traps", Phys. Rev. A **69**, 033608 (2004).

[248] P. Muruganandam and S. Adhikari, "Fortran programs for the time-dependent Gross–Pitaevskii equation in a fully anisotropic trap", Comput. Phys. Comm. **180**, 1888–1912 (2009).

[249] R. K. Kumar, V. Lončar, P. Muruganandam, S. K. Adhikari, and A. Balaž, "C and Fortran OpenMP programs for rotating Bose–Einstein condensates", Comput. Phys. Comm. **240**, 74–82 (2019).

[250] W. Bao, H. Wang, and P. A. Markowich, "Ground, Symmetric and Central Vortex States in Rotating Bose-Einstein Condensates", Commun. Math. Sci. **3**, 57–88 (2005).

[251] W. Bao and Q. Du, "Computing the Ground State Solution of Bose–Einstein Condensates by a Normalized Gradient Flow", SIAM J. Sci. Comput. **25**, 1674–1697 (2004).

[252] W. Bao, I.-L. Chern, and F. Y. Lim, "Efficient and spectrally accurate numerical methods for computing ground and first excited states in Bose–Einstein condensates", J. Comput. Phys. **219**, 836–854 (2006).

[253] X. Antoine and R. Duboscq, "GPELab, a Matlab toolbox to solve Gross–Pitaevskii equations I: Computation of stationary solutions", Comput. Phys. Comm. **185**, 2969–2991 (2014).

[254] J. J. García-Ripoll and V. M. Pérez-García, "Vortex bending and tightly packed vortex lattices in Bose-Einstein condensates", Phys. Rev. A **64**, 053611 (2001).

[255] J. J. García-Ripoll and V. M. Pérez-García, "Optimizing Schrödinger Functionals Using Sobolev Gradients: Applications to Quantum Mechanics and Nonlinear Optics", SIAM J. Sci. Comput. **23**, 1316–1334 (2001).

[256] I. Danaila and P. Kazemi, "A New Sobolev Gradient Method for Direct Minimization of the Gross–Pitaevskii Energy with Rotation", SIAM J. Sci. Comput. **32**, 2447–2467 (2010).

[257] G. Vergez, I. Danaila, S. Auliac, and F. Hecht, "A finite-element toolbox for the stationary Gross–Pitaevskii equation with rotation", Comput. Phys. Comm. **209**, 144–162 (2016).

[258] J. Javanainen and J. Ruostekoski, "Symbolic calculation in development of algorithms: split-step methods for the Gross–Pitaevskii equation", J. Phys. A: Mat. Gen. **39**, L179 (2006).

[259] B.-W. Jeng, Y.-S. Wang, and C.-S. Chien, "A two-parameter continuation algorithm for vortex pinning in rotating Bose–Einstein condensates", Comput. Phys. Comm. **184**, 493–508 (2013).

[260] C. M. Dion and E. Cancès, "Spectral method for the time-dependent Gross-Pitaevskii equation with a harmonic trap", Phys. Rev. E **67**, 046706 (2003).

[261] T.-L. Ho, "Bose-Einstein Condensates with Large Number of Vortices", Phys. Rev. Lett. **87**, 060403 (2001).

[262] D. Butts and D. Rokhsar, "Predicted signatures of rotating Bose–Einstein condensates", Nature **397**, 327–329 (1999).

[263] A. Aftalion, X. Blanc, and J. Dalibard, "Vortex patterns in a fast rotating Bose-Einstein condensate", Phys. Rev. A **71**, 023611 (2005).

[264] E. J. Mueller and T.-L. Ho, "Two-Component Bose-Einstein Condensates with a Large Number of Vortices", Phys. Rev. Lett. **88**, 180403 (2002).

[265] N. R. Cooper, S. Komineas, and N. Read, "Vortex lattices in the lowest Landau level for confined Bose-Einstein condensates", Phys. Rev. A **70**, 033604 (2004).

[266] G. Watanabe, G. Baym, and C. J. Pethick, "Landau Levels and the Thomas-Fermi Structure of Rapidly Rotating Bose-Einstein Condensates", Phys. Rev. Lett. **93**, 190401 (2004).

[267] E. B. Sonin, "Ground state and Tkachenko modes of a rapidly rotating Bose-Einstein condensate in the lowest-Landau-level state", Phys. Rev. A **72**, 021606 (2005).

[268] A. Aftalion, X. Blanc, and F. Nier, "Vortex distribution in the Lowest Landau Level", Phys. Rev. A **73**, 011601 (2006).

[269] M. Cozzini, S. Stringari, and C. Tozzo, "Vortex lattices in Bose-Einstein condensates: From the Thomas-Fermi regime to the lowest-Landau-level regime", Phys. Rev. A **73**, 023615 (2006).

[270] S. I. Matveenko, D. Kovrizhin, S. Ouvry, and G. V. Shlyapnikov, "Vortex structures in rotating Bose-Einstein condensates", Phys. Rev. A **80**, 063621 (2009).

[271] S. Komineas and N. R. Cooper, "Vortex lattices in Bose-Einstein condensates with dipolar interactions beyond the weak-interaction limit", Phys. Rev. A **75**, 023623 (2007).

[272] L. Mingarelli, E. E. Keaveny, and R. Barnett, "Simulating infinite vortex lattices in superfluids", J. Phys.: Condens. Matter **28**, 285201 (2016).

[273] T. S. Wood, M. Mesgarnezhad, G. W. Stagg, and C. F. Barenghi, "Quasiperiodic boundary conditions for three-dimensional superfluids", Phys. Rev. B **100**, 024505 (2019).

[274] D. Landau and E. Lifshitz, *Statistical Physics Part 1, Vol. 5* (Butterworth Heinmann, Oxford, 1981).

[275] N. R. Cooper, N. K. Wilkin, and J. M. F. Gunn, "Quantum Phases of Vortices in Rotating Bose-Einstein Condensates", Phys. Rev. Lett. **87**, 120405 (2001).

[276] S. Komineas and N. R. Cooper, "Vortex lattices for ultracold bosonic atoms in a non-Abelian gauge potential", Phys. Rev. A **85**, 053623 (2012).

[277] V. Fock, "Bemerkung zur Quantelung des harmonischen Oszillators im Magnetfeld", Z. Phys. **47**, 446–448 (1928).

[278] D. Yoshioka, B. I. Halperin, and P. A. Lee, "Ground State of Two-Dimensional Electrons in Strong Magnetic Fields and $\frac{1}{3}$ Quantized Hall Effect", Phys. Rev. Lett. **50**, 1219–1222 (1983).

[279] N. Byers and C. N. Yang, "Theoretical Considerations Concerning Quantized Magnetic Flux in Superconducting Cylinders", Phys. Rev. Lett. **7**, 46–49 (1961).

[280] M. Abramowitz and I. A. Stegun, *Handbook of mathematical functions with formulas, graphs, and mathematical tables*, Vol. 55 (US Government printing office, 1948).

[281] P. B. Blakie, "Numerical method for evolving the projected Gross-Pitaevskii equation", Phys. Rev. E **78**, 026704 (2008).

[282] J. P. Boyd, *Chebyshev and Fourier Spectral Methods*, 2nd (Dover, New York, 2000).

[283] P. J. Prince and J. R. J.R. Dormand, "High order embedded Runge-Kutta formulae", Journal of Computational and Applied Mathematics **7**, 67–75 (1981).

[284] T. J. Dekker, "A floating-point technique for extending the available precision", Numerische Mathematik **18**, 224–242 (1971).

[285] J. Schole, B. Nowak, and T. Gasenzer, "Critical dynamics of a two-dimensional superfluid near a nonthermal fixed point", Phys. Rev. A **86**, 013624 (2012).

[286] N. D. Mermin and H. Wagner, "Absence of Ferromagnetism or Antiferromagnetism in One- or Two-Dimensional Isotropic Heisenberg Models", Phys. Rev. Lett. **17**, 1133–1136 (1966).

[287] P. C. Hohenberg, "Existence of Long-Range Order in One and Two Dimensions", Phys. Rev. **158**, 383–386 (1967).

[288] P. M. Chaikin and T. C. Lubensky, *Principles of Condensed Matter Physics* (Cambridge University Press, 1995).

[289] V. Berezinskii, "Destruction of long-range order in one-dimensional and two-dimensional systems having a continuous symmetry group", Sov. Phys. JETP **32**, 493–500 (1971).

[290] J. M. Kosterlitz and D. J. Thouless, "Ordering, metastability and phase transitions in two-dimensional systems", J. Phys. C: Solid State Physics **6**, 1181–1203 (1973).

[291] D. J. Bishop and J. D. Reppy, "Study of the Superfluid Transition in Two-Dimensional ^{4}He Films", Phys. Rev. Lett. **40**, 1727–1730 (1978).

[292] E. Small, R. Pugatch, and Y. Silberberg, "Berezinskii-Kosterlitz-Thouless crossover in a photonic lattice", Phys. Rev. A **83**, 013806 (2011).

[293] R. J. Fletcher, M. Robert-de-Saint-Vincent, J. Man, N. Navon, R. P. Smith, K. G. H. Viebahn, and Z. Hadzibabic, "Connecting Berezinskii-Kosterlitz-Thouless and BEC Phase Transitions by Tuning Interactions in a Trapped Gas", Phys. Rev. Lett. **114**, 255302 (2015).

[294] N. Prokof'ev, O. Ruebenacker, and B. Svistunov, "Critical Point of a Weakly Interacting Two-Dimensional Bose Gas", Phys. Rev. Lett. **87**, 270402 (2001).

[295] N. Prokof'ev and B. Svistunov, "Two-dimensional weakly interacting Bose gas in the fluctuation region", Phys. Rev. A **66**, 043608 (2002).

[296] L. Giorgetti, I. Carusotto, and Y. Castin, "Semiclassical field method for the equilibrium Bose gas and application to thermal vortices in two dimensions", Phys. Rev. A **76**, 013613 (2007).

[297] M. Holzmann and W. Krauth, "Kosterlitz-Thouless Transition of the Quasi-Two-Dimensional Trapped Bose Gas", Phys. Rev. Lett. **100**, 190402 (2008).

[298] T. P. Simula, M. J. Davis, and P. B. Blakie, "Superfluidity of an interacting trapped quasi-two-dimensional Bose gas", Phys. Rev. A **77**, 023618 (2008).

[299] R. N. Bisset, M. J. Davis, T. P. Simula, and P. B. Blakie, "Quasicondensation and coherence in the quasi-two-dimensional trapped Bose gas", Phys. Rev. A **79**, 033626 (2009).

[300] R. Bisset, *C-Field and Mean-Field Treatments of the Quasi-Two-Dimensional Harmonically Confined Bose Gas* (University of Otago, New Zealand, 2009).

[301] C. J. Foster, P. B. Blakie, and M. J. Davis, "Vortex pairing in two-dimensional Bose gases", Phys. Rev. A **81**, 023623 (2010).

[302] M. Holzmann, M. Chevallier, and W. Krauth, "Universal correlations and coherence in quasi-two-dimensional trapped Bose gases", Phys. Rev. A **81**, 043622 (2010).

[303] L. Mathey and A. Polkovnikov, "Light cone dynamics and reverse Kibble-Zurek mechanism in two-dimensional superfluids following a quantum quench", Phys. Rev. A **81**, 033605 (2010).

[304] T. M. Wright, N. P. Proukakis, and M. J. Davis, "Many-body physics in the classical-field description of a degenerate Bose gas", Phys. Rev. A **84**, 023608 (2011).

[305] S. P. Cockburn and N. P. Proukakis, "Ab initio methods for finite-temperature two-dimensional Bose gases", Phys. Rev. A **86**, 033610 (2012).

[306] S. Nazarenko, M. Onorato, and D. Proment, "Bose-Einstein condensation and Berezinskii-Kosterlitz-Thouless transition in the two-dimensional nonlinear Schrödinger model", Phys. Rev. A **90**, 013624 (2014).

[307] L. Mathey, K. J. Günter, J. Dalibard, and A. Polkovnikov, "Dynamic Kosterlitz-Thouless transition in two-dimensional Bose mixtures of ultracold atoms", Phys. Rev. A **95**, 053630 (2017).

[308] M. Karl and T. Gasenzer, "Strongly anomalous non-thermal fixed point in a quenched two-dimensional Bose gas", New Journal of Physics **19**, 093014 (2017).

[309] P. Comaron, F. Larcher, F. Dalfovo, and N. P. Proukakis, "Quench dynamics of an ultracold two-dimensional Bose gas", Phys. Rev. A **100**, 033618 (2019).

[310] K. Gawryluk and M. Brewczyk, "Signatures of a universal jump in the superfluid density of a two-dimensional Bose gas with a finite number of particles", Phys. Rev. A **99**, 033615 (2019).

[311] K. Brown, T. Bland, P. Comaron, and N. P. Proukakis, "Periodic quenches across the Berezinskii-Kosterlitz-Thouless phase transition", Phys. Rev. Research **3**, 013097 (2021).

[312] *Example movies of lattice melting.* https://journals.aps.org/pre/supplemental/10.1103/PhysRevE.102.033309.

[313] A. J. Groszek, P. Comaron, N. P. Proukakis, and T. P. Billam, "Crossover in the dynamical critical exponent of a quenched two-dimensional Bose gas", Phys. Rev. Research **3**, 013212 (2021).

[314] H. H. Rugh, "Dynamical approach to temperature", Phys. Rev. Lett. **78**, 772–774 (1997).

[315] H. H. Rugh, "A geometric, dynamical approach to thermodynamics", J. Phys. A: Math. and Gen. **31**, 7761–7770 (1998).

[316] H. H. Rugh, "Microthermodynamic formalism", Phys. Rev. E **64**, 055101 (2001).

[317] M. J. Davis and S. A. Morgan, "Microcanonical temperature for a classical field: Application to Bose-Einstein condensation", Phys. Rev. A **68**, 053615 (2003).

[318] M. J. Davis and P. B. Blakie, "Calculation of the microcanonical temperature for the classical Bose field", J. Phys. A: Mat. Gen. **38**, 10259–10271 (2005).

[319] D. Foster, *Hydrodynamic Fluctuations, Broken Symmetry and Correlation Functions* (1975).

[320] G. Baym, *Mathematical Methods in Solid State and Superfluid Theory* (1969).

[321] C. H. K. Williamson, "Vortex Dynamics in the Cylinder Wake", Annual Review of Fluid Mechanics **28**, 477–539 (1996).

[322] T. Winiecki, B. Jackson, J. F. McCann, and C. S. Adams, "Vortex shedding and drag in dilute Bose-Einstein condensates", J. Phys. B: At. Mol. Opt. Phys. **33**, 4069–4078 (2000).

[323] C. F. Barenghi, "Is the Reynolds number infinite in superfluid turbulence?", Physica D: Nonlinear Phenomena **237**, 2195–2202 (2008).

[324] G. W. Stagg, R. W. Pattinson, C. F. Barenghi, and N. G. Parker, "Critical velocity for vortex nucleation in a finite-temperature Bose gas", Phys. Rev. A **93**, 023640 (2016).

[325] T. Winiecki, J. F. McCann, and C. S. Adams, "Pressure Drag in Linear and Nonlinear Quantum Fluids", Phys. Rev. Lett. **82**, 5186–5189 (1999).

[326] U. Giuriato, G. Krstulovic, and D. Proment, "Clustering and phase transitions in a 2D superfluid with immiscible active impurities", J. Phys. A: Mat. Theor. **52**, 305501 (2019).

[327] G. W. Stagg, N. G. Parker, and C. F. Barenghi, "Superfluid Boundary Layer", Phys. Rev. Lett. **118**, 135301 (2017).

[328] D. Clément, A. F. Varón, J. A. Retter, L. Sanchez-Palencia, A. Aspect, and P. Bouyer, "Experimental study of the transport of coherent interacting matter-waves in a 1D random potential induced by laser speckle", New Journal of Physics **8**, 165–165 (2006).

[329] S. Pilati, S. Giorgini, and N. Prokof'ev, "Superfluid Transition in a Bose Gas with Correlated Disorder", Phys. Rev. Lett. **102**, 150402 (2009).

[330] S. Pilati, S. Giorgini, M. Modugno, and N. Prokof'ev, "Dilute Bose gas with correlated disorder: a path integral Monte Carlo study", New Journal of Physics **12**, 073003 (2010).

[331] L. Pezzé, M. Robert-de-Saint-Vincent, T. Bourdel, J.-P. Brantut, B. Allard, T. Plisson, A. Aspect, P. Bouyer, and L. Sanchez-Palencia, "Regimes of classical transport of cold gases in a two-dimensional anisotropic disorder", New Journal of Physics **13**, 095015 (2011).

[332] T. Bourdel, "Phase diagrams of two-dimensional and three-dimensional disordered Bose gases in the local density approximation", Phys. Rev. A **86**, 063626 (2012).

[333] F. Jendrzejewski, A. Bernard, K. Müller, P. Cheinet, V. Josse, M. Piraud, L. P. andL. Sanchez-Palencia, A. Aspect, and P. Bouyer, "Three-dimensional localization of ultracold atoms in an optical disordered potential", Nature Physics **8**, 398–403 (2012).

[334] S. Krinner, D. Stadler, J. Meineke, J.-P. Brantut, and T. Esslinger, "Superfluidity with disorder in a thin film of quantum gas", Phys. Rev. Lett. **110**, 100601 (2013).

[335] G. Carleo, G. Boéris, M. Holzmann, and L. Sanchez-Palencia, "Universal Superfluid Transition and Transport Properties of Two-Dimensional Dirty Bosons", Phys. Rev. Lett. **111**, 050406 (2013).

[336] C. Meldgin, U. Ray, P. Russ, D. Chen, D. M. Ceperley, and B. DeMarco, "Probing the Bose glass–superfluid transition using quantum quenches of disorder", Nature Phys. **12**, 646–649 (2016).

[337] K. Damle, S. N. Majumdar, and S. Sachdev, "Phase ordering kinetics of the Bose gas", Phys. Rev. A **54**, 5037–5041 (1996).

[338] J. Schole, B. Nowak, and T. Gasenzer, "Critical dynamics of a two-dimensional superfluid near a nonthermal fixed point", Phys. Rev. A **86**, 013624 (2012).

[339] A. J. Groszek, M. J. Davis, D. M. Paganin, K. Helmerson, and T. P. Simula, "Vortex Thermometry for Turbulent Two-Dimensional Fluids", Phys. Rev. Lett. **120**, 034504 (2018).

[340] J. Hofmann, S. S. Natu, and S. Das Sarma, "Coarsening Dynamics of Binary Bose Condensates", Phys. Rev. Lett. **113**, 095702 (2014).

[341] L. A. Williamson and P. B. Blakie, "Universal Coarsening Dynamics of a Quenched Ferromagnetic Spin-1 Condensate", Phys. Rev. Lett. **116**, 025301 (2016).

[342] L. A. Williamson and P. B. Blakie, "Coarsening Dynamics of an Isotropic Ferromagnetic Superfluid", Phys. Rev. Lett. **119**, 255301 (2017).

[343] M. Kulczykowski and M. Matuszewski, "Phase ordering kinetics of a nonequilibrium exciton-polariton condensate", Phys. Rev. B **95**, 075306 (2017).

[344] P. Comaron, G. Dagvadorj, A. Zamora, I. Carusotto, N. P. Proukakis, and M. H. Szymańska, "Dynamical Critical Exponents in Driven-Dissipative Quantum Systems", Phys. Rev. Lett. **121**, 095302 (2018).

[345] V. N. Gladilin and M. Wouters, "Multivortex states and dynamics in nonequilibrium polariton condensates", J. Phys. A: Mat. Theor. **52**, 395303 (2019).

[346] Q. Mei, K. Ji, and M. Wouters, "Spatiotemporal scaling of two-dimensional nonequilibrium exciton-polariton systems with weak interactions", Phys. Rev. B **103**, 045302 (2021).

[347] S. G. Johnson, "Notes on FFT-based differentiation", `https://math.mit.edu/~stevenj/fft-deriv.pdf` (2011).

[348] G. R. Dennis, J. J. Hope and M. T. Johnsson, "XMDS2: Fast, scalable simulation of coupled stochastic partial differential equations", Computer Physics Communications **184**, 201–208 (2013).

[349] C. Raman, M. Köhl, R. Onofrio, D. S. Durfee, C. E. Kuklewicz, Z. Hadzibabic, and W. Ketterle, "Evidence for a Critical Velocity in a Bose-Einstein Condensed Gas", Phys. Rev. Lett. **83**, 2502–2505 (1999).

[350] B. Jackson, J. F. McCann, and C. S. Adams, "Dissipation and vortex creation in Bose-Einstein condensed gases", Phys. Rev. A **61**, 051603 (2000).

[351] A. Griffin, *Excitations in a Bose–condensed liquid* (Cambridge University Press).

[352] E. M. Lifshitz and L. P. Pitaevskii, *Statistical Physics, Part 2: Theory of the Condensed State* (Butterworth Heinmann).

[353] A. Ramanathan, K. C. Wright, S. R. Muniz, M. Zelan, W. T. Hill, C. J. Lobb, K. Helmerson, W. D. Phillips, and G. K. Campbell, "Superflow in a Toroidal Bose-Einstein Condensate: An Atom Circuit with a Tunable Weak Link", Phys. Rev. Lett. **106**, 130401 (2011).

[354] B. Eller, O. Oladehin, D. Fogarty, C. Heller, C. W. Clark, and M. Edwards, "Producing flow in racetrack atom circuits by stirring", Phys. Rev. A **102**, 063324 (2020).

[355] A. Cidrim, F. E. A. dos Santos, L. Galantucci, V. S. Bagnato, and C. F. Barenghi, "Controlled polarization of two-dimensional quantum turbulence in atomic Bose-Einstein condensates", Phys. Rev. A **93**, 033651 (2016).

[356] P. Anderson and P. Itoh, "Pulsar Glitches and restlessness as a hard superfluid phenomenon", Nature **256**, 25–27 (1975).

[357] P. B. Jones, "Motion of Neutron Vortices in the Inner Crust of a Neutron Star", Phys. Rev. Lett. **79**, 792–795 (1997).

[358] P. B. Jones, "Strong Interaction of Vortices with Attractive Point Defects, and Applicationto Neutron Star Rotation", Phys. Rev. Lett. **81**, 4560–4563 (1998).

[359] P. Donati and P. M. Pizzochero, "Is there Nuclear Pinning of Vortices in Superfluid Pulsars?", Phys. Rev. Lett. **90**, 211101 (2003).

[360] B. Link, "Dynamics of Quantum Vorticity in a Random Potential", Phys. Rev. Lett. **102**, 131101 (2009).

[361] K. W. Schwarz, "Vortex Pinning in Superfluid Helium", Phys. Rev. Lett. **47**, 251–254 (1981).

[362] F. De Blasio and G. Lazzari, "Lattice defects in the crust of a neutron star", Nuclear Physics A **633**, 391–405 (1998).

[363] P. B. Jones, "Nature of Fault Planes in Solid Neutron Star Matter", The Astrophysical Journal **595**, 342–345 (2003).

[364] D. S. Tsakadze and S. D. Tsakadze, J. Exp. Theor. Phys. Lett. **22** (1975).

[365] E. L. Andronikashvili, J. S. Tsakadze, and S. J. Tsakadze, "Spontaneous acceleration of slowly rotating Helium II— A manifestation of a phase transition in the system of macroscopic quantum vortices", J. Low Temp. Phys. **34**, 13–16 (1979).

[366] R. Bhat, M. J. Holland, and L. D. Carr, "Bose-Einstein Condensates in Rotating Lattices", Phys. Rev. Lett. **96**, 060405 (2006).

[367] L. Warszawski, A. Melatos, and N. G. Berloff, "Unpinning triggers for superfluid vortex avalanches", Phys. Rev. B **85**, 104503 (2012).

[368] H. Helmholtz, "Lxiii. on integrals of the hydrodynamical equations, which express vortex-motion", The London, Edinburgh, and Dublin Philosophical Magazine and Journal of Science **33**, 485–512 (1867).

[369] G. Kirchhoff and K. Hensel, *Vorlesungen über mathematische Physik*, Vol. 1 (Druck und Verlag von BG Teubner, 1883).

[370] L. Onsager, International Conference of Theoretical Physics (Science Council of Japan, Kyoto and Tokyo), 877–880 (1953).

[371] G. L. Eyink and K. R. Sreenivasan, "Onsager and the theory of hydrodynamic turbulence", Rev. Mod. Phys. **78**, 87–135 (2006).

[372] H. M. Nilsen, G. Baym, and C. J. Pethick, "Velocity of vortices in inhomogeneous Bose–Einstein condensates", Proc. Nat. Acad. Sci. **103**, 7978 (2006).

[373] D. M. Jezek and H. M. Cataldo, "Vortex velocity field in inhomogeneous media: A numerical study in Bose-Einstein condensates", Phys. Rev. A **77**, 043602 (2008).

[374] S. Middelkamp, P. G. Kevrekidis, D. J. Frantzeskakis, R. Carretero-González, and P. Schmelcher, "Bifurcations, stability, and dynamics of multiple matter-wave vortex states", Phys. Rev. A **82**, 013646 (2010).

[375] S. Middelkamp, P. J. Torres, P. G. Kevrekidis, D. J. Frantzeskakis, R. Carretero-González, P. Schmelcher, D. V. Freilich, and D. S. Hall, "Guiding-center dynamics of vortex dipoles in Bose-Einstein condensates", Phys. Rev. A **84**, 011605 (2011).

[376] P. Torres, P. Kevrekidis, D. Frantzeskakis, R. Carretero-González, P. Schmelcher, and D. Hall, "Dynamics of vortex dipoles in confined Bose–Einstein condensates", Phys. Lett. A **375**, 3044–3050 (2011).

[377] P. J. Torres, R. Carretero-González, P. S. S. Middelkamp, D. J. Frantzeskakis, and P. Kevrekidis, "Vortex interaction dynamics in trapped Bose-Einstein condensates", Communications on Pure and Applied Analysis **10**, 1589–1615 (2011).

[378] A. V. Murray, A. J. Groszek, P. Kuopanportti, and T. Simula, "Hamiltonian dynamics of two same-sign point vortices", Phys. Rev. A **93**, 033649 (2016).

[379] J. H. Kim, W. J. Kwon, and Y. Shin, "Role of thermal friction in relaxation of turbulent Bose-Einstein condensates", Phys. Rev. A **94**, 033612 (2016).

[380] F. E. A. dos Santos, "Hydrodynamics of vortices in Bose-Einstein condensates: A defect-gauge field approach", Phys. Rev. A **94**, 063633 (2016).

[381] X. Yu and A. S. Bradley, "Emergent Non-Eulerian Hydrodynamics of Quantum Vortices in Two Dimensions", Phys. Rev. Lett. **119**, 185301 (2017).

[382] E. Rickinson, N. G. Parker, A. W. Baggaley, and C. F. Barenghi, "Diffusion of quantum vortices", Phys. Rev. A **98**, 023608 (2018).

[383] Y. P. Sachkou, C. G. B. G. I. Harris, O. R. Stockdale, S. Forstner, M. T. Reeves, X. He, D. L. McAuslan, A. S. Bradley, M. J. Davis, and W. P. Bowen, "Coherent vortex dynamics in a strongly interacting superfluid on a silicon chip", Science **366**, 1480–1485 (2019).

[384] O. R. Stockdale, M. T. Reeves, X. Yu, G. Gauthier, K. Goddard-Lee, W. P. Bowen, T. W. Neely, and M. J. Davis, "Universal dynamics in the expansion of vortex clusters in a dissipative two-dimensional superfluid", Phys. Rev. Research **2**, 033138 (2020).

[385] A. van Kan, A. Alexakis, and M.-E. Brachet, "Intermittency of three-dimensional perturbations in a point-vortex model", Phys. Rev. E **103**, 053102 (2021).

[386] T. Kanai and W. Guo, "True Mechanism of Spontaneous Order from Turbulence in Two-Dimensional Superfluid Manifolds", Phys. Rev. Lett. **127**, 095301 (2021).

[387] R. Pakter and Y. Levin, "Nonequilibrium Statistical Mechanics of Two-Dimensional Vortices", Phys. Rev. Lett. **121**, 020602 (2018).

[388] D. Maestrini and H. Salman, "Entropy of Negative Temperature States for a Point Vortex Gas.", J. Stat. Phys. **176**, 981–1008 (2019).

[389] R. Numasato and M. Tsubota, "Possibility of Inverse Energy Cascade in Two-Dimensional Quantum Turbulence.", J. Low Temp. Phys. **158** (2010).

[390] H. Aref, "Point vortex dynamics: A classical mathematics playground", J. Math. Phys. **48**, 065401 (2007).

[391] R. Navarro, R. Carretero-González, P. J. Torres, P. G. Kevrekidis, D. J. Frantzeskakis, M. W. Ray, E. Altuntaş, and D. S. Hall, "Dynamics of a Few Corotating Vortices in Bose-Einstein Condensates", Phys. Rev. Lett. **110**, 225301 (2013).

[392] L. Campbell and K. O'Neil, "Statistics of two-dimensional point vortices and high-energy vortex states.", J. Stat. Phys. **65**, 495–529 (1991).

[393] M. Peach and J. S. Koehler, "The Forces Exerted on Dislocations and the Stress Fields Produced by Them", Phys. Rev. **80**, 436–439 (1950).

[394] A. A. Svidzinsky and A. L. Fetter, "Stability of a Vortex in a Trapped Bose-Einstein Condensate", Phys. Rev. Lett. **84**, 5919–5923 (2000).

[395] J. R. Anglin, "Vortices near surfaces of Bose-Einstein condensates", Phys. Rev. A **65**, 063611 (2002).

[396] P. Mason, N. G. Berloff, and A. L. Fetter, "Motion of a vortex line near the boundary of a semi-infinite uniform condensate", Phys. Rev. A **74**, 043611 (2006).

[397] P. Mason and N. G. Berloff, "Motion of quantum vortices on inhomogeneous backgrounds", Phys. Rev. A **77**, 032107 (2008).

[398] B. Jackson, J. F. McCann, and C. S. Adams, "Vortex line and ring dynamics in trapped Bose-Einstein condensates", Phys. Rev. A **61**, 013604 (1999).

[399] E. Lundh and P. Ao, "Hydrodynamic approach to vortex lifetimes in trapped Bose condensates", Phys. Rev. A **61**, 063612 (2000).

[400] A. A. Svidzinsky and A. L. Fetter, "Dynamics of a vortex in a trapped Bose-Einstein condensate", Phys. Rev. A **62**, 063617 (2000).

[401] P. G. Kevrekidis, W. Wang, R. Carretero-González, D. J. Frantzeskakis, and S. Xie, "Vortex precession dynamics in general radially symmetric potential traps in two-dimensional atomic Bose-Einstein condensates", Phys. Rev. A **96**, 043612 (2017).

[402] P. K. Newton, *The N-vortex problem: analytical techniques*, Vol. 145 (Springer Science & Business Media, 2013).

[403] J. B. Weiss and J. C. McWilliams, "Nonergodicity of point vortices", Physics of Fluids A: Fluid Dynamics **3** (1991).

[404] M. A. Stremler and H. Aref, "Motion of three point vortices in a periodic parallelogram", Journal of Fluid Mechanics **392**, 101–128 (1999).

[405] K. Kawasaki, "Topological defects and non-equilibrium", Progress of Theoretical Physics Supplement **79**, 161–190 (1984).

[406] M. T. Reeves, K. Goddard-Lee, G. Gauthier, O. R. Stockdale, H. Salman, T. Edmonds, X. Yu, A. S. Bradley, M. Baker, H. Rubinsztein-Dunlop, M. J. Davis, and T. W. Neely, "Turbulent relaxation to equilibrium in a two-dimensional quantum vortex gas", Phys. Rev. X **12**, 011031 (2022).

[407] V. L. Ginzburg and L. P. Pitaevskii, Sov. Phys. JETP **7**, 858 (1958).

[408] J. W. Bruce and P. J. Giblin, *Curves and Singularities* (Cambridge University Press, 1984), p. 36.

[409] G. M. Falco, T. Nattermann, and V. L. Pokrovsky, "Weakly interacting Bose gas in a random environment", Phys. Rev. B **80**, 104515 (2009).

[410] J. Eisert, M. Friesdorf, and C. Gogolin, "Quantum many-body systems out of equilibrium", Nature Phys **11**, 124–130 (2015).

[411] P. Wiegmann and A. G. Abanov, "Anomalous Hydrodynamics of Two-Dimensional Vortex Fluids", Phys. Rev. Lett. **113**, 034501 (2014).

[412] S. Whitaker, "Flow in porous media I: A theoretical derivation of Darcy's law.", Transport in Porous Media, 3–25 (1986).

[413] L. Amico *et al.*, "Roadmap on Atomtronics: State of the art and perspective", AVS Quantum Sci. **3**, 039201 (2021).

[414] T. M. Wright, C. J. Foster, and M. J. Davis, "Superfluidity and Anomalous Correlations in a Two-Dimensional Bose Gas", IQEC/CLEO Pacific Rim (2011).